THE UNIVERSITY *of* EDINBURGH

REALISTIC NUMERICAL MODELLING OF GROUND PENETRATING RADAR FOR LANDMINE DETECTION

IRAKLIS GIANNAKIS

Doctor of Philosophy

The University of Edinburgh

2016

To my family

Στους γονείς μου Ευδοξία και Γεώργιο

Στην αδερφή μου Μαρία

Στις γιαγιάδες μου Μαρία και Χρυσάνθη

Στους παππούδες μου Ηρακλή και Γεώργιο

Emotion without action is irrelevant.

–Jody Williams

DECLARATION

I hereby declare that this thesis and the work reported herein was composed and originated entirely by myself, under the supervision of Dr. Antonios Giannopoulos in the School of Engineering at The University of Edinburgh.

The following conference and journal publications are as a result of the research conducted for this thesis, which has not been submitted for any other degree or professional qualification.

Journals

- **Giannakis, I.**, Giannopoulos, A. and Warren, C., "A Realistic FDTD Numerical Modelling Framework of Ground Penetrating Radar for Landmine Detection," *IEEE Journal of Selected Topics in Applied Earth Observations and Remote Sensing.* (Accepted for publication).

- **Giannakis, I.** and Giannopoulos, A., (2015), "Time-Synchronised Convolutional Perfectly Matched Layer for Improved Absorbing Performance in FDTD," *IEEE Antennas and Wireless Propagation Letters*, volume 14, pages 690-693.

- **Giannakis, I.** and Giannopoulos, A., (2014), "A Novel Piecewise Linear Recursive Convolution Approach for Dispersive Media Using the Finite-Difference Time-Domain Method," *IEEE Transactions on Antennas and Propagation*, volume 62, number 5, pages 2669-2678.

Conferences

- **Giannakis, I.**, Giannopoulos, A., Warren, C. and Davidson, N., (2015), "Numerical modelling and Neural Networks for landmine detection using Ground Penetrating Radar," *8th International Workshop on Advanced Ground Penetrating Radar*, Florence.

- Warren, C., Giannopoulos, A. and **Giannakis, I.**, (2015), "An advanced GPR modelling framework, the next generation of gprMax," *8th International Workshop on Advanced Ground Penetrating Radar*, Florence.

- **Giannakis, I.** and Giannopoulos, A., (2014), "Realistic Modelling of High Frequency Ground Penetrating Radar for Near Surface Applications," *19th European Meeting of Environmental and Engineering Geophysics*, Athens.

- **Giannakis, I.**, Giannopoulos, A. and Davidson, N., (2014), "Realistic modelling of ground penetrating radar for landmine detection using FDTD," *15th International Conference on Ground Penetrating Radar (GPR)*, pages 954-959, Brussels.

- **Giannakis, I.**, Giannopoulos, A. and Pajewski, L., (2014), "Numerical Modelling of Ground Penetrating Radar Antennas," *EGU General Assembly*, Vienna.

- **Giannakis, I.**, Giannopoulos, A. and Davidson, N., (2012), "Incorporating dispersive electrical properties in FDTD GPR models using a general Cole-Cole dispersion function," *14th International Conference on Ground Penetrating Radar (GPR)*, Shanghai.

Awards

- **Shortlisted for the R. W. P. King award**. The R. W. P. King award is given to an author under 35 years of age for the best paper published in IEEE Transactions on Antennas and Propagation during the previous year.

- **Best paper oral presentation**. Awarded to the best paper submitted by a PhD or post-doc in the 15th International Conference on Ground Penetrating Radar 2014.

- **Shortlisted for the best paper oral presentation**. The paper was among the 7 papers nominated for the best paper oral presentation during the 14th International Conference on Ground-Penetrating Radar 2012.

Edinburgh, 2016

Iraklis Giannakis

ABSTRACT

Ground-Penetrating Radar (GPR) is a popular non-destructive geophysical technique with a wide range of diverse applications. Civil engineering, hydrogeophysics, forensic, glacier geology, human detection and borehole geology are some of the fields in which GPR has been applied with successful or promising results. One of the most mainstream applications of GPR is landmine detection. A lot of methods have been suggested over the years to assist the landmine detection issue. Metal detectors, trained rats or dogs, chemical methods and electrical resistivity tomography are –amongst others– some of the suggested techniques. The non-destructive nature of GPR makes it an attractive choice for a problem such as demining in which contact to the ground is not allowed. The main advantage of GPR is its ability to detect both metallic and non-metallic targets. Furthermore, GPR can provide an insight regarding the nature of the target (e.g. size, burial depth, type). From the above, it is evident that GPR can potentially reduce the false alarms emerging from small metallic objects (e.g. bullets, wires, etc.) usually encountered in battle-fields and industrialised areas. Combining the robustness of the metal detector with the resolution of GPR results in a reliable and efficient detection framework which has been successfully applied in Cambodia and Afghanistan.

Despite the promising, and in some cases impressive results, aspects of GPR can be further improved in an effort to optimise GPR's performance and decrease its limitations. The validation of a GPR system is usually achieved through the so called Receiver Operation Characteristics (ROC) which depicts the probability of detection with respect to the false alarm rate. ROC is a highly nonlinear function which is sensitive to the environment as well as to the antenna unit.

Landmines are typically small objects, often less than 10 cm diameter, which are shallow buried, usually in less than 10 cm depth, and sometimes almost exposed. In order for the landmines to be resolved, high frequency antennas are essential. The latter are sensitive to soil's inhomogeneities, rough surface, water puddles, vegetation and so on. Apart from that, the near field nature of the problem makes the antenna unit part of the medium which contributes to the unwanted clutter. The above, outlines the multi-parametric nature of the problem for which no straightforward approach has yet to be proposed.

Numerical modelling is a practical and solid approach to understand the physical behaviour of a system. In the case of GPR for landmine detection,

numerical modelling can be a practical tool for designing and optimising antennas in synthetic but nonetheless realistic conditions. Apart from that, evaluation of a processing method only to a specific environment is not a robust approach and does not provide any evidence for its wider inclusivity and limitations. However, evaluation in different conditions can become costly and unpractical. Numerical modelling can tackle this problem by providing data for a wide range of scenarios. An extensive database of simulated responses, apart from being a practical testbed, can be also employed as a training set for machine learning. A multi-variable problem like demining, in order to be addressed using machine learning, requires a large amount of data. These must equally include all possible different scenarios i.e. different landmines, in different media with stochastically varied properties and topography. Additionally, different heights of the antenna and different depths of the landmines must also be examined. Numerical modelling seems to be a practical approach to achieve an equally distributed and coherent dataset like the one briefly described above.

Numerical modelling of GPR for landmine detection has been applied in the past using generic antennas in simplified and clinical scenarios. This approach can be used in an educational context just to provide a rough estimation of GPR's performance. In the present thesis a realistic numerical scheme is suggested in which, simplifications are kept to a minimum. The numerical solver, employed in the suggested numerical scheme, is the Finite-Difference Time-Domain (FDTD) method. Both the dispersive properties and the Absorbing Boundary Condition (ABC) are implemented through novel and accurate techniques. In particular, a novel method which implements an inclusive susceptibility function is suggested and it is shown that surpasses the performance of the previous approaches while retaining their computational efficiency. Furthermore, Perfectly Matched Layer (PML) and more specifically Convolutional Perfectly Matched Layer (CPML) is implemented through a novel time-synchronised scheme which it is proven to be more accurate compared to the traditional CPML with no additional computational requirements.

An accurate numerical solver, although essential, is not the only requirement for a realistic numerical framework. Accurate implementation of the geometry and the dielectric properties of the simulated model is highly important, especially when it comes to high-frequency near-field scenarios such as GPR for landmine detection. In the suggested numerical scheme, both the soil's properties as well as the rough surface are simulated using fractal correlated noise. It is shown, that fractals can sufficiently represent Earth's topography and give rise to semi-variograms often encountered in real soils. Regarding the dielectric properties of the soils, a semi-analytic function is employed which relates soil's dielectric properties to its sand fraction, clay fraction, sand density,

bulk density and water volumetric fraction. Subsequently, the semi-analytic function is approximated using a Debye function that can be easily implemented to FDTD. Vegetation is also implemented to the model using a novel method which simulates the geometry of vegetation through a stochastic process. The experimentally-derived dielectric properties of vegetation are approximated –similarly to soil's dielectric properties– with a Debye expansion. The antenna units tested in the numerical scheme are two bow-tie antennas based on commercially available transducers. Regarding the targets, three landmines are chosen, namely, PMN, PMA-1 and TS-50. Dummy landmines are used in order to obtain their geometrical characteristics and comparison between measured and numerically evaluated traces are used to tune the dielectric properties of the modelled landmines. Lastly, water puddles are realistically implemented in the model in an effort to realistically simulate high-saturated scenarios.

The proposed numerical scheme has been employed in order to test and evaluate widely used post-processing methods. The results clearly illustrate that post-processing methods are sensitive to the antenna unit as well as the medium. This highlights the importance of an accurate numerical scheme as a testbed for evaluating different GPR systems and post-processing approaches in wide range of scenarios.

Using an equivalent 2D numerical scheme –restricted to 2D due to computational constrains– preliminary results are given regarding the effectiveness of Artificial Neural Network (ANN) subject to an adequate and equally distributed database. The results are promising, showing that ANN can be successfully employed for detection as well as classification using only a single trace as input. A basic requirement to do so is a representative training set. This can be synthetically generated using a realistic numerical framework. The above, provide solid arguments for further expanding the proposed machine learning scheme to the more computationally demanding 3D case.

LAY SUMMARY

Anti-Personnel (AP) landmines are small palm-shaped explosive devices that are designed to maim or injure their victims. They are typically shallow buried, no more than 10 cm and in many cases they are almost exposed with only a small layer of dust covering them. Demining is a process that tries to detect and disable AP landmines in an non-destructive way while balancing between safety and efficiency.

Ground-Penetrating Radar (GPR) is a very promising demining method that has been successfully applied in Afghanistan, Cambodia and so on. The present thesis focuses on the numerical modelling of GPR for AP landmine detection. Many aspects related to numerical modelling were investigated and novel methods have been proposed in order to increase the reliability of the numerical framework.

Having the ability to generate synthetic but nonetheless realistic data can be a powerful tool for comparing different antenna units and processing frameworks. Through this research, strong evidence is provided which indicates that the performance of GPR is highly sensitive to the environment as well as to the antenna system.

Lastly, a representative and well-labeled database can be generated using the proposed numerical framework. Consequently, a question arises if machine learning can take advantage of this. Through an initial 2D numerical study, strong evidence is given which supports the premise that using an equally distributed and representative training set, Artificial Neural Network (ANN) can be trained and successfully used for both detection and classification purposes.

ACKNOWLEDGMENTS

I would like to express my sincere gratitude to my supervisor Dr. Antonios Giannopoulos for his continuous support and guidance during my PhD. His coherent knowledge on the subject, his passion for research and his optimism were invaluable. I could not have imagined having a better advisor and mentor for my PhD.

My sincere thanks also goes to Prof. Panagiotis Tsourlos from Aristotle University of Thessaloniki. He was and still is a mentor to me and the person who introduced me to the world of research. I could not thank him enough for his guidance and the opportunities he gave me throughout my studies.

I also want to thank Dr. Nigel Davidson from the Defence Science and Technology Laboratory (DSTL) for supervising this project and also for his enthusiastic support and involvement.

Special thanks goes to my fellow colleagues from the Alexander Graham Bell, the William Rankine and the John Muir building, of whom there are too many to mention specifically, for the friendly atmosphere and the stimulating environment they provide the last four years. It was a joy and a memorable experience working there.

I want to sincerely thank all the countries that have welcomed me and all the interesting people I met during my PhD. Special thanks goes to my conference-mates Nectaria Diamanti and Craig Warren for the great times we had around the world.

Completing this work would have been more difficult without the support of my friends both in Greece and Scotland. I would like to thank my flatmates Athanasios Stavridis and Georgios Koutsovoulos for their honest friendship, the endless discussions and the memorable times that we had.

Last but not least I would like to thank my family for their endless love and support, all of them have been an inspiration to me and I will always be in dept to them.

CONTENTS

LIST OF FIGURES

LIST OF TABLES

ACRONYMS

ABC Absorbing Boundary Condition

ADE Auxiliary Differential Equation

ADI Alternating-Direction Implicit

ANN Artificial Neural Network

AP Anti-Personnel

ASaS Adaptive Shifted and Scaled

C-C Complex-Conjugate

CFS-PML Complex Frequency Shifted Perfectly Matched Layer

CO Common Offset

CMP Common Mid-Point Reflection

CPML Convolutional Perfectly Matched Layer

CRIM Complex Refractive Index Model

CD Current Density

DNAPL Dense Non Aqueous Phase Liquids

ECDF Edinburgh Compute and Data Facility

ERT Electrical Resistivity Tomography

FD Finite-Differences

FDTD Finite-Difference Time-Domain

FEM Finite Element Method

FETD Finite Element Time-Domain

ICBL International Campaign to Ban Landmines

ICRC International Committee of the Red Cross

GPR Ground-Penetrating Radar

MoM Method of Moments

NGO Non-Government Organisations

PCA Principal Components Analysis

PD Polarisation Density

POD Probability of Detection

PEC Perfect Electric Conductor

PFA Probability of False Alarm

PLRC Piecewise Linear Recursive Convolution

PML Perfectly Matched Layer

PMC Perfect Magnetic Conductor

PSO Particle Swarm Optimisation

PSTD Pseudo-Spectral Time-Domain

RAM Random-Access Memory

RC Recursive Convolution

RIPML Recursive Integration Perfectly Matched Layer

ROC Receiver Operation Characteristics

SCG Scaled Conjugate Gradiend-descent

SC-PML Stretched Coordinates Perfectly Matched Layer

SFCW Stepped Frequency Carrier Wave

SNR Signal to Noise Ratio

SP Self Potential

SVD Singular Value Decomposition

SVM Support Vector Machines

TE Transverse Electric

TM Transverse Magnetic

TLM Transmission Line Matrix

TNT trinitrotoluene

TRC Trapezoidal Recursive Convolution

UN United Nations

UPML Uniaxial Perfectly Matched Layer

UWB Ultra Wide Band

UXO Unexploded Ordnance

WARR Wide-Angle Reflection-Refraction

1 INTRODUCTION

1.1 MOTIVATION AND AIMS OF THE RESEARCH

GPR is a widely used non-destructive geophysical technique. GPR has found applications in a wide range of fields, which vary from locating rebars in concrete (Buyukozturk, 1998) to glaciology (Blindow et al., 2012) and forensic applications (Koppenjan et al., 2004). One of the most mainstream GPR's application is demining (Daniels, 2006). The main technique which is traditionally used for landmine detection is the metal detector. The latter, cannot detect plastic landmines and also is vulnerable to false alarms due to the presence of small metallic objects (bullets, metal wires and so on) (Kaneko et al., 2014). GPR has the ability to detect both plastic and metal landmines and also has the potential to decrease the false alarm rate. Due to the ultra-wide band nature of GPR, adequate information is retrieved, nonetheless, interpretation of this information is not straightforward. In addition to that, the small depth which the landmines are buried, combined with the small size of the targets, requires the use of high frequency antennas which are constrained to operate within a small proximity to the ground. The above, increase the unwanted clutter and make the antenna unit an important part of the problem which contributes to the scattering field and highly affect the performance of GPR.

Landmines can be found in a variety of environments each of which gives rise to a diverse set of scattering fields. Processing algorithms as well as antenna units need to address the problem of diversity i.e. need to perform equally well in different environments. Otherwise it is necessary to clearly state the limitations and the applicability of any suggested GPR system.

GPR systems are evaluated in test-fields which are called mine lanes. It has been reported in the literature that clinical mine lanes can give a false impression regarding the capabilities of GPR systems which when tested in realistic-complex environments they often do not achieve the expected performance (Daniels, 2006). Performing experiments in different environments and having control of the field conditions can become both time-consuming as well as expensive.

Numerical modelling has the potential to overcome these issues. Through numerical modelling, processing algorithms can be tested in a variety of well controlled environments. In addition, antenna units can be easily tested and optimised in a practical and cost-effective manner. Apart from that, large

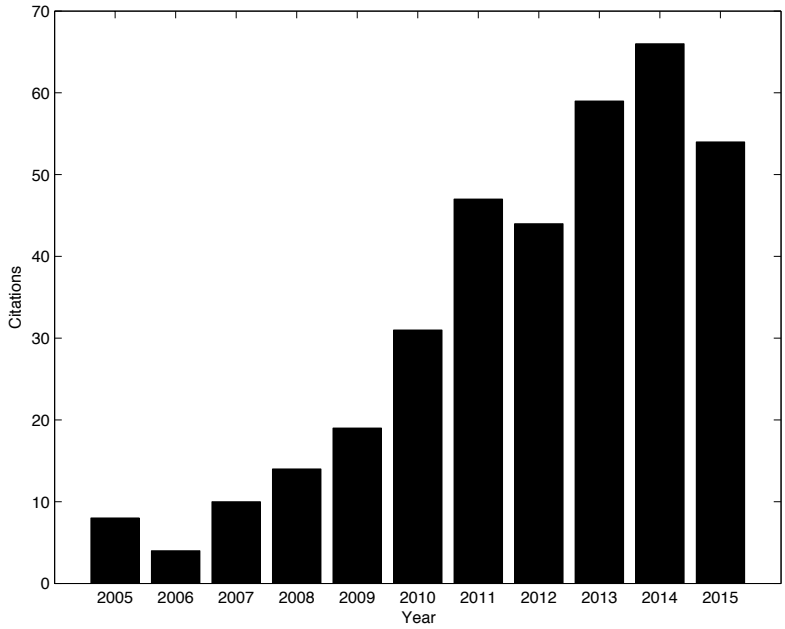

Figure 1: Publications that have cited gprMax (www.gprmax.com) from 2005-2015.

datasets for different types of environments, targets and antennas can be numerically evaluated and subsequently employed for training purposes in pattern recognition algorithms like ANN.

Therefore, numerical modelling is considered as a promising tool which can be used to address issues related to demining. In order to do so, numerical modelling must realistically simulate all the aspects of the model, namely, the shallow surface of the soil, the antenna unit, the rough surface, vegetation, water puddles and landmines. Both the geometry and the dielectric properties must be realistically implemented into the models. Simplified models with ideal dipoles over homogenous half-spaces, although they can provide a rough estimation of the performance of GPR, nonetheless, they can not be used to validate GPR systems neither assist machine learning.

1.1.1 *Numerical modelling for landmine detection using GPR*

Numerical modelling has been extensively used by the GPR community in order to asses the performance of GPR and also as an alternative interpretation tool (Cassidy, 2007). This is illustrated in Fig. 1 in which the number of publications that have cited a free GPR numerical simulator gprMax (Giannopoulos, 2005) (www.gprmax.com) is illustrated. It is evident that the popularity of numerical modelling increases almost linearly with time. The main reason for that is the fact that the computational resources needed for an accurate numerical

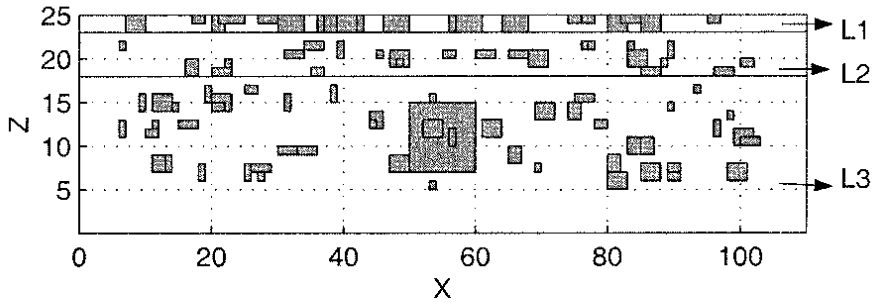

Figure 2: Soil's inhomogeneities (L3), vegetation (L2) and rough surface (L1) modelled using randomly placed boxes (Gurel and Oguz, 2001).

modelling scheme are now trivially accessible by universities and research institutes.

A first attempt to model a full GPR scenario was done by Bourgeois and Smith (1996) and Bourgeois and Smith (1997) in which bowtie and dipole antennas were simulated using FDTD. The modelled antennas were placed on top of oil emulsions which they resemblance the dielectric properties of soils. The effective permittivity of the medium was implemented using a Debye pole. The modelled scenario was successfully validated using real data. Giannopoulos (1997) also employed FDTD in order to model GPR scenarios using clinical homogenous models similar to Bourgeois and Smith (1996) and Bourgeois and Smith (1997). In the same concept, Giovanneschi et al. (2013) modelled homogenous media with flat surface in which cylindrical targets were buried in different depths. The dielectric properties were simulated using a constant electric permittivity plus a conductive term. The resulting synthetic traces were subsequently used in order to evaluate the time-frequency transform for identifying features associated with shallow-buried targets (landmine-like objects). More complicated targets, which resemblance AP landmines were modelled by Alawneh (2004) in free space. Simple excitation sources were employed in an effort to retrieve the characteristic reflectivity of a set of AP landmines. Ho et al. (2008) used FDTD in order to model accurate models of landmines (for which, no details were given due to confidentiality issues) buried in a clinical homogenous soil with flat surface. The dielectric properties were implemented using a constant permittivity plus a conductive term. A resistive-loaded dipole was used for their simulations. Although the pair antenna-landmine was realistically modelled, a homogenous half-space, simulated using a constant permittivity plus a conductive term is an oversimplification which can overestimate the performance of GPR. Similar simplified models were used by Roth et al. (2005) in an effort to validate a deconvolution-based detection framework. Lopera and Milisavljevic (2007) used FDTD to model

2D homogenous soils with flat surface. The dielectric properties of soil's were calculated using the semi-empirical model suggested by Dobson et al. (1984). Although the semi-empirical model describes a dispersive electric permittivity which contains ionic plus dipolar losses, nonetheless Lopera and Milisavljevic (2007) implemented only the constant part of the real permittivity plus a conductive term. Clutter in the model was introduced by Gurel and Oguz (2000, 2001), Oguz and Gurel (2002) and Gurel and Oguz (2003). In their work soil's inhomogeneities were implemented using randomly placed boxes. The rough surface as well as the vegetation were implemented –similar to soil's inhomogeneities– using randomly spaced boxes (see Fig. 2). Regarding the dielectric properties, a constant permittivity plus a conductive term were implemented to FDTD. Nishimoto et al. (2006) employed FDTD in order to simulate 2D homogenous models with a rough surface. The roughness of the surface was modelled using a Gaussian correlation. Simple targets were used to simulate landmine-like objects. Similar to the previous approaches, a constant permittivity plus a conductive term were used to simulate the dielectric properties of the soil.

Gonzalez-Huici et al. (2007) and Gonzalez-Huici (2012) used frequency domain numerical solvers to simulate a generic antenna and two mine-like objects buried in a realistically modelled soil. The soil as well as the surface were modelled using random noise with a given correlation step. Using the aforementioned numerical scheme, a library of traces was generated which was subsequently used in an effort to discriminate between AP landmines and false alarm targets. Although the dielectric properties were simulated using a constant permittivity plus a conductive term (thus, neglecting the dipolar losses of soils), nonetheless Gonzalez-Huici et al. (2007) and Gonzalez-Huici (2012) introduced realistic clutter to the simulations which substantially increased the reliability of the resulting synthetic data.

Notice that in all the aforementioned modelling frameworks, generic types of bowtie and dipole antennas, ideal Hertzian dipoles and line sources were employed. In addition, different types of generic antennas have been investigated by numerous researchers and their performance were evaluated using numerical modelling. Namely, spiral antennas (Sato et al., 2005, Van Genderen et al., 2003), low dielectric conical horns (Teggatz et al., 2005), air-coupled wedge antennas (Savelyev et al., 2007), Vivaldi (Sato et al., 2003, 2005), horn-fed bowtie (Youn and Chen, 2005), dielectric rode antennas (Youn and Chen, 2005), vee dipoles (Nuzzo et al., 2014), dielectric-filled TEM horn (Bart et al., 2000), ridged horn antennas (Panzner et al., 2010) and bowtie antennas (Gonzalez-Huici et al., 2007, Gonzalez-Huici, 2012, Metwaly, 2007, Tesfamariam, 2013).

Numerous GPR systems, both handheld (for AP landmine detection) and arrays (for anti-tank landmine detection) were designed and some of them are commercially available. Daniels (2004) provides a review of the research related to GPR systems divided by country of origin. Handheld devices are primarily used for AP landmine detection and they are usually consist of a GPR system accompanied by a metal detector. These devices are called dual sensors, examples of dual sensors are the well-known MINEHOUND and HSTAMID (Daniels, 2004). Modelling these systems is particularly difficult due to confidentiality constrains and to our knowledge there is no published numerical framework using commercial systems designed specifically for demining.

The same problems (arising from confidentiality constrains) occur for commercial systems designed for more generic GPR applications, namely, engineering, forensic, geophysical and so on. Nonetheless, through reverse engineering, sufficiently accurate models of commercial antennas can be achieved (Warren, 2009). The commercial antennas GSSI 1.5 GHz and MALA 1.2 GHz have been succesfully modelled by Warren and Giannopoulos (2011) and Warren and Giannopoulos (2012). Although these antennas are not specifically designed for landmine detection , nonetheless, the high frequency pulses which these systems employ combined with their ground coupled nature and the fact that they are easily accessible make them attractive choices for evaluating and demonstrating the capabilities of an accurate numerical framework for AP landmine detection.

1.1.2 *Objectives*

The key objectives of the present thesis are outlined as follows:

- Develop software tools which will increase the accuracy of the numerical solver (in the present case FDTD).
- Create a numerical scheme which will realistically (and in a straightforward manner) implement soil, rough surface, vegetation, antenna units and landmines into the model. Both the geometry and the dielectric properties must be accurately modelled.
- Use the proposed numerical scheme to investigate if antennas and processing methods are case sensitive and underline the need for a more coherent and inclusive evaluation of GPR systems.
- Evaluate the performance of ANN subject to an adequate and complete training set.

1.2 THESIS STRUCTURE

The following paragraphs outline the basic structure of the thesis:

Chapter 2: The global AP landmine crisis is described. Graphs and statistics are given in order to illustrate some aspects of the issue and depict the magnitude of the problem. Chapter 2 also focuses on the Ottawa treaty and the effects it had and still has. Lastly, an introduction on the demining techniques is given with an emphasis on GPR.

Chapter 3: The basic principles of GPR are presented and emphasis is given on the post-processing techniques applied to raw data. In addition, data gathering techniques are described and widely used terms in GPR community (A-Scan, B-Scan, C-Scan etc.) are explained.

Chapter 4: Maxwell's equations are presented and the physical interpretation of dielectric properties is given. Chapter 4 also focuses on the dielectric properties of soils. The dispersive mechanisms within soils are analysed and the functions which are mainly used to describe the dielectric properties of soils are outlined.

Chapter 5: The aim of this chapter is to provide a basic background on the FDTD method. Numerical errors as well as stability conditions are defined and novel methods to implement dispersive properties and to truncate the grid's boundaries are suggested.

Chapter 6: In this chapter, a numerical framework is proposed in order to simulate GPR for landmine detection. A detailed description of the suggested scheme is given and simulation results are provided which are subsequently used to evaluate antennas and processing algorithms.

Chapter 7: A case study is presented in which a numerically evaluated database is used for ANN training purposes. The training set is synthetically generated using a (equivalent to the one presented in Chapter 6) 2D numerical scheme. The purpose of the present study is to investigate the performance of ANN subject to a representative training set.

Chapter 8: This chapter summarises the thesis outputs and outlines the suggested future work.

2

THE GLOBAL ANTI-PERSONNEL MINE CRISIS

The present chapter is a brief introduction on the global AP landmine issue, focusing on its consequences and the counter-measurements taken to tackle it. It starts with a historical overview of the use of landmines from World War I till now. The lack of military utility of AP landmines is discussed and the importance of it to the Ottawa treaty (officially known as Convention on the Prohibition of the Use, Stockpiling, Production and Transfer of AP mines and on their Destruction) is highlighted. Lastly, a general review of the demining methods is given, focusing on GPR and the reasons why it is considered one of the most sophisticated and advanced demining techniques.

2.1 INTRODUCTION

The term "landmine" describes any explosive device buried under the ground which is designed to kill, maim or destroy enemy targets (pedestrian troops, vehicles etc.) (Random House Dictionary, 2012). Unexploded Ordnance (UXO) are explosive weapons which did not explode as they were designed to do so. The nature of these explosives makes them unstable posing a danger to the local communities. The difference between UXO's and landmines is that the latter are designed and created in order to pose an invisible threat which can be active for long time after the war. Although anti-vehicle landmines require excessive pressure (such as the weight of a military vehicle) to explode, AP landmines can be triggered easily, sometimes even from the weight of small animals. Because of that, the victims of AP landmines are usually civilians who are killed or maimed long after the war is over (Cameron et al., 1998). The vast number of civilians killed or maimed from AP landmines is the reason why the issue of AP landmines is accounted as a humanitarian crisis known as "The Anti-Personnel Mine Crisis" (Cameron et al., 1998).

Landmines, were initially employed during World War I. Artillery shells with exposed fuses were used by the German army as anti-vehicle weapons. These early improvised devices were replaced after the discovery of TNT which gave rise to the modern anti-vehicle landmines (Cameron et al., 1998). Modern anti-vehicles landmines were extensively used during World War II. According to the US Defence intelligence agency (1992) more than 300 million anti-vehicle

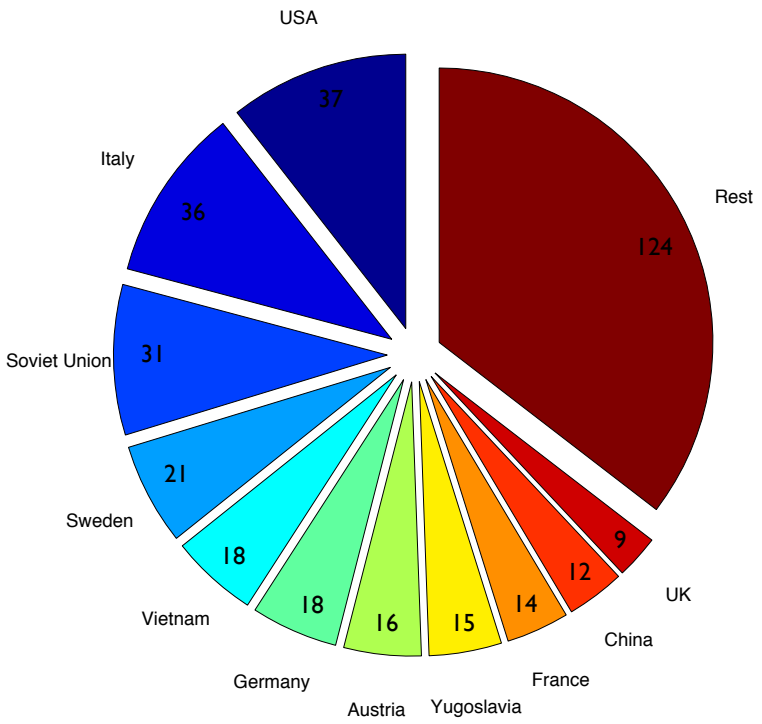

Figure 3: Types of AP landmines produced the last 25 years by country (Cameron et al., 1998).

landmines were placed during World War II, mostly by the Soviet Union, Germany and the United states of America.

The first AP landmines were initially used in an effort to protect anti-vehicle landmines from pedestrian troops. Improvised and handmade mechanisms which involved grenades and electric fuses were firstly employed during World War I (Cameron et al., 1998). Later on, AP landmines started to be used on their own. It is interesting to note that the first independent usage of AP landmines was to demoralise the enemy. Although never officially admitted, during World War II it was reported that soldiers used to booby-trap everyday objects even dead bodies (Cameron et al., 1998) in an attempt to terrorise the enemy with a practically null military utility.

AP landmines are small and light objects, their diameter varies from 5-15 cm and their average weight is roughly 400 grams. They are typically shallow buried (less than 10 cm) and can be frequently found exposed due to erosion. AP landmines are divided into blast and fragmentation landmines. Blast AP landmines are designed in order to maim the individual who steps on them. The soil debris, the rock fragments, the melted plastic and the power of the explosion usually blows off the victim's leg. In the worst scenario, AP landmines have the potential to be lethal although they are designed to maim and not kill the victims. This is done because an injured soldier is proven to be more costly

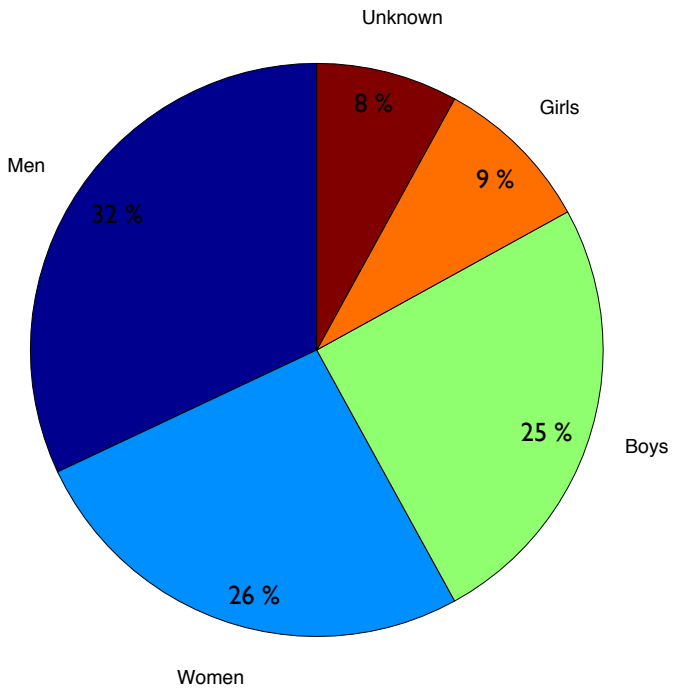

Figure 4: AP landmine victims by gender in Africa (LCD3, The World Bank).

for the enemy (Cameron et al., 1998). Fragmentation AP landmines are typically larger than blast AP landmines with higher metal content which makes them easier to be detected using metal detectors as well as GPR. They are designed to fire fragments to different directions creating a killing radius. Both blast and fragmentation AP landmines can be further divided into subcategories, namely, scatterable AP landmines (AP landmines that can be scattered from a plane) and bounding AP landmines (AP landmines that when activated launch of the ground and explode when they reach approximately one meter height).

AP landmines are simple devices which can be trivially manufactured with a limited amount of resources (usually 3-5 $ per AP landmine) (Cameron et al., 1998). This is one of the reasons which explains the extensive production and usage of AP landmines over the years. The last 25 years more than 350 types of AP landmines were constructed in 52 different countries (HRW and PHR, 1993). Fig. 3 presents the main manufacturing countries by number of different AP landmines types. According to the International Committee of the Red Cross (ICRC), AP landmines kill or maim more than a thousand victims every month (UN, 1994) (mostly civilians, see Fig. 4). The ICRC estimates that the last fifty years more damage has been done from AP landmines than nuclear and chemical weapons combined (ICRC, 1996). As stated by Cameron et al. (1998), AP landmines are the modern edition of salting the enemy's soil in order to poison and pollute the area for a long time after the war. Even a few

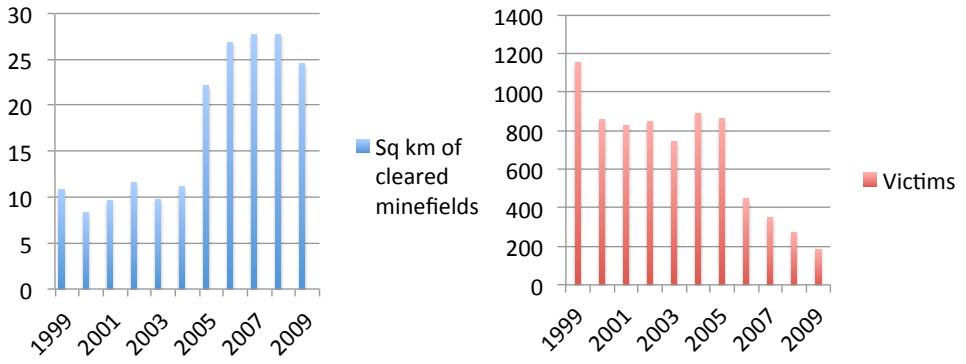

Figure 5: Cleared areas and AP landmine victims in Cambodia from 1999 to 2009 (Cambodian Mine Action Centre, 2014).

number of casualties or exposed landmines can pollute an area for a long time and give reasons for major population movements as has been demonstrated in Cambodia, Bosnia and Africa (Cameron et al., 1998). The above facts justify the fact that AP landmines are accounted as one of the worst cases of global pollution (Cameron et al., 1998).

The solution to the AP landmine crisis is humanitarian demining, although it is proven to be a very slow procedure (Acheroy, 2007). As stated by ICRC (1996), with the current rate of removal, and in the ideal scenario in which the use of landmines is globally stopped, it would take more than a thousand years and 33 billion dollars to clear the active minefields. In addition, ten new landmines are placed for every cleared one (Gooneratne et al., 2004) and in absolute numbers 2-5 million mines are planted every year (ICRC, 1996). The facts above create the need for faster and more efficient demining methods. Despite the aforementioned imbalance between cleared and uncleared minefields, demining can have very positive effects in reducing the number of AP landmine victims as it is clearly illustrated in Fig. 5 (Cambodian Mine Action Centre, 2014).

Humanitarian demining has three basic tasks: marking the boundaries of the affected areas, locating the targets and subsequently disable them. The United Nations (UN) humanitarian clearance standards are 99.6 %. This means that in a minefield which consists with 1000 AP landmines it is unacceptable to leave more than 4 AP landmines on the ground (Cameron et al., 1998). When the clearance is over, the members of the crew are holding hands and they walk around the cleared area while local communities are watching (Cameron et al., 1998).

Humanitarian demining faces many difficulties which emerge from the large number of different types of AP landmines as well as the large diversity of the environments in which they can be found. AP landmines can be found

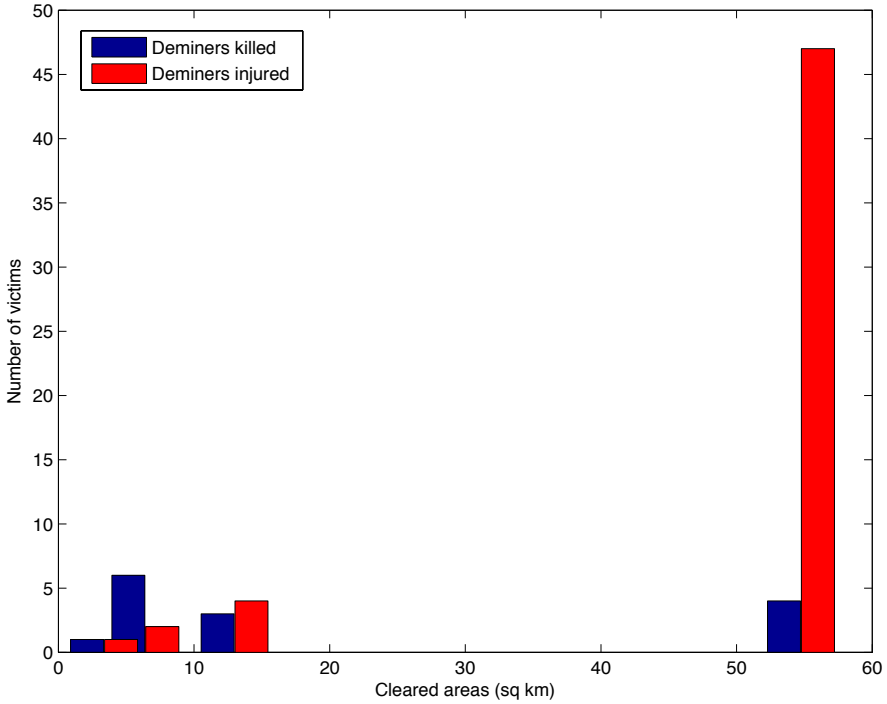

Figure 6: Cleared areas with respect to accidents for 2000-2009 in Zimbabwe, Bolivia, Iran and Latvia (LCD3, The World Bank).

in deserts, mountain areas, urban environments and so on (Daniels, 2006). In addition, landmine-affected areas are frequently abandoned for years, this implies that when demining takes place, usually the area is covered with dense vegetation. Removing vegetation is risky due to very thin tripwires connected to explosive devices (Cameron et al., 1998). The thin tripwires are hidden in vegetation and they are not always visibly detectable. This makes demining risky and despite the advance of new technologies, one deminer is maimed or killed for every 1000-2000 AP disabled landmines (Cameron et al., 1998). Fig. 6 illustrates the injured and killed deminers with respect to the cleared areas. Decreasing the accidents rate to a minimum while retaining operational efficiency (with respect to time) is the main goal of the research associated with demining.

2.2 THE ANTI-LANDMINE MOVEMENT AND THE OTTAWA TREATY

From the early 1970s, awareness was started to raise over the fast growing AP landmine issue. One of the first Non-Government Organisations (NGO) for humanitarian clearance programs was created in Afghanistan in 1980 by a former British army sergeant. His job was agricultural development but soon he realised that it was an impossible task due to the heavy AP

landmine contamination (Cameron et al., 1998). In 1991, the first appeal for an international ban of the landmines has been done in the US Congress by a member of the women's commission on refugee women and children. The appeal was made after spending months in the refugee camps in Cambodia which is one of the most landmine-infected countries (due the abuse of AP landmines during the civil war in 1970) (Cameron et al., 1998). Cambodia's landmine problem triggered the Human Rights Watch as well as the Physicians For Human Rights to call for a global ban of AP landmines in 1991 (Cameron et al., 1998). Subsequently, the Vietnam Veterans of America Foundation, after spending time to help the AP landmine victims in Cambodia, they concluded that the only solution was to ban landmines and they launched a campaign to do so (Cameron et al., 1998).

The humanitarian consequences of AP landmines (although devastating) were used primarily in an effort to increase the public image of the anti-landmine movements and to attract the attention of the media. The main argument against AP landmines was their military utility combined with the unbalanced suffering they cause to civilians (Cameron et al., 1998). This was backed up by The Law of Land Warfare (1956) which states that the civilian casualties must not be out of proportion compared to the military advantages gained (Cameron et al., 1998). The International Humanitarian law also prohibits the use of weapons that cause unnecessary suffer, unbalanced with their military utility (Cameron et al., 1998). These criteria were used to prohibit the use of biological and chemical weapons in the biological weapons convention in 1972 (Cameron et al., 1998). The same criteria were used to support the premise that AP landmines, similar to biological weapons, should be banned.

The limited military utility of the AP landmines was one of the key reasons for the success of the anti-landmine movement. The main argument in favour of AP landmines is that they shape the battlefield and force the enemy to disadvantageous formations (Cameron et al., 1998). However, this is not in good agreement with experience. During the Gulf War, a wall consisted of 9 million landmines was breached within just two hours (ICRC, 1996). In addition, there are reported cases of non-humane strategies like moving troops over minefields in order to rapidly clear them (Cameron et al., 1998). Apart from that, it has been reported that troops have been frequently trapped inside their own minefields (Cameron et al., 1998). Based on similar cases to the ones described above, fifteen former senior military officers signed an open letter to the USA president which states the lack of military utility of AP landmines and advise president Clinton to ban the use of them (Letter to President Clinton, 1996).

In 1997 an organised investigation was committed by the ICRC in order to validate and analyse the utility of the AP landmines. The investigation is considered reliable, since 55 military officers from 19 different countries took part. Their conclusion is clearly and briefly outlined by Cameron et al. (1998):

"No case was found in which the use of anti-personnel mines played major role in determining the outcome of a conflict; they had little or no effect on the outcome of hostilities; they had only limited effect on unprotected infantry; and while these weapons had a marginal tactical value under specific conditions the effects are very limited and may even be counterproductive" (Cameron et al., 1998).

The early anti-landmine movements and the growing public exposure led to the first Ottawa meeting held on 3-5 October of 1996 (Cameron et al., 1998). The meeting outperformed the expectations with 50 countries signing that the ban of landmines is a serious issue which should be addressed rapidly (Cameron et al., 1998). At the end of the meeting the foreign Minister of Canada Mr. Axworthy challenge the diplomats who attended the meeting, to meet in Ottawa within a time period of a year with a simple and clear banning treaty.

The following months, a lot of meetings and campaigns took place in order to negotiate and raise awareness about the treaty. The most important were the negotiations in Oslo (Cameron et al., 1998) in which the treaty was very rigorously and clearly defined (Cameron et al., 1998):

General obligations
1. *Each State Party undertakes never under any circumstances:*
A) To use anti-personnel mines.
B) To develop, produce, otherwise acquire, stockpile, retain or transfer to anyone, directly or indirectly, anti-personnel mines.
C) To assist, encourage or induce, in any way, anyone to engage in any activity prohibited to a State Party under this Convention.
2. *Each State Party undertakes to destroy or ensure the destruction of all anti-personnel mines in accordance with the provisions of this Convention.*

After the Oslo negations, on 10 October of 1997, the Nobel price was given to the International Campaign to Ban Landmines (ICBL) and to the main co-ordinator Jody Williams (Cameron et al., 1998). The Nobel price increased the public image and helped towards the following convention in Ottawa in which the Oslo agreement was going to be signed. In 3 December of 1997 in

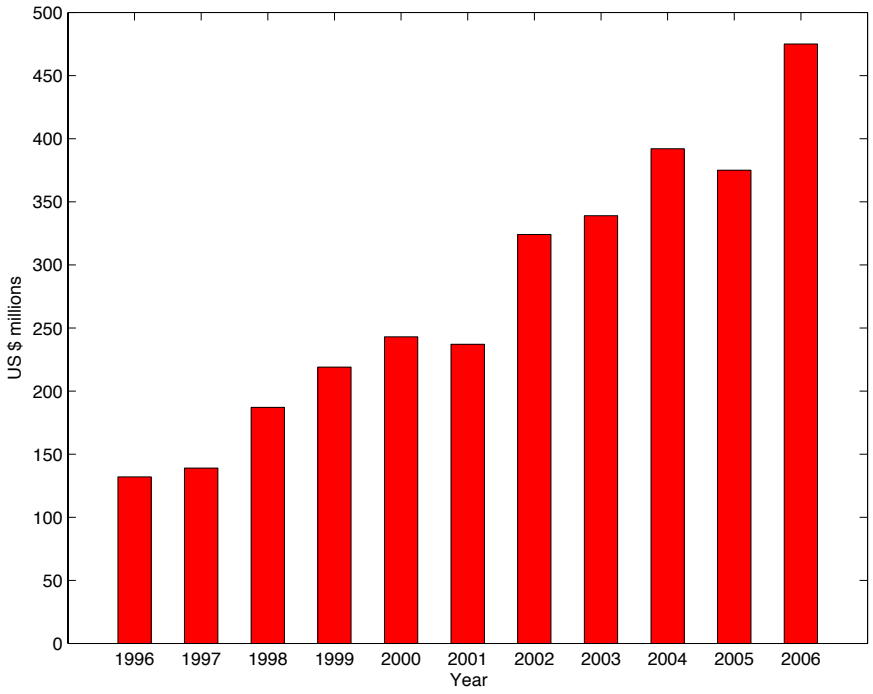

Figure 7: Global mine action funding for 1996-2006 (Landmine Monitor Report, 2007).

Ottawa, 122 countries signed the ban of AP landmines. Later on, more countries followed and today 162 countries are members of treaty. Although USA, Russia and China are still no members of the convention, nonetheless the Ottawa treaty was a humanitarian triumph which clearly marked the beginning of the end of probably the worst case of global pollution.

2.3 DEMINING METHODS

In the years followed the Ottawa treaty, funding for mine action was increased almost linearly with time (Landmine Monitor Report, 2007) as it is illustrated in Fig. 7. This led to the development of new demining methods and to the advancement of the already existed ones.

A large number of demining methods have been suggested over the years, the most common (and the first humanitarian demining method used) is the metal detector (Acheroy, 2007, Claudio et al., 1998). The drawbacks of the latter are A) failure to detect plastic landmines (the majority of modern landmines are almost entirely plastic (UN, 1994)), B) high sensitivity to metal fragments which increases the false alarm rate (Gooneratne et al., 2004) and C) unreliable in soils with high metal content (Cameron et al., 1998). Other demining methods vary from trained dogs, trained rats (APOPO, 2006), chemical methods, nuclear methods (Acheroy, 2007, Gooneratne et al., 2004), to more geophysical based

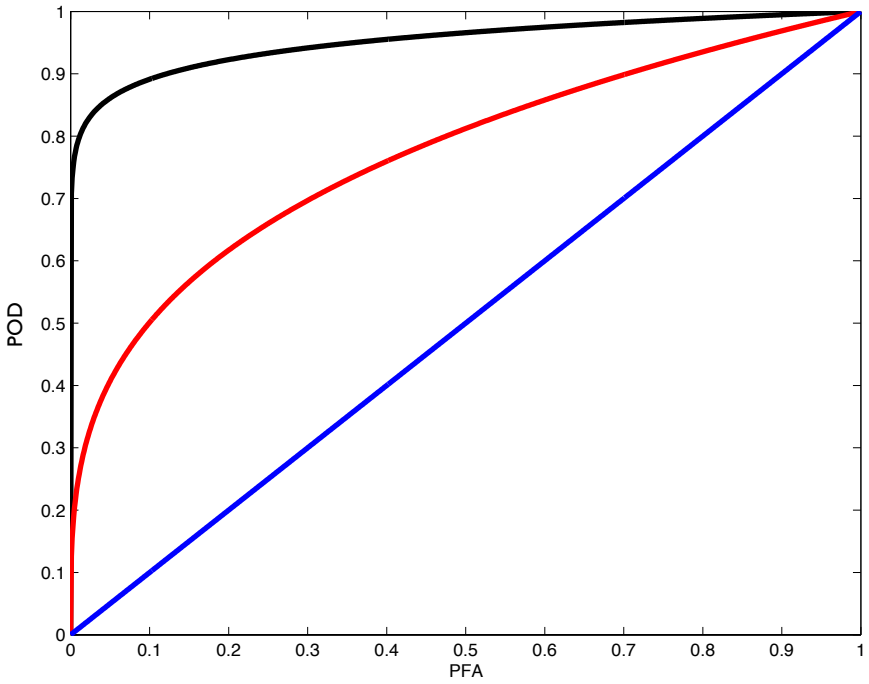

Figure 8: Three different ROC curves are illustrated with increasing performance (blue < red < black). POD: Probability of Detection, PFA: Probability of False Alarm.

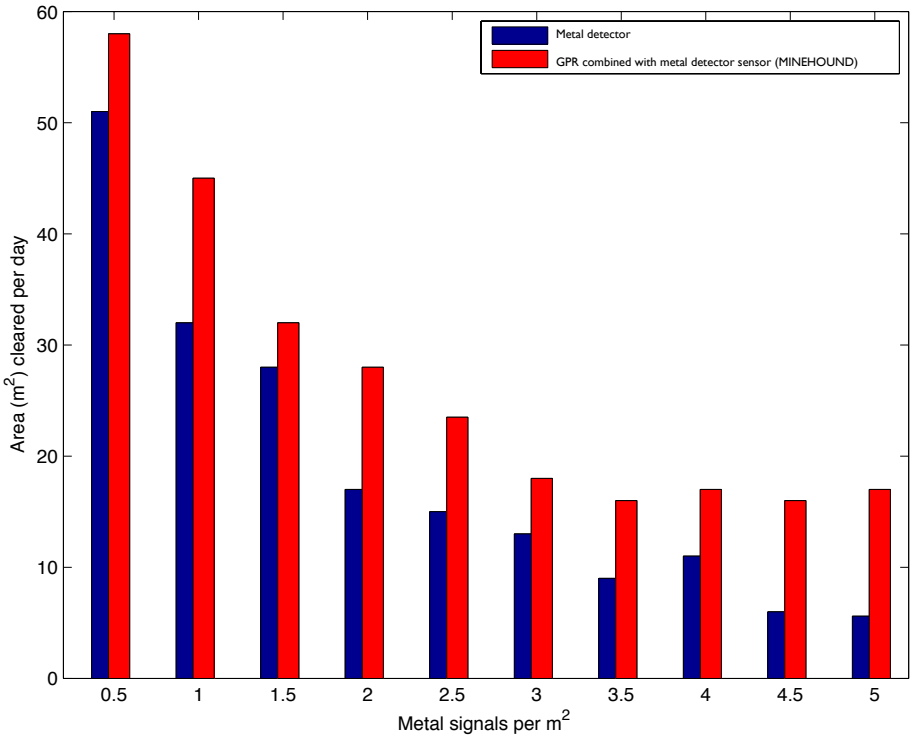

Figure 9: Productivity of metal detector compared with dual sensor (MINEHOUND) in Cambodia minefields (Daniels et al., 2014).

approaches like acoustic/seismic (Gooneratne et al., 2004, Schroder and Scott, 2000) and electrical resistivity techniques (Church et al., 2006, Metwaly, 2007). The performance of the demining methods is demonstrated through the ROC curve. The ROC curve expresses the Probability of Detection (POD) with respect to the Probability of False Alarm (PFA). In other words ROC curve lllustrates the accuracy of a demining method with respect to its time-efficiency. Fig. 8 illustrates three different ROC curves with increasing performance.

Ground-Penetrating Radar (GPR) is a non-destructive geophysical method which uses time-varying electromagnetic fields in order to retrieve information regarding the subsurface's dielectric properties. GPR has been extensively used for various applications (Daniels, 2004) and it is a well established geophysical technique. Regarding landmine detection, GPR combined with metal detector can reduce the false alarm rate which results to an overall decrease of the time needed for clearance (Daniels et al., 2014) (see Fig. 9). Dual sensors which combine both GPR and metal detectors have been developed and successfully applied in Cambodia and Afghanistan (Daniels et al., 2014, Sato et al., 2007).

The basic advantage of GPR compared with metal detector is its ability to detect plastic landmines. In addition, GPR retrieves adequate information, which with the right processing can give us an insight regarding the nature of the scattering sources (depth, shape, dielectric properties etc.). However, in complex environments, clutter may mask the landmine's signature which makes the interpretation difficult and unreliable. Also rocky environments as well as minefields with rough surface can increase the false alarm rate substantially (Daniels et al., 2014).These issues are discussed and analysed in the next chapters.

3

BASIC PRINCIPLES OF GROUND PENETRATING RADAR

This chapter is a brief introduction of the basic principles of GPR. The limitations and capabilities of GPR are mapped and detailed descriptions of the data-gathering methods are given. In addition, widely used terms in GPR community (A-Scan, B-Scan, C-Scan etc.) are explained and examples are provided in order to clarify their utility and importance. Lastly, frequently-used post-processing methods are discussed and some initial examples are given to illustrate their effectiveness.

3.1 INTRODUCTION

GPR is a special case of a more inclusive group which is known as near surface applied geophysics (Everett, 2013). The term is self-explanatory and describes a group of geophysical techniques (Electrical Resistivity Tomography (ERT), Self Potential (SP) method, potential fields methods, GPR, seismic reflection-refraction etc.) which aim to retrieve information regarding the distribution of subsurface's physical properties (electrical resistivity, elastic parameters, dielectric properties and so on). GPR is used in order to map the distribution of the dielectric properties –electric permittivity, magnetic permeability and conductivity– of the subsurface. The interpretation of the subsurface's dielectric properties can subsequently reveal the nature of the buried targets. Although direct imaging of the dielectric properties of the subsurface is theoretically plausible, and recent advancements have illustrated the ability to do so (Meles, 2011), the so called full-waveform inversion is still a computationally expensive approach for which an accurate model of the antenna unit is essential. These problems leave space for more indirect methods of interpretation. These have the advantage of practicality and simple applicability even in real-time problems. Post-processing methods that focus on retrieving quantitative information regarding the subsurface have been extensively used for a wide range of applications with satisfactory results (Daniels, 2004).

GPR has a unique characteristic compared with other geophysical techniques and that is the diversity of its applications. Traditionally, GPR is used in engineering (Negri and Quarta, 2012, Pajewski et al., 2013) and security

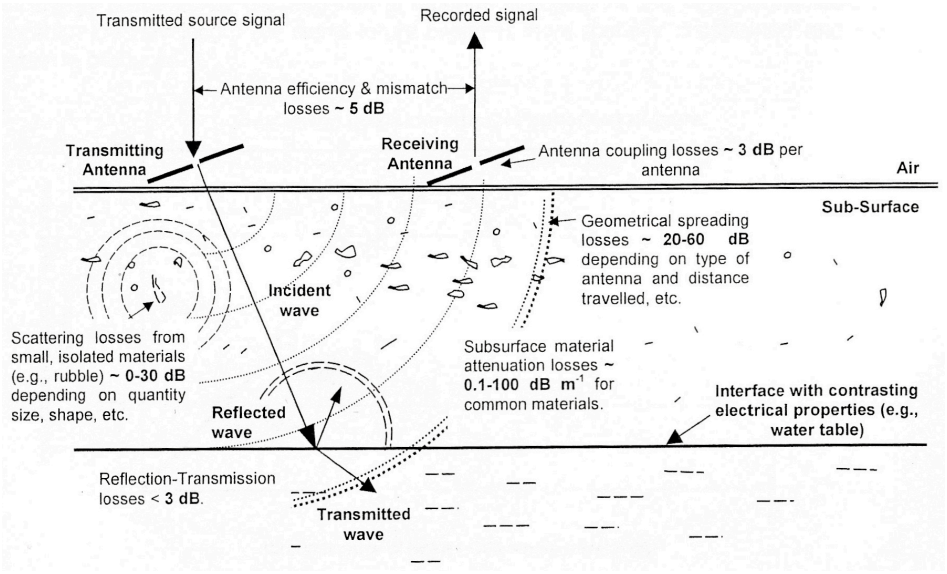

Figure 10: The loss mechanisms encountered in GPR (Cassidy, 2008).

applications (landmine detection, forensic etc.) (Daniels, 2004) but it has also been extensively used for geophysical/geological applications (Bristow, 2004, Hai et al., 2014, Kowalczyk et al., 2014), planetary exploration (Fa, 2013) and archeological inspections (Conyers, 1997). This creates a big community which embraces the scientific fields of electrical engineering, geology, geophysics and signal processing (Daniels, 2004).

A simplified description of GPR, is that of a typical radar which transmits an ultra wide-band electromagnetic pulse into the ground in an effort to detect subsurface dielectric contrasts. The propagation of the pulse into the ground has direct implications on the limitations and the uniquenesses of GPR compared with traditional radar. The energy which is reflected from the ground surface combined with the losses within the ground as well as the geometrical spreading and the reflected energy from unwanted clutter can substantially reduce the pulse's amplitude as it propagates inside the soil (see Fig. 10). These loss mechanisms reduce the depth range for which GPR can be reliably used. The depth range is also highly related to the central frequency of the pulse. This is because the losses within the ground (which are associated mostly with the water content of the soil) are proportional to the frequency of the pulse. Using lower frequencies reduces the effects of the loss mechanisms, nonetheless, lower frequencies do not come without drawbacks. The reflected energy from targets is proportional to the dielectric contrast between the target and the medium as well as the size of the target with respect to the wavelength of the pulse (Balanis, 1989). In other words, lower frequencies can not resolve small

targets. Therefore, it is evident that as the depth range increases the resolution decreases.

The frequency range of GPR can theoretically vary from 1 MHz (below 1 MHz the electromagnetic fields can be described by the diffusion equation and do not act as waves) to 10 GHz (which is the relaxation frequency of water, this creates extreme losses which make GPR unreliable). For the mainstream applications of GPR, a frequency range of 10 MHz - 3 GHz is usually employed.

GPR antennas can be both mono-static (when the transmitter and the receiver are the same antenna) and multi-static (when the transmitter and the receiver are different antennas). Both of these types can be employed in contact with the ground or off the ground. In addition, the polarisation of the transmitter can be parallel (co-polarised) or perpendicular (cross-polarised) to the polarisation of the receiver.

The antenna units can be furthermore divided into time-domain (the majority of the commercial GPR systems) and frequency domain antennas. Time-domain antennas transmit a short pulse (200 ps to 50 ns) with an amplitude between 20-200 V (Gonzalez-Huici, 2013). The shape of the pulse is typically a derivative of a Gaussian pulse with a given central frequency and bandwidth. Time-domain radar is also referred to as Ultra Wide Band (UWB) due to the large frequency bandwidth of employed pulse. Frequency-domain GPR, also referred to as Stepped Frequency Carrier Wave (SFCW), transmits a series of discreet frequencies which are subsequently transformed to time-domain through an inverse Fourier transform.

3.2 DATA COLLECTION AND PROCESSING

Three different methods for data collection are mainly applied in GPR surveys. Namely, the Common Mid-Point Reflection (CMP), the Wide-Angle Reflection-Refraction (WARR) and the Common Offset (CO) method (Warren, 2009).

The WARR method uses a steady source location while the receivers are distributed along the survey line (see Fig. 11). WARR is traditionally used for stratigraphy investigations and it was initially applied to seismic exploration. The CMP method uses one receiver and one transmitter. The distance between them is gradually and symmetrically increasing along a common point (see Fig. 11). CMP enhances the reflection at the common point and it is majorly used to obtain velocity profiles (Warren, 2009). CMP (similar to WARR) was primarily used and established in seismic surveys. The main method of data collection which is applied in mainstream GPR applications (landmine detection, archaeological investigations etc.) is the CO method.

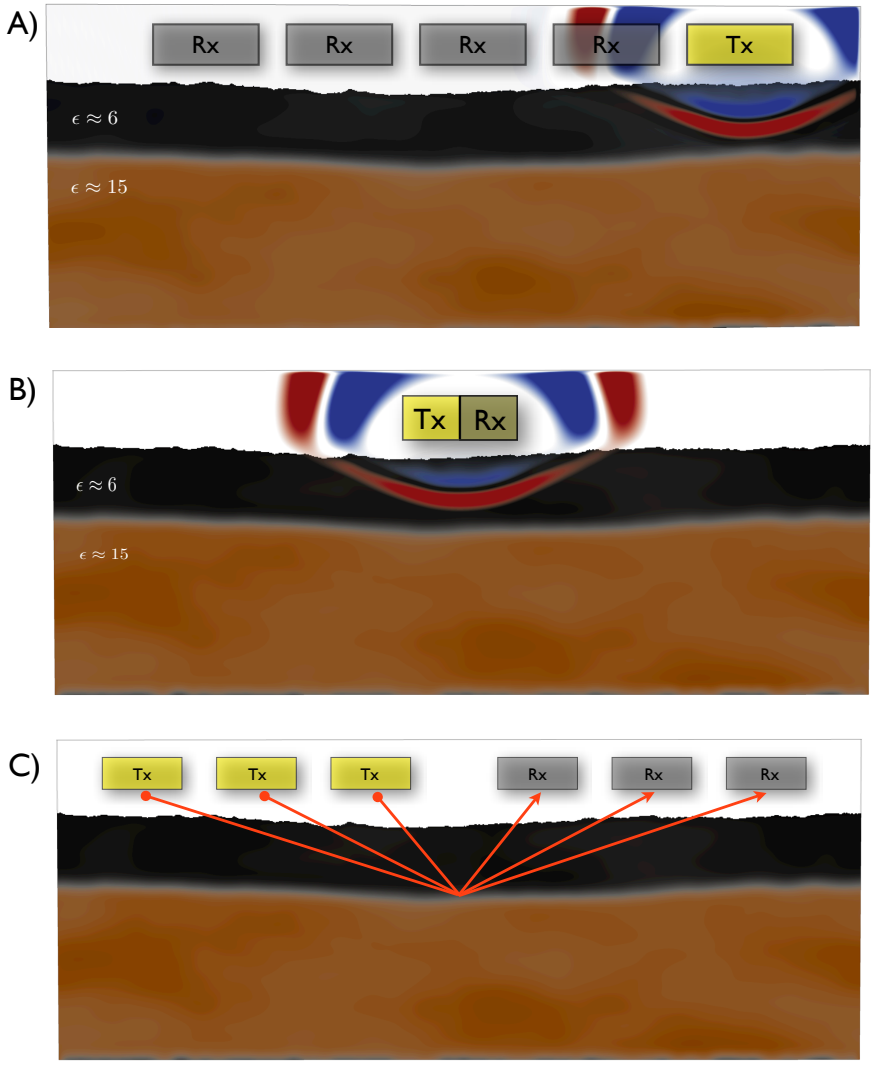

Figure 11: A) Wide Angle Refraction method (WARR), B) Common offset method (CO) and C) Common Mid-Point method (CMP).

CO uses one transmitter and one receiver which are placed right next to each other (see Fig. 11). CO GPR is usually applied to time domain antennas (Gonzalez-Huici, 2013) and it is the only method (to our knowledge) employed for demining purposes. Fig. 12 illustrates how CO GPR is applied to assist demining. A UWB pulse with a relatively high central frequency (0.5-3 GHz) is transmitted into the ground. The direct response combined with the reflection from the ground surface (due to the nature of the problem, the GPR system cannot be in contact with the ground) is firstly received and subsequently the response from the target arrives.

The post-processing methods used in GPR differ for each data gathering technique. Since the CO method is almost exclusively used for landmine detection,

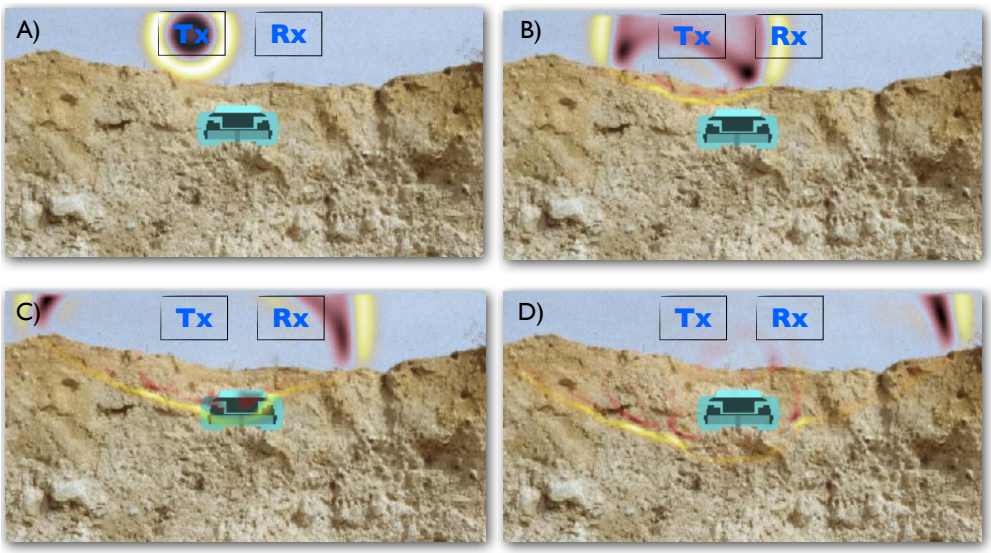

Figure 12: GPR for landmine detection. An AP landmine TS-50 is placed under the surface. A), B), C) and D) illustrate different snapshots for increasing time steps. The response from the target arrives after the ground reflection combined with the unwanted clutter from the soil's inhomogeneities.

the following sections will focus on the post-processing methods associated with it.

The received signal using CO GPR is called A-Scan or A-trace or just trace. Each individual A-Scan contains information regarding the local area around the measurement point. Plotting A-Scans from different measurement points together results to a more inclusive and clear information regarding the sub-surface. This is called B-Scan and it is presented in Fig. 13. For convenience, B-Scans are usually illustrated as images. The colour of each pixel is related with the magnitude of the received signal in the specific time-space coordinates (see Fig. 14). Another method to illustrate GPR data is to plot the gathered normalised energy which is defined as

$$P(x) = \frac{\int_0^\infty E_u\left(x,t\right)^2 dt}{\max\limits_x \left(\int_0^\infty E_u\left(x,t\right)^2 dt\right)} \tag{3.1}$$

where $u \in \{x, y, z\}$, (x, y, z) are the spatial coordinates, t is the time, $P(x)$ is the normalised energy and E_u is the received electric field. Gathering the normalised energy in two dimensions (x, y) results to a 2D image known as C-scan.

Landmine detection using GPR is a unique and highly complicated problem. The small size of the landmines combined with their shallow depth creates the need for high frequency pulses in order for the targets to be resolved. High frequency pulses result to unwanted clutter emerging (primarily) from soil's

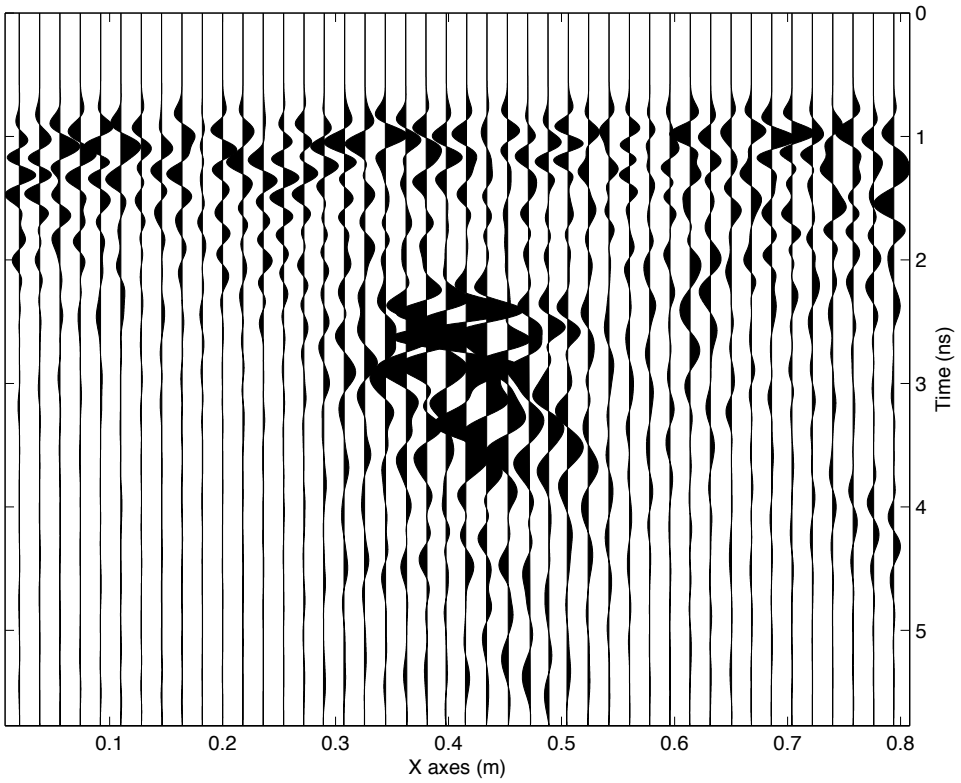

Figure 13: A B-Scan is consisted of A-Scans plotted with respect to their point of measurement.

heterogeneities and rough surfaces. In addition, the antenna unit must operate in a small proximity to the ground which gives rise to ringing noise corrupting the desired signal. Unwanted clutter combined with losses and ringing noise decrease the overall signal to noise ratio (noise here is used with a more inclusive meaning in order to define the unwanted signal i.e., unwanted clutter plus the error inherent to the antenna system) making detection difficult and in some cases unreliable.

Different processing approaches have been suggested in an effort to address demining using GPR. Processing schemes for a specific antenna unit is suggested by Groenenboom and Yarovoy (2002) and validation in real field conditions is provided. An adapted ground removal technique is proposed by Brunzell (1999) in an effort to suppress the irregular clutter emerging from rough surfaces. In the same context, Merwe and Gupta (2000) suggested an exponential based approximation of the clutter which is subsequently subtracted from the original data. Mayordomo and Yarovoy (2008) gives a review of the ground removal techniques emphasising on high pass filter, moving average removal, ASaS filter (Wu et al., 2001) and two-sided linear prediction. Principal Components Analysis (PCA) and Singular Value Decomposition (SVD) (Park et al., 2013) have also

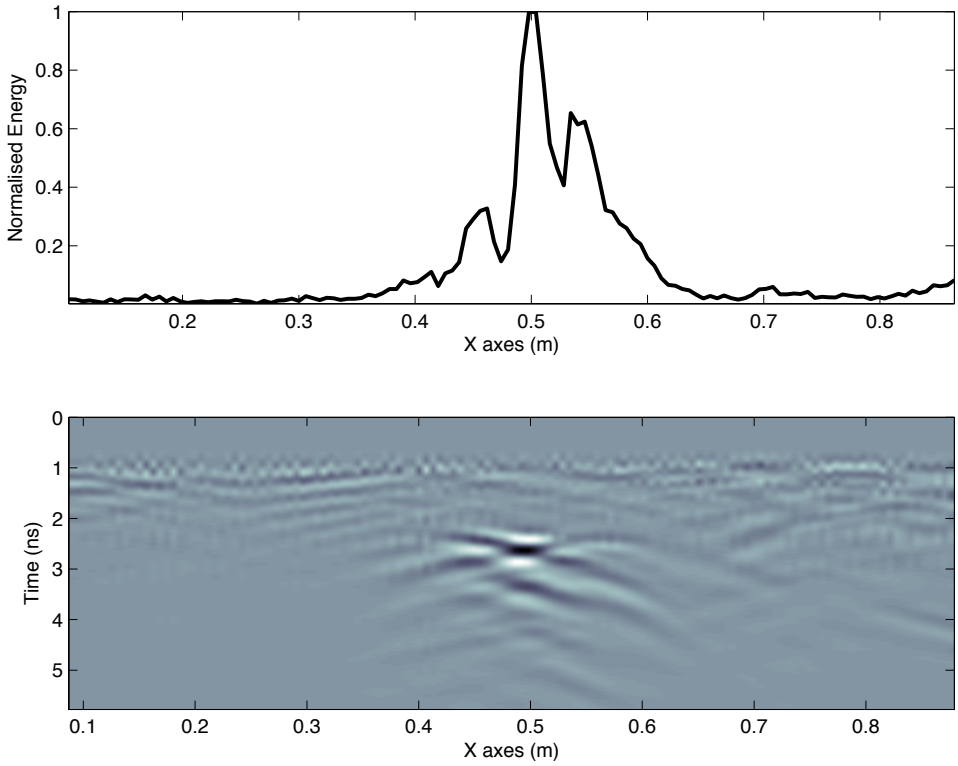

Figure 14: The B-Scan of Fig. 13 illustrated as image and its corresponding normalised energy.

been proposed in order to eliminate high and low correlation features associated with the ground bounce and the high frequency clutter. Focusing methods have been primarily applied for anti-vehicle landmine detection (Daniels, 2008) and only in detection schemes in which accurate positioning is available (Schofield et al., 2014). Regarding AP landmine detection, an interesting comparison between microwave tomographic inversion, F-K migration and back-projection is given by Gonzalez-Huici et al. (2014).

Next, a brief outline is given of a representative set of processing methods applied to GPR. These approaches are going to be tested and examined in synthetically evaluated data in latter chapters. For the sake of completeness, an introduction on how and why these techniques work is necessary.

3.2.1 *Time-Varying Gain*

The amplitude of electromagnetic waves is reduced as they propagate inside the soil. This is the result of A) the geometrical spreading of the energy, B) the loss mechanisms within the soil and C) the inhomogeneities which reflect a fraction of the energy back (see Fig. 10). From the above, it is evident that the

amplitude of the late reflections are going to be orders of magnitude smaller compared with the early reflections. To overcome this, a time-varying gain is usually applied prior to any processing technique (Annan, 1999). The term time-varying gain describes the multiplication of the received signal with a function defined by the user. The function must increase with time and usually it converges to an arbitrarily chosen maximum.

3.2.2 *Average Removal*

Average removal is a very common processing method applied to GPR data. It is a simple way to subtract the direct wave and the ground reflection by taking advantage of the correlation these components have along the survey line. Prior to average removal, it is usual to ensure that the mean of the received signal over time is equal to zero (3.2). Subsequently the average of all the received traces are subtracted from the trace of interest (3.3) (Annan, 1999, Cassidy, 2009, Daniels et al., 2014, Kim et al., 2007)

$$E'(x,t) = E(x,t) - \frac{1}{T}\sum_{i=1}^{T} E(x,i), \tag{3.2}$$

$$E''(x,t) = E'(x,t) - \frac{1}{N}\sum_{i=1}^{N} E'(i,t) \tag{3.3}$$

where $E(x,t)$ is the received signal, N is the number of traces and T is the number of time steps.

3.2.3 *Singular Value Decomposition (SVD)*

SVD is a robust technique which aims to reduce the ringing noise (Kim et al., 2007, Riaz and Ghafoor, 2013) and to subtract the ground bounce from the raw data. A superficial interpretation of SVD is that the latter decomposes an image into different sub-images each of which contains features with gradually increasing correlation.

SVD states that a 2D matrix (in our case a B-Scan) can be expressed as

$$\mathbf{E} = \mathbf{U}\mathbf{S}\mathbf{V}^T \tag{3.4}$$

or alternatively as

$$\mathbf{E} = \sum_{i=1}^{w} \lambda_i \mathbf{u}_i \mathbf{v}_i \tag{3.5}$$

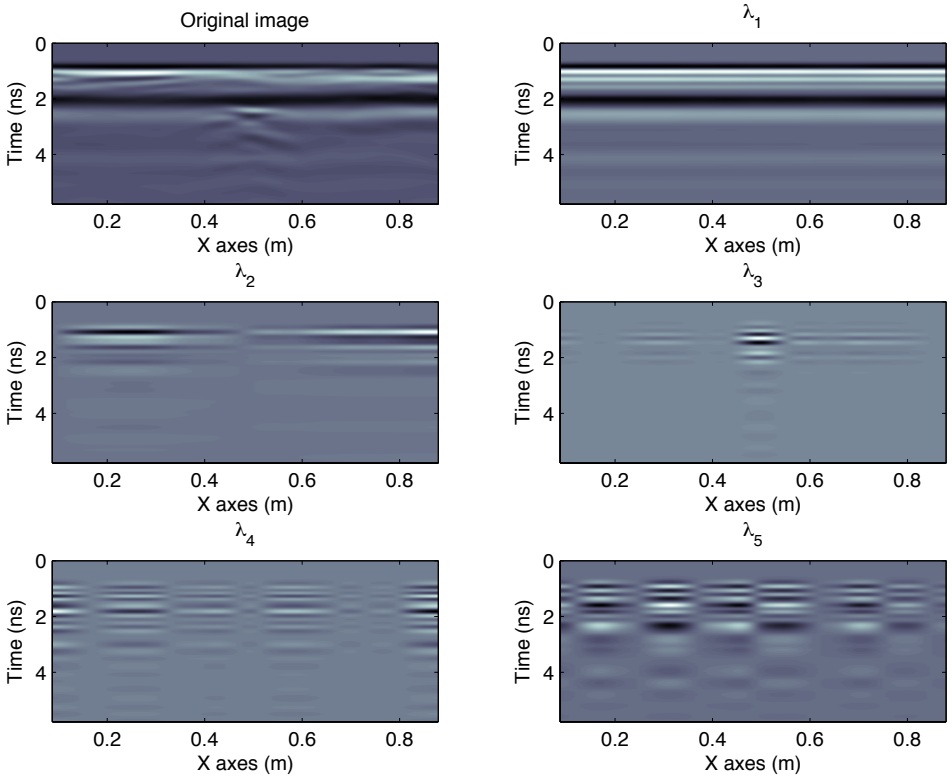

Figure 15: A B-Scan decomposed into different eigenimages. It is evident that large eigenvalues correspond to high correlated features (ringing noise, direct response and ground bounce) of the image while low eigenvalues are related to low correlated features (targets response and high-frequency clutter).

where $\mathbf{U} = [\mathbf{u}_1,\ \mathbf{u}_2....\mathbf{u}_w]$ and $\mathbf{V} = [\mathbf{v}_1,\ \mathbf{v}_2....\mathbf{v}_w]$ ($\mathbf{u}_i$ and $\mathbf{v}_i$ are vectors) are orthogonal matrices which are called eigenvectors and $\mathbf{S}$ is a diagonal matrix which contains the eigenvalues λ where $S_{i,i} = \lambda_i$ and $\lambda_i > \lambda_{i+1}$ (Kreyszig, 1999). The SVD filter keeps a set of eigenvalues while the rest are set to zero.

SVD filter can vary according to the application of interest. Regarding GPR, a band pass SVD filter is typically employed which sets the large and the low eigenvalues to zero. The utility of a band pass SVD filter is based on the fact that large eigenvalues are associated to features with high correlation while small eigenvalues are related to features with low correlation. This is illustrated in Fig. 15 in which the large eigenvalues are related to the ringing noise (plus the direct response and the ground reflection), the third eigenvalue is related to the response of the target and smaller eigenvalues are associated with high-frequency clutter.

3.2.4 *Principal Component Analysis (PCA)*

PCA is a well-known technique for reducing the dimensionality of the data. Regarding GPR, PCA can be used to eliminate high correlated features (which are related to the direct response, the ground reflection and the ringing noise) as well as low correlated features which are related to high frequency unwanted clutter. PCA and SVD share the same mathematical concept of eigenimages (Bostanudin, 2013, Riaz et al., 2013) and as it is illustrated in Fig. 16, both of them result to similar outputs.

Initially, the average trace is subtracted from the data set

$$A(x,t) = E(x,t) - \frac{1}{T}\sum_{i=1}^{T} E(x,i). \tag{3.6}$$

Subsequently the covariance matrix of $A(x,t)$ is evaluated

$$\mathbf{Cx} = \frac{1}{T-1}\mathbf{A}\mathbf{A}^T. \tag{3.7}$$

The eigenvectors of the covariance matrix are calculated through SVD

$$\mathbf{Cx} = \mathbf{U}\mathbf{S}\mathbf{V}^T. \tag{3.8}$$

The eigenvector matrix $\mathbf{U}$ is then used to transform the averaged data to

$$\mathbf{Y} = \mathbf{U}^T\mathbf{A}. \tag{3.9}$$

Lastly, the data are reconstructed through

$$\mathbf{E}_r = \mathbf{Y}_m\mathbf{A}. \tag{3.10}$$

where $\mathbf{Y}_m$ is the matrix which contains the preferred eigenvectors. By using a band pass PCA filter the large and low eigenvectors (associated with the ringing noise and the high-frequency clutter respectively) are set to zero.

3.2.5 *F-K Filter*

F-K filter is an annotation for frequency-wavenumber filter. Through F-K filter the low frequencies and the low wavenumbers which are associated with the ringing noise, the ground bounce and the direct response, can be filtered

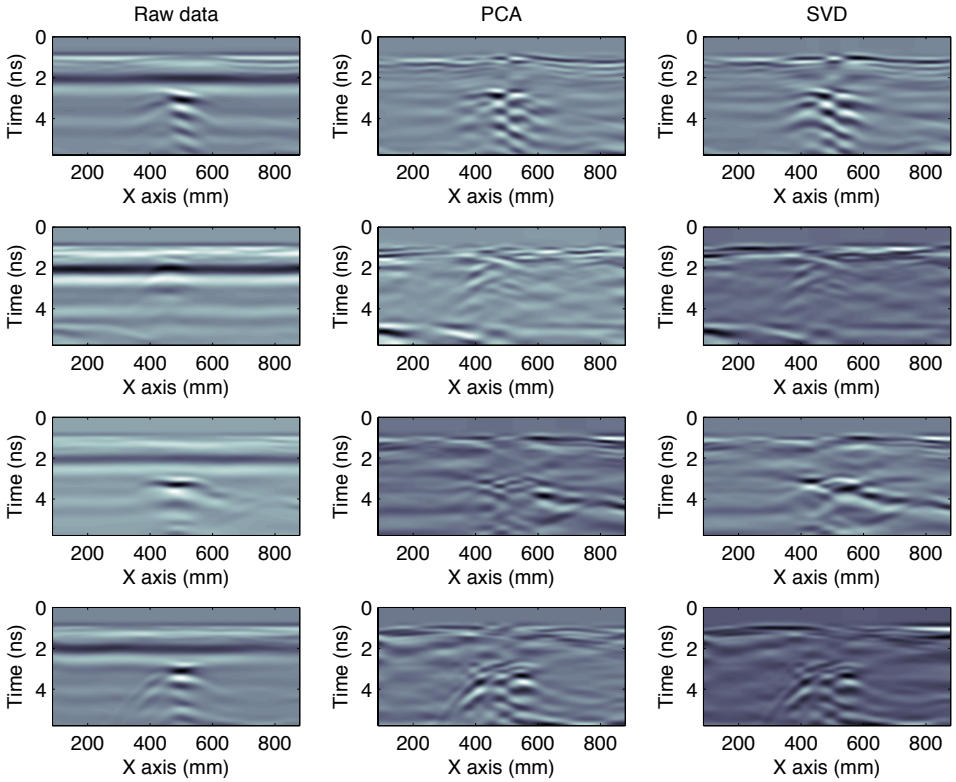

Figure 16: A comparison between PCA and SVD using four different scenarios. Both of them filter out 3 dominant eigenvalues (SVD) or eigenvectors (PCA). PCA and SVD result to similar B-Scans. A quadratic gain is also applied to the raw data.

out (Cassidy, 2009, Daniels, 2004, Kim et al., 2007, Tesfamariam, 2013). F-K filtering can be done directly to the F-K domain through a 2D Fourier transformation (Davies, 1990). A more straightforward and practical way to apply an F-K high pass filter is by using the following window filter (Davies, 1990)

$$E'_u(i_0, j_0) = E_u(i_0, j_0) - \sum_{i=i_0-K}^{i_0+K} \sum_{j=j_0-K}^{j_0+K} \frac{E_u(i,j)}{(2K+1)^2} \exp\left(-\left(\frac{(i-i_0)^2}{2\sigma_x^2} + \frac{(j-j_0)^2}{2\sigma_y^2}\right)\right) \tag{3.11}$$

where K defines the size of the window and σ_x, σ_y are constants related to the F-K range of the resulting image.

3.2.6 *Adaptive Shifted and Scaled (ASaS) Method*

ASaS searches for the optimised reference trace amongst a data pool which, when shifted and scaled appropriately, resembles the trace of interest. Subsequently, the optimised (scaled and shifted) reference is subtracted from the trace. This can be expressed mathematically as

$$\underset{x_0,A,\tau}{\operatorname{argmin}} \sum_{q=1}^{Q} \left(E_u(x,\omega_q) - A \cdot E_{r,u}(x_0,\omega_q) e^{-j\omega_q \tau} \right)^2 \tag{3.12}$$

where A and τ are the tuned scaling factor and time shift respectively associated with the optimised reference trace $E_u(x_0,\omega_q)$. The above optimisation is computationally expensive since it requires global optimisers to deal with the non-convexity of the present parameter-space. This can be tackled by dividing the problem into three steps. At the first step, the reference trace is arbitrarily chosen usually from the neighbourhood close to the trace of interest. This is due to the fact that searching for the optimised reference, results to a non-smooth highly random parameter-space which can be treated only by using brute force approaches (i.e. searching every trace in order to retrieve the optimised one). Real-time applications like landmine detection don't have the luxury to use brute force approaches as they need to be as time-efficient as possible.

After choosing the reference trace, the optimised time shift is evaluated from (Brunzell, 1999)

$$\underset{\tau}{\operatorname{argmax}} \sum_{q=1}^{Q} \left| E_u(x,\omega_q)^* E_u(x_0,\omega_q) e^{-j\omega_q \tau} \right|. \tag{3.13}$$

Equation (3.13) is the cross-correlation between the time-shifted reference and the trace of interest ($E_u(x,\omega_q)^*$ corresponds to the complex conjugate of $E_u(x,\omega_q)$). The above optimisation scheme (3.13) is based on the fact that the cross-correlation between two functions is maximised when the peaks of these functions are synchronised. After τ is calculated, the optimised weight A is derived from (Brunzell, 1999)

$$A = \frac{\sum_{q=1}^{Q} \left| E_u(x,\omega_q)^* E_u(x_0,\omega_q) e^{-j\omega_q \tau} \right|}{\sum_{q=1}^{Q} E_u(x,\omega_q)^2}. \tag{3.14}$$

Equation (3.14) states that the optimised weight A is the one which when multiplied with the autocorrelation of the reference trace results to the cross-correlation between the reference trace and the trace of interest.

ASaS is a two step procedure which solves two optimisation problems as the reference trace is picked randomly from the near neighbourhood of the trace of interest. The optimisations are non-linear and are evaluated using global optimisers (genetic algorithms, particle swarm optimisation etc.).

Here a more efficient approach is proposed that involves only one linear optimisation. This does not require the use of iterative approaches like global optimisers neither the use of non-linear inversion. As it was presented above, the goal of ASaS is to minimise the following function:

$$\underset{A,\tau}{\operatorname{argmin}} \sum_{q=1}^{Q} \left(E_u(x,\omega_q) - A \cdot E_u(x_0,\omega_q) e^{-j\omega_q \tau} \right)^2 . \tag{3.15}$$

Instead of (3.15) we choose to minimise a different function which it is possible to be expressed in a linear form

$$\underset{A,\tau}{\operatorname{argmin}} \sum_{q=1}^{Q} \left(\ln\left(E_u(x,\omega_q)\right) - \ln\left(A \cdot E_u(x_0,\omega_q) e^{-j\omega_q \tau} \right) \right)^2 . \tag{3.16}$$

Equation (3.16) can be written as

$$\underset{A,\tau}{\operatorname{argmin}} \sum_{q=1}^{Q} \left(\ln\left(\frac{E_u(x,\omega_q)}{E_u(x_0,\omega_q)} \right) - \ln(A) + j\omega_q \tau \right)^2 . \tag{3.17}$$

It is evident that (3.17) is a linear over-determined system which can be expressed as

$$\begin{bmatrix} 1 & -j\omega_1 \\ 1 & -j\omega_2 \\ 1 & -j\omega_3 \\ . & \\ . & \\ . & \\ 1 & -j\omega_Q \end{bmatrix} \begin{bmatrix} ln(A) \\ \tau \end{bmatrix} = \begin{bmatrix} \ln\left(\frac{E_u(x,\omega_1)}{E_u(x_0,\omega_1)}\right) \\ \ln\left(\frac{E_u(x,\omega_2)}{E_u(x_0,\omega_2)}\right) \\ \ln\left(\frac{E_u(x,\omega_3)}{E_u(x_0,\omega_3)}\right) \\ . \\ . \\ . \\ \ln\left(\frac{E_u(x,\omega_Q)}{E_u(x_0,\omega_Q)}\right) \end{bmatrix}$$

this can be written using matrix notation as $\mathbf{A} \cdot \mathbf{B} = \mathbf{C}$ and the solution is given through the least squares method $\mathbf{B} = \left(\mathbf{A}^T \mathbf{A}\right)^{-1} \mathbf{A}^T \mathbf{C}$.

The suggested approach must be applied to the frequency range of the pulse. Choosing wider frequency range can result to instabilities.

Fig. 17 and 18 illustrate an example of an AP landmine (PMN) buried inside a saturated soil (details about the modelling scheme are given in chapter 6). All

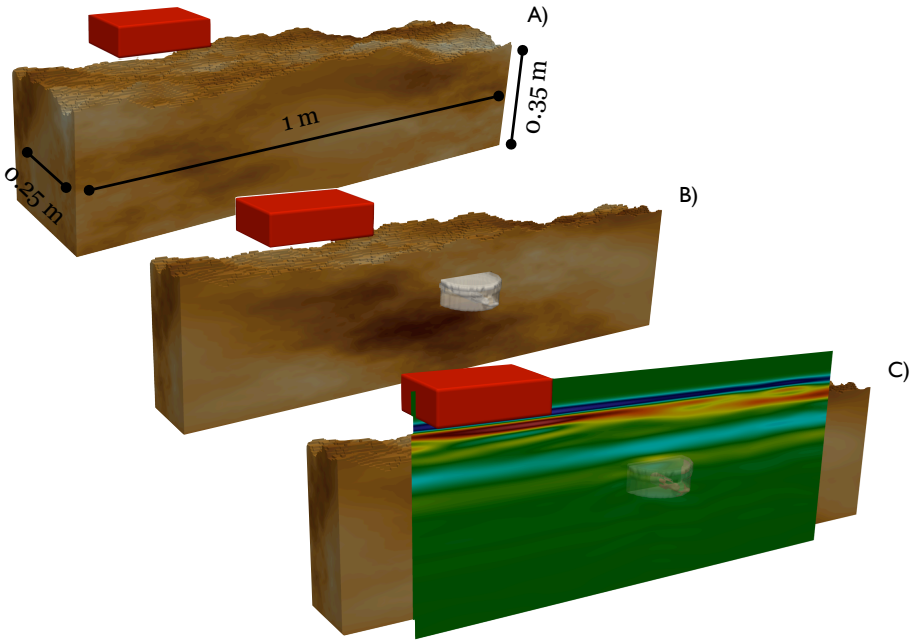

Figure 17: A) The investigated model, B) a slice which reveals the position of the AP landmine PMN, and C) the resulting B-Scan (raw data).

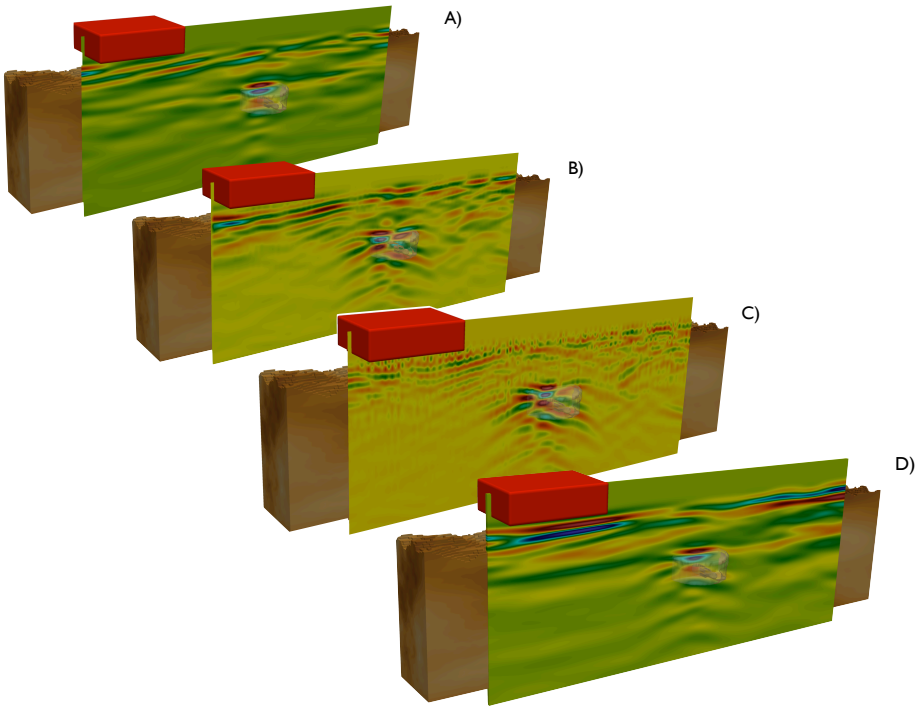

Figure 18: Different processing approaches applied to the raw data calculated from the model illustrated in Fig. 17. A) Linear gain and SVD (the 3 dominant eigenvalues are filtered out), B) linear gain and ASaS, C) linear gain and F-K filter and D) linear gain and average removal.

the methods described in this section are tested on this scenario as illustrated in Fig. 17. As it is shown in Fig. 18, all the aforementioned approaches perform equally well. This is not always the case. In chapter 6, examples are given that support the premise that the performance of processing algorithms is highly related to the environment as well as the antenna unit.

4

MAXWELL'S EQUATIONS AND DIELECTRIC PROPERTIES OF MATTER

An overview of the laws governing electromagnetic wave propagation is firstly presented emphasising on the physical interpretation of the dielectric properties of matter and in particular on the dielectric properties of water-soil mixtures. Widely used models for describing the dielectric properties of soils are presented and a physical explanation of the effects of soil parameters to the overall dielectric properties is given.

4.1 MAXWELL'S EQUATIONS

Every phenomenon which is related with electrodynamics is macroscopically described by the Lorentz force law and a set of vector equations named Maxwell's equations. The latter, combined with the gravitational law and the law of motion, consist the fundamentals of classical physics (Feynman, 1964). Maxwell's equations can be expressed in both differential and integral form and they are derived as a generalisation from the Ampere's, Faraday's and Gauss law for both magnetic and electric fields.

4.1.1 *Ampere's law*

Ampere's law states that the line integral of the magnetic field around a closed curve segment is equal to the electric current passing through the surface which is surrounded by the closed loop (Balanis, 1989)

$$\oint \vec{H} \cdot d\vec{L} = I, \tag{4.1}$$

where I is the electric current intensity (A) and $\vec{H}$ is the magnetic field intensity (A/m). Replacing the current intensity with the surface integral of the current density inside the closed loop, yields equation (4.2). Where J is the current intensity per unit area (A/m^2), S is the surface surrounded by the closed loop and $\vec{n}$ is the unit vector perpendicular to ds. The current density J can be divided into the conductivity current density $\vec{J}_c = \sigma\vec{E}$, the displacement current density $\vec{J}_d = \frac{\partial \vec{D}}{\partial t}$ and the impressed (artificially added) source current

density $\vec{J}_s$. Where σ is the conductivity (S/m), $\vec{E}$ is the electric field (V/m) and $\vec{D}$ is the electric flux density (C/m^2).

$$\begin{aligned}\oint \vec{H} \cdot d\vec{L} &= \iint_S \vec{J} \cdot \vec{n} ds \\ &= \iint_S \left(\vec{J}_c + \vec{J}_d + \vec{J}_s\right) \cdot \vec{n} ds \\ &= \iint_S \left(\sigma \vec{E} + \frac{\partial \vec{D}}{\partial t} + \vec{J}_s\right) \cdot \vec{n} ds\end{aligned} \tag{4.2}$$

Equation (4.2) is the integral form of the first (the order is arbitrarily chosen based on the order that Maxwell's equations are usually presented) Maxwell's equation. The most commonly used differential form of (4.2) can be derived using the Stoke's theorem (Kreyszig, 1999)

$$\nabla \times \vec{H} = \sigma \vec{E} + \frac{\partial \vec{D}}{\partial t} + \vec{J}_s. \tag{4.3}$$

4.1.2 *Faraday's law*

Faraday's law describes how changes of the magnetic field over time are related to the resulting electric voltage (Krauss, 1991)

$$V = -\frac{d}{dt} \iint_S \vec{B} \cdot \vec{n} ds. \tag{4.4}$$

Equation (4.4) can be written in a more general form (using $V = \oint \vec{E} \cdot d\vec{L}$) as

$$\oint \vec{E} \cdot d\vec{L} = -\iint_S \frac{\partial \vec{B}}{\partial t} \cdot \vec{n} ds, \tag{4.5}$$

where V is the voltage (V) and B is the intensity of the magnetic field (T). Equation (4.5) is the integral form of the second Maxwell's equation. Using the Stoke's theorem (Kreyszig, 1999) the differential form of equation (4.5) is derived

$$\nabla \times \vec{E} = -\frac{\partial \vec{B}}{\partial t}. \tag{4.6}$$

It is common to add an equivalent magnetic current density ($\mathrm{V/m^2}$) (Taflove and Hagness, 2000) to (4.6) in order to implement magnetic losses and impressed sources to the model

$$\nabla \times \vec{E} = -\frac{\partial \vec{B}}{\partial t} - M_c = -\frac{\partial \vec{B}}{\partial t} - M_s - \sigma^* H_s, \tag{4.7}$$

where M_s denotes the magnetic impressed sources and σ^* stands for the equivalent magnetic losses (Ω/m) (Taflove and Hagness, 2000). Magnetic impressed sources imply that magnetic monopoles exist although there are no experimental evidences to support their existence. Nonetheless, exist or not, magnetic impressed sources can be seen as artificial-imaginary sources which are used as a mathematical tool to assist electromagnetic-related problems.

4.1.3 *Gauss law for electric fields*

Gauss law (or Gauss flux theorem) for electric fields, relates the charge density with the resulting electric field (Krauss, 1991). Gauss law states that the surface integral of the electric flux on a closed surface is equal to the total charge surrounded by that surface

$$\iint_S \vec{D} \cdot ds = \iiint_V \rho \, dv = Q, \tag{4.8}$$

where Q is the total charge (C) inside the closed surface S and ρ is the charge intensity per volume area ($\mathrm{C/m^3}$). Applying Gauss vector theorem (Kreyszig, 1999) to (4.8), results to the differential form of the third equation of Maxwell

$$\nabla \cdot \vec{D} = \rho. \tag{4.9}$$

Gauss law for electric fields is essential in order to derive the conservation of charge, which all experimental evidence point to. The conservation of charge states that no charge can be created neither destroyed spontaneously, but must be transferred from one point to another (Feynman, 1964). This principle was first stated in writing by Benjamin Franklin, who wrote:

"... it is now discovered and demonstrated, both here and in Europe, that the electric Fire is a real Element, or Species of Matter, not created by the Friction, but collected only."

–Benjamin Franklin. June 1747 (Yale University Press, 1961).

The conservation of charge, although its significance, is not part of Maxwell's equations. This is because it can be directly derived from them. Taking the divergence of Ampere's law in a source free region (4.3) yields

$$\nabla \cdot \nabla \times \vec{H} = \nabla \cdot \vec{J}_c + \frac{\partial \left(\nabla \cdot \vec{D} \right)}{\partial t}. \tag{4.10}$$

Using (4.9), (4.10) and the fact that the divergence of the curl is always equal to zero ($\nabla \cdot \nabla \times \vec{H} = 0$) results to

$$\nabla \cdot \vec{J}_c = \lim_{S \to 0} \iint_S \frac{\vec{J}_c}{\Delta u} \cdot \vec{n} ds = -\frac{\partial \rho}{\partial t}, \tag{4.11}$$

where Δu is the volume surrounded by the surface S. Equation (4.11) can be written as

$$Q(S,t) = -\int_0^t \left(\lim_{S \to 0} \iint_S \vec{J}_c \cdot \vec{n} ds \right) dt, \tag{4.12}$$

notice that the units of $\vec{J}$ are $\mathrm{A/m^2}$ or alternative $\mathrm{C/(s \cdot m^2)}$. Equation (4.12) mathematically describes that the gathered charge over time inside an infinitesimal volume equals with the outgoing charge density minus the ingoing charge density inside the infinitesimal volume. In other words, changing the charge density requires movement of charges, no electric charge can be created neither destroyed spontaneously.

4.1.4 *Gauss law for magnetic fields*

The Gauss law for magnetics results from the fact that there is no evidence to support that magnetic monopoles exist. This is expressed mathematically as (Krauss, 1991)

$$\iint_S \vec{B} \cdot \vec{n} ds = 0. \tag{4.13}$$

Applying the Gauss vector theorem to equation (4.13) results to the differential form of the fourth equation of Maxwell

$$\nabla \cdot \vec{B} = 0. \tag{4.14}$$

In the case that magnetic monopoles exist, Gauss law for magnetics must include the magnetic charge density ρ_m similar to (4.9)

$$\nabla \cdot \vec{B} = \rho_m. \tag{4.15}$$

4.2 DIELECTRIC PROPERTIES

The behaviour of materials under physical laws is related to specific physical properties which identify and characterise matter. The properties which they describe the behaviour of the matter under the influence of electric and magnetic fields are known as dielectric properties. This is an inclusive term which holds as special cases the electric permittivity, the magnetic permeability and the electric conductivity. Dielectric properties are of great importance since they are related to all aspects of classical electrodynamics.

4.2.1 *Electric permittivity, magnetic permeability and electric conductivity*

The electric permittivity was first introduced by Coulomb (Krauss, 1991) as a property of matter which "permits" the influence of the static electric force. Coulomb's law states

$$f = \frac{1}{4\pi\epsilon}\frac{Q_1 Q_2}{r^2}, \tag{4.16}$$

where f is the force (N) that two particles apply to each other, Q_1 and Q_2 are the charge of the associated particles (C), r is the distance between them (m) and ϵ is the electric permittivity of the background medium. From (4.16) it can be easily derived that the units of ϵ are $\frac{\mathrm{C}^2}{\mathrm{Nm}^2}$. For conveniency, the more simple F/m is used where $\mathrm{F} = \frac{\mathrm{C}^2}{\mathrm{Nm}}$.

To understand what magnetic permeability is, it is convenient to start with the Biot-Savart law (4.17)

$$d\vec{B} = \frac{\mu}{4\pi}\frac{\vec{I} \times d\vec{L}}{r^2}. \tag{4.17}$$

Equation (4.17) relates the infinitesimal magnetic field dB with the current I running through an infinitesimal conductor dL, the distance r between the conductor and the measurement point and a constant μ which is related to the nature of the background medium.

The constant μ is called magnetic permeability and from (4.17) can be derived that the units of μ (given the fact that B use as units Tesla (T) which is equal to $\mathrm{N}/(\mathrm{A}\cdot\mathrm{m})$) are N/A^2.

Electric conductivity is a constant which quantifies how easily electric current I flows in a material under the influence of an electric field $\vec{E}$. This is expressed by Ohm's law

$$\vec{J_c} = \sigma\vec{E}. \tag{4.18}$$

From (4.18) it is derived that the units of conductivity are $\mathrm{A}/(\mathrm{Vm})$ but more commonly S/m is used where $\mathrm{S} = \mathrm{A}/\mathrm{V}$.

Dielectric properties are incorporated to Maxwell's equations through the constitutive equations (Balanis, 1989). Constitutive equations relate the electric flux density $\vec{D}$, the magnetic field $\vec{B}$ and the current density $\vec{J_c}$ with the electric permittivity ϵ (4.19), the magnetic permeability μ (4.20) and the electric conductivity σ respectively (4.21).

$$\vec{D} = \epsilon * \vec{E} = \int_0^t \epsilon(\tau)\vec{E}(t-\tau)d\tau \tag{4.19}$$

$$\vec{B} = \mu * \vec{H} = \int_0^t \mu(\tau)\vec{H}(t-\tau)d\tau \tag{4.20}$$

$$\vec{J_c} = \sigma * \vec{E} = \int_0^t \sigma(\tau)\vec{E}(t-\tau)d\tau \tag{4.21}$$

In the special case in which the dielectric properties are frequency independent, the convolution operators in (4.19)-(4.21) are transformed to simple multiplications.

From (4.3), (4.6), (4.19), (4.20), (4.21) and using the relationship $j\omega = \mathcal{L}\left(\frac{\partial}{\partial t}\right)$ (where $\mathcal{L}$ denotes the Fourier transform, $j = \sqrt{-1}$ and ω is the angular frequency (Kreyszig, 1999)), Maxwell's equations can be rewritten in frequency domain as

$$j\omega\vec{E}_\omega\left(\epsilon + \frac{\sigma}{j\omega}\right) = \nabla\times\vec{H}_\omega \tag{4.22}$$

$$j\omega\mu\vec{H}_\omega = -\nabla\times\vec{E}_\omega. \tag{4.23}$$

The underscore ω denotes that the fields are in frequency domain. Notice that ϵ, μ and σ can be real, purely imaginary or complex numbers.

From (4.22) and (4.23) it is evident that the dielectric properties affect all the phenomena related with classical electrodynamics and not only the static

cases for which they were initially introduced (4.16), (4.17) and (4.18). In order to get a clear insight on how dielectric properties affect electromagnetic waves we first derive the electromagnetic wave equation. Taking the curl of equations (4.22) and (4.23) leads to

$$j\omega\left(\epsilon+\frac{\sigma}{j\omega}\right)\nabla\times\vec{E}_\omega=\nabla\times\nabla\times\vec{H}_\omega \tag{4.24}$$

$$j\omega\mu\nabla\times\vec{H}_\omega=-\nabla\times\nabla\times\vec{E}_\omega. \tag{4.25}$$

Substituting (4.22) to (4.25) yields

$$\vec{E}_\omega\left(j\omega\mu\sigma-\omega^2\mu\epsilon\right)=-\nabla\times\nabla\times\vec{E}_\omega. \tag{4.26}$$

From (4.9) and (4.19) can be easily derived, that for a source-free region $\nabla\cdot\vec{E}_\omega = 0$. Applying this and the vector identity $\nabla\times\nabla\times\vec{E}_\omega=\nabla\left(\nabla\cdot\vec{E}_\omega\right)-\nabla^2\vec{E}_\omega$ to (4.26) leads to

$$\nabla^2\vec{E}_\omega-\gamma^2\vec{E}_\omega=0. \tag{4.27}$$

Equation (4.27) is the generic Helmholtz equation. In time domain, (4.27) expresses the scalar wave equation firstly derived from Jean le Rond d'Alembert for one dimensional problems and later on generalised for three dimensional problems by Daniel Bernouli (Speiser, 2008). In the same manner, the scalar wave equation for magnetic fields is derived

$$\nabla^2\vec{H}_\omega-\gamma^2\vec{H}_\omega=0. \tag{4.28}$$

The complex constant γ is known as the propagation constant and it is equal with

$$\gamma=\sqrt{j\omega\mu\left(\sigma+j\omega\epsilon\right)}=\alpha+j\beta. \tag{4.29}$$

For convenience, γ is usually expanded into its real (α) and imaginary parts (β), where

$$\alpha=\omega\sqrt{\frac{\mu\epsilon}{2}\left(\sqrt{1+\left(\frac{\sigma}{\omega\epsilon}\right)^2}-1\right)} \tag{4.30}$$

$$\beta = \omega \sqrt{\frac{\mu\epsilon}{2}\left(\sqrt{1+\left(\frac{\sigma}{\omega\epsilon}\right)^2}+1\right)}. \tag{4.31}$$

Solving (4.27) assuming a plane (i.e. $\frac{\partial E_z}{\partial x} = \frac{\partial E_z}{\partial z} = 0$ and $E_x = E_y = 0$) and monochromatic wave yields

$$E_z(y,t) = \left(A_1 e^{\alpha y} e^{j\beta y} + A_2 e^{-\alpha y} e^{-j\beta y}\right) e^{j\omega t} = E_z\left(y,\omega\right) e^{j\omega t}, \tag{4.32}$$

where A_1 and A_2 are constants and $E_z\left(y,\omega\right)$ is the solution of (4.27) subject to the aforementioned assumptions (monochromatic and plane wave). The solution described in (4.32) is a complex function, which can be expanded into a summation of a real and imaginary part. From the superposition theorem for differential equations (Kreyszig, 1999), it is concluded that both the real and the imaginary part of the complex solution given in (4.32) are (individually) still valid solutions for (4.27) (for a plane monochromatic wave). Subject to the conditions described above, a real solution for (4.27) is derived

$$\begin{aligned} E_z(y,t) &= Re\left\{\left(A_1 e^{\alpha y} e^{j\beta y} + A_2 e^{-\alpha y} e^{-j\beta y}\right) e^{j\omega t}\right\} \\ &= A_1 e^{\alpha y}\cos\left(\omega t + \beta y\right) + A_2 e^{-\alpha y}\cos\left(\omega t - \beta y\right). \end{aligned} \tag{4.33}$$

Equation (4.33) describes a plane monochromatic wave which travels in two different directions along y axis. The first part of (4.33) describes a wave propagating along $-y$ direction and the second part describes a wave propagating along $+y$ direction. Using the superposition theorem for differential equations we can furthermore derive the solution of a plane monochromatic wave traveling along y direction

$$E_z(y,t) = A_2 e^{-\alpha y}\cos\left(\omega t - \beta y\right). \tag{4.34}$$

Fig. 19 illustrates a monochromatic (1 GHz) plane wave inside a material with $\sigma = 0.001$ Sm^{-1}, $\epsilon = 15.85 \times 10^{-12}$ Fm^{-1} and $\mu = 4\pi \times 10^{-7}$ Am^{-2}. The simple and elegant form of (4.34) can give us an insight on how dielectric properties affect the propagation of electromagnetic waves. The velocity of the electromagnetic waves is defined as the velocity for which a constant phase is propagating in space (see Fig. 19). Based on that, it can be easily proven that the velocity of the wave described in (4.34) is equal to

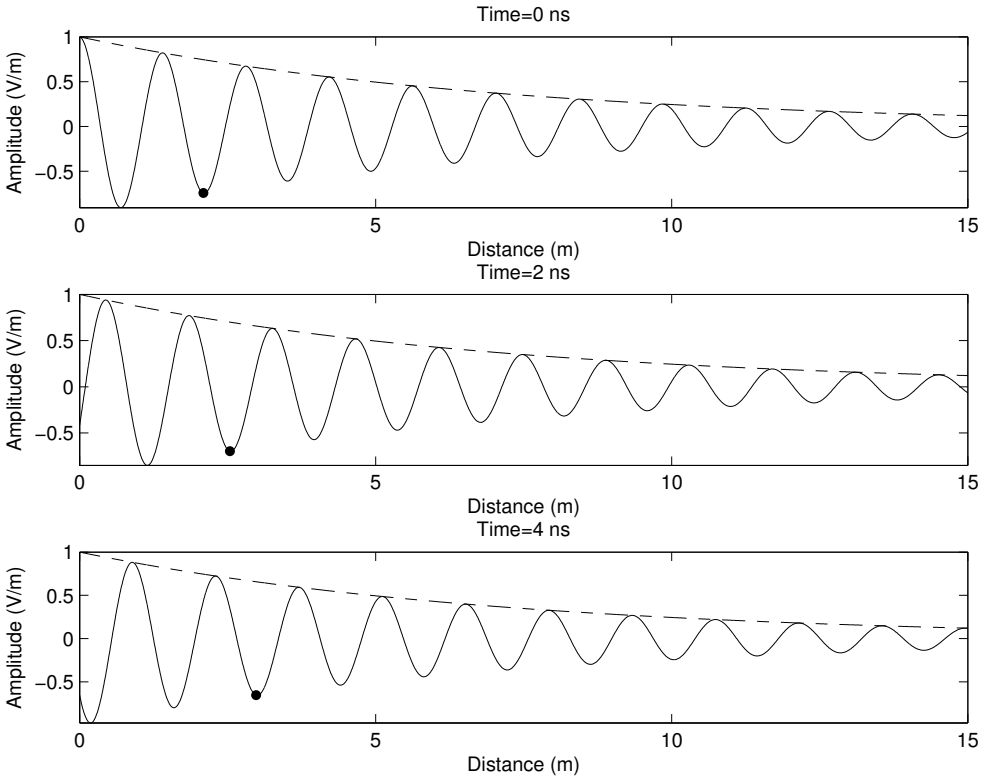

Figure 19: A monochromatic plane wave propagating inside a medium with $\sigma = 0.001$ Sm^{-1}, $\epsilon = 15.85 \times 10^{-12}$ Fm^{-1} and $\mu = 4\pi \times 10^{-7}$ Am^{-2}. The angular frequency (ω) is 1 GHz. With solid lines are the fields for three different time steps (0, 2 and 4 ns) along the y axis. Dots, map an arbitrarily chosen constant phase and dotted lines illustrate the exponential decay due to the conductivity of the medium.

$$v = \frac{\omega}{\beta}. \tag{4.35}$$

For $\sigma = 0$ using (4.31) and (4.35) leads to

$$v = \frac{1}{\sqrt{\mu\epsilon}}. \tag{4.36}$$

The units of electric permittivity and magnetic permeability are $\frac{\mathrm{C}^2}{\mathrm{Nm}^2}$ and $\frac{\mathrm{N}}{\mathrm{C/s}^2}$ respectively. Therefore, it is easy to show that (4.36) has units of velocity $\frac{\mathrm{m}}{\mathrm{s}}$.

Equation (4.34) describes a monochromatic plane wave propagating along y direction. If $\alpha \neq 0$ then the wave decays along the y direction (see Fig. 19). If $\sigma \neq 0$ and ϵ, μ are finite non-zero numbers then from (4.30) is derived that $\alpha \neq 0$. This implies that conductive media absorb energy which results to the decay of the electromagnetic waves. The absorbed energy is transformed to heat which is generated from the current density flowing through conductive

media (Krauss, 1991). Decay also occurs if the electric permittivity or the magnetic permeability are complex numbers. This is observable in (4.22) in which conductivity (σ) can be interpreted as the imaginary part of a more inclusive complex electric permittivity.

The dielectric properties of free space were experimentally derived and they are equal with $\sigma = 0$, $\epsilon = 8.85 \times 10^{-12}$ Fm^{-1} and $\mu = 4\pi \times 10^{-7}$ Am^{-2} (Krauss, 1991). From the above, it is easy to prove that the velocity of electromagnetic waves (4.36) in vacuum is approximately equal with $v = 2.99792 \times 10^8$ m/s. The resulting value resembles the experimentally calculated velocity of light (Maxwell, 1865). This led Maxwell to comment

"The agreement of the results seems to show that light and magnetism are affections of the same substance, and that light is an electromagnetic disturbance propagated through the field according to electromagnetic laws."

–James, Clerck Maxwell, December 1865 (Maxwell, 1865)

Electrical permittivity and magnetic permeability are usually expressed with respect to the dielectric properties of free space. When this happens, the terms "relative" electric permittivity (4.37) and "relative" magnetic permeability (4.38) are used,

$$\epsilon_r = \frac{\epsilon}{\epsilon_0} \tag{4.37}$$

$$\mu_r = \frac{\mu}{\mu_0}, \tag{4.38}$$

where ϵ_r and μ_r are the relative permittivity and permeability respectively, ϵ_0 and μ_0 are the dielectric properties of free space and ϵ and μ are the dielectric properties of the material.

Spatial variations of the dielectric properties and more specific spatial variations of the electric permittivity (since for most dielectric media $\mu = \mu_0$ (Balanis, 1989)) are directly related with the scattered field. This can be illustrated by deriving the reflection coefficients of a monochromatic plane wave propagating into a two-layered medium. Expanding the electric field into incident, reflected and transmitted fields yields

$$\vec{E_i} = \vec{x} \cdot Ae^{-j\gamma_1 z} \tag{4.39}$$

$$\vec{E_r} = \vec{x} \cdot \Gamma^b Ae^{j\gamma_1 z} \tag{4.40}$$

$$\vec{E}_t = \vec{x} \cdot T^b A e^{-j\gamma_2 z} \tag{4.41}$$

where $\vec{x}$ is the unit vector along the x axis, A is a constant and Γ^b and T^b are the reflection and the transmission coefficients respectively. Substitute (4.39)-(4.41) to (4.7) yields

$$\vec{H}_i = \vec{y} \cdot \frac{A}{\sqrt{\mu_1/\epsilon_1}} e^{-j\gamma_1 z} \tag{4.42}$$

$$\vec{H}_r = -\vec{y} \cdot \frac{\Gamma^b}{\sqrt{\mu_1/\epsilon_1}} A e^{j\gamma_1 z} \tag{4.43}$$

$$\vec{H}_t = \vec{y} \cdot \frac{T^b}{\sqrt{\mu_2/\epsilon_2}} A e^{-j\gamma_2 z} \tag{4.44}$$

where $\vec{y}$ is the unit vector along y axis and ϵ_1, μ_1 and ϵ_2, μ_2 are the dielectric properties of the two layers respectively.

Using the boundary conditions of the tangential fields (Balanis, 1989) yields

$$1 + \Gamma^p = T^b \tag{4.45}$$

$$\frac{1}{\sqrt{\frac{\mu_1}{\epsilon_1}}} \left(1 - \Gamma^b\right) = \frac{1}{\sqrt{\frac{\mu_2}{\epsilon_2}}} T^b. \tag{4.46}$$

Equations (4.45) and (4.46) form a system of equations which results to (Balanis, 1989)

$$\Gamma^b = \frac{\sqrt{\frac{\mu_2}{\epsilon_2}} - \sqrt{\frac{\mu_1}{\epsilon_1}}}{\sqrt{\frac{\mu_2}{\epsilon_2}} + \sqrt{\frac{\mu_1}{\epsilon_1}}} \tag{4.47}$$

$$T^b = \frac{2\sqrt{\frac{\mu_2}{\epsilon_2}}}{\sqrt{\frac{\mu_2}{\epsilon_2}} + \sqrt{\frac{\mu_1}{\epsilon_1}}}. \tag{4.48}$$

From (4.47) and (4.48) is evident that the reflection as well as the transmission coefficients are highly related to the spatial variations of dielectric properties.

A more inclusive approach not restricted to plane waves to show how dielectric contrasts give rise to scattering fields, is through the so-called split-field formulation. Split-field formulation divides both the electric and the magnetic field into two parts, namely, instinct (4.49) and scattering field (4.50)

$$\vec{E}_t = \vec{E}_i + \vec{E}_{sc} \tag{4.49}$$

$$\vec{H}_t = \vec{H}_i + \vec{H}_{sc}. \tag{4.50}$$

Where the subscript t indicates the total field, i the incident field and sc is the scattered field. The incident field is the field which would occur in an arbitrarily chosen distribution of dielectric properties. In the present case, a homogenous distribution is chosen in order to illustrate the effects of dielectric inhomogeneities. Substituting (4.49) and (4.50) to (4.3) and (4.6) respectively and furthermore assuming a zero conductivity (for simplicity) yields

$$\nabla \times \left(\vec{E}_i + \vec{E}_{sc}\right) = -\mu \frac{\partial \left(\vec{H}_i + \vec{H}_{sc}\right)}{\partial t} \tag{4.51}$$

$$\nabla \times \left(\vec{H}_i + \vec{H}_{sc}\right) = \epsilon \frac{\partial \left(\vec{E}_i + \vec{E}_{sc}\right)}{\partial t}. \tag{4.52}$$

Since the incident field is Maxwellian it is valid to state that

$$\nabla \times \vec{E}_i = -\mu_i \frac{\partial \vec{H}_i}{\partial t} \tag{4.53}$$

$$\nabla \times \vec{H}_i = \epsilon_i \frac{\partial \vec{E}_i}{\partial t}, \tag{4.54}$$

where μ_i and ϵ_i are the homogenous dielectric properties used to calculate the incident field. By subtracting the incident from the total field, yields (Luebbers and Kunz, 1993)

$$\nabla \times \vec{E}_{sc} = -\mu \frac{\partial \vec{H}_{sc}}{\partial t} - (\mu - \mu_i) \frac{\partial \vec{H}_i}{\partial t} = -\mu \frac{\partial \vec{H}_{sc}}{\partial t} - M_{sc} \tag{4.55}$$

$$\nabla \times \vec{H}_{sc} = \epsilon \frac{\partial \vec{E}_{sc}}{\partial t} + (\epsilon - \epsilon_i) \frac{\vec{E}_i}{\partial t} = \epsilon \frac{\partial \vec{E}_{sc}}{\partial t} + J_{sc}. \tag{4.56}$$

From (4.55) and (4.56) it is evident that the scattering field can be expressed as a Maxwellian field excited by an electric (J_s) and a magnetic (M_s) impressed sources (Balanis, 1989). The aforementioned sources are directly related to the inhomogeneities since $J_s = (\epsilon - \epsilon_i) \frac{\vec{E}_i}{\partial t}$ and $M_s = (\mu - \mu_i) \frac{\vec{H}_i}{\partial t}$.

4.2.2 *Linear dispersive media*

Dielectric properties may vary with respect to the frequency as well as the field's amplitude. According to that, materials can be categorised into four types (Taflove, 2005):

- *Linear*: The dielectric properties are constant within the frequency range of interest and independent with respect to the field's amplitude.
- *Linear dispersive*: The dielectric properties vary with respect to the frequency but not with respect to the field's amplitude.
- *Non-linear*: The dielectric properties vary with respect to the field's amplitude and they are constant for the frequency range of interest.
- *Non-linear dispersive*: The dielectric properties are related both to the frequency as well as the field's amplitude.

Linear dispersive materials are of great interest due to the fact that materials like water (Semenov, 1995, Zahn et al., 1986), human tissues (Garrett and Fear, 2014), meta-materials (Abraham et al., 2003) and soils (Hoekstra and Delaney, 1974) have a dispersive behaviour for a wide range of frequencies and a linear behaviour for the usually employed field intensities.

Different dispersion mechanisms give rise to different frequency depended behaviour. Furthermore, a combination of dispersion mechanisms can lead to complex dispersive properties, which, as it will be shown in later chapters are difficult to be implemented into time-domain numerical solvers. The most important functions used to describe the behaviour of linear dispersive materials are the Debye, Lorentz, Drude, Havriliak-Negami, and the Jonsher function.

–Debye relaxation

Debye relaxation (Debye, 1929) is described by a complex valued electric permittivity which is expressed in frequency domain as (Luebbers and Kunz, 1993)

$$\epsilon = \epsilon_\infty + \chi_\omega \tag{4.57}$$

$$\chi_\omega = \sum_{p=1}^{P} \frac{\epsilon_{s,p} - \epsilon_\infty}{1 + j\omega t_{0,p}}, \tag{4.58}$$

where χ_ω is known as the susceptibility function (Balanis, 1989) which describes the dispersive part of the electric permittivity, ϵ_s and ϵ_∞ are the electric

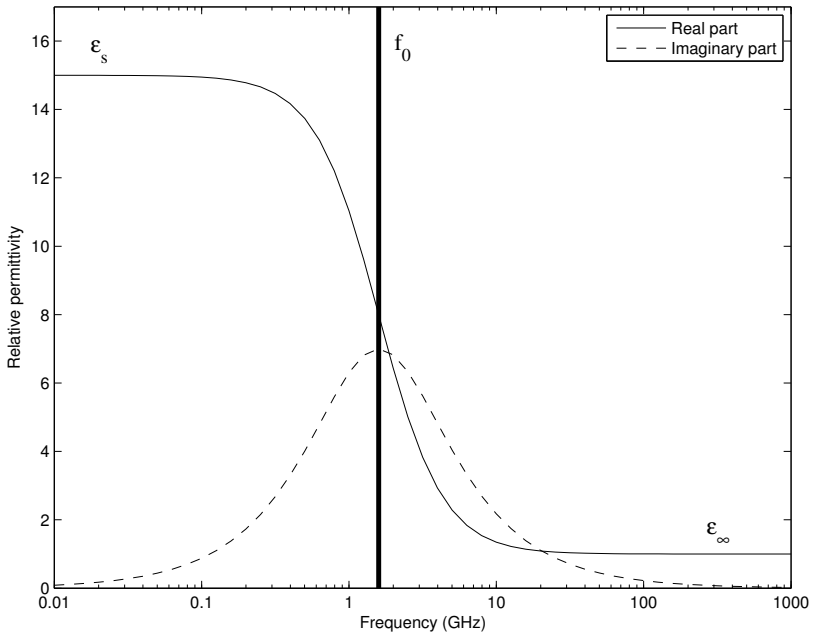

Figure 20: Both real and imaginary parts of a Debye function with $\epsilon_s = \epsilon_0$, $\epsilon_\infty = 15 \cdot \epsilon_0$ and $t_0 = 0.1$ ns. The relaxation frequency equals with $f_0 = \frac{1}{2\pi t_0}$.

permittivity for zero and infinity frequency respectively and t_0 is the relaxation time. The relaxation frequency (i.e. the frequency for which the imaginary part as well as the first derivative of the real part $\frac{\partial Re\{\epsilon\}}{\partial \omega}$ reach their maximum value) is directly related to the relaxation time through $f_0 = \frac{1}{2\pi t_0}$ (see Fig. 20).

The susceptibility function in time domain equals with

$$\chi(t) = \sum_{p=1}^{P} \frac{\epsilon_{s,p} - \epsilon_\infty}{t_{0,p}} e^{-\frac{t}{t_{0,p}}}. \tag{4.59}$$

The time domain expression of the electric permittivity does not have any physical interpretation but nonetheless it is essential for solving Maxwell's equations using time-domain numerical solvers. Moreover, the exponential nature of (4.59) is critical to the implementation of Debye media using FDTD (Luebbers and Kunz, 1993). Without it, the recursive evaluation of the arising convolution would require an excessive amount of computational resources.

–Lorentz relaxation

The susceptibility function of Lorentz media is expressed as (Taflove, 2005)

$$\chi(\omega) = \sum_{p=1}^{P} \frac{(\epsilon_{s,p} - \epsilon_\infty)\,\omega_p^2}{\omega_p^2 + 2j\omega\delta_p - \omega^2}, \tag{4.60}$$

where ω_p is the undamped resonant frequency and δ_p is the damping coefficient (Taflove, 2005). Transforming (4.60) to time domain yields

$$\chi(t) = \sum_{p=1}^{P} \frac{(\epsilon_{s,p} - \epsilon_\infty)\,\omega_p^2}{\sqrt{\omega_p^2 - \delta_p^2}} e^{-\delta_p t} \sin\left(t\sqrt{\omega_p^2 - \delta_p^2}\right). \tag{4.61}$$

Equation (4.61) cannot be recursively evaluated using FDTD. One way to overcome this obstacle is to rewrite (4.61) as

$$\chi(t) = \sum_{p=1}^{P} Re\left\{ -j\frac{(\epsilon_{s,p} - \epsilon_\infty)\,\omega_p^2}{\sqrt{\omega_p^2 - \delta_p^2}} e^{\left(-\delta_p + j\left(\sqrt{\omega_p^2 - \delta_p^2}\right)\right)t} \right\}. \tag{4.62}$$

The exponential nature of (4.62) is crucial for the efficient implementation of Lorentz media using FDTD (Taflove, 2005).

–Drude relaxation

Drude relaxation is expressed in frequency domain as (Luebbers and Kunz, 1993)

$$\chi(\omega) = \sum_{p=1}^{P} \frac{\omega_p^2}{\omega\left(j v_{c,p} - \omega\right)} = -\sum_{p=1}^{P} \frac{\left(\omega_p / v_{c,p}\right)^2}{1 + j\frac{\omega}{v_{c,p}}} + \frac{1}{j\omega}\sum_{p=1}^{P} \frac{\omega_p^2}{v_{c,p}}, \tag{4.63}$$

where $v_{c,p}$ is known as the collision frequency (Luebbers and Kunz, 1993), a term widely used to plasma physics for which the Drude function was initially introduced. From (4.58) and (4.63), it is evident that a Drude medium can be expressed as a negative Debye function plus a conductive term. Transforming (4.63) to time domain yields

$$\chi(t) = \sum_{p=1}^{P} \frac{\omega_p^2}{v_{c,p}} t - \sum_{p=1}^{P} \frac{\omega_p^2}{v_{c,p}} e^{-v_{c,p} t}. \tag{4.64}$$

–Havriliak-Negami relaxation

Havriliak-Negami is an inclusive function which holds as special cases the Debye, Cole-Cole (Cole K. and Cole R., 1941) and Cole-Davidson relaxation. It has a similar structure with the Debye model and it was first used to describe the dielectric properties of polymers (Havriliak and Negami, 1967).

The frequency domain expression of the Havriliak-Negami function is (Havriliak and Negami, 1967)

$$\chi(\omega) = \frac{\epsilon_s - \epsilon_\infty}{\left(1 + (j\omega t_0)^a\right)^b}, \tag{4.65}$$

where a and b are constants. If $a = b = 1$, then (4.65) reduces to Debye medium, if $b = 1$ and $0 < a < 1$ to Cole-Cole medium and if $a = 1$ and $0 < b < 1$ to Cole-Davidson medium. The time domain response of (4.65) is given by (Causley and Petropoulos, 2013)

$$\chi(t) = \frac{1}{2\pi j} \int_{\zeta - j\infty}^{\zeta + j\infty} \frac{(\epsilon_s - \epsilon_\infty)\, e^{st}}{\left(1 + (st)^a\right)^b} ds. \tag{4.66}$$

Havriliak-Negami as well as Cole-Cole and Cole-Davidson media cannot be directly implemented to FDTD. To address this issue, approximations of (4.65) (usually, a multi-Debye function) are employed. Increasing the approximation's order of accuracy results to more computational requirements.

–Jonscher media

Jonscher function was first suggested by Jonscher (1977) and it is widely used to describe the dielectric properties of concrete (Taoufik et al., 2008) and soils (Gregoire and Hollender, 2004). The frequency domain expression of Jonscher function is given by

$$\chi(\omega) = \sum_{p=1}^{P} A_p \left(\frac{\omega}{\omega_p}\right)^{n_p - 1} \left(1 - j \cdot \cot\left(\frac{n_p \pi}{2}\right)\right). \tag{4.67}$$

An interesting property of (4.67) is that the ratio between the imaginary and the real part of the electric permittivity is constant for all the frequencies. This characteristic is also encountered in the constant Q-factor approach (or quality Q-factor) (4.68) (Bano, 2004) which, is also widely used for expressing the frequency-depended elastic properties of soils (Kjartansson, 1979)

$$\chi(\omega) = \sum_{p=1}^{P} A_p \left(-j\frac{\omega}{\omega_p}\right)^{n_p - 1} = \frac{\epsilon''}{\epsilon'} = \frac{1}{Q}. \tag{4.68}$$

Where A_p and n_p are constants, ω_p is the reference frequency and ϵ'' and ϵ'

are the imaginary and the real part of the permittivity respectively. The time domain expression of (4.68) is

$$\chi(t) = \sum_{p=1}^{P} \frac{A_p \omega_p}{\Gamma(1-n)} (\omega_p t)^{-n}, \tag{4.69}$$

where Γ is the gamma function (Kreyszig, 1999). Similar to Havriliak-Negami, Jonscher function as well as steady Q-factor cannot be directly implemented to FDTD. Multi-Debye functions are usually employed in order to approximate Jonscher function for a given frequency range.

4.2.3 *Dielectric properties of soils*

A wide range of GPR's applications focus on sensing and mapping the shallow subsurface of the Earth, which mostly consists of soil and rocks i.e. Earth materials. Dielectric properties of Earth materials are of great importance since they can affect GPR's performance in various ways: reducing the intensity of the scattering field, reducing the central frequency of the pulse, which subsequently results to the decrease of GPR's resolution and so on. Thus, an accurate description of soil's dielectric properties is crucial in order to be able to predict the performance of GPR and to get an insight on the scattering mechanisms within the shallow subsurface.

Soil's dielectric properties is the subject of a continuous research which aims to clearly define the soil's dielectric properties with respect to their composition and structure. Campell and Ulricks (1969) illustrate a sufficient amount of experimental results in which dry samples of earth materials do not show signs of dispersive behaviour at microwave frequencies. VonHippel (1954) shows cases of water-saturated soils with a frequency depended behaviour similar to water. The cases above gave early indications that water is responsible for the soil's dispersive properties (Hoekstra and Delaney, 1974). Later studies (Dobson et al., 1985) proved with no doubt the aforementioned premise and highlighted the importance of water for describing the dielectric properties of soils.

Since soil's dielectric properties are closely related to water, a description of water's electric permittivity is crucial for deriving an inclusive formula for describing the dielectric properties of soils. The Debye model with a single Debye pole ($P = 1$ in (4.58)) has been widely used to describe the dielectric properties of pure water. The Debye relaxation is in good agreement with experiments, (Kaatze and Uhlendorf, 1981, Liebe et al., 1991) nevertheless, cases have been reported (Grant et al., 1957) in which pure water behaves like a Cole-Cole medium (4.65).

Lane and Saxton (1952) introduced a conductive term to the standard Debye model in order to include the ionic conductivity resulting from the water's salinity

$$\epsilon_w = \epsilon_{w,\infty} + \frac{\epsilon_{w,s} - \epsilon_{w,\infty}}{1 + j\omega t_{w,0}} + \frac{\sigma_w}{j\omega\epsilon_0}, \tag{4.70}$$

where σ_w is the conductive term due to the electrolytes, and $\frac{\epsilon_{w,\infty}}{\epsilon_0} = 4.9$ (Lane and Saxton, 1952). Klein and Swift (1977) found that $\epsilon_{w,s}$ is related to temperature and they came up with an empirical formula which describes the temperature-dependent static permittivity of water

$$\epsilon_{w,s} = \epsilon_0 \left(88.045 - 0.4147 \cdot T + 6.295 \times 10^{-4} T^2 + 1.075 \times 10^{-5} T^3\right), \tag{4.71}$$

where T is the temperature (^{o}C). Equation (4.71) is in good agreement with the results of Malmberg and Maryott (1956) who experimentally derived a third order polynomial similar to (4.71) in an effort to describe the temperature-depentent real part of water's permittivity for low frequencies. Similar to $\epsilon_{w.s}$, the relaxation time of water $t_{w,0}$ also varies with temperature (Phuong Tran et al., 2012)

$$\begin{aligned} t_{w,0} = \frac{1}{2\pi}(&1.1109 \times 10^{-10} - 3.824 \times 10^{-12} T \\ &+ 6.938 \times 10^{-14} T^2 - 5.096 \times 10^{-16} T^3). \end{aligned} \tag{4.72}$$

The conductive term σ_w is related with both the temperature and the salinity of the water and it can be described through the following equations (Stogryn, 1971)

$$\sigma_w(T, S) = \sigma(25, S)\, e^{-\Delta\beta} \tag{4.73}$$

$$\Delta = 25 - T \tag{4.74}$$

$$\begin{aligned} \beta = &2.033 \times 10^{-2} + 1.266 \times 10^{-4}\Delta \\ &+ 2.464 \times 10^{-6}\Delta^2 - S(1.849 \times 10^{-5} \\ &- 2.551 \times 10^{-7}\Delta + 2.551 \times 10^{-8}\Delta^2) \end{aligned} \tag{4.75}$$

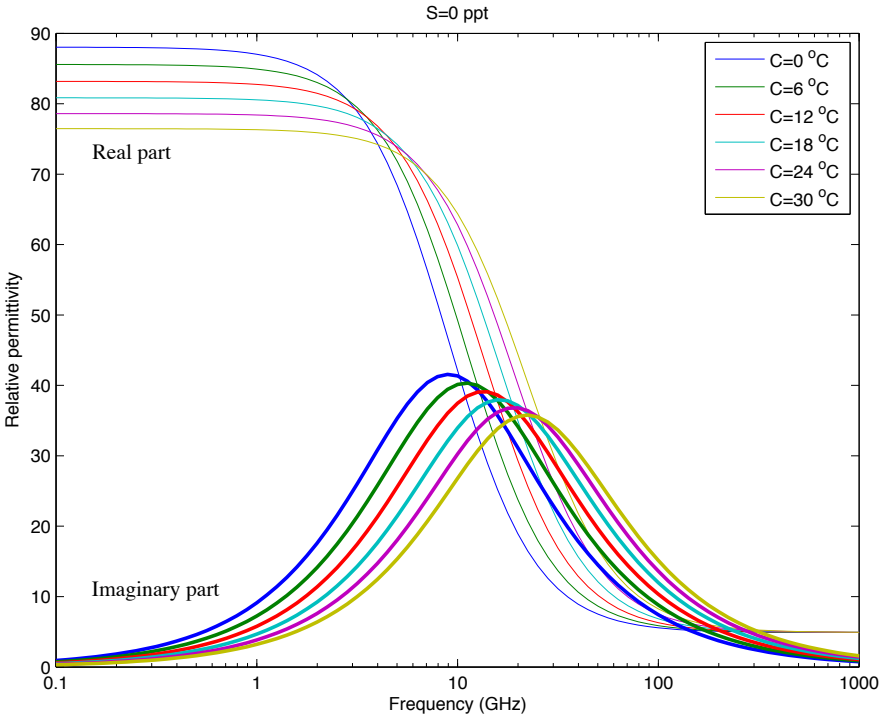

Figure 21: Relative electric permittivity of water for $S = 0$ and for temperatures varying from $T = 0 - 30$ ^{o}C.

$$\sigma\,(25, T) = S(0.182521 - 1.46192 \times 10^{-3} S$$
$$+2.09324 \times 10^{-5} S^2 - 1.28205 \times 10^{-7} S^3) \tag{4.76}$$

where S is the salinity in parts per thousands (ppt) (Klein and Swift, 1977). Fig. 21 and 22 illustrate the relative permittivity of water for different sets of temperatures and salinities. From (4.73)-(4.76) yields that salinity affects only the conductive term (although salinity can marginally affect both $\epsilon_{w,s}$ and $t_{w,s}$ (Klein and Swift, 1977)). Furthermore, using (4.70) is derived that only the imaginary part of the electric permittivity is salinity-dependent (see Fig. 22).

This behaviour can bee seen also in solis. Sreenivas et al. (1994) conducted several experiments measuring the permittivity of different saturated soils while changing their water's salinity. Their results showed that salinity has no effects on the real part of the electric permittivity. Their experiments also demonstrated that salinity is proportional to the imaginary part of the permittivity for all the soils used in the experiments (Sreenivas et al., 1994). Soil's dielectric properties are clearly affected by their water content which is undoubtely a major parameter but not the only one.

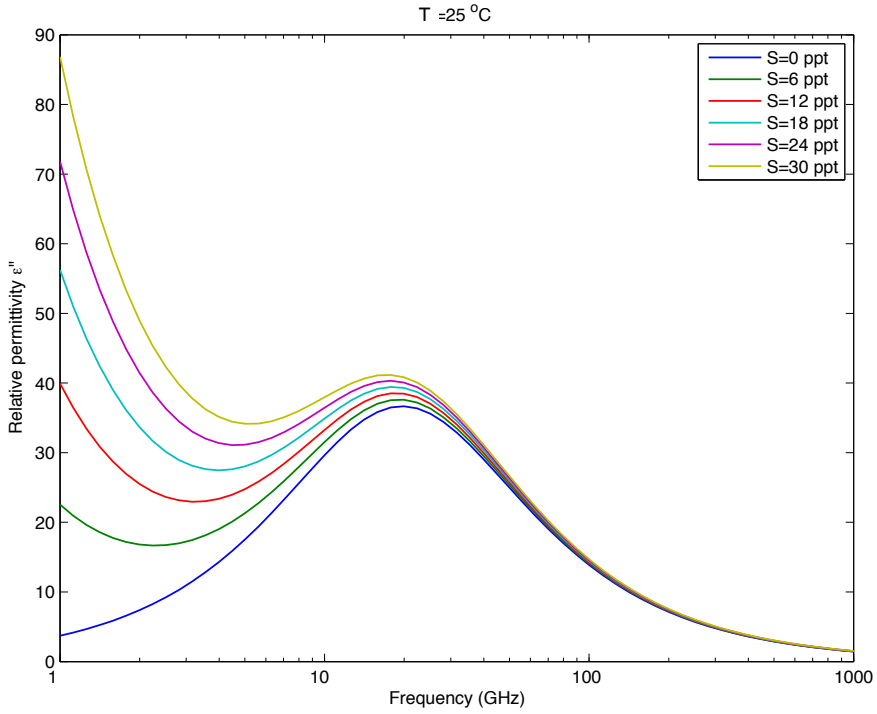

Figure 22: Imaginary part of the relative electric permittivity of water for $T = 25\ ^oC$ and for salinities varying from $S = 0 - 30$ ppt.

Birchak et al. (1974) through simple calculations derived a semi-empirical formula which makes the assumption that the soil is a two-phase medium. Subsequently, an apparent electric permittivity is calculated through

$$E_x(z) = Ae^{-\int_0^Z \gamma(z)dz} = Ae^{-\gamma' Z} \tag{4.77}$$

where A is a constant and γ' is the apparent propagation constant which is defined as

$$\gamma' = \frac{1}{Z}\int_0^Z \gamma(z)dz. \tag{4.78}$$

Assuming a two-phase soil structure (water and soil particles), (4.78) can be simplified to

$$\gamma' = f_s\gamma_s + f_w\gamma_w \tag{4.79}$$

where γ_s is the propagation constant of sand particles, γ_w is the propagation constant of water and f_s and f_w are the volumetric fractions of sand particles and water respectively ($f_s + f_w = 1$). A valid simplification for soils is that the

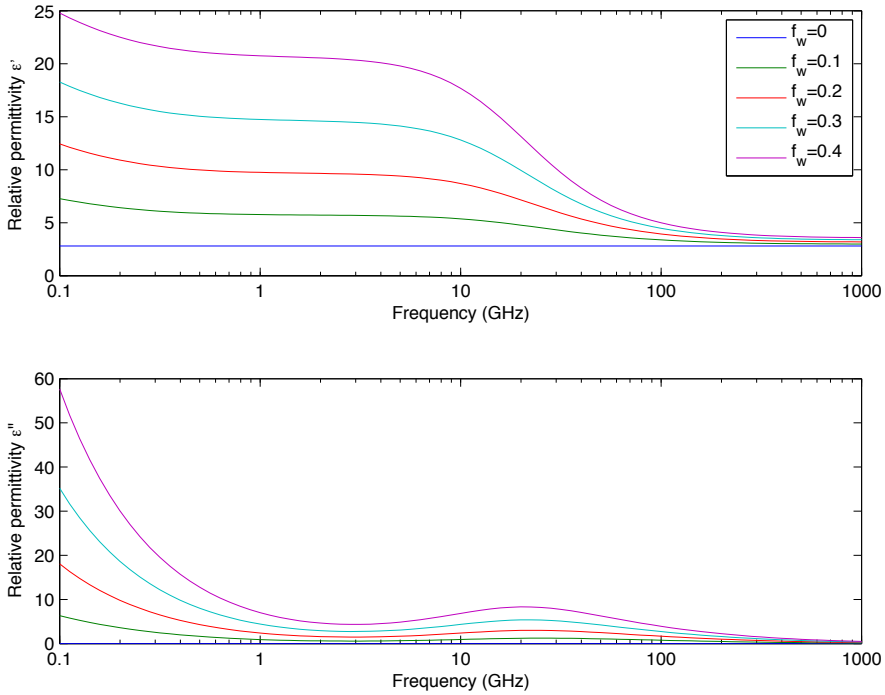

Figure 23: Dielectric properties calculated using the CRIM model. The soil's properties are $\frac{\epsilon_s}{\epsilon_0} = 2.8$, $T = 25\ ^oC$, $S = 10$ ppt and $f_w = 0 - 0.4$ with step 0.1.

magnetic permeability is equal with the magnetic permeability of free space (Birchak et al., 1974), substituting this to (4.29) and expressing the conductive term as part of the complex electric permittivity yields

$$\gamma = j\omega\sqrt{\mu_0\epsilon}. \tag{4.80}$$

Substituting the propagation constants of water and sand particles to (4.79) yields

$$\sqrt{\epsilon_m} = f_s\sqrt{\epsilon_s} + f_w\sqrt{\epsilon_w}, \tag{4.81}$$

where ϵ_m is the complex electric permittivity of the soil and ϵ_s and ϵ_w are the dielectric properties of sand particles and water respectively (both real and imaginary parts). Equation (4.81) is known as the Complex Refractive Index Model (CRIM) model and it was suggested as an improvement to the model initially proposed by Brown (1956).

Fig. 23 illustrates the dielectric properties calculated using CRIM. The properties of the soil are $\frac{\epsilon_s}{\epsilon_0} = 2.8$, $T = 25\ ^oC$, $S = 10$ ppt and $f_w = 0 - 0.4$ with step 0.1. It is evident that the velocity (i.e. the real part of the real electric permittivity) is dispersive for low frequencies (<1 GHz). This is not in

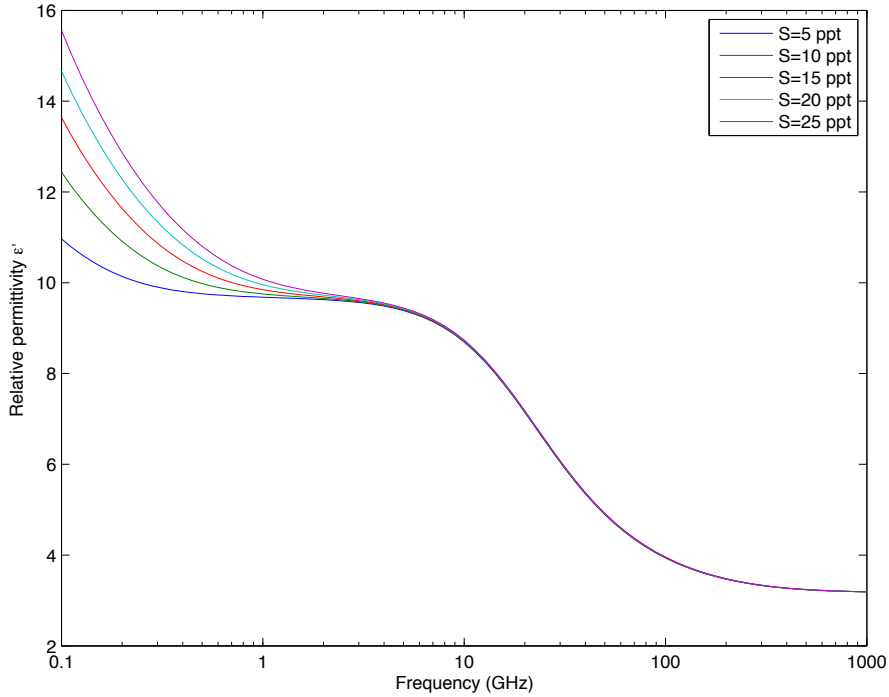

Figure 24: Real electric permittivity calculated using CRIM. The soil's properties are $\frac{\epsilon_s}{\epsilon_0} = 2.8$, $T = 25\ ^oC$, $f_w = 0.2$ and $S = 5 - 25$ ppt with step equals 5 ppt.

good agreement with early experimental evidences which indicate a frequency independent velocity for frequencies ranging from 1 MHz to 1 GHz (Davis and Annan, 1977). Later studies however, show that a low dispersion can occur in low frequencies (<1 GHz) which can be described using a Cole-Cole function (Bradford, 2007). Still, the pattern predicted using CRIM is not in good agreement with the Cole-Cole model. Fig. 24 shows that CRIM predicts a dependence of the real part of the electric permittivity to the salinity of water (for frequencies below 1 GHz). This, again is not in good agreement with the experimental evidences which clearly indicate an independence of the real part of the permittivity to the salinity of the water (Sreenivas et al., 1994). The above illustrate the limitations of CRIM when it comes to low frequencies.

Topp et al. (1980) conducted a series of experiments which indicate that the real electric permittivity of soils –for relatively low frequencies– is practically indepedent of temperature, salinity of water and soils density. They also suggested a method with which the real electric permittivity of soils (for relatively low frequencies) can be calculated. Their method is based on an experimentally derived formula which associates the real electric permittivity with soil's water content

$$\epsilon_m(0.01 - 1\ GHz) = \epsilon_0 \left(3.03 + 9.3 \cdot f_w + 146 \cdot f_w^2 - 76.7 \cdot f_w^3\right). \quad (4.82)$$

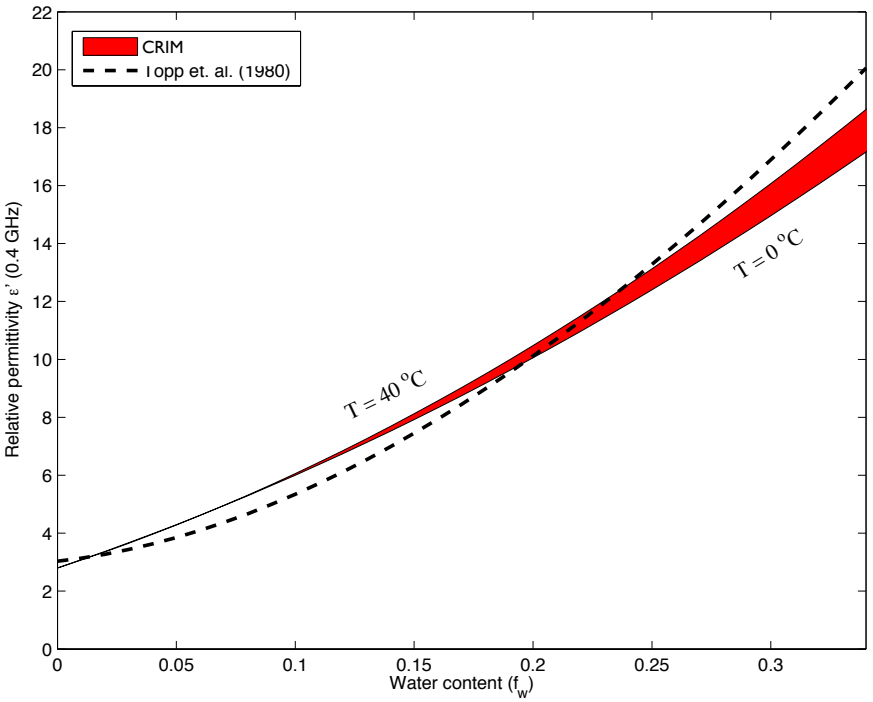

Figure 25: Real relative permittivity calculated using CRIM and the method suggested by Topp et al. (1980). The red area illustrates the range of values of the real relative permittivity calculated using CRIM for temperatures T=0-40 ^oC.

Equation (4.82) is used in order to validate CRIM. Fig. 25 shows the real relative permittivity calculated using both CRIM and the method suggested by Topp et al. (1980). The soil's properties are $\frac{\epsilon_s}{\epsilon_0} = 2.8$ (typical value for sand particles), $S = 10$ ppt and $T = 0 - 40\ ^oC$. The real electric permittivity was calculated for 0.4 GHz (notice that for that frequency the salinity-dependency of CRIM is not so dominant). The results using CRIM are in good agreement with (4.82). In addition, CRIM also predicts a (practical) temperature-independency of the real part of the permittivity which all the experimental evidences points to (Topp et al., 1980).

CRIM is a reliable and a straightforward approach for expressing the dielectric properties of soils based on a simplified, but nonetheless compact physical basis. In an effort to increase the performance of CRIM, equation (4.81) can be generalised in a more inclusive form (Shutko and Reutov, 1982)

$$\epsilon_m{}^{\alpha} = \sum_{q=1}^{Q} f_q \epsilon_q{}^{\alpha}, \tag{4.83}$$

where f_q is the volumetric fraction of the $q$ith component, ϵ_q is its electrical

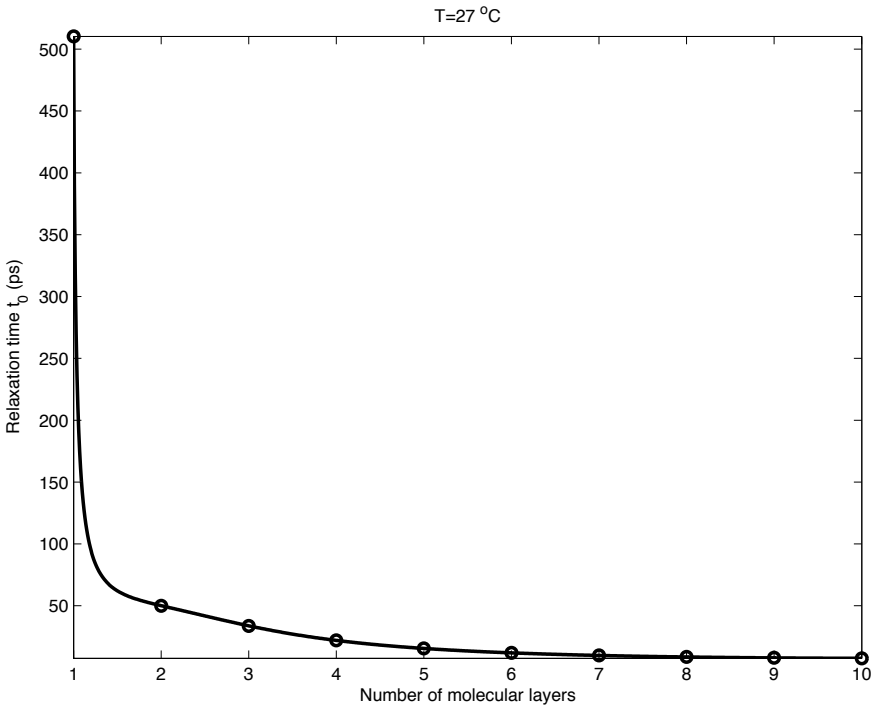

Figure 26: Relaxation time of water for different distances from the soil's particle.

permittivity (Shutko and Reutov, 1982) and α is an experimentally derived constant (Phuong Tran et al., 2012).

Using (4.83), clay materials as well as air inclusions can be included in the predicted dielectric properties. Apart from different minerals and textures, soils contains also water. The dielectric behaviour of that water depends on its position with respect to soil's particles. Bound water is the water which occurs close to the soil's particle ($<$ 10 number of monomolecular layers of water) and free water is the water which is relative far from them ($>$ 10 number of monomolecular layers of water) (Boyarskii et al., 2002). Free water is defined as the water which is able to move obeying the hydraulic laws (Boyarskii et al., 2002) in contrast with bound water which is attached to the soil's particle due to electric forces acting at the surface of the latter. The dielectric properties of the bound water depends on how far from the soil's particle the water is (Boyarskii et al., 2002). Based on that, and using experimental data, Boyarskii et al. (2002) suggested a formula which predicts the dielectric properties of bound water for $T = 27\ ^oC$. They concluded that only the relaxation time (t_0) changes with respect to the water position and this dependence is expressed through

$$t_0(h) = (-4.9648 \times 10^{24} h^2 - 3.0867 \times 10^{11} ln(h) - \frac{7.5092 \times 10^3}{h} + 3.9121 \times 10^{18} h - 5.2036 \times 10^{12})^{-1}, \quad (4.84)$$

where h is the distance from the soil's particle counted in cm (also counted in water molecular layers, the water's molecular diameter is equal to 2.8×10^{-8} cm) and t_s is the relaxation time calculated in seconds (Boyarskii et al., 2002). The physical interpretation of this phenomenon is that the contact of the water molecules with the free surface of the soil's particles changes the structure of water making it behave (regarding its dielectric properties) like a hybrid water-ice mixture (Trabelsi and Nelson, 2006). Fig. 26 illustrates the dependence of water's relaxation time to its distance from the soil's particle. It is evident that the relaxation time converges to 7.7 ps at the 10ith molecular distance. The same relaxation time can be calculated from (4.72) for $T = 27\ ^oC$ which is an indicator that water which exists beyond the 10ith molecular layer behaves like free water as it is defined in (4.70)-(4.76). .

Modelling bound water using (4.83) results to a summation of Debye functions. Each one of them corresponds to a different relaxation time from a different molecular layer (see Fig. 27). Cole-Cole, Cole-Davidson and the more inclusive Havriliak-Negami function described in (4.65) are indirect ways to express a distribution of Debye relaxations (Hill, 1969, Trabelsi and Nelson, 2006). This is the reason why Cole-Cole models have been extensively used to describe the dielectric properties of soils (Bradford, 2007, Xiaoxian et al., 2000).

Based on the above, it is evident that in clay environments more Debye poles are needed to express the dielectric properties of the soil. The reasons for that lay in the fact that in clay environments, although the porosity is larger compared to sand, the free water is less due to the small size of the clay grains (<0.002 mm). This results to a large free surface on which bound water can occur. In order to validate this, the technique suggested by Giannakis et al. (2012) is used to approximate Cole-Cole soil functions (experimentally derived (Bradford, 2007)) with a summation of Debye relaxations. Two Cole-Cole functions are used to describe the dielectric properties of two soil types, namely, saturated sand (4.85) and wet clay (4.86) (Bradford, 2007).

$$\epsilon_{sand} = \epsilon_0 \left(29 + \frac{29 - 25.6}{1 + (j\omega \cdot 22.2 \times 10^{-9})^{0.88}} + \frac{0.45 \times 10^{-3}}{j\omega\epsilon_0} \right) \quad (4.85)$$

$$\epsilon_{clay} = \epsilon_0 \left(43 + \frac{43 - 20.7}{1 + (j\omega \cdot 18.3 \times 10^{-9})^{0.66}} + \frac{42.5 \times 10^{-3}}{j\omega\epsilon_0} \right) \quad (4.86)$$

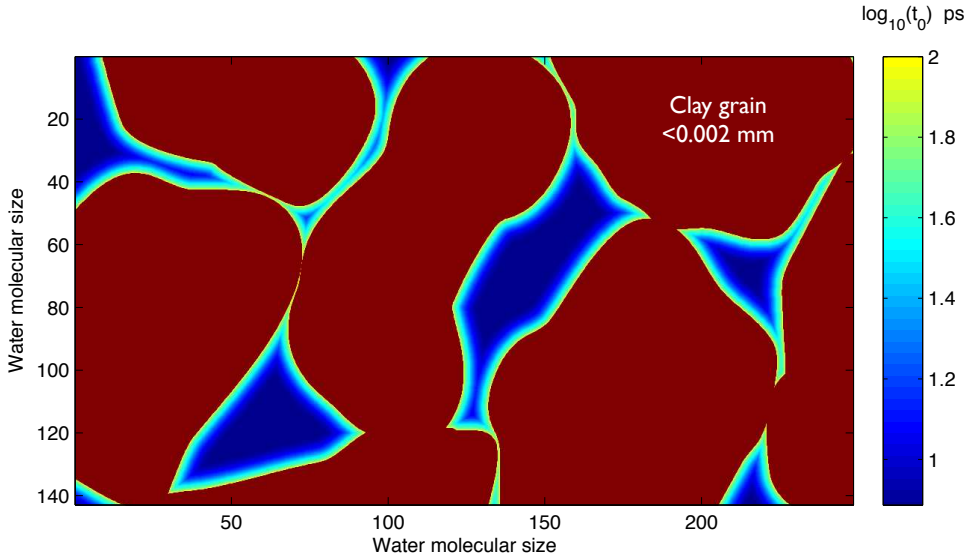

Figure 27: Distribution of relaxation times around clay grains based on (4.84) (Boyarskii et al., 2002). The water's molecular diameter is equal to 2.8×10^{-8} cm.

The Cole-Cole functions are used to fit experimental data for frequencies below 1.2 GHz. Fig. 28 and 29 illustrate the Cole-Cole functions and their corresponding Debye approximations for saturated sand and wet clay. As it is predicted, saturated sand can be adequately approximated using less Debye poles compared with wet clay. Notice that the relaxation time for both saturated sand (4.85) and wet clay (4.86) is shifted to lower frequencies compared with the relaxation time of free-water. This is due to the decrease of relaxation time in bound water as it is described in (4.84) and illustrated in Fig. 26. In the case of CRIM (4.81) (see Fig. 23), low frequency dispersion is an artefact with no physical explanation as it can be seen from the derivation of (4.81) in which a two phase soil is assumed (no bound water is accounted in the derivation). This is the reason why extending the calculations to even lower frequencies results to absurd dielectric properties (see Fig. 24).

Based on the above, it can be predicted that packed saturated rocks, in which bound water occurs, can be modelled using Cole-Cole functions. This is indeed true for sedimentary rocks like saturated sandstones and carbonate rocks (Sengwa and Soni, 2006, Taherian et al., 1990). Sedimentary rocks are successfully modelled also using a Jonscher function (4.67) (Gregoire and Hollender, 2004), although as it is reported by Taherian et al. (1990) Cole-Cole is proved to be a more appropriate choice. Apart from that, the fact that Cole-Cole is directly derived from a distribution of Debye poles, makes it more

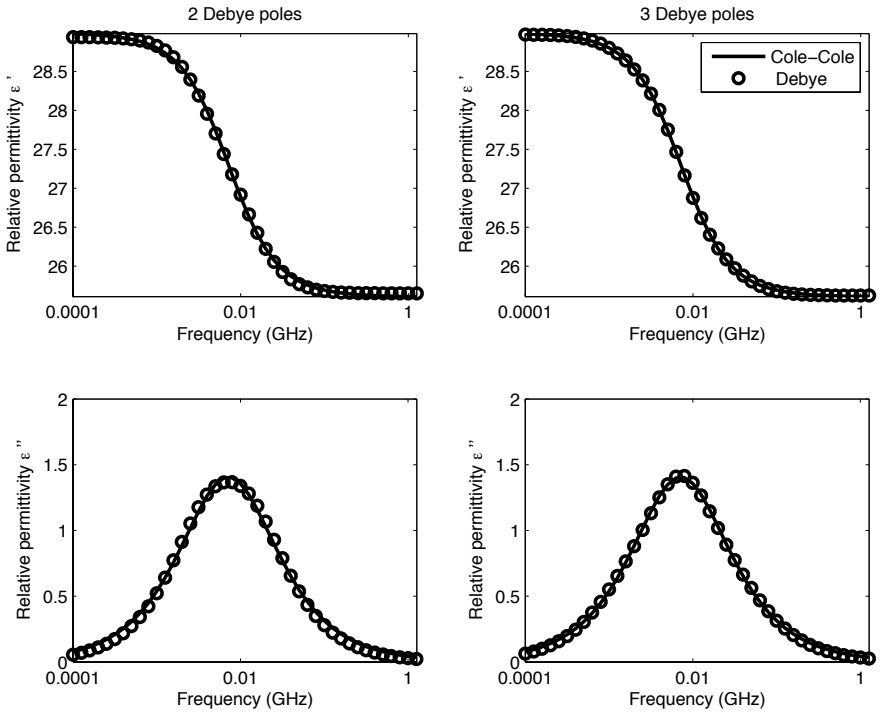

Figure 28: The Cole-Cole dipolar relaxation for saturated sand (4.85) and its multi-pole Debye approximations using two and three Debye poles. The conductivity terms for both Cole-Cole and multi-pole Debye relaxations are neglected since they stay the same in both formulations.

physically representative for describing the effects of bound water to the overall dielectric properties for both soils and rocks.

For high frequency applications (>0.3 GHz), bound water practically doesn't affect the scattering field. Still, bound water can indirectly affect the validity of the predicted dielectric properties. This happens because bound water is part of the overall moisture of the soil and in models like CRIM (4.81) it is assumed that behaves like free water. While this may be a good approximation for sands (mostly consisted with free water), it fails to predict the dielectric properties of clays since the majority of the water content in clays consists with bound water which only affects the lower frequencies.

Dobson et al. (1985) suggested a rigorous formula which defines the dielectric properties of soils for frequencies ranging from 1.4-18 GHz. The soil's permittivity suggested by Dobson et al. (1985) is expressed with respect to parameters for which is not trivial to have knowledge on (free Gouy-layer, bound Sterm-layer, depolarisation ellipsoid factors etc.). Due to that, Dobson et al. (1985) proposed a semi-empirical model which relates the dielectric properties of soils with traditionally used soil's properties, namely, clay fraction, sand fraction, water volumetric fraction, density of soil particles and bulk density.

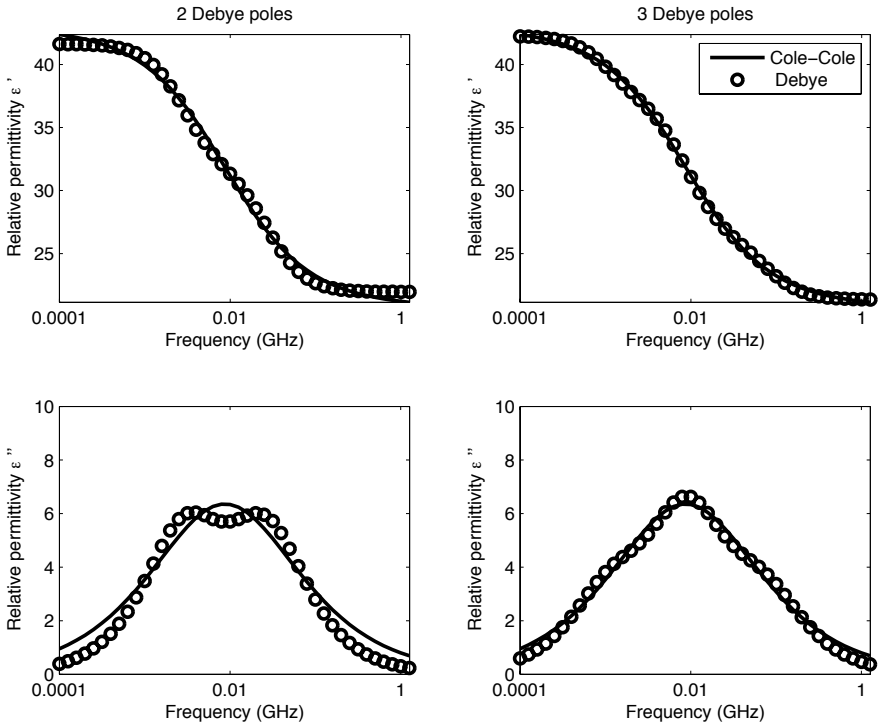

Figure 29: Similar to Fig. 28 for wet clay (4.86).

This approach underestimates ϵ' and overestimates ϵ'' for frequencies below 1.4 GHz. In order to overcome that, Peplinski et al. (1995) and Peplinski et al.b (1995) proposed a correction to the semi-empirical model suggested by Dobson et al. (1985). The updated semi-empirical model is valid for the frequency range of 0.3-1.3 GHz. These models are based on (4.83) assuming a three phase soil which consists of soil particles, water and air inclusions (Dobson et al., 1985). In contrast with CRIM which uses (4.83) to calculate the complex dielectric properties (i.e. both real and imaginary parts of permittivity), the semi-empirical model uses (4.83) to calculate both the real and the imaginary parts individually.

The semi-empirical model is described in the equations (4.87)-(4.95), where $\epsilon = \epsilon' - j\epsilon''$, j is the imaginary unit $(j = \sqrt{-1})$, f_w is the water volumetric fraction, ρ_s is the sand particles density (g/cm^3), ρ_b is the bulk density of the soil (g/cm^3), ϵ_s is the relative permittivity of the sand particles, $a = 0.65$ is an experimentally derived constant and S and C are the sand and clay mass fractions respectively ($0 \leq S, C \leq 1$ and $S + C = 1$). The complex relative electric permittivity of the water is $\epsilon_w = \epsilon'_w + j\epsilon''_w$ where $t_{0,w} = 9.23$ ps is the relaxation time for $T = 20\ ^oC$, $\epsilon_{w,s} = 80.1$ and $\epsilon_{w,\infty} = 4.9$ are the relative electrical permittivity of the water for zero and infinity frequency respectively

(Peplinski et al., 1995). The term σ_f is a linearly proportional term to the conductivity σ.

$$\epsilon'_{(1.4-18\ GHz)} = \left(1 + \frac{\rho_b}{\rho_s}(\epsilon_s^a - 1) + f_w^{\beta'}\epsilon_w^{'a} - f_w\right)^{1/a} \tag{4.87}$$

$$\epsilon'_{(0.3-1.3\ GHz)} = 1.15\epsilon^{'}_{(1.4-18\ GHz)} - 0.68 \tag{4.88}$$

$$\epsilon'' = f_w^{\frac{\beta''}{a}}\left(\epsilon''_w + \frac{\sigma_f}{\omega\epsilon_0}\frac{(\rho_s - \rho_b)}{\rho_s f_w}\right) \tag{4.89}$$

$$\epsilon_s = (1.01 + 0.44\rho_s)^2 - 0.062 \tag{4.90}$$

$$\beta' = 1.2748 - 0.519 \cdot S - 0.152 \cdot C \tag{4.91}$$

$$\beta'' = 1.33797 - 0.603 \cdot S - 0.166 \cdot C \tag{4.92}$$

$$\epsilon_w = \epsilon_{w,\infty} + \frac{\epsilon_{w,s} - \epsilon_{w,\infty}}{1 + j\omega t_{0,w}} \tag{4.93}$$

$$\sigma_{f(1.4-18\ GHz)} = -1.645 + 1.939\rho_b - 2.25622 \cdot S + 1.594 \cdot C \tag{4.94}$$

$$\sigma_{f(0.3-1.3\ GHz)} = 0.0467 + 0.2204\rho_b - 0.411 \cdot S + 0.6614 \cdot C. \tag{4.95}$$

Fig. 30 and 31 illustrate the calculated dielectric properties using the model suggested by Peplinski et al. (1995) for two different soil types. The properties of the first soil (Fig. 4.17) are $\rho_s = 2.66\ (gr/cm^3)$, $\rho_b = 2\ (gr/cm^3)$, $S = 0.9$ and $C = 0.1$. The second case is similar with the previous using $S = 0.1$ and $C = 0.9$. It is evident that increasing the clay content results to the decrease of the real part of the permittivity (i.e. increase of the velocity). This is not in good agreement with the general experience which expects low velocities in clay environments. The apparent peculiar result can be explained from the fact that clay environments (due to the high porosity of clay) have more water content which results to the decrease of the velocity. Dry clay has equal or less real part of permittivity compared with dry sand (Daniels, 2004), also due to the high porosity of clays, dry clays results to a large fraction of air which will add to the overall increase of the velocity.

Clay fraction, majorly affects the imaginary part of the electric permittivity. The imaginary part of the electric permittivity consists of two parts, one which is related with the conductive term and one which is related to the Debye relaxation due to the dipolar relaxation of the water. Increasing the

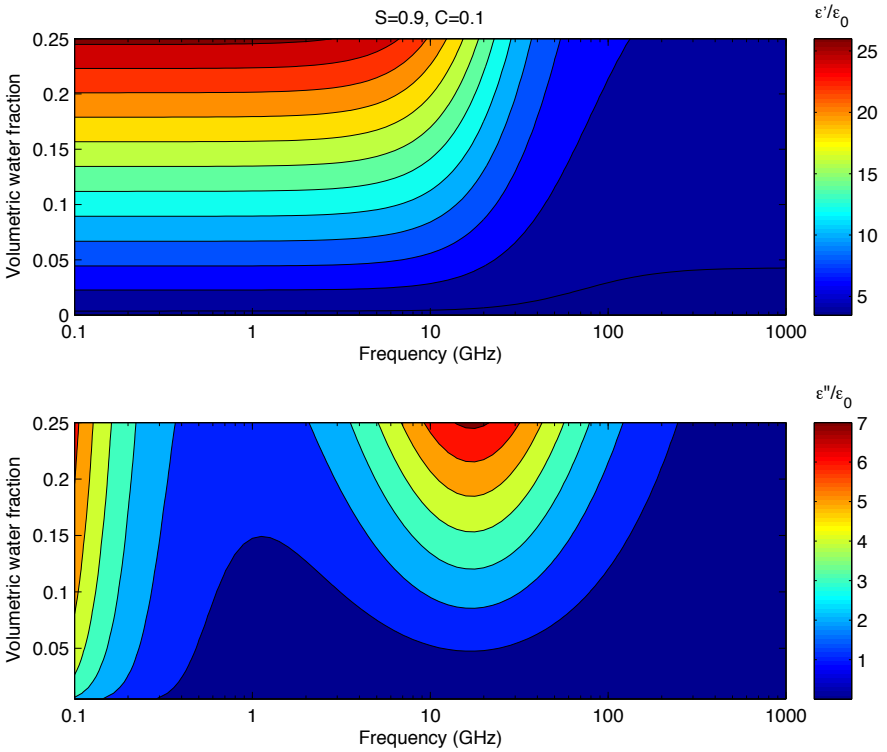

Figure 30: Real and imaginary part of the relative electrical permittivity using the model suggested by Peplinski et al. (1995). The soil's parameters are $\rho_s = 2.66\ (gr/cm^3)$, $\rho_b = 2\ (gr/cm^3)$, $S = 0.9$, $C = 0.1$ and for $f_u = 0 - 0.25$.

water volumetric fraction results in the increase of the imaginary part (i.e. the attenuation) and also increases the contribution of the Debye relaxation. Increasing the clay fraction makes the losses to be primarily related to the conductive term and decreases the effects of the Debye relaxation. This is the result of the inability of clays to support free water. Due to that, dipolar relaxations near the relaxation frequency of the water are shifted to lower frequencies which are not accounted to the semi-empirical model.

Fig. 32 illustrates a comparison between the calculated real permittivity using the model suggested by Topp et al. (1980) and the semi-empirical model for 0.3-1.3 GHz described in (4.87)-(4.95). The soil's properties are $S = 0.1$, $C = 0.9$, $\rho_b = 1\ gr/cm^3$ and $\rho_s = 2.66\ gr/cm^3$. The calculated permittivities are in good agreement for clay soils (as it is shown in Fig. 32) but as the sand fraction increases, the semi-empirical model tends to overestimate the real permittivity. The approach suggested by Topp et al. (1980) although its popularity it is independent of the soil's structure which is not in good agreement with experimental evidence which point to the opposite direction (Dobson et al., 1984). That means that the dependence of the semi-empirical method to the soil structure although it is not in good agreement with Topp et al.

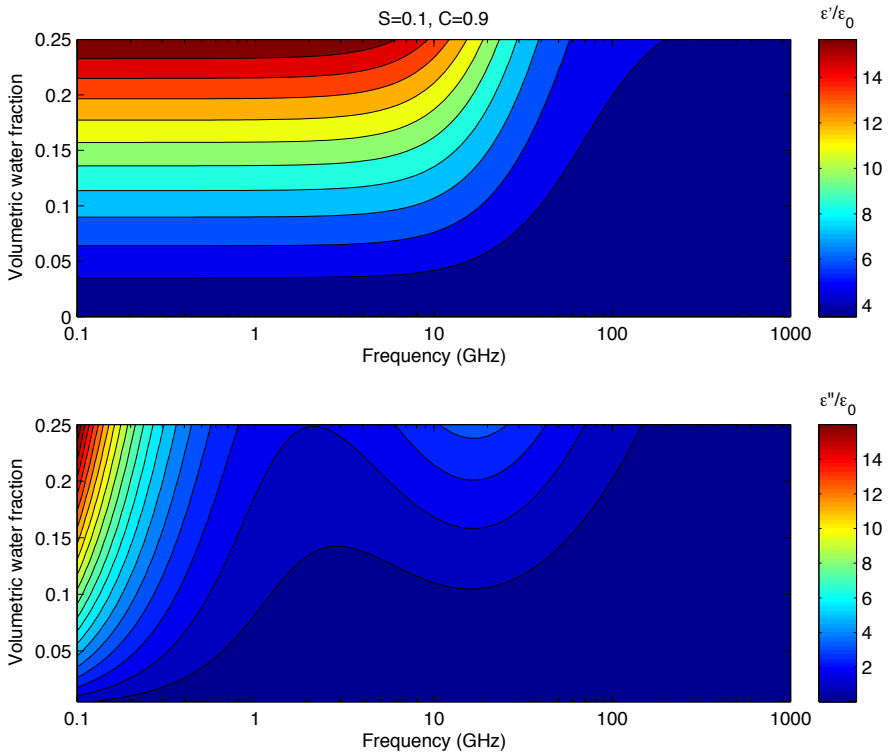

Figure 31: Similar to Fig. 30 for $S = 0.1$ and $C = 0.9$.

(1980) is still a rational conclusion which is backed up by experimental evidence (Dobson et al., 1984). Nonetheless, increasing the sand fraction (using the semi-empirical model) results to a linear relationship between the permittivity and the water content. This is the basic drawback of the semi-empirical model since measured permittivities don't show this kind of linear behaviour with respect to water content (Dobson et al., 1985).

The semi-empirical model is particularly attractive for high frequency applications. The reasons for that, is the elegant form with which the dielectric properties of the soils are defined. Readily available properties like sand or clay fractions are used in order to describe the electric permittivity which is in good agreement with experimental data for a wide range of frequencies (Peplinski et al., 1995). The dispersive behaviour resulting from the occurrence of free water is included in the semi-empirical model while the effects of bound water (i.e. Cole-Cole behaviour) are neglected since they affect lower frequencies. Another reason for considering the semi-empirical model an attractive choice for high frequency applications, is that for the frequency range of 0.5-3 GHz, the function described in (4.87)-(4.95) can be sufficient approximated with a single Debye pole (Giannakis et al., 2014). This makes the implementation of semi-empirical model to FDTD computationally efficient and straightforward.

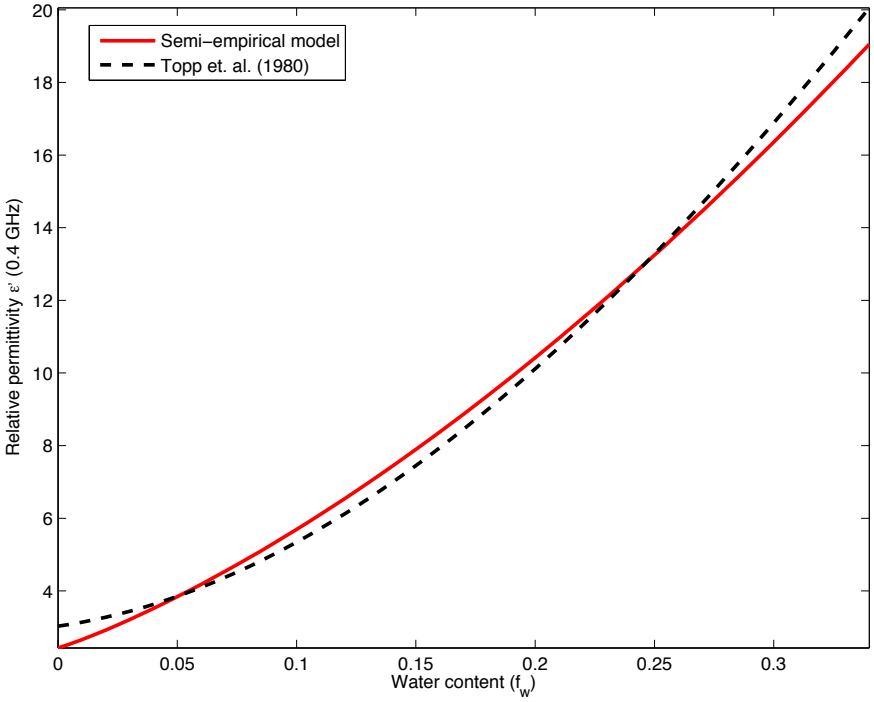

Figure 32: Real relative permittivity calculated for 0.4 GHz using the semi-empirical method (Peplinski et al., 1995) and the method suggested by Topp et al. (1980). The properties of the soil are, $S = 0.1$, $C = 0.9$, $\rho_b = 1\ gr/cm^3$ and $\rho_s = 2.66\ gr/cm^3$.

5

THE FINITE-DIFFERENCE TIME-DOMAIN METHOD

The aim of this chapter is to overview the use of finite differences in developing the FDTD method as applied to electrodynamics. The numerical errors as well as the stability conditions of FDTD are presented and analysed. This chapter also focuses on novel and computationally efficient approaches to model dispersive media using an inclusive time-domain relaxation function which holds as special cases the widely used Debye, Drude and Lorentz media. Lastly, PML is explained and a novel method for implementing it to FDTD is proposed.

5.1 INTRODUCTION

Maxwell's equations describes all the macroscopic phenomena related to electrodynamics. Predicting and modelling the propagation of electromagnetic waves in any arbitrarily chosen medium requires the solution of Maxwell's equations subject to boundary conditions. This is not an easy task and so far, analytical solutions have been derived only for simple and clinical scenarios (Hertzian dipole in homogenous space (Balanis, 1989), scattering field of a circular cylinder (Balanis, 1989), ideal dipole over stratified media (Lambot, 2007, Sommerfeld, 1909)).

For more complex and realistic problems, numerical techniques are employed in an effort to approximate Maxwell's equations within the order of accuracy of the selected method. The scientific field which deals with the numerical evaluation of Maxwell's equations is known as computational electrodynamics. A number of methods have been proposed to address this issue (Sadiku, 2000), the most widely used are, the Method of Moments (MoM) (Peterson et al., 1998), the Finite Element Method (FEM) (Jin, 2002), FDTD (Fang, 1989, Gedney, 2011, Giannopoulos, 1997, Luebbers and Kunz, 1993, Taflove, 2005, Taflove et al., 2013, Yee, 1966), FD implicit techniques (Crank and Nicolson, 1947, Namiki, 1999), Finite Element Time-Domain (FETD) (Jin, 2002, Lee et al., 1997, Zhu et al., 2011), the Pseudo-Spectral Time-Domain (PSTD) method (Liu, 1997) and the Transmission Line Matrix (TLM) method (Giannopoulos, 1997).

All the methods above employ different approximation schemes in an effort to numerically evaluate Maxwell's equations. Their common point, is that for ideally infinite computational resources the numerical solution converges to

the analytical one. Apart from that, each method has its unique characteristics making them suitable to some problems and not attractive to others. The MoM is a semi-analytic, frequency domain technique that calculates the current density which occurs in boundaries between media. Subsequently, the fields emerging from these currents are analytically calculated. This indicates, that for simple models having small number of boundaries, and for monochromatic waves, MoM is very attractive approach. Thats not the case for time-domain applications dealing with complex geometries with a large number of boundaries. Frequency domain techniques like FEM (Jin, 2002), are attractive when a small number of frequencies need to be modelled. Apart from that, the implicit nature of frequency domain methods requires the storage of large matrices which increases the Random-Access Memory (RAM) requirements. FETD is a time-domain finite element approach which has the advantages of the unstructured and adaptive finite element grid. The drawback of FETD is the need of a large sparse matrix which increases RAM requirements. This issue can be partly addressed by using hybrid FDTD-FETD subdomain schemes (Zhu et al., 2011). The PSTD method evaluates time derivatives using a second order accuracy FD scheme. The spatial derivatives are calculated using the differentiation theorem of the Fourier transform (Taflove and Hagness, 2000). PSTD is an attractive method for modelling time-domain problems but has difficulties modelling PEC and sharp boundaries with large dielectric contrasts (Taflove and Hagness, 2000).

FDTD method is an inclusive term which describes the synchronisation of numerically evaluated derivatives in space and time using central FD schemes. The abbreviation FDTD was first used by Taflove (1980) to describe the method initially suggested by Yee (1966). The original method proposed by Yee (1966), uses second order accurate derivatives both in time and space, in order to explicitly evaluate Maxwell's equations using a leapfrog approach. Apart from electrodynamics, FDTD has been successfully applied to a diverse set of fields like quantum physics (Moxley et al., 2013), hydrodynamics (Neuman and Richtmyer, 1950) and so on.

FDTD is a fully explicit method which doesn't require the solution of linear systems and deals with the problem locally i.e. the calculated fields are described with respect to the fields around them. This makes the parallelisation of FDTD efficient (Guo et al., 2012). The time domain nature of FDTD requires only a simple run to calculate the response for a wide range of frequencies (Taflove and Hagness, 2000) making it particularly attractive for ultra wide-band problems. Dispersive as well as nonlinear media can be accurately and efficiently treated using FDTD. In contrast with PSTD, FDTD can accurately simulate PEC as well as Perfect Magnetic Conductor (PMC) in a straightforward manner.

For the reasons above, FDTD is one of the most widely used methodologies for numerically evaluating Maxwell's equations. The original paper by Yee (1966) has more than 3500 citations from a wide range of scientific fields varying from medical applications (Furse, 2006) to photonics (Kong and Choi, 2009). Although its popularity, FDTD doesn't come without drawbacks. The most important of which, is the constrain of time and spatial discretisation ratio which is the result of the explicit nature of the method. FD implicit techniques like the Crank-Nicolson method (Crank and Nicolson, 1947) or the Alternating-Direction Implicit (ADI) technique (Namiki, 1999), manage to overcome the issue of stability. Nonetheless, time steps far from the Courant limit (Taflove and Hagness, 2000), although stable, result to larger numerical errors (Garcia, 2002).

In the present thesis, FDTD is chosen in order to model GPR for AP landmine detection. The unique characteristics of near field high frequency problems can be adequately addressed using FDTD. Large electrical structures needed to be modelled in order to accurate simulate the antenna units, the targets, soils and so on. FDTD is a very fast and efficient method which is an attractive choice for computationally heavy problems. GPR is an ultra wide-band time domain technique and FDTD is particularly attractive for this type of problems. Regarding the dielectric properties, dispersive media like water and saturated soils can be accurately and efficiently simulated using FDTD. Soil's are highly complex media with stochastic geometry, FDTD is suitable for modelling complex structures with arbitrarily number of boundaries and dielectric contrasts. In addition, PEC which are crucial for modelling antenna units, AP landmines and false alarm targets can be efficiently and easily modelled using FDTD.

The above reasons are related with the utility of FDTD and its ability to address the problems arising in GPR modelling for AP landmine detection. Apart from this, another reason for choosing FDTD is its simplicity and elegance. The theoretical foundation of FDTD is easy to grasp and as it is stated by Gedney (2011) "everyone can FDTD".

5.2 FINITE DIFFERENCES METHOD

5.2.1 *General principles*

FD is a numerical method for approximating derivatives of arbitrarily integer order. FD uses information around the point of interest in order to locally approximate a given function. The $n$ith ($n \in \mathbb{Z}$) derivative of the approximation is subsequently analytically evaluated (Kunz, 1957).

For introductory reasons the well known central FD is presented in (5.1). A superficial interpretation of this equation, states that the infinitesimal small ∂x is approximated by a relatively small but nonetheless finite value (thus the name "finite differences").

$$\frac{\partial f(x)}{\partial x} = \lim_{\Delta x \to 0} \frac{f(x + \frac{\Delta x}{2}) - f(x - \frac{\Delta x}{2})}{\Delta x} \approx \frac{f(x + \frac{\Delta x}{2}) - f(x - \frac{\Delta x}{2})}{\Delta x}. \quad (5.1)$$

Using the Fourier transformation, a more rigorous interpretation of the central FD scheme in (5.1) can be derived. Using the identities $\mathcal{L}\left(\frac{\partial f(x)}{\partial x}\right) = jkf(k)$, $\mathcal{L}f(x + \Delta x) = e^{jk\Delta x} f(k)$ and $e^{jk\Delta x} = \cos(k\Delta x) + j \cdot \sin(k\Delta x)$ (Kreyszig, 1999), equation (5.1) can be expressed in wavenumber domain as

$$jk \approx \frac{e^{jk\frac{\Delta x}{2}} - e^{-jk\frac{\Delta x}{2}}}{\Delta x} = j\frac{2\sin\left(k\frac{\Delta x}{2}\right)}{\Delta x}. \quad (5.2)$$

Where k is the angular wavenumber, $j = \sqrt{-1}$ and $\mathcal{L}$ denotes the Fourier transform.

Equation (5.2) gives an insight on the nature of the approximation. The accuracy of (5.2) can be rigorously evaluated by expanding $\sin(k\Delta x/2)$ in terms of Taylor series

$$jk \approx jk\left(1 + \sum_{i=1}^{\infty}\left(\frac{(-1)^i}{2}\right)\frac{\left(\frac{k\Delta x}{2}\right)^{2i}}{(1+2i)!}\right). \quad (5.3)$$

From (5.3) it is evident that the approximation error equals with

$$R(k, \Delta x) = jk\sum_{i=1}^{\infty}\left(\frac{(-1)^i}{2}\right)\frac{\left(\frac{k\Delta x}{2}\right)^{2i}}{(1+2i)!}. \quad (5.4)$$

The error of the central FD is proportional to the wavenumber of the approximated function as well as the discretisation step (Δx). The error is usually expressed using the big $O(x)$ notation (Knuth, 1998). The big $O(x)$ notation is defined as $||O(x)|| \leq ||Cx||$, where C is a constant (Knuth, 1998). Based on that, the error in (5.4) can be simply defined as $O(\Delta x^2)$. Thus, equation (5.1) can be rewritten (without the need of the approximation symbol) as

$$\frac{\partial f(x)}{\partial x} = \frac{f(x + \frac{\Delta x}{2}) - f(x - \frac{\Delta x}{2})}{\Delta x} + \sum_{i=1}^{\infty} O\left(\Delta x^{2i}\right). \quad (5.5)$$

The order of accuracy of FD is defined as the smallest power in which Δx is raised in the big $O(\Delta x)$ notation. This approach is based on the fact that

usually $\Delta x < 1$. The latter, implies that $O(\Delta x^n) > O(\Delta x^{n+1})$. From the above it is evident that $O(\Delta x^2)$ is the biggest term of the summation in (5.5). Thus, using $O(\Delta x^2)$ to define the order of accuracy is a valid approach with which different FD schemes can be compared and analysed.

From (5.5) it is derived that the central FD in (5.5) is a second order accurate approximation of the first derivative. FD schemes with different order of accuracy can be derived by employing Taylor series. Taylor series holds as special cases all the possible polynomials. Thus, Taylor series is an attractive choice to locally approximate given functions. Apart from that, polynomials can be easily differentiated using inclusive formulas that can be applied to any arbitrary order of differentiation (Kopal, 1955).

Taylor series express a given function with respect to its derivatives in a specific point. Series like the Euler-forward or the Euler-backward as well as Maclauirin and Stirling series are all special cases of Taylor series.

Euler's-forward series:

$$f(x_0+\Delta x) = f(x_0) + \frac{\partial f(x_0)}{\partial x}\Delta x + \frac{\partial^2 f(x_0)}{\partial x^2}\frac{\Delta x^2}{2!} + \frac{\partial^3 f(x_0)}{\partial x^3}\frac{\Delta x^3}{3!}.... \quad (5.6)$$

Euler's-backward series:

$$f(x_0-\Delta x) = f(x_0) - \frac{\partial f(x_0)}{\partial x}\Delta x + \frac{\partial^2 f(x_0)}{\partial x^2}\frac{\Delta x^2}{2!} - \frac{\partial^3 f(x_0)}{\partial x^3}\frac{\Delta x^3}{3!}.... \quad (5.7)$$

Series resulting from substracting (5.7) from (5.6):

$$f(x_0+\Delta x) = f(x_0-\Delta x) + \frac{\partial f(x_0)}{\partial x}2\Delta x + \frac{\partial^3 f(x_0)}{\partial x^3}\frac{2\Delta x^3}{3!} + \frac{\partial^5 f(x_0)}{\partial x^5}\frac{2\Delta x^5}{5!}..... \quad (5.8)$$

Series resulting from averaging (5.7) and (5.6) (Stirling's series):

$$\frac{f(x_0+\Delta x)+f(x_0-\Delta x)}{2} = f(x_0) + \frac{\partial^2 f(x_0)}{\partial x^2}\frac{\Delta x^2}{2!} + \frac{\partial^4 f(x_0)}{\partial x^4}\frac{\Delta x^4}{4!}..... \quad (5.9)$$

From (5.6), (5.7) and (5.8) it is easy to derive three different FD schemes for approximating the first derivative

Forward difference:

$$\frac{f(x_0+\Delta x)-f(x_0)}{\Delta x} = \frac{\partial f(x_0)}{\partial x} + O(\Delta x). \quad (5.10)$$

Backward difference:

$$\frac{f(x_0) - f(x_0 - \Delta x)}{\Delta x} = \frac{\partial f(x_0)}{\partial x} + O(\Delta x). \tag{5.11}$$

Central difference:

$$\frac{f(x_0 + \Delta x) - f(x_0 - \Delta x)}{2\Delta x} = \frac{\partial f(x_0)}{\partial x} + O(\Delta x^2). \tag{5.12}$$

Assuming that $\Delta x < 1$, it is evident that the central FD scheme (5.12) is a better approximation compared with (5.10) and (5.11). Using (5.9), the second order derivative can be approximated using a second order accurate FD scheme

$$\frac{f(x_0 + \Delta x) - 2f(x_0) + f(x_0 - \Delta x)}{\Delta x^2} = \frac{\partial^2 f(x_0)}{\partial x^2} + O(\Delta x^2). \tag{5.13}$$

The above approaches have an educational value in a sense that describe the main idea of FD. Namely, the approximation of the derivative operation (jk) by using information near the point of interest. In order to calculate FD schemes for different order of derivatives with different order of accuracy a more inclusive and systematic approach is needed.

5.2.2 *Inclusive quadrature formula*

Stiefel (1963) described a coherent way for calculating FD approximations of nth derivatives for arbitrary order of accuracy. This technique is based on Taylor series and results to a linear system of equations from which the FD coefficients are derived. The method described by Stiefel (1963) is constrained to positive non-zero n, i.e. can be applied only to derivatives.

Here we present a modified and more inclusive version with which not only the coefficients for numerical differentiation but also the coefficients for numerical integration and numerical interpolation are calculated within the same context. Initially, the function of interest is approximated using a subset of its Taylor series expansion

$$f(x) = \sum_{k=0}^{\infty} \alpha_k x^k \approx \sum_{k=0}^{N} \alpha_k x^k, \tag{5.14}$$

where α_k are constants. From (5.14), it is derived that the nth ($n \in \mathbb{Z}$) order derivative of $f(x)$ is

$$\frac{\partial^n f(x)}{\partial x^n} \approx \sum_{k=0}^{N} \alpha_k x^{k-n} \prod_{m=0}^{n-1} (k-m) \prod_{d=n-1}^{-2} (k-d-1)^{-1}. \tag{5.15}$$

Notice that the empty product (i.e. $\prod_{n=m}^{M}$ for $M < m$) is equal with one (Ingham and Vaughan, 1990).

The general quadrature approximation of (5.15) (which holds as special case the method suggested by Stiefel (1963)) for the point of interest (x_u) is equal by definition to

$$\frac{\partial^n f(x_u)}{\partial x^n} \approx \sum_{s=1}^{L} b_s f(x_s). \tag{5.16}$$

where b_s are the FD coefficients. Substituting (5.14) to (5.16) yields

$$\frac{\partial^n f(x_u)}{\partial x^n} \approx \sum_{s=1}^{L} b_s \sum_{k=0}^{N} \alpha_k x_s^k. \tag{5.17}$$

Combining (5.15) and (5.17), a system of linear equations is derived

$$\sum_{s=1}^{L} b_s \sum_{k=0}^{N} \alpha_k x_s^k \approx \sum_{k=0}^{N} \alpha_k x_u^{k-n} \prod_{m=0}^{n-1} (k-m) \prod_{d=n-1}^{-2} (k-d-1)^{-1}. \tag{5.18}$$

If we assume that the remaining terms in (5.14) equal to zero (i.e. $\sum_{k=N+1}^{\infty} \alpha_k x^k = 0$) then, the approximation of (5.18) becomes equality. By equating same order terms, equation (5.14) can be re-written in matrix notation $\boldsymbol{A} \cdot \boldsymbol{b} = \boldsymbol{C}$ as:

$$\begin{bmatrix} \alpha_0 x_1^0 & . & \alpha_0 x_L^0 \\ \alpha_1 x_1^1 & . & \alpha_1 x_L^1 \\ \alpha_2 x_1^2 & . & \alpha_2 x_L^2 \\ . & & \\ . & & \\ . & & \\ \alpha_N x_1^N & . & \alpha_N x_L^N \end{bmatrix} \begin{bmatrix} b_1 \\ b_2 \\ b_3 \\ . \\ . \\ . \\ b_L \end{bmatrix} = \begin{bmatrix} \alpha_0 x_u^{0-n} \prod_{m=0}^{n-1}(0-m) \prod_{d=n-1}^{-2}(0-d-1)^{-1} \\ \alpha_1 x_u^{1-n} \prod_{m=0}^{n-1}(1-m) \prod_{d=n-1}^{-2}(1-d-1)^{-1} \\ \alpha_2 x_u^{2-n} \prod_{m=0}^{n-1}(2-m) \prod_{d=n-1}^{-2}(2-d-1)^{-1} \\ . \\ . \\ . \\ \alpha_N x_u^{N-n} \prod_{m=0}^{n-1}(N-m) \prod_{d=n-1}^{-2}(N-d-1)^{-1} \end{bmatrix}$$

The matrix above can be simplified by eliminating the α_k coefficients. This implies that the coefficients b_s which calculate exactly the nth derivative of a polynomial $1 + x + x^2 + x^3 .... x^N$ are also valid for any polynomial

$\alpha_0 + \alpha_1 x + \alpha_2 x^2 + \alpha_3 x^3 .... \alpha_N x^N$. Furthermore, assuming that $x_u = \Delta x$ and $x_s = w(s)\Delta x$, yields

$$\begin{bmatrix} 1 & 1 & . & 1 \\ w_1 & w_2 & . & w_L \\ w_1^2 & w_2^2 & . & w_L^2 \\ . & & & \\ . & & & \\ . & & & \\ w_1^N & w_2^N & . & w_L^N \end{bmatrix} \begin{bmatrix} b_1 \cdot \Delta x^n \\ b_2 \cdot \Delta x^n \\ b_3 \cdot \Delta x^n \\ . \\ . \\ . \\ b_L \cdot \Delta x^n \end{bmatrix} = \begin{bmatrix} \prod_{m=0}^{n-1}(0-m) \prod_{d=n-1}^{-2}(0-d-1)^{-1} \\ \prod_{m=0}^{n-1}(1-m) \prod_{d=n-1}^{-2}(1-d-1)^{-1} \\ \prod_{m=0}^{n-1}(2-m) \prod_{d=n-1}^{-2}(2-d-1)^{-1} \\ . \\ . \\ . \\ \prod_{m=0}^{n-1}(N-m) \prod_{d=n-1}^{-2}(N-d)^{-1} \end{bmatrix}$$

When the order (N) of the polynomial used to approximate the real function is equal with the number of the FD coefficients (L), then the system is well determined and an exact solution can be found. When $N > L$, the system becomes overdetermined and can be solved using the least squares method ($\boldsymbol{b = \left(A^T A\right)^{-1} A^T C}$), although it is not recommended. For $n = 0$, the suggested approach is transformed to an inclusive interpolation formula and for $n < 0$ to a numerical integration formula. Notice that the calculated coefficients for $n < 0$ are used to calculate $\int f(\Delta x)dx = \int_0^{\Delta x} f(x)dx$. From (5.16) yields that

$$\frac{\partial^n f(x)}{\partial x^n} = \frac{\sum_{s=1}^{L} B_s f(x_s)}{\Delta x^n} + R. \tag{5.19}$$

Where $B_s = b_s \Delta x^n$ (the solutions of the well determined linear system) and R is the error arising from the approximation in (5.14) and it is defined as

$$R = \frac{\sum_{s=1}^{L} B_s F(x_s)}{\Delta x^n}. \tag{5.20}$$

The function $F(x)$ is the summation of the remaining terms in (5.14)

$$F(x) = \sum_{k=N+1}^{\infty} \alpha_k x^k. \tag{5.21}$$

Using the approach explained previously, the FD coefficients of the first deriva-

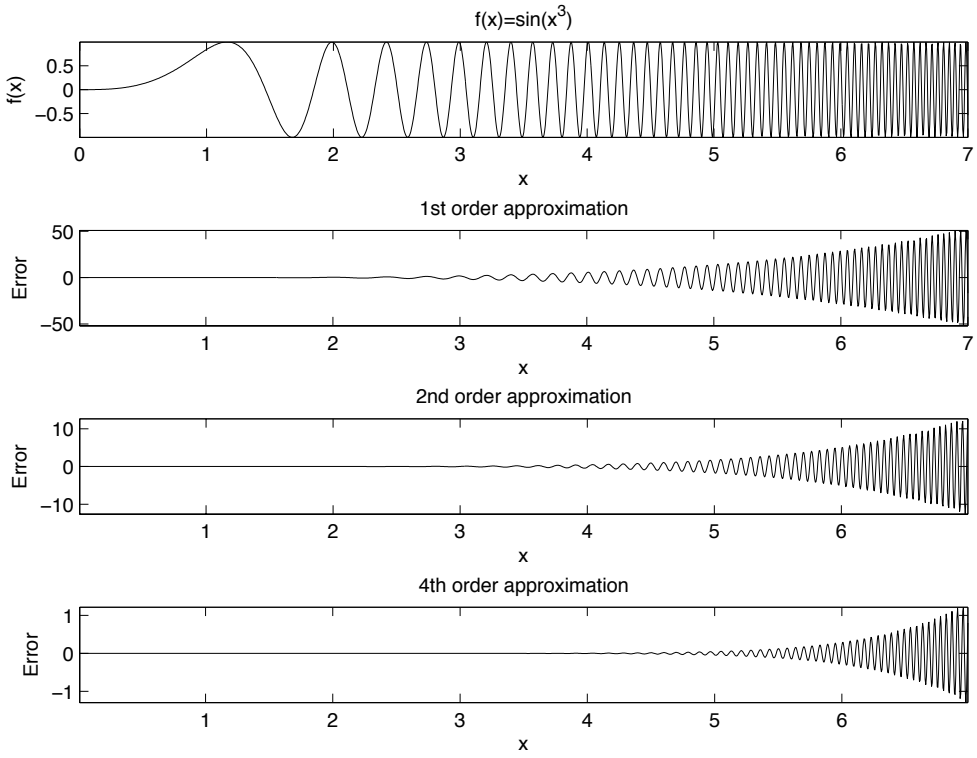

Figure 33: The first, second and fourth order of accuracy FD schemes are used to numerically evaluate the first derivative of $f(x)$. A chirp-like function ($f(x) = \sin(x^3)$) is employed in an effort to illustrate the correlation between frequency and numerical error (see (5.3)). The discretisation step equals $\Delta x = 0.005$.

tive for first (5.22), second (5.23) and fourth (5.24) order of accuracy are derived. An equally spaced grid with length Δx is chosen.

$$\frac{\partial f(x_u)}{\partial x} = \frac{f(x_u + \Delta x) - f(x_u)}{\Delta x} + O(\Delta x) \tag{5.22}$$

$$\frac{\partial f(x_u)}{\partial x} = \frac{f(x_u + \Delta x) - f(x_u - \Delta x)}{2\Delta x} + O(\Delta x^2) \tag{5.23}$$

$$\frac{\partial f(x_u)}{\partial x} = \frac{f(x_u - 2\Delta x) - f(x_u + 2\Delta x)}{12\Delta x} + \frac{2}{3}\frac{f(x_u + \Delta x) - f(x_u - \Delta x)}{\Delta x} + O(\Delta x^4). \tag{5.24}$$

Fig. 33 illustrates the numerically evaluated derivatives using (5.22), (5.23) and (5.24). A chirp-like function ($f(x) = \sin(x^3)$) is used in order to illustrate how the accuracy varies with respect to the frequency (see (5.3)). The step is chosen to be $\Delta x = 0.005$. As it is expected, increasing the order of accuracy decreases the error between analytically and numerically evaluated derivatives. From the

above, it is evident that higher order approximations or smaller discretisation steps result to a wider frequency range for which the approximation can be considered valid within a predefined order of accuracy.

5.3 FDTD GRID

The term "FDTD (n_t, n_s)" describes a numerical technique that employes synchronised (both in space and time) numerically evaluated derivatives using FD. The parenthesis terms indicate the order of accuracy of time (n_t) and spatial (n_s) derivatives. The original FDTD described by Yee (1966) is second order in both space and time i.e. FDTD $(2, 2)$. Regardless of the order of accuracy, the FDTD grid (i.e. the distribution of the fields both spatially and in time) stays the same. This is due to the central FD schemes which are necessary in order for FDTD to sustain its synchronisation. The term synchronisation states that the electric and the magnetic fields are arranged in a way such as the spatial and the time derivatives to be numerically evaluated at the same time-space point. This arrangement is known as the Yee cell.

Fig. 34 illustrates the field's distribution of a TM mode in an FDTD grid. Notice that the fields are staggered. This may seem unpractical but it is crucial in order to explicitly evaluate Maxwell's equations while retaining synchronisation. Maxwell's equations for a TM mode are

$$\frac{\partial H_x}{\partial t} = -\frac{1}{\mu}\frac{\partial E_z}{\partial y} \tag{5.25}$$

$$\frac{\partial H_y}{\partial t} = \frac{1}{\mu}\frac{\partial E_z}{\partial x} \tag{5.26}$$

$$\frac{\partial E_z}{\partial t} = \frac{1}{\epsilon}\left(\frac{\partial H_y}{\partial x} - \frac{\partial H_x}{\partial y} - \sigma E_z - J_z\right). \tag{5.27}$$

Using the field's distribution illustrated in Fig. 34 and a second order central FD (5.12), Maxwell's equations can be approximated as follows

$$H_y|^{n+1}_{i,j+1/2} = H_y|^{n}_{i,j+1/2} + \frac{\Delta t}{\mu\Delta}\left(E_z|^{n+1/2}_{i+1/2,j+1/2} - E_z|^{n+1/2}_{i-1/2,j+1/2}\right) \tag{5.28}$$

$$H_x|^{n+1}_{i-1/2,j+1} = H_x|^{n}_{i-1/2,j+1} + \frac{\Delta t}{\mu\Delta}\left(E_z|^{n+1/2}_{i-1/2,j+1/2} - E_z|^{n+1/2}_{i-1/2,j+3/2}\right) \tag{5.29}$$

$$E_z|^{n+1/2}_{i-1/2,j+1/2} = E_z|^{n-1/2}_{i-1/2,j+1/2} - \frac{\Delta t}{\epsilon}\left(\sigma E_z|^{n}_{i-1/2,j+1/2} + J_z|^{n}_{i-1/2,j+1/2}\right)$$

$$+\frac{\Delta t}{\epsilon\Delta}\left(H_x|^{n}_{i-1/2,j} - H_x|^{n}_{i-1/2,j+1} + H_y|^{n}_{i,j+1/2} - H_y|^{n}_{i-1/2,j+1/2}\right) \tag{5.30}$$

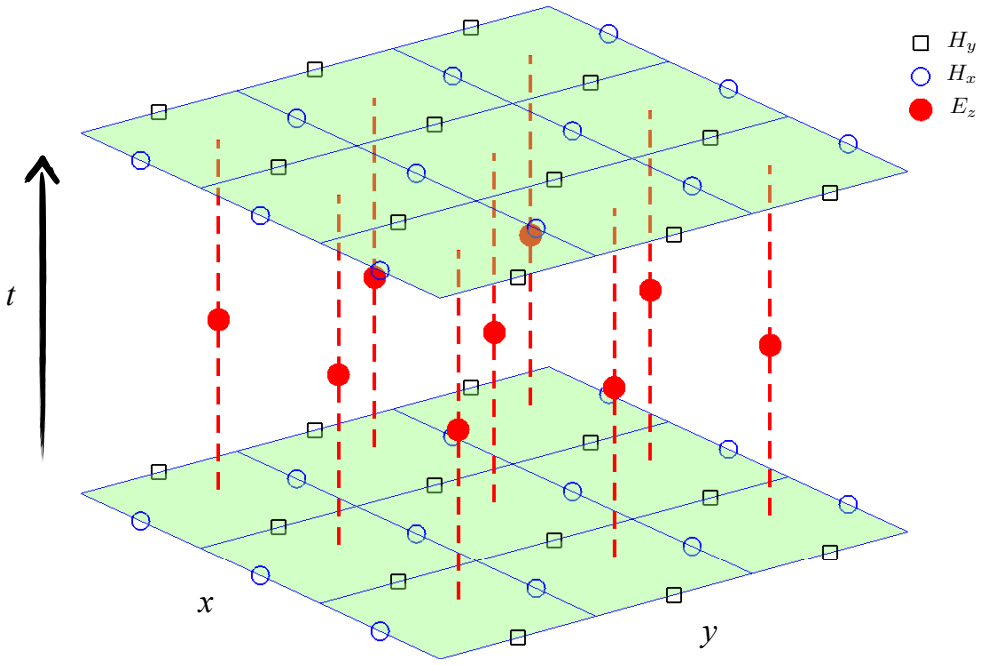

Figure 34: Arrangement of the electric and the magnetic fields for a TM FDTD grid.

where Δt and Δ are the time and the spatial steps respectively. The indices correspond to $F|^n_{i,j} = F(i\Delta,\ j\Delta,\ n\Delta t)$. From Fig. 34 and (5.30) it is evident that the values of E_z are evaluated at $E_z|^{n+1/2}$ for different n. In (5.30) the term $E_z|^n_{i+1/2,j+1/2}$ is not part of the FDTD grid. Due to that, $E_z|^n_{i+1/2,j+1/2}$ is approximated by a second order interpolation scheme (which can be derived using the method described in chapter 3.2.2)

$$E_z|^n_{i+1/2,j+1/2} = \frac{E_z|^{n+1/2}_{i+1/2,j+1/2} + E_z|^{n-1/2}_{i+1/2,j+1/2}}{2} + O\left(\Delta t^2\right). \tag{5.31}$$

Substitute (5.31) to (5.30) yields

$$E_z|^{n+1/2}_{i-1/2,j+1/2} = C_a E_z|^{n-1/2}_{i-1/2,j+1/2} - C_b \Delta \cdot J_z|^n_{i-1/2,j+1/2}$$

$$+C_b \left(H_x|^n_{i-1/2,j} - H_x|^n_{i-1/2,j+1} + H_y|^n_{i,j+1/2} - H_y|^n_{i-1,j+1/2}\right) \tag{5.32}$$

$$C_a = \frac{1 - \frac{\sigma \Delta t}{2\epsilon}}{1 + \frac{\sigma \Delta t}{2\epsilon}} \tag{5.33}$$

$$C_b = \frac{\frac{\Delta t}{\epsilon \Delta}}{1 + \frac{\sigma \Delta t}{2\epsilon}} \tag{5.34}$$

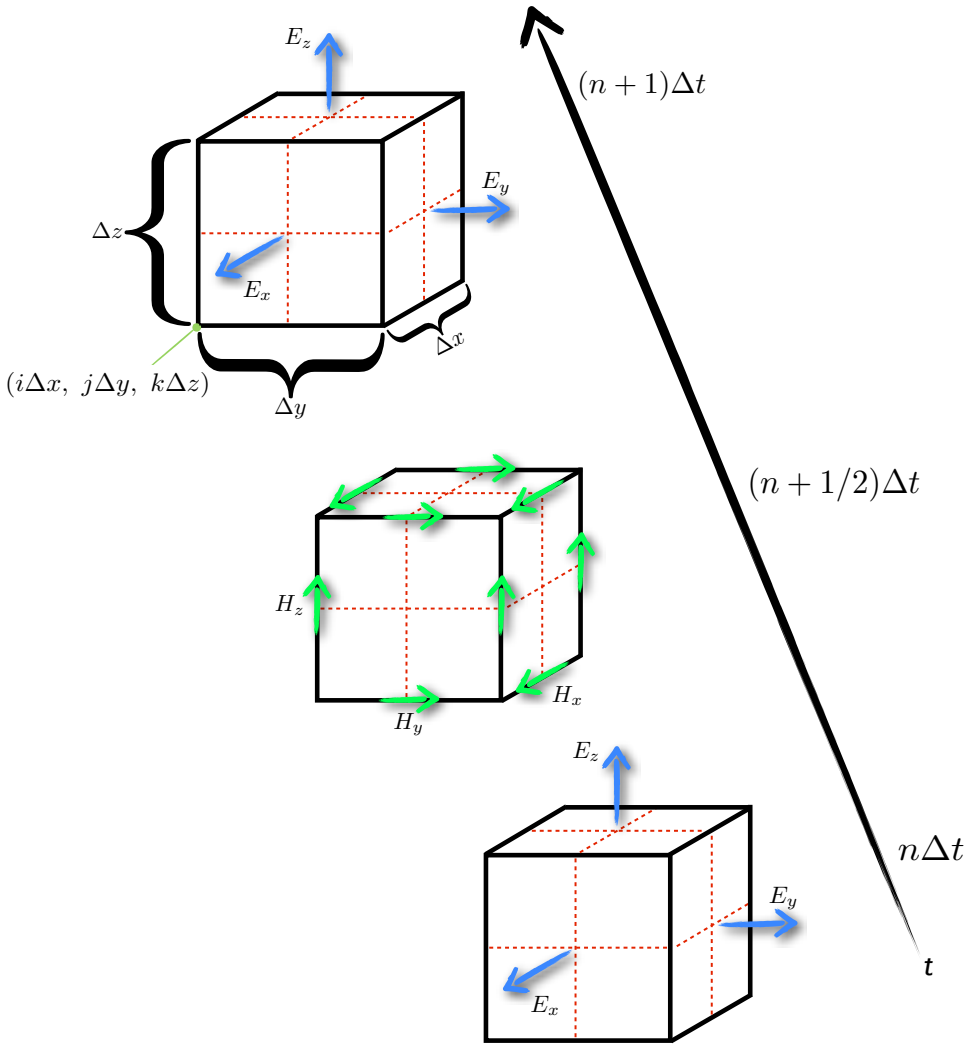

Figure 35: Arrangement of the electric and the magnetic fields in a 3D FDTD grid.

From (5.28), (5.29) and (5.32) it is evident that Maxwell's equations can be evaluated explicitly (i.e. iteratively), without the need of a simultaneous solution of equations. Although fields are staggered, their numerically evaluated derivatives retain their synchronisation. Through this, FDTD elegantly manages to balance between computational efficiency and accuracy.

In the same manner, FDTD can be trivially expanded to 3D. Fig. 35 illustrates the arrangement of the fields for a 3D FDTD grid. Notice, that similar to the 2D case, all the electric fields are evaluated at the same time step while the magnetic fields are evaluated half time step away. Both the electric and the magnetic fields are also spatially collocated. Applying a central FD approximation for the derivatives and a second order interpolation for the conductive term, the 3D FDTD equations are derived (see Appendix A).

5.3.1 *Stability and numerical dispersion*

In chapter 5.2.1, the numerical error of FD schemes is rigorously defined. The order of accuracy is proven to be sensitive to the discretisation step as well as the frequency of the function. FDTD is a numerical method in which numerically evaluated time and spatial derivatives interact with each other. Each of these FD schemes individually, contribute to the overall approximation error of FDTD. It is convenient to describe the numerical error through the so-called numerical dispersion i.e. a non-physical dispersion which is the product of numerical errors (Taflove, 2005).

The numerical dispersion for 1D and 2D can be straightforwardly derived by expressing FDTD equations to the frequency-wavenumber domain (Taflove, 2005). For the 3D case, Taflove and Brodwin (1975) used the compact form of Maxwell's equations which led to a linear system. Setting its determinant to zero, results to the numerical dispersion relationship of 3D FDTD grids (Taflove, 2005).

We derive the numerical dispersion following a more simple approach which employs the scalar wave equation (4.27)

$$\nabla^2 F_u - \gamma^2 F_u = 0 \tag{5.35}$$

where $F \in \{H, E\}$ and $u \in \{x, y, z\}$. Expanding (5.35) and assuming that $\sigma = 0$ yields

$$\frac{\partial^2 F_u}{\partial x^2} + \frac{\partial^2 F_u}{\partial y^2} + \frac{\partial^2 F_u}{\partial z^2} + \frac{\omega^2}{c^2} F_u = 0 \tag{5.36}$$

which in wavenumber domain is equal to

$$-\left(k_x^2 + k_y^2 + k_z^2\right) F_u + \frac{\omega^2}{c^2} F_u = 0. \tag{5.37}$$

FDTD (2,2) uses second order central FD schemes for evaluating the time and the spatial derivatives. This implies that the following approximations take place (see equation (5.2))

$$\omega \approx \frac{e^{j\omega\Delta t/2} - e^{-j\omega\Delta t/2}}{j\Delta t} = \frac{2\sin(\omega\Delta t/2)}{\Delta t} \tag{5.38}$$

$$k_u \approx \frac{e^{jk_u\Delta u/2} - e^{-jk_u\Delta u/2}}{j\Delta t} = \frac{2\sin(k_u\Delta u/2)}{\Delta u}. \tag{5.39}$$

Substituting (5.38) and (5.39) to (5.37) and eliminating F_u yields

$$\frac{\sin^2(\omega\Delta t/2)}{c^2\Delta t^2} = \frac{\sin^2(k_x\Delta x/2)}{\Delta x^2} + \frac{\sin^2(k_y\Delta y/2)}{\Delta y^2} + \frac{\sin^2(k_z\Delta z/2)}{\Delta z^2}. \quad (5.40)$$

Equation (5.40) describes the numerical dispersion which occurs due to numerical errors in 3D FDTD (2,2) (Taflove and Brodwin, 1975, Taflove, 2005). By expanding the sin terms in Taylor series, it is easy to prove that $\lim_{A\to 0}\sin(A) = A$. Applying this to (5.40) and assuming that $\Delta t = \partial t$ and $\Delta u = \partial u$ yields

$$c = \frac{\omega}{\sqrt{k_x^2 + k_y^2 + k_z^2}}. \quad (5.41)$$

The latter is the analytic relationship between the velocity of the electromagnetic wave (c), the angular frequency (ω) and the wavenumber (k). When finite Δu and Δt are used, numerical errors and instabilities arise.

It is more convenient to express k_u in a parametric form. Using the relationship $k^2 = k_x^2 + k_y^2 + k_z^2$ yields

$$k_x = k \cdot \cos(\theta)\cos(\phi) \quad (5.42)$$

$$k_y = k \cdot \sin(\theta)\cos(\phi) \quad (5.43)$$

$$k_z = k \cdot \sin(\phi) \quad (5.44)$$

where $\frac{\pi}{2} < \phi < -\frac{\pi}{2}$ is the latitude and $0 < \theta < 2\pi$ is the longitude of a sphere with radius k. Substituting (5.42)-(5.44) to (5.40) and assuming a uniform grid ($\Delta x = \Delta y = \Delta z = \Delta u$) yields

$$\frac{\Delta u^2}{c^2\Delta t^2}\sin^2(\omega\Delta t/2) = \sin^2(k \cdot \cos(\theta)\cos(\phi)\,\Delta u/2) \quad (5.45)$$
$$+\sin^2(k \cdot \sin(\theta)\cos(\phi)\,\Delta u/2) + \sin^2(k \cdot \sin(\phi)\,\Delta u/2).$$

Solving (5.45) for ω results to

$$\omega = \frac{2}{\Delta t}\sin^{-1}(\xi) \quad (5.46)$$

where

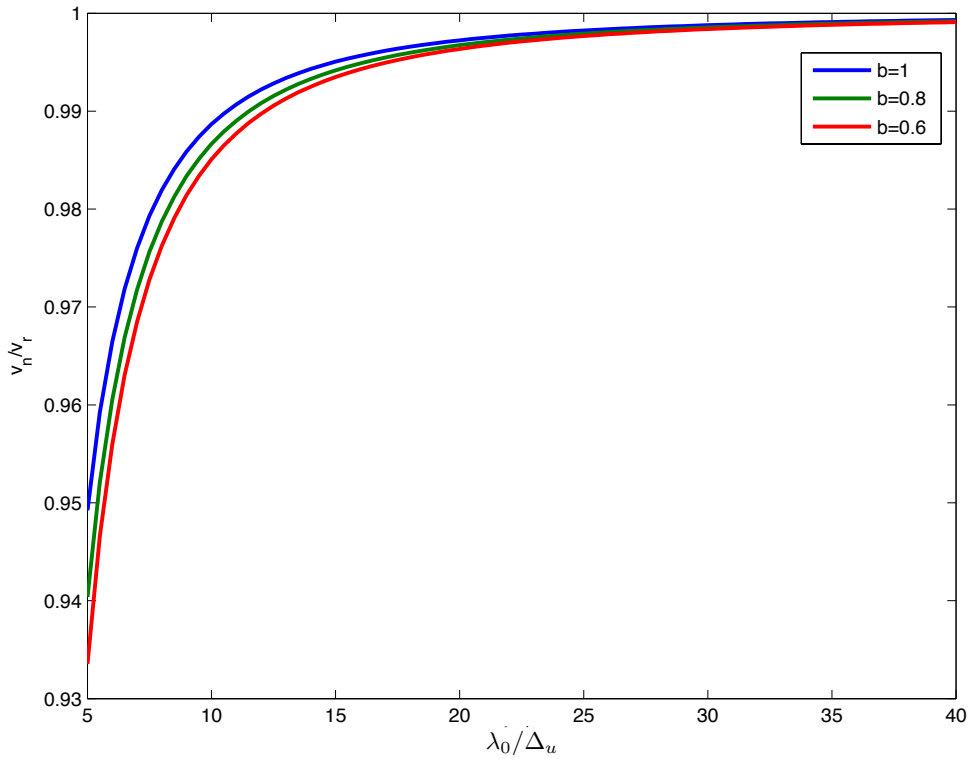

Figure 36: Velocity error of a uniform 3D FDTD (2,2). The time and spatial steps are related with $\frac{c\Delta t}{\Delta u} = \frac{b}{\sqrt{3}}$. The ratio $\frac{\nu_n}{\nu_r}$ is the ratio between the numerical (ν_n) and the real (ν_r) velocity.

$$\xi = \frac{c\Delta t}{\Delta u}(\sin^2(k \cdot \cos(\theta)\cos(\phi)\,\Delta u/2) \tag{5.47}$$
$$+\sin^2(k \cdot \sin(\theta)\cos(\phi)\,\Delta u/2) + \sin^2(k \cdot \sin(\phi)\,\Delta u/2))^{1/2}.$$

From (5.46), it is implied that when $\xi > 1$, ω becomes a complex number ($\omega = \omega_r + j\omega_i$). A complex angular frequency results to numerical instabilities (Taflove, 2005). With the term numerical instability we define the exponential growth which occurs when a wave travels subject to a complex angular frequency ($F(t,r) = F_0 e^{\omega_i t} e^{-j\omega_r t - jkr}$). From the above, it is evident that for a uniform 3D FDTD (2,2), the stability condition (the so-called Courant limit) (Gedney, 2011) can be defined as

$$\frac{c\Delta t}{\Delta u} \leq \frac{1}{\sqrt{3}}. \tag{5.48}$$

It is easy to prove that for the 1D case the stability condition is $\frac{c\Delta t}{\Delta u} \leq 1$ and for 2D $\frac{c\Delta t}{\Delta u} \leq \frac{1}{\sqrt{2}}$.

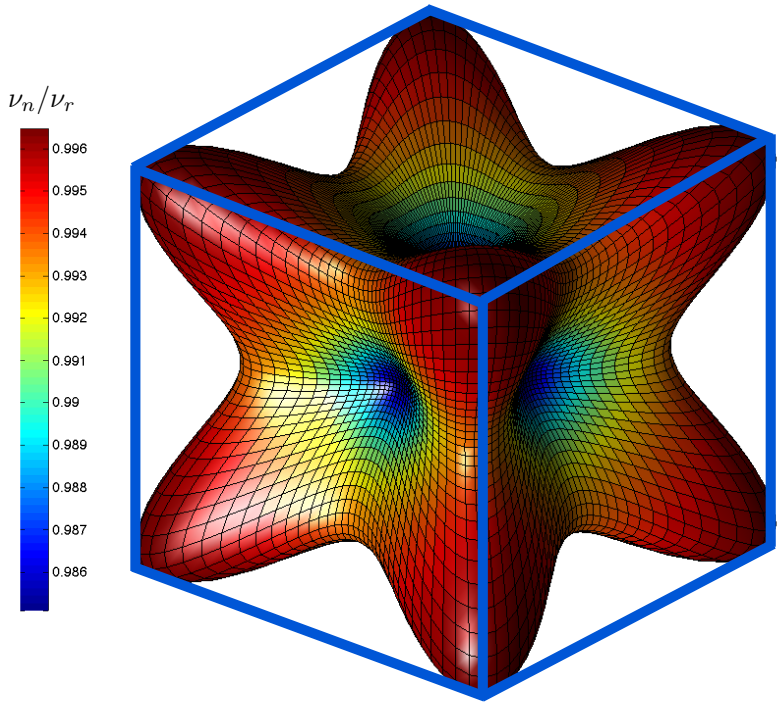

Figure 37: Numerical anisotropy of a uniform 3D FDTD (2,2). The ratio between the numerical (ν_n) and the real (ν_r) velocity is calculated for different angles. The time and the spatial step are related with $\frac{c\Delta t}{\Delta u} = 0.6/\sqrt{3}$ and $N = 10$. The box illustrates the Yee cell.

The 1D FDTD, when using the Courant limit to define the ratio between time and spatial steps, results to zero numerical errors (Taflove, 2005). This peculiar result shows that for 1D, the central difference scheme suggested by Yee (Yee, 1966) gives exact and not approximate solutions. Unfortunately, this is limited only to plane waves (1D) in homogenous media. Complicated structures and models which require more than one dimension are subjected to numerical errors, the order of which can be analytically estimated.

Following the approach suggested by Taflove (2005), we choose an arbitrary frequency and subsequently its corresponding numerical wavenumber is calculated from (5.45). Using this frequency and its numerical wavenumber, the numerical velocity is calculated. The latter is subsequently compared with the real velocity in an effort to get an insight on the artefacts arising from the numerical nature of FDTD. Equation (5.45) can be re-written in the more convenient form

$$\frac{1}{S^2}\sin^2\left(\frac{\pi S}{N}\right) = \sin^2\left(k\cdot\cos\left(\theta\right)\cos\left(\phi\right)\Delta u/2\right) \tag{5.49}$$

$$+\sin^2\left(k\cdot\sin\left(\theta\right)\cos\left(\phi\right)\Delta u/2\right) + \sin^2\left(k\cdot\sin\left(\phi\right)\Delta u/2\right).$$

Where $N = \frac{\lambda_0}{\Delta u}$ (i.e. how many steps are used to resolve the reference wavelength λ_0) and $S = c\Delta t/\Delta u$.

Equation (5.49) has closed form solutions only for $\theta = \phi = 0$ (Taflove, 2005). In order to calculate (5.49) for different angles of propagation it is convenient to state (5.49) as a minimisation problem, namely

$$\underset{k}{\operatorname{argmin}} \; || \frac{1}{S^2} \sin^2 \left(\frac{\pi S}{N} \right) - \sin^2 \left(k \cdot \cos(\theta) \cos(\phi) \, \Delta u/2 \right) \tag{5.50}$$

$$- \sin^2 \left(k \cdot \sin(\theta) \cos(\phi) \, \Delta u/2 \right) - \sin^2 \left(k \cdot \sin(\phi) \, \Delta u/2 \right) ||.$$

Equation (5.50) can be solved using non-convex optimisation techniques (Horst et al., 2000) which gives the ability for k to be complex and can overcome local minima. Complex k occurs when S is smaller than a transition value, this results to sub-luminal velocities and numerical attenuation (Schneider and Wagner, 1999, Taflove, 2005).

Fig. 36 illustrates the ratio $\frac{\nu_n}{\nu_r}$ with respect to N for $\theta = \phi = 0$. Where ν_n and ν_r are the numerical and the real velocity respectively. Due to the stability condition, $S = b/\sqrt{3}$ with $b \leq 1$. From Fig. 36 it is evident that the performance of FDTD is optimised when S is exactly on the Courant limit. In order to investigate the numerical anisotropy due to numerical errors, equation (5.50) is minimised for different angles, $S = 0.6/\sqrt{3}$ and for $N = 10$. Fig. 37 shows that the waves which are normal to the sides of the Yee cell are less accurate compared to the ones propagating towards the edges.

The main advantage of FDTD is that it can explicitly calculate spatial and time derivatives which are synchronised in both space and time. The latter is achieved by using central FD schemes. The original FDTD suggested by Yee (Yee, 1966) uses a second order central FD to evaluate both space and time derivatives. Similarly, higher order approximations can be applied, and as long as these approximations are central FD, the explicit nature as well as the synchronisation of FDTD will be preserved. The central FD scheme is defined as

$$\frac{\partial F(n)}{\partial u} \approx \frac{1}{\Delta u} \sum_{s=1}^{M} \left(c_{s,1} F \left(n + \frac{s}{2} \right) - c_{s,2} F \left(n - \frac{s}{2} \right) \right). \tag{5.51}$$

The coefficients c_s can be found using the method described in chapter (3.2.2).

Due to symmetry it can be proved that $c_{s1} = c_{s2}$ (Kantartzis and Tsiboukis, 2006). Thus, (5.51) can be simplified as

$$\frac{\partial F(n)}{\partial u} \approx \frac{1}{\Delta u} \sum_{s=1}^{M} c_s \left(F\left(n + \frac{s}{2}\right) - F\left(n - \frac{s}{2}\right) \right). \tag{5.52}$$

Using (5.52) and working with the same way as in (5.38) and (5.39) yields

$$\omega \approx \sum_{s=1}^{M} \frac{2c_s \sin\left(\omega \Delta t \left(\frac{2s-1}{2}\right)\right)}{\Delta t} \tag{5.53}$$

$$k_u \approx \sum_{s=1}^{M} \frac{2c_s \sin\left(k_u \Delta u \left(\frac{2s-1}{2}\right)\right)}{\Delta u}. \tag{5.54}$$

Substituting (5.53) and (5.54) to (5.37) results to

$$\left(\sum_{s=1}^{M} \frac{c_s \sin\left(\omega \Delta t \left(\frac{2s-1}{2}\right)\right)}{c\Delta t} \right)^2 = \sum_{u \in \{x,y,z\}} \left(\sum_{s=1}^{M} \frac{c_s \sin\left(k_u \Delta u \left(\frac{2s-1}{2}\right)\right)}{\Delta u} \right)^2. \tag{5.55}$$

Equation (5.55) is the dispersion relationship for any arbitrary order of accuracy. From (5.55) it is proven that the stability criteria is sensitive to the order of accuracy. For FDTD (2,4), the stability criteria is equal to $\frac{c\Delta t}{\Delta u} \leq \frac{\sqrt{36}}{7}$, for FDTD (4,4) the Courant limit is the same as FDTD (2,2) (Fang, 1989) and so on. Similarly, the numerical errors as well as the numerical anisotropy change when different FDTD schemes are employed. Higher order approximations increase the accuracy at the cost of increasing the computational resources.

In the next sections the implementation of dispersive media into FDTD as well as the truncation of the FDTD boundaries is discussed. Novel methods are proposed which are shown to improve upon previous approaches while retaining computational efficiency. The suggested techniques are second order accurate in time and can be easily applied to any spatial order of accuracy.

5.4 DISPERSIVE MATERIALS IMPLEMENTATION

FDTD is a very popular numerical technique for solving Maxwell's equations for a wide range of different media, including materials with frequency dependent properties. In a number of applications, single and multi-pole Lorentz, Debye and Drude functions are widely used because they allow us to simulate the electric susceptibility of a range of materials amongst them: water (Pieraccini et al., 2009), human tissues (Clegg and Robinson, 2010, Gabriel, 1996, Ireland and Abbosh, 2013, Lazebnik et al., 2007) cold plasma (Li et al., 2013, Liu et al.,

2010), gold (Vial et al., 2005), soils (Atteia and Hussein, 2010, Bergmann et al., 1998, Giannakis et al., 2012, Matzier, 1998, Teixeira et al., 1998, Uduwawala et al., 2005, Wang and Oristaglio, 2000) and so on.

Electric susceptibility $\chi(t)$ is defined as the function relating the polarisation density to the electric field by $\vec{P} = \chi(t) * \vec{E}$. In essence, both the real and the imaginary part of a complex electric permittivity variation are included in the electric susceptibility function. In this section, for simplicity we define, in the same way as used by Kelley and Luebbers (1996) and Luebbers et al. (1990)), the electric susceptibility $\chi(t)$ using the definition of electric flux density as $\vec{D} = \epsilon_0\epsilon_\infty\vec{E} + \epsilon_0\chi(t) * \vec{E}$. In such definition, the effects of any frequency-independent parts of the medium's relative permittivity are included within ϵ_∞ (relative permittivity at infinite frequency).

A number of different methodologies have been suggested for numerically implementing dispersive materials into the FDTD. The resulting methods can be roughly divided in three categories: 1) Auxiliary Differential Equation (ADE) methods (Alsunaidi and Al-Jabr, 2009, Han et al., 2006, Joseph et al., 1991, Kashiwa and Fukai, 1990, Okoniewski et al., 1997, Takayama and Klaus, 2002), 2) Z-transform methods (Sullivan, 1992, 1994, Weedon and Rappaport, 1997) and 3) the recursive convolution methods (Chen et al., 1998, Fan and Liu, 2000, Kelley and Luebbers, 1996, Lin and Thylen, 2009, Liu et al., 2003, Luebbers et al., 1990, 1991, Luebbers and Hunsberger, 1992, Shibayama et al., 2009, Siushansian and Vetri, 1997). A systematic review of the methods related to ADE and recursive convolution are given by Taflove and Hagness (2000) and Young and Nelson (2001). In addition, an interesting review about the modelling techniques used to simulate Lorentz media is given by Lin and Thylen (2009).

Inclusive algorithms, with a uniform implementation for a wide range of materials, are very attractive especially in situations where materials with different dispersion mechanisms need to be modelled. An inclusive ADE algorithm for modelling Lorentz, Debye and Drude media is presented by Alsunaidi and Al-Jabr (2009). The algorithm needs two additional variables to be stored per pole for both Drude, Lorentz, Debye and conductive term mechanisms. A more efficient ADE inclusive algorithm which is based on a complex-conjugate pole-residue method is presented by Han et al. (2006). This uses an inclusive electric susceptibility function which holds as special cases the Debye, Lorentz and Drude medium.

PLRC introduced by Kelley and Luebbers (1996) is an efficient method for dealing with dispersive materials. PLRC assumes that the electric field has a piecewise linear behaviour and also uses a central FD scheme in order to calculate the derivative of the polarisation density in time. In other words, it

implicitly assumes that the polarisation density can be accurately simulated by a second order polynomial in each time interval. PLRC is a widely used method, and one of the key reasons for its popularity, is that it is an accurate algorithm which can simulate materials with an inclusive susceptibility function which holds as special cases the Lorentz, Debye and Drude media. This makes the implementation of dispersive materials in FDTD codes easy and practical and at the same time retains its computational efficiency (Fan and Liu, 2000, Han et al., 2006). Standard PLRC methodologies require two additional variables for each Lorentz medium and one additional variable for each Drude or Debye medium. Complex media like the ones described by the Havriliak-Negami equation can be approximated by multi-Debye functions (Clegg and Robinson, 2010, Giannakis et al., 2012) and can be implemented very effectively using PLRC (Kelley et al., 2007). Also, inclusive algorithms like PLRC and complex-conjugate pole-residuals method (Han et al., 2006) that can simulate susceptibility functions which hold as special cases the Debye, Lorentz and Drude relaxations are more computationally efficient for modelling complex materials like Ag (Han et al., 2006) and graphene (Lin et al., 2012).

Next, two new novel recursive convolution based methodologies are presented which in their development make only the assumption that the first time derivative of the electric field is constant in each time interval – in other words that the electric field is piecewise linear between time steps – and do not make any assumptions about the variation in time of the polarisation density. Instead, an analytical calculation of the polarisation density is used subject to the assumption that the electric field has a piecewise linear behaviour in each time interval. As a result of reducing the number of the assumptions made in the derivation of the recursive algorithm, the proposed methods are found to be systematically improved compared with PLRC for Debye, Lorentz and Drude media and at the same time they preserve the main advantages of recursive convolution techniques.

5.4.1 *Polarisation Density Method*

Maxwell's equations for an isotropic, linear, non-magnetic, dispersive medium are given by

$$\nabla \times \vec{H} = \epsilon_0 \epsilon_\infty \frac{\partial \vec{E}}{\partial t} + \sigma \vec{E} + \epsilon_0 \sum_{s=1}^{N} \frac{\partial \vec{P}_s}{\partial t} \tag{5.56}$$

$$\nabla \times \vec{E} = -\mu_0 \frac{\partial \vec{H}}{\partial t} \tag{5.57}$$

$$\vec{P}_s = \chi_s(t) * \vec{E}(t). \tag{5.58}$$

Where $\vec{P}_s$ is the polarisation density for each dispersive pole and N is the total number of dispersive poles. The susceptibility function $\chi_s(t)$ used here is an inclusive function which holds as special cases the Debye, Drude and Lorentz relaxations (Fan and Liu, 2000)

$$\chi_s(t) = Re\{W_s e^{Q_s \cdot t}\}. \tag{5.59}$$

We then define $\vec{R}_s$ to be a complex function having as its real part the polarisation density $\vec{P}_s$

$$\vec{R}_s = W_s e^{Q_s \cdot t} * \vec{E}(t). \tag{5.60}$$

Where W_s and Q_s can, in general, be both real and complex numbers; if they are both real, then $\vec{R}_s = \vec{P}_s$. For Debye and Drude media both W_s and Q_s are real, while for a Lorentz medium W_s is purely imaginary and Q_s is generally a complex number with both non-zero real and imaginary parts. In the proposed algorithms W_s can also be complex with both non-zero real and imaginary parts and Q_s could be a purely imaginary or real number (similarly to the complex-conjugate pole-residue method (Han et al., 2006)).

Equation (5.60) can be written as

$$\vec{R}_s = W_s \int_0^t e^{Q_s \cdot (t-\tau)} \vec{E}(\tau) d\tau = W_s e^{Q_s \cdot t} \int_0^t e^{-Q_s \cdot \tau} \vec{E}(\tau) d\tau \tag{5.61}$$

which in discritized form is given by

$$\vec{R}_s^{(n+1)\Delta t} = W_s \; e^{Q_s (n+1)\Delta t} \int_0^{n\Delta t} e^{-Q_s \cdot \tau} \vec{E}(\tau) d\tau +$$

$$+ W_s e^{Q_s (n+1)\Delta t} \int_{n\Delta t}^{(n+1)\Delta t} e^{-Q_s \cdot \tau} \vec{E}(\tau) d\tau. \tag{5.62}$$

Because $\vec{R}_s^{n\Delta t} = W_s e^{Q_s \cdot n\Delta t} \int_0^{n\Delta t} e^{-Q_s \tau} \vec{E}(\tau) d\tau$ it can be easily shown that (5.62) can be rewritten as

$$\vec{R}_s^{(n+1)\Delta t} = e^{Q_s \cdot \Delta t} \vec{R}_s^{n\Delta t} + W_s e^{Q_s \cdot (n+1)\Delta t} \int_{n\Delta t}^{(n+1)\Delta t} e^{-Q_s \cdot \tau} \vec{E}(\tau) d\tau. \tag{5.63}$$

To solve the integral in (5.63), subject to the constrain that the electric field has a piecewise linear behaviour in each time interval, the integration by parts rule is applied instead of using the approach suggested by Kelley and Luebbers (1996). In order to apply the integration by parts rule the integral in (5.63) is re-written as

$$\int_{n\Delta t}^{(n+1)\Delta t} e^{-Q_s \cdot \tau} \vec{E}(\tau) d\tau = -\frac{1}{Q_s} \int_{n\Delta t}^{(n+1)\Delta t} \frac{\partial \left(e^{-Q_s \cdot \tau} \right)}{\partial \tau} \vec{E}(\tau) d\tau. \tag{5.64}$$

Applying the integration by parts rule in the integral of the right hand side of (5.64) and assuming that the first derivative of the electric field is constant over each time interval $n\Delta t - (n+1)\Delta t$ results in

$$\int_{n\Delta t}^{(n+1)\Delta t} \frac{\partial \left(e^{-Q_s \cdot \tau} \right)}{\partial \tau} \vec{E}(\tau) d\tau = e^{-Q_s \cdot \tau} \vec{E}(\tau) \,|_{n\Delta t}^{(n+1)\Delta t} - \frac{\partial \vec{E}(\tau)}{\partial \tau} \int_{n\Delta t}^{(n+1)\Delta t} e^{-Q_s \cdot \tau} d\tau. \tag{5.65}$$

The assumption of the linearity of the electric field, which is directly implied by the assumption that its first derivative with respect to time is constant, is consistent with the development of an algorithm that is suited for a general second order accuracy in time FDTD scheme. The second order of accuracy of the assumption of linearity is proven in Appendix B.

Substituting (5.65) into (5.64) and subsequently using the result into (5.63) and employing a central FD to calculate the time derivative of the electric field in (5.65) results in

$$\vec{R}_s^{(n+1)\Delta t} = e^{Q_s \Delta t} \vec{R}_s^{n\Delta t} + A_s \vec{E}^{(n+1)\Delta t} + B_s \vec{E}^{n\Delta t} \tag{5.66}$$

$$A_s = -\frac{W_s}{Q_s} - \frac{W_s}{Q_s^2 \Delta t} \left(1 - e^{Q_s \Delta t} \right) \tag{5.67}$$

$$B_s = e^{Q_s \Delta t} \frac{W_s}{Q_s} + \frac{W_s}{Q_s^2 \Delta t} \left(1 - e^{Q_s \Delta t} \right). \tag{5.68}$$

If we assume that the derivative $\frac{d\vec{R}_s}{dt}^{(n+1/2)\Delta t}$ of the polarisation density can be accurately obtained using a central FD scheme

$$\frac{\partial \vec{R}_s}{\partial t}^{(n+1/2)\Delta t} = \frac{\vec{R}_s^{(n+1)\Delta t} - \vec{R}_s^{n\Delta t}}{\Delta t} = \frac{\vec{R}_s^{n\Delta t}}{\Delta t}\left(e^{Q_s \Delta t} - 1\right) + \frac{A_s}{\Delta t}\vec{E}^{(n+1)\Delta t} + \frac{B_s}{\Delta t}\vec{E}^{n\Delta t} \tag{5.69}$$

and by further substituting the real part of (5.69) into (5.56) and using a central FD scheme for the calculation of $\frac{d\vec{E}}{dt}^{(n+1/2)\Delta t}$ and a semi-implicit technique for the calculation of $\vec{E}^{(n+1/2)\Delta t}$ we arrive at

$$\vec{E}^{(n+1)\Delta t} = \frac{CB}{CA}\vec{E}^{n\Delta t} - \frac{1}{CA}\vec{\Phi}^{n\Delta t} + \frac{1}{CA}\nabla \times \vec{H}^{(n+1/2)\Delta t} \tag{5.70}$$

$$\vec{\Phi}^{n\Delta t} = \frac{\epsilon_0}{\Delta t}\sum_{s=1}^{N} Re\{\vec{R}_s^{n\Delta t}\left(e^{Q_s \Delta t} - 1\right)\} \tag{5.71}$$

$$CA = \frac{\epsilon_0 \epsilon_\infty}{\Delta t} + \frac{\epsilon_0}{\Delta t}\sum_{s=1}^{N} Re\{A_s\} + \frac{\sigma}{2} \tag{5.72}$$

$$CB = \frac{\epsilon_0 \epsilon_\infty}{\Delta t} - \frac{\epsilon_0}{\Delta t}\sum_{s=1}^{N} Re\{B_s\} - \frac{\sigma}{2}. \tag{5.73}$$

Equations (5.71), (5.72), (5.73) can be shown to be the same as the coefficients of the update equation of the electric field (5.70) using PLRC (Kelley and Luebbers, 1996) (with a semi-implicit scheme to calculate $\sigma\vec{E}^{(n+1/2)\Delta t}$ in (5.56)). From (5.69) it is evident that a central difference scheme is used in order to calculate the time derivative of the polarisation density. In (5.70) and (5.71) $\vec{\Phi}^{n\Delta t}$ is used as a temporary holding value for the summation containing the $\vec{R_s}^{n\Delta t}$ terms and therefore there is no need for extra memory storage.

In order to improve upon the standard PLRC algorithm instead of using a central FD scheme as in (5.69), the time derivative of the polarisation density at the required time instance is calculated analytically. To achieve this (5.63) is re-written for $t = (n + \alpha)\Delta t$ ($\alpha \in [0\ \ 1]$) as

$$\vec{R}_s^{(n+\alpha)\Delta t} = e^{Q_s \cdot \alpha \Delta t}\vec{R}_s^{n\Delta t} + W_s \cdot e^{Q_s \cdot (n+\alpha)\Delta t} \int_{n\Delta t}^{(n+\alpha)\Delta t} e^{-Q_s \cdot \tau}\vec{E}(\tau)d\tau. \tag{5.74}$$

The integral in (5.74) can be calculated using the integration by parts rule similarly to (5.63). In order to do this (5.74) is cast as

$$\vec{R}_s^{(n+\alpha)\Delta t} = e^{Q_s \alpha \Delta t} \vec{R}_s^{n\Delta t} - \frac{W_s}{Q_s} e^{Q_s (n+\alpha)\Delta t} \int_{n\Delta t}^{(n+\alpha)\Delta t} \frac{\partial (e^{-Q_s \tau})}{\partial \tau} \vec{E}(\tau) d\tau. \quad (5.75)$$

Therefore, the integral in (5.75) can be obtained by

$$\int_{n\Delta t}^{(n+\alpha)\Delta t} \frac{\partial (e^{-Q_s \tau})}{\partial \tau} \vec{E}(\tau) d\tau = e^{-Q_s \tau} \vec{E}(\tau) \mid_{n\Delta t}^{(n+\alpha)\Delta t} - \frac{\partial \vec{E}(\tau)}{\partial \tau} \int_{n\Delta t}^{(n+\alpha)\Delta t} e^{-Q_s \tau} d\tau. \quad (5.76)$$

Because of the assumption of the linearity of the electric field in each time interval the term $e^{-Q_s \tau} \vec{E}(\tau) \mid_{n\Delta t}^{(n+\alpha)\Delta t}$ in (5.76) is equal to

$$\begin{aligned} & e^{-Q_s \tau} \vec{E}(\tau) \mid_{n\Delta t}^{(n+\alpha)\Delta t} = \\ & \quad e^{-Q_s (n+\alpha)\Delta t} \left(\vec{E}^{n\Delta t} + \frac{\vec{E}^{(n+1)\Delta t} - \vec{E}^{n\Delta t}}{\Delta t} \alpha \Delta t \right) \\ & \quad - e^{-Q_s n \Delta t} \vec{E}^{n\Delta t}. \end{aligned} \quad (5.77)$$

From (5.75), (5.76) and (5.77) it can be easily shown that $\vec{R}_s^{(n+\alpha)\Delta t}$ equals

$$\vec{R}_s^{(n+\alpha)\Delta t} = e^{Q_s \alpha \Delta t} \vec{R}_s^{n\Delta t} + NA_s \vec{E}^{(n+1)\Delta t} + NB_s \vec{E}^{n\Delta t} \quad (5.78)$$

where

$$NA_s = -\frac{W_s}{Q_s} \alpha - \frac{W_s}{Q_s^2 \Delta t} \left(1 - e^{Q_s \alpha \Delta t} \right) \quad (5.79)$$

$$NB_s = -\frac{W_s}{Q_s} (1 - \alpha) + \frac{W_s}{Q_s} e^{Q_s \alpha \Delta t} + \frac{W_s}{Q_s^2 \Delta t} \left(1 - e^{Q_s \alpha \Delta t} \right). \quad (5.80)$$

For $\alpha = 1$, $NA_s = A_s$ and $NB_s = B_s$. The derivative of the polarisation density at $(n + \alpha)\Delta t$ between two time intervals ($n =$ constant and $\alpha \in [0 \;\; 1]$) can be written as

$$\frac{\partial \vec{R}_s^{(n+\alpha)\Delta t}}{\partial t} = \frac{\partial \vec{R}_s^{(n+\alpha)\Delta t}}{\partial (n + \alpha) \Delta t} = \frac{1}{\Delta t} \frac{\partial \vec{R}_s^{(n+\alpha)\Delta t}}{\partial \alpha}. \quad (5.81)$$

From equations (5.78), (5.79), (5.80), and (5.81) it can be shown that the

analytic expression of the derivative $\frac{\partial \vec{R}_s^{(n+1/2)\Delta t}}{\partial t}$, subject to the constrain that the electric field is piecewise linear in each time interval, equals to

$$\frac{\partial \vec{R}_s^{(n+1/2)\Delta t}}{\partial t} = Q_s e^{Q_s \frac{\Delta t}{2}} \vec{R}_s^{n\Delta t} + \\ + \frac{1}{\Delta t}\left(\frac{\partial NA_s}{\partial \alpha}\vec{E}^{(n+1)\Delta t} + \frac{\partial NB_s}{\partial \alpha}\vec{E}^{n\Delta t}\right). \tag{5.82}$$

The derivatives with respect to α in (5.82) can be calculated analytically using (5.79) and (5.80). Substituting the real part of (5.82) into (5.56) and using the same discretisation as in (5.70) yields the same equation (5.70) but with different coefficients

$$\vec{\Phi}^{n\Delta t} = \epsilon_0 \sum_{s=1}^{N} Re\{Q_s e^{Qs\frac{\Delta t}{2}} \vec{R}_s^{n\Delta t}\} \tag{5.83}$$

$$CA = \frac{\epsilon_0 \epsilon_\infty}{\Delta t} + \frac{\epsilon_0}{\Delta t}\sum_{s=1}^{N} Re\{L_s\} + \frac{\sigma}{2} \tag{5.84}$$

$$CB = \frac{\epsilon_0 \epsilon_\infty}{\Delta t} - \frac{\epsilon_0}{\Delta t}\sum_{s=1}^{N} Re\{K_s\} - \frac{\sigma}{2} \tag{5.85}$$

where

$$L_s = \frac{W_s}{Q_s}\left(e^{Q_s\frac{\Delta t}{2}} - 1\right) \tag{5.86}$$

$$K_s = \frac{W_s}{Q_s}\left(1 - e^{Q_s\frac{\Delta t}{2}}\right) + \Delta t \cdot W_s e^{Q_s\frac{\Delta t}{2}}. \tag{5.87}$$

The algorithm stores in a temporary memory variable the value of $\vec{E}^{n\Delta t}$ and then calculates $\vec{E}^{(n+1)\Delta t}$ from (5.70) using the coefficients given in (5.83), (5.84), (5.85), $\vec{E}^{n\Delta t}$ and $\nabla \times \vec{H}^{(n+1/2)\Delta t}$. Subsequently $\vec{R}_s^{(n+1)\Delta t}$ is calculated from (5.78) using $\vec{R}_s^{n\Delta t}$, $\alpha = 1$, the coefficients given in (5.79), (5.80), $\vec{E}^{(n+1)\Delta t}$ and the temporary memory variable which stores $\vec{E}^{n\Delta t}$. $\vec{R}_s^{(n+1)\Delta t}$ is used to calculate $\vec{\Phi}^{(n+1)\Delta t}$ from (5.83) which is used for the calculation of $\vec{E}^{(n+2)\Delta t}$. When W_s and Q_s are real numbers only one additional memory variable is needed to be stored, if W_s or Q_s are complex numbers one complex variable is required (*i.e.* both real and imaginary parts need to be stored). In addition, an equivalent ADE derivation of this method based on Laplace transformation is presented in Appendix C.

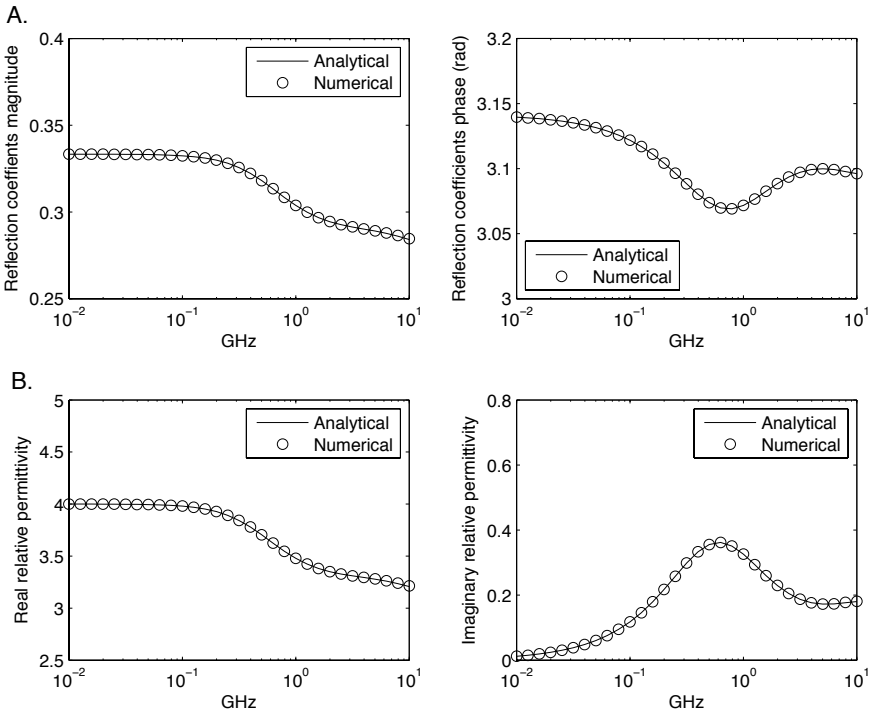

Figure 38: Multi-Debye medium. A) Comparison between the numerical (polarisation density method) and analytical reflection coefficients. B) Comparison between the numerical (polarisation density method) and the analytical relative permittivity.

5.4.2 *Current density method*

In this alternative method the dispersive properties are expressed by using apparent current density sources. Therefore (5.56) is written as

$$\nabla \times \vec{H} = \epsilon_0 \epsilon_\infty \frac{\partial \vec{E}}{\partial t} + \sigma \vec{E} + \epsilon_0 \sum_{s=1}^{N} \vec{J}_s \tag{5.88}$$

where,

$$\vec{J}_s = \chi_s(t) * \frac{\partial \vec{E}}{\partial t}. \tag{5.89}$$

We define $\vec{T}_s$ as a complex function with its real part being the current density $\vec{J}_s = Re\{\vec{T}_s\}$.

$$\vec{T}_s = W_s e^{Q_s t} * \frac{\partial \vec{E}}{\partial t}. \tag{5.90}$$

The identity $\frac{\partial}{\partial t}\left(\chi_s(t) * \vec{E}\right) = \chi_s(t) * \frac{\partial \vec{E}}{\partial t}$ (Poularikas, 1996) illustrates the

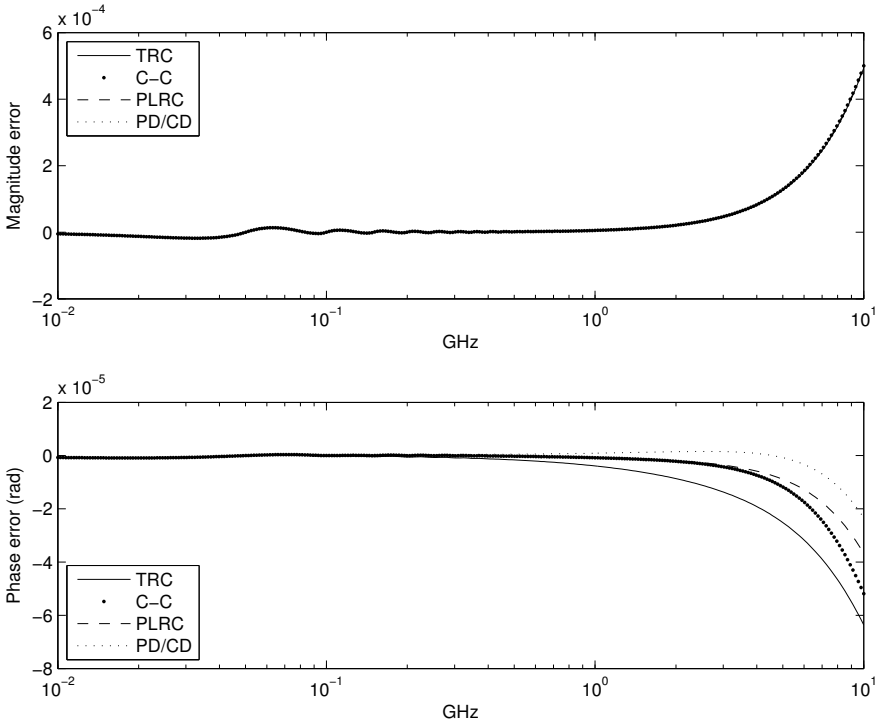

Figure 39: Multi-Debye medium: Error between analytical and numerical reflection coefficients for TRC, PLRC, Complex-Conjugate (C-C) method, Current Density (CD) method and Polarisation Density (PD) method.

difference between the polarisation density and the current density method. In the case of the polarisation density method the convolution between the electric susceptibility function and the electric field is recursively calculated and subsequently the derivative – left hand side of the identity – is analytically obtained. In the case of current density method, the convolution between the electric susceptibility and the first time derivative of the electric field – right hand side of the identity – is calculated. Both methods assume that the electric field is linear between time steps.

In the same way that (5.75) was derived, assuming that the derivative of the electric field is constant in each time interval it can be shown that

$$\vec{T}_s^{(n+\alpha)\Delta t} = e^{Q_s \alpha \Delta t} \vec{T}_s^{n\Delta t} + W_s e^{Q_s (n+\alpha)\Delta t} \frac{\partial \vec{E}^{(n+1/2)\Delta t}}{\partial t} \int_{n\Delta t}^{(n+\alpha)\Delta t} e^{-Q_s \tau} d\tau. \quad (5.91)$$

Using a central difference scheme to calculate the derivative of the electric field in time, (5.91) becomes

$$\vec{T}_s^{(n+\alpha)\Delta t} = e^{Q_s \alpha \Delta t} \vec{T}_s^{n\Delta t} - \frac{W_s}{Q_s} \frac{\vec{E}^{(n+1)\Delta t} - \vec{E}^{n\Delta t}}{\Delta t} \left(1 - e^{Q_s \alpha \Delta t}\right). \quad (5.92)$$

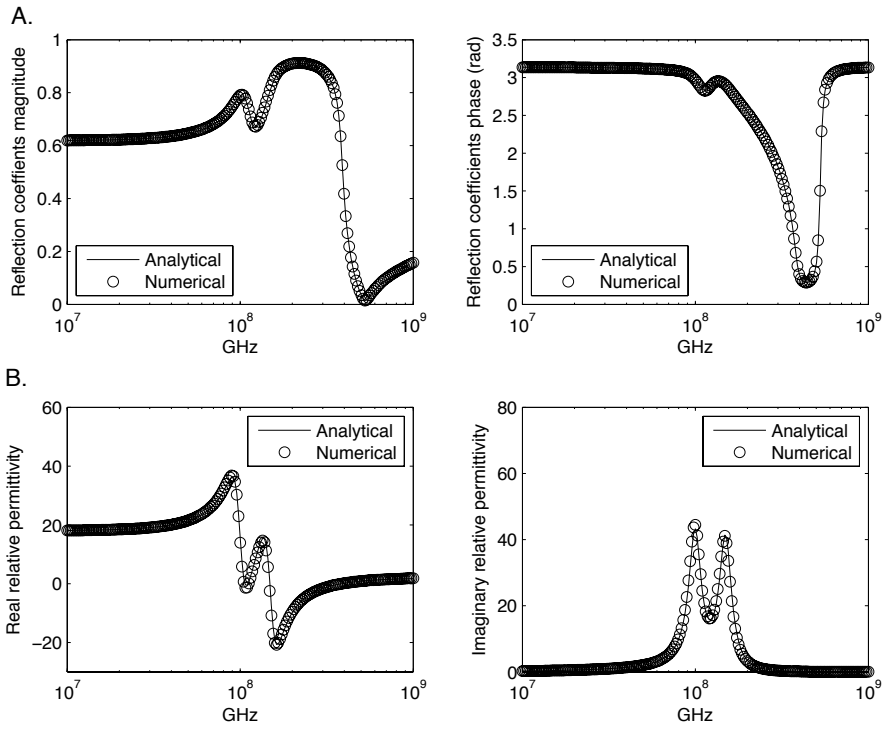

Figure 40: Multi-Lorentz medium. A) Comparison between numerical (current density method) and analytical reflection coefficients. B) Comparison between numerical (current density method) and analytical relative permittivity.

Substituting (5.92) to (5.89) and subsequently into (5.88) for $\alpha = \frac{1}{2}$ and discretizing as was done in (5.70) yields (5.70) with

$$\vec{\Phi}^{n\Delta t} = \epsilon_0 \sum_{s=1}^{N} Re\{e^{Qs\frac{\Delta t}{2}} \vec{T}_s^{n\Delta t}\} \tag{5.93}$$

$$CA = \frac{\epsilon_0 \epsilon_\infty}{\Delta t} - \frac{\epsilon_0}{\Delta t} \sum_{s=1}^{N} Re\{Z_s\} + \frac{\sigma}{2} \tag{5.94}$$

$$CB = \frac{\epsilon_0 \epsilon_\infty}{\Delta t} - \frac{\epsilon_0}{\Delta t} \sum_{s=1}^{N} Re\{Z_s\} - \frac{\sigma}{2} \tag{5.95}$$

where,

$$Z_s = \frac{W_s}{Q_s} \left(1 - e^{Q_s \frac{\Delta t}{2}}\right). \tag{5.96}$$

The algorithm works in the same way as the polarisation density method described previously. To find $\vec{T}^{(n+1)\Delta t}$ for the next iteration we calculate (5.92) for $\alpha = 1$. It is evident that no semi-implicit approximations are used to calculate $\vec{T}^{(n+1/2)\Delta t}$, the current density term is calculated analytically subject

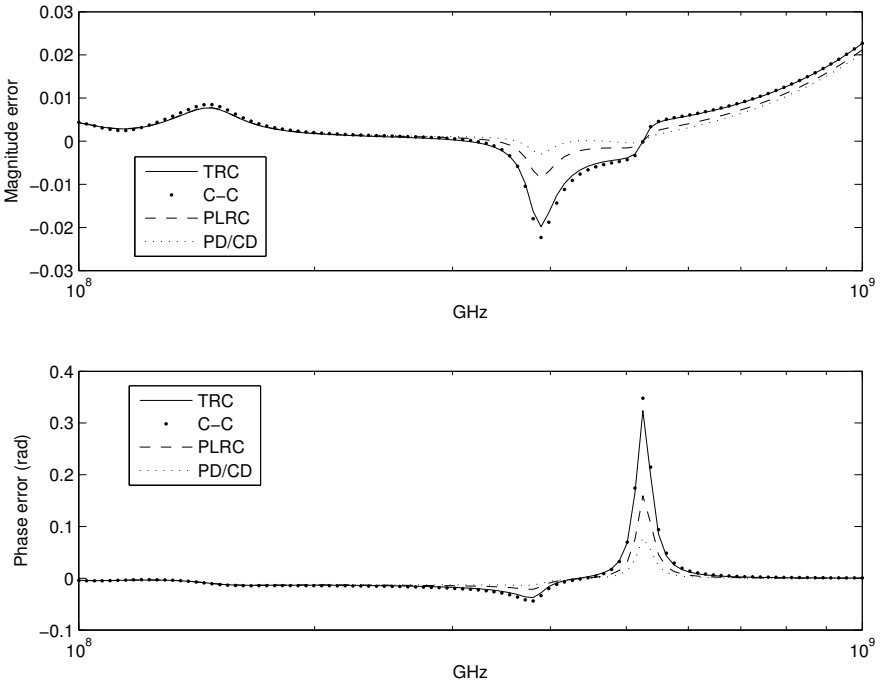

Figure 41: Multi-Lorentz medium: Error between analytical and numerical reflection coefficients for TRC, PLRC, Complex-Conjugate (C-C) method, Current Density (CD) and Polarisation Density (PD).

to the constrain that the electric field has a piece-wise linear behaviour. From (5.92), (5.93), (5.94), and (5.95) it is evident that one less pre-calculated variable is needed to be stored compared with PLRC and the polarisation density method. An alternative ADE interpretation of this algorithm based on a power series method is given in Appendix D.

5.4.3 *Numerical Examples*

Debye Relaxation

For a Debye medium the susceptibility function is equal to (Luebbers et al., 1990)

$$\chi_s(t) = \frac{\Delta\epsilon_s}{t_{0,s}} e^{-t/t_{0,s}} \tag{5.97}$$

where $\Delta\epsilon_s = \epsilon_s - \epsilon_\infty$, ϵ_s and ϵ_∞ are the relative permittivity for zero and

infinite frequency respectively and $t_{0,s}$ is the relaxation time. From (5.59) and (5.97) it is evident that

$$W_s = \frac{\Delta\epsilon_s}{t_{0,s}} \tag{5.98}$$

$$Q_s = -\frac{1}{t_{0,s}}. \tag{5.99}$$

In order to test the two proposed algorithms, we compare numerically obtained reflection coefficients to analytical ones from a simple 1D problem of a plane wave normally incident from vacuum onto a two-pole Debye medium. For the numerical calculations, an 1D FDTD algorithm was used with $\Delta x = 0.3$ mm and $\Delta t = 1$ ps. The multi-Debye medium characteristics were $\epsilon_\infty = 3$, $\Delta\epsilon_1 = 0.7$, $\Delta\epsilon_2 = 0.3$, $t_{0,1} = 271$ ps, $t_{0,2} = 10.8$ ps and $\sigma = 0$. Figure 38 presents the comparison between the analytical and the numerical reflection coefficients and relative permittivity for the polarisation density method. The analytical and the numerical results are in excellent agreement showing the accuracy of the proposed algorithm. Results obtained by the current density method are almost identical to the ones obtained from the polarisation density method although the two formulations are not. The polarisation density method is slightly better by an almost negligible amount.

The two proposed algorithms in this paper are compared with the PLRC (Kelley and Luebbers, 1996), the complex-conjugate pole-residue method (Han et al., 2006) and the TRC (Siushansian and Vetri, 1997) method. These are all algorithms that can implement an inclusive susceptibility function which holds as special cases the Debye, Lorentz and Drude media relaxations which make them very attractive for modelling complex materials like graphene (Lin et al., 2012). An 1D FDTD model, as used previously, is employed to test all the other methods mentioned above and the errors between the analytical and the numerical reflection coefficients are shown in Figure 39. The overall errors for all the methods have the same order of magnitude because all of them are computationally efficient algorithms with approximately second order accuracy. Regarding the amplitude error the differences between the methods proposed in this paper are negligible, for the phase error as shown in Figure 39 the new methods proposed here performed better when compared to the PLRC, TRC and complex-conjugate method.

5.4.4 *Lorentz Relaxation*

For a Lorentz medium the susceptibility function is equal to (Luebbers and Hunsberger, 1992)

$$\chi_s(t) = Re\{-j\gamma_s e^{(-\alpha_s + j\beta_s)t}\} \tag{5.100}$$

$$\alpha_s = \delta_s \tag{5.101}$$

$$\beta_s = \sqrt{\omega_{p,s}^2 - \delta_s^2} \tag{5.102}$$

$$\gamma_s = \frac{\omega_{p,s}^2 \Delta\epsilon_s}{\beta_s} \tag{5.103}$$

where $\omega_{p,s}$ is the resonant frequency, $\delta_{p,s}$ is the damping factor and $j = \sqrt{-1}$. From (5.59) and (5.100) yields

$$W_s = -j\gamma_s = -j\frac{\omega_{p,s}^2 \Delta\epsilon_s}{\beta_s} \tag{5.104}$$

$$Q_s = -\alpha_s + j\beta_s = -\delta_s + j\sqrt{\omega_{p,s}^2 - \delta_s^2}. \tag{5.105}$$

To assess the accuracy of the formulations, numerically obtained reflection coefficients from a plane wave incident from vacuum onto a two-pole Lorentz medium are compared to the analytical ones. The 1D FDTD parameters are $\Delta x = 30$ *p*m and $\Delta t = 0.1$ as. The properties of the Lorentz medium are set to $\epsilon_\infty = 2$, $\Delta\epsilon_1 = 8$, $\omega_{p.1} = 200\pi$ PHz, $\delta_{p,1} = 0.1 \cdot \omega_{p,1}$, $\Delta\epsilon_2 = 8$, $\omega_{p,2} = 300\pi$ PHz and $\delta_{p,2} = 0.1 \cdot \omega_{p,2}$. Figure 40 shows the comparison between the analytical and the numerical reflection coefficients and relative permittivity obtained using the current density method. The same example is repeated using the polarisation density, TRC, PLRC and the complex-conjugate method. The errors are shown in Figure 41. Both the amplitude and the phase related errors are reduced for the new algorithms with the polarisation density to be slightly better when compared to the current density method.

Comparisons between reflection coefficients of plane waves incident normally from vacuum onto a dispersive media have been widely used in the literature to evaluate the accuracy of different algorithms. This raises the question of how comprehensive 1D examples are. Therefore, in this section, numerical and analytical results are compared from a 2D TM_z Lorentzian waveguide. The characteristics of the Lorentz medium inside the waveguide are $\epsilon_\infty = 2$, $\Delta\epsilon_1 = 8$, $\omega_{p,1} = 200\pi$ ps and $\delta_{p,1} = 0.1 \cdot \omega_{p,1}$. The FDTD characteristics of the

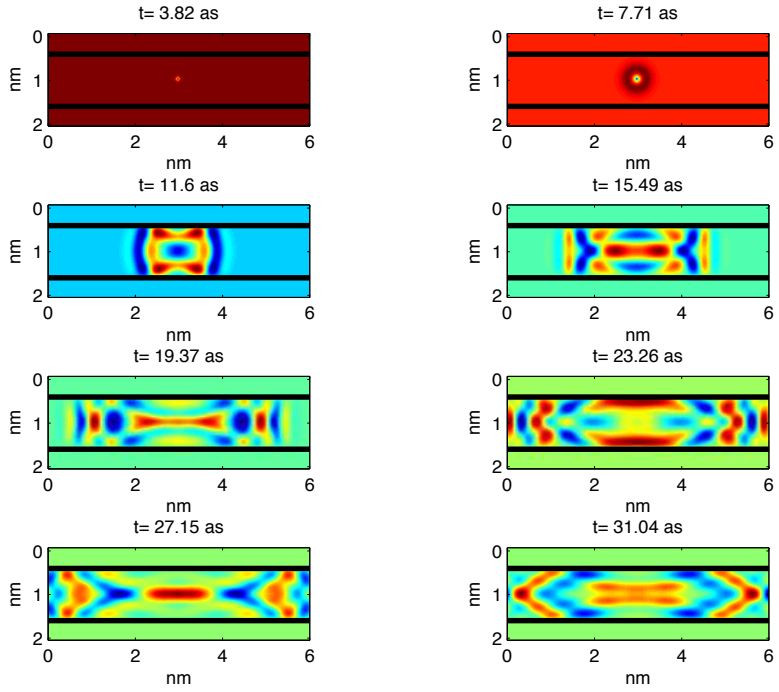

Figure 42: Pulse propagating into a Lorentzian waveguide. The contours illustrate the electric field (E_z).

model are $dx = 30$ pm and $dt = 70.711$ zs (Courant limit). The waveguide's width is $40 \cdot \Delta x$. An electric line source is placed in the center of the waveguide and the excitation pulse is a Gaussian-modulated sinusoidal function with central frequency 100 PHz and fractional bandwidth equals to 5. The received field is sampled at a location $5 \cdot \Delta x$ away from the source's position along x axis. Figure 42 shows the geometry of the Lorentzian waveguide model and presents a number of snapshots that illustrate how the pulse is propagating inside it.

Figure 43 compares the numerical – using the current density method – and the analytical $\vec{E}_z$ calculated at the receiver position. In order to further compare the errors between the methods presented here and other approaches the same test was repeated using polarisation density, PLRC, TRC and the complex-conjugate method. By summing the absolute values of the differences between the analytical and numerical results and subsequently normalising these errors to the maximum error (in this case to the error from complex-conjugate method), a comparison could be made of the relative performance of each approach. Figure 44 presents these normalised errors obtained from all the methods above. The techniques proposed in this section show reduced overall errors when compared with PLRC, TRC and the complex-conjugate methods.

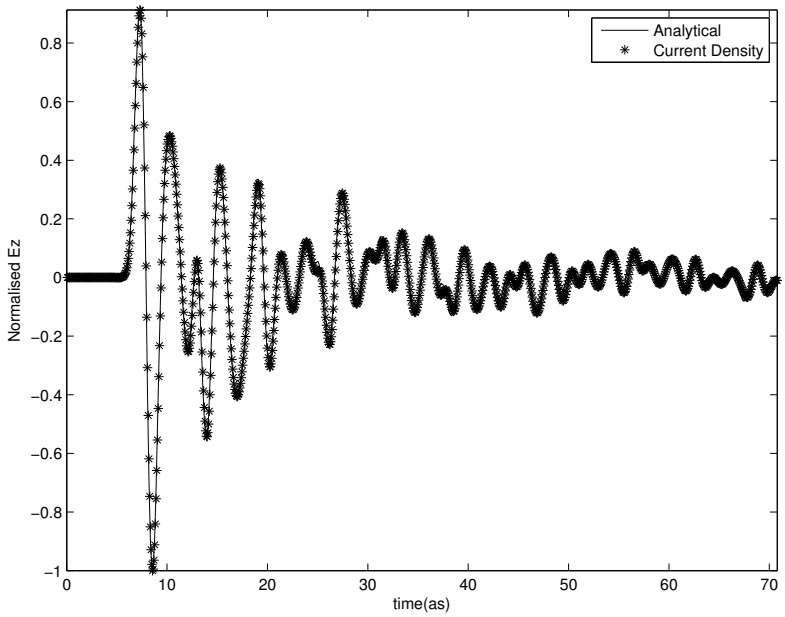

Figure 43: Comparison between numerical and analytical results using the current density method.

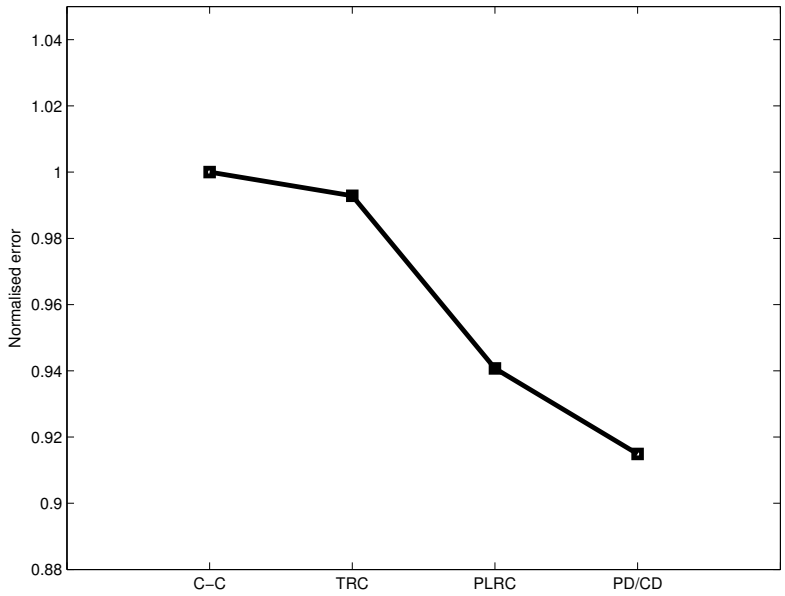

Figure 44: Normalised summation of the absolute error between numerical and analytical results using PLRC, TRC, Complex-Conjugate (C-C), Current Density (CD) and Polarisation Density (PD).

Again, it has been found that the polarisation density method is marginally better when compared with the current density method.

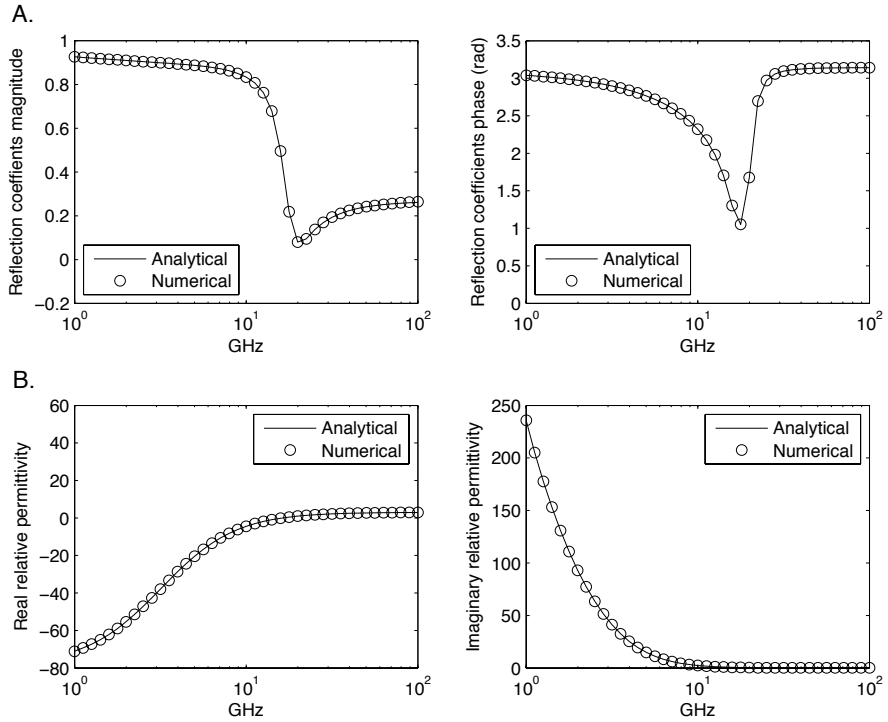

Figure 45: Drude medium. A) Comparison between the numerical (polarisation density method)l and analytical reflection coefficients. B) Comparison between the numerical (polarisation density method)l and analytical relative permittivity.

5.4.5 *Drude Relaxation*

For Drude medium the susceptibility function is equal to (Luebbers and Kunz, 1993)

$$\chi_s(t) = \frac{\omega_{p,s}^2}{v_{c,s}} \left(1 - e^{-v_{c,s}t}\right). \tag{5.106}$$

From (5.56), (5.59) and (5.106) we derive

$$\sigma = \sum_{s=1}^{N} \frac{\epsilon_0 \omega_{p,s}^2}{v_{c,s}} \tag{5.107}$$

$$W_s = -\frac{\omega_{p,s}^2}{v_{c,s}} \tag{5.108}$$

$$Q_s = -v_{c,s}. \tag{5.109}$$

Similarly to the previous examples, numerical and analytical reflection coefficients from a plane wave incident onto a Drude medium are compared. The properties of the Drude medium are $\epsilon_\infty = 3$, $\omega_{p.1} = 57.4\pi$ GHz and $v_{c,1} = 200$

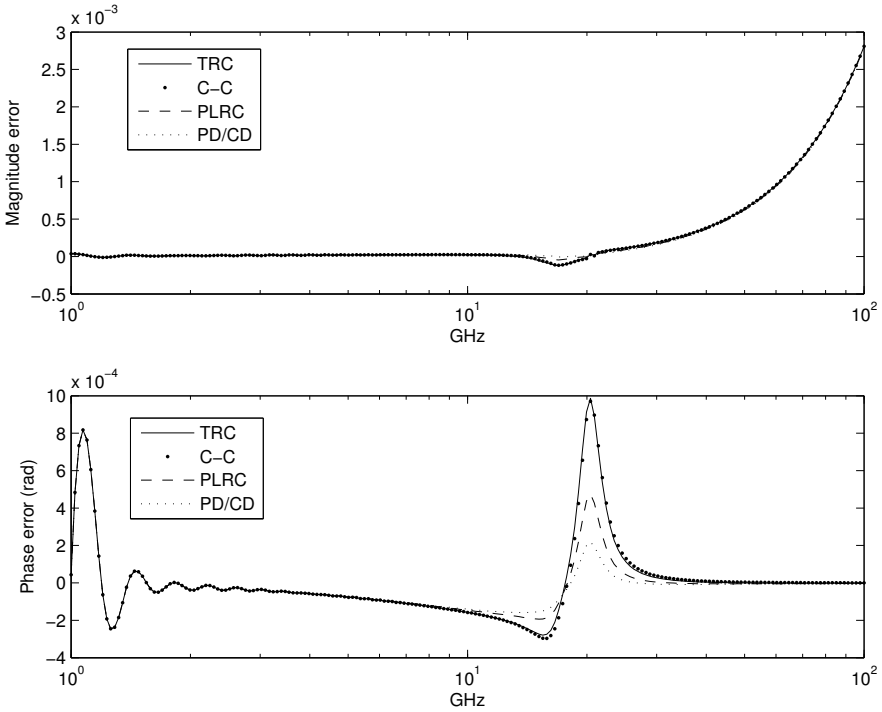

Figure 46: Drude medium: Error between analytical and numerical reflection coefficients for TRC, PLRC, Complex-Conjugate (C-C) method, Current Density (CD) method and Polarisation Density (PD) method.

GHz. The 1D FDTD parameters are $\Delta x = 75$ μm and $\Delta t = 0.25$ ps. Figure 45 shows the numerical and the analytical reflection coefficients and the numerical and analytical relative permittivity calculated using the polarisation density method. The current density method performed equally well. The same numerical test is repeated using TRC, PLRC and the complex-conjugate methods and the errors are shown in Figure 46. Similarly to the previous results, both the amplitude and the phase related errors for the Drude medium have been found to be less for the new proposed algorithms with the polarisation density to perform again slightly better when compared to the current density method.

5.5 PERFECTLY MATCHED LAYER

FDTD, regardless of the order of accuracy, lacks information when it comes to its boundaries. A superficial approach to solve this problem is to assume a zero field value at the boundaries (PEC or PMC). Choosing a finite value rather than zero would result to static fields that would mask the time-varying electromagnetic fields. Assuming a PEC or PMC at the boundaries results to unnatural reflections which would not occur in open region problems like GPR.

The most efficient with respect to accuracy approach would be to increase the size of the grid ideally to infinity in order to delay the unnatural reflections from the PEC or PMC boundaries. This approach would make FDTD in-practical for today's computer standards. The first attempt to find a practical solution to this problem was made by Mur (1981) and later on, Liao et. al (1984) and Higdom (1986) suggested different techniques in an effort to efficiently truncate the boundaries of FDTD. These methodologies are the most famous representatives of the so-called analytical absorbing boundary conditions. Analytical boundary conditions try to predict the values of the fields at the boundaries by using information from the fields inside the grid. The method suggested by Liao et. al (1984) is an appropriate choice for explaining the nature of analytical absorbing boundary conditions. The reason for that, is because, as it is explained by Taflove (2005), Liao's absorbing boundary condition can be interpreted as a space and time extrapolation using the Newton's interpolation formula. In other words, polynomials are used to approximate the fields inside the grid and subsequently the aforementioned polynomials are employed in order to predict the values at the boundaries.

PML was introduced independently by Berenger (1994) and Chew and Weedon (1994) and has since become the most used and well known absorbing boundary condition employed in FDTD. The reasons for that, are that compared with previous approaches, PML is more accurate (Taflove, 2005), more stable (Berenger, 2007) and can be efficiently applied to complex media (dispersive, anisotropic, non-linear) (Gedney, 2011).

PML describes a medium which is theoretically reflection-less for any wave, regardless of the polarisation or the angle of incident. The parameters of PML can be chosen such as the electromagnetic wave attenuates inside the PML region. Using the above characteristics of PML (i.e. reflection-less and lossy) we can truncate the boundaries of the FDTD grid by using a $n$ith layer PML in which the fields are going to fade out without giving rise to any reflections.

Different approaches for implementing PML in FDTD grids have been suggested which can be roughly categorised into: split field formulations (Berenger, 1994), Stretched Coordinates Perfectly Matched Layer (SC-PML) (Chew and Weedon, 1994) and Uniaxial Perfectly Matched Layer (UPML) (Gedney, 1996). The SC-PML is considered possibly as the most attractive choice for implementing PML. The reasons for that are: that it makes the understanding of PML easier (Taflove, 2005), it is easier to incorporate it in cylindrical and spherical coordinate systems (Texeira et al., 1995), through SC-PML more elegant implementations can be obtained with which the PML is incorporated as a correction term (Drossaert and Giannopoulos, 2007, Giannopoulos, 2008), dispersive and lossy media can be trivially treated (Cummer, 2003) and lastly, it increases

the computational efficiency of Complex Frequency Shifted Perfectly Matched Layer (CFS-PML) (Roden and Gedney, 2000).

The CFS-PML was first introduced by Kuzuoglu and Mittra (1996) and it is proven (Becache et al., 2004) that can adequately reduce the late time reflections which occur when using SC-PML (Abarbanel et al., 2002). It has been also shown that CFS-PML decreases the numerical reflections related with the over-absorption of the propagating evanescent waves inside the PML region (Berenger, 1999, 2000, 2007).

Roden and Gedney (2000) suggested an elegant and computationally efficient way to implement CFS-PML. This method is based on an SC-PML formulation and is referred to as the Convolutional Perfectly Matched Layer (CPML). CPML uses a recursive convolution approach first introduced by Luebbers et al. (1991) (aimed for implementing dispersive media in FDTD) to evaluate the convolution between the complex frequency shifted stretching function and the spatial derivatives of the magnetic and the electric fields. An alternative interpretation of CPML based on an ADE formulation is presented by Gedney and Zhao (2010), both of them result to the same equations.

Different methods for evaluating a convolution recursively have been suggested since the first Recursive Convolution (RC) (Luebbers et al., 1991) method was proposed. PLRC (Kelley and Luebbers, 1996) and TRC (Siushansian and Vetri, 1997) are considered second order accurate algorithms (Siushansian and Vetri, 1997) and have been proven more accurate compared to RC for both dispersive media (Kelley and Luebbers, 1996) and PML (Giannopoulos, 2008) implementations. In contrast to standard RC, as introduced for modelling dispersive media, in CPML a TRC approach is employed by default. This is the result of convolving spatial derivatives that are at half a time step apart from the corresponding fields that are being updated by the FDTD equations. Therefore, CPML rivals other second order accurate techniques based on recursive integration (Giannopoulos, 2008), bilinear transform (Zhiansun and Ma, 2012) and Z-transform (Li and Dai, 2006). As it is stated by Gedney (2011), CPML is the most robust and efficient method for truncating FDTD grids.

Due to its popularity, CPML is described in the next chapters. A semi-implicit approach is suggested which increases the accuracy of CPML without further increasing its computational requirements. Since CPML is a SC-PML, the latter is employed in order to explain how and why PML is indeed a perfectly matched layer.

5.5.1 *Theoretical foundations of PML*

SC-PML is a highly original technique which was suggested by Chew and Weedon (1994) and has been shown (Taflove, 2005) that it is a different interpretation of the split-field PML suggested by Berenger (1994). The basic idea of SC-PML is that it stretches the spatial coordinates of the grid to the complex plane. Although the concept sounds difficult to be conceived, nonetheless, SC-PML manages to make the implementation of PML straightforward and inclusive for any complex medium (Taflove, 2005).

The stretching coordinates are expressed as (Taflove, 2005)

$$x_{st} = \int_0^x s_x dx, \qquad y_{st} = \int_0^y s_y dy, \qquad z_{st} = \int_0^z s_z dz, \tag{5.110}$$

which results to

$$\frac{\partial}{\partial x_{st}} = \frac{1}{s_x}\frac{\partial}{\partial x}, \qquad \frac{\partial}{\partial y_{st}} = \frac{1}{s_y}\frac{\partial}{\partial y}, \qquad \frac{\partial}{\partial z_{st}} = \frac{1}{s_z}\frac{\partial}{\partial z}. \tag{5.111}$$

Based on (5.110) and (5.111), Maxwell's equations can be rewritten as

$$j\omega\epsilon\vec{E}_\omega = \nabla_s \times \vec{H}_\omega \tag{5.112}$$

$$j\omega\mu\vec{H}_\omega = -\nabla_s \times \vec{E}_\omega \tag{5.113}$$

$$\nabla_s = \frac{1}{s_x}\frac{\partial}{\partial x}\vec{x} + \frac{1}{s_y}\frac{\partial}{\partial y}\vec{y} + \frac{1}{s_z}\frac{\partial}{\partial z}\vec{z}. \tag{5.114}$$

Applying the curl operator (using the stretched coordinates) on both sides of (5.112), results to

$$j\omega\epsilon\nabla_s \times \vec{E}_\omega = \nabla_s \times \nabla_s \times \vec{H}_\omega. \tag{5.115}$$

Substitute (5.113) to (5.115) yields

$$\omega^2\epsilon\mu\vec{H}_\omega = \nabla_s \times \nabla_s \times \vec{H}_\omega. \tag{5.116}$$

The new stretched coordinates must satisfy the Gauss law for both electric (4.9) and magnetic fields (4.15). If not, magnetic and electric charges would be

gathered inside PML acting as impressed sources with a continuously increasing amplitude. Gauss law for magnetics inside PML is expressed (using (5.113)) as

$$\nabla_s \cdot \vec{H}_\omega = -\frac{1}{j\omega\mu}\nabla_s \cdot \nabla_s \times \vec{E}_\omega = 0. \tag{5.117}$$

The divergent of the curl is always zero (Kreyszig, 1999), but notice that in (5.117) we use the divergence and the curl for the stretched coordinates. In order for (5.117) to be valid, the divergence of the curl using stretched coordinates must be equal to zero. Expanding $\nabla_s \cdot \nabla_s \times \vec{F}$ ($\vec{F}$ is an arbitrarily vector) results

$$\begin{aligned}\nabla_s \cdot \nabla_s \times \vec{F} = &\frac{1}{s_x}\frac{\partial}{\partial x}\left(\frac{1}{s_y}\frac{\partial F_z}{\partial y} - \frac{1}{s_z}\frac{\partial F_y}{\partial z}\right) \\ &-\frac{1}{s_y}\frac{\partial}{\partial y}\left(\frac{1}{s_x}\frac{\partial F_z}{\partial x} - \frac{1}{s_z}\frac{\partial F_x}{\partial z}\right) \\ &+\frac{1}{s_z}\frac{\partial}{\partial z}\left(\frac{1}{s_x}\frac{\partial F_y}{\partial x} - \frac{1}{s_y}\frac{\partial F_x}{\partial y}\right),\end{aligned} \tag{5.118}$$

which is equal to zero only if $\frac{\partial s_u}{\partial v} = 0$, where $u, v \in \{x, y, z\}$ and $u \neq v$. Using the constrains implied by (5.118), equation (5.116) and the identity $\nabla_s \times \nabla_s \times \vec{F} = \nabla_s\left(\nabla_s \cdot \vec{F}\right) - \nabla_s^2\vec{F}$ (Kreyszig, 1999) results to

$$\nabla_s^2\vec{H}_\omega + \omega^2\epsilon\mu\vec{H}_\omega = 0. \tag{5.119}$$

The latter can be expanded to (notice that the Laplacian is applied to a vector and not a scalar)

$$\nabla_s^2 H_{\omega,x} + \omega^2\epsilon\mu H_{\omega,x} = 0 \tag{5.120}$$

$$\nabla_s^2 H_{\omega,y} + \omega^2\epsilon\mu H_{\omega,y} = 0 \tag{5.121}$$

$$\nabla_s^2 H_{\omega,z} + \omega^2\epsilon\mu H_{\omega,z} = 0. \tag{5.122}$$

Equations (5.120)-(5.122) are valid for the following plane wave solutions

$$H_{\omega,x} = A_x e^{j\omega t} e^{-js_x\gamma_x x - js_y\gamma_y y - js_z\gamma_z z} \tag{5.123}$$

$$H_{\omega,y} = A_y e^{j\omega t} e^{-js_x\gamma_x x - js_y\gamma_y y - js_z\gamma_z z} \tag{5.124}$$

$$H_{\omega,z} = A_z e^{j\omega t} e^{-js_x\gamma_x x - js_y\gamma_y y - js_z\gamma_z z} \tag{5.125}$$

where A_u are constants and $\gamma^2 = \gamma_x^2 + \gamma_y^2 + \gamma_z^2$. Substituting (5.123)-(5.125) to (5.112) yields

$$E_{\omega,x} = \left(A_z \frac{\gamma_y}{\omega\epsilon} - A_y \frac{\gamma_z}{\omega\epsilon}\right) e^{j\omega t} e^{-js_x\gamma_x x - js_y\gamma_y y - js_z\gamma_z z} \tag{5.126}$$

$$E_{\omega,y} = \left(A_x \frac{\gamma_z}{\omega\epsilon} - A_z \frac{\gamma_x}{\omega\epsilon}\right) e^{j\omega t} e^{-js_x\gamma_x x - js_y\gamma_y y - js_z\gamma_z z} \tag{5.127}$$

$$E_{\omega,z} = \left(A_y \frac{\gamma_x}{\omega\epsilon} - A_x \frac{\gamma_y}{\omega\epsilon}\right) e^{j\omega t} e^{-js_x\gamma_x x - js_y\gamma_y y - js_z\gamma_z z}. \tag{5.128}$$

Equations (5.123)-(5.128) describe an electromagnetic wave traveling inside a PML medium. A non-PML medium follows the same equations with $s_x = s_y = s_z = 1$.

Now we will examine what values of s_x, s_y and s_z give rise to a zero reflection from a plane interface (oriented at $x = 0$) formed by a PML and a non-PML medium. From continuity of the tangential fields (Balanis, 1989) it can be derived that, in order for the reflection coefficient to be equal to zero and the transmission coefficient to be equal to one, both the amplitude and the phase of the fields across the boundary should be equal. Notice that the amplitudes of the fields in 5.123-5.128 are the same regardless if the medium is PML or not. Thus, in order for the boundary to be reflection-less the phase between the two fields should be equal

$$e^{-js_x\gamma_x x - js_y\gamma_y y - js_z\gamma_z z} = e^{-j\gamma_x x - j\gamma_y y - j\gamma_z z}. \tag{5.129}$$

Equation (5.129) is valid for $x = 0$ and for every y and z only when $s_y = s_z = 1$. Notice that s_x can be any non-zero real or complex number. For $s_x = s_{x,r} + js_{x,i}$, equations (5.123)-(5.128) can be rewritten as

$$H_{\omega,x} = A_x e^{j\omega t} e^{-s_{x,i}x} e^{-js_{x,r}\gamma_x x - js_y\gamma_y y - js_z\gamma_z z} \tag{5.130}$$

$$H_{\omega,y} = A_y e^{j\omega t} e^{-s_{x,i}x} e^{-js_{x,r}\gamma_x x - js_y\gamma_y y - js_z\gamma_z z} \tag{5.131}$$

$$H_{\omega,z} = A_z e^{j\omega t} e^{-s_{x,i}x} e^{-js_{x,r}\gamma_x x - js_y\gamma_y y - js_z\gamma_z z} \tag{5.132}$$

$$E_{\omega,x} = \left(A_z \frac{\gamma_y}{\omega\epsilon} - A_y \frac{\gamma_z}{\omega\epsilon}\right) e^{j\omega t} e^{-s_{x,i}x} e^{-js_{x,r}\gamma_x x - js_y\gamma_y y - js_z\gamma_z z} \tag{5.133}$$

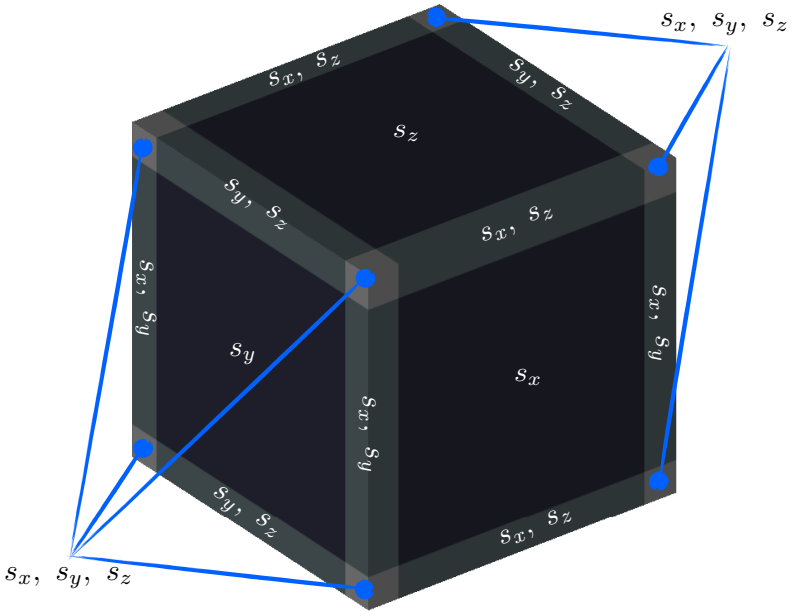

Figure 47: The distribution of s_u in a PML-FDTD grid.

$$E_{\omega,y} = \left(A_x \frac{\gamma_z}{\omega\epsilon} - A_z \frac{\gamma_x}{\omega\epsilon} \right) e^{j\omega t} e^{-s_{x,i}x} e^{-js_{x,r}\gamma_x x - js_y\gamma_y y - js_z\gamma_z z} \tag{5.134}$$

$$E_{\omega,z} = \left(A_y \frac{\gamma_x}{\omega\epsilon} - A_x \frac{\gamma_y}{\omega\epsilon} \right) e^{j\omega t} e^{-s_{x,i}x} e^{-js_{x,r}\gamma_x x - js_y\gamma_y y - js_z\gamma_z z}. \tag{5.135}$$

From (5.130)-(5.135), it is evident, that electromagnetic plane waves (regardless of the angle of incident and polarisation) will attenuate along the x direction inside the PML region. The aforementioned attenuation combined with the reflection-less nature of PML is the reasons why PML is an effective approach for truncating FDTD boundaries.

In order for the reflection coefficients to be zero from a PML-PML planar interface the following is necessary (similarly as (5.129))

$$e^{-js_{1,x}\gamma_x x - js_{1,y}\gamma_y y - js_{1,z}\gamma_z z} = e^{-js_{2,x}\gamma_x x - js_{2,y}\gamma_y y - js_{3,y}\gamma_z z}. \tag{5.136}$$

The latter stands for $x = 0$ and for every y and z only if $s_{1,y} = s_{2,y}$, $s_{1,z} = s_{2,z}$ and for any complex $s_{1,x}$ and $s_{2,x}$.

Working in the same way for different planar interfaces results to the PML-FDTD scheme illustrated in Fig. 47. In all the domain the constrains resulting from the Gauss law ($\frac{\partial s_u}{\partial v} = 0$) must be applied to avoid instabilities.

5.5.2 *Semi-implicit CPML*

It has been shown, that in some cases, CPML does not perform as well as other second order PML methods (Giannopoulos, 2008). A closer inspection of the algorithm reveals that this is not due to the order of accuracy of the numerically evaluated convolution, but due to the fact that the implemented CFS-PML by the CPML is not properly synchronized with the main FDTD algorithm.

Here, a new simple semi-implicit scheme is proposed which results to the synchronisation of CPML with the main FDTD without increasing the computational cost. The effects of the proposed synchronisation to the overall performance of CPML are shown through 2D and 3D numerical examples.

Maxwell's equations (in frequency domain) using CFS-PML can be written in the general form as

$$j\omega\vec{D}_\omega = \nabla_s \times \vec{H}_\omega \tag{5.137}$$

$$j\omega\vec{B}_\omega = -\nabla_s \times \vec{E}_\omega \tag{5.138}$$

$$\nabla_s = \frac{1}{s_x}\frac{\partial}{\partial x}\vec{x} + \frac{1}{s_y}\frac{\partial}{\partial y}\vec{y} + \frac{1}{s_z}\frac{\partial}{\partial z}\vec{z} \tag{5.139}$$

$$s_u = \kappa_u + \frac{\sigma_u}{\alpha_u + j\omega\epsilon_0} \tag{5.140}$$

where κ_u, σ_u and α_u are constants ($u \in \{x, y, z\}$) which define the complex frequency shifted stretching function proposed by Kuzuoglu and Mittra (1996) (5.140).

Transforming (5.137) and (5.138) to time domain results to

$$\frac{\partial\vec{D}}{\partial t} = \nabla_\kappa \times \vec{H} + \nabla_\zeta \times \vec{H} \tag{5.141}$$

$$\frac{\partial\vec{B}}{\partial t} = -\nabla_\kappa \times \vec{E} - \nabla_\zeta \times \vec{E} \tag{5.142}$$

$$\nabla_\kappa = \frac{1}{\kappa_x}\frac{\partial}{\partial x}\vec{x} + \frac{1}{\kappa_y}\frac{\partial}{\partial y}\vec{y} + \frac{1}{\kappa_z}\frac{\partial}{\partial z}\vec{z} \tag{5.143}$$

$$\nabla_\zeta = \zeta_x * \frac{\partial}{\partial x}\vec{x} + \zeta_y * \frac{\partial}{\partial y}\vec{y} + \zeta_z * \frac{\partial}{\partial z}\vec{z} \tag{5.144}$$

$$\zeta_u = -\frac{\sigma_u}{\epsilon_0\kappa_u^2} e^{-\left(\frac{\sigma_u}{\epsilon_0\kappa_u} + \frac{\alpha_u}{\epsilon_0}\right)t}. \tag{5.145}$$

For the case of D_x, following the procedure described by Roden and Gedney (2000) yields

$$\delta_{\Delta t}\left(D^{n+1/2}_{x_{i+\frac{1}{2},j,k}}\right) =$$

$$\frac{1}{k_y}\Lambda_{\Delta y}\left(H^{n+1/2}_{z_{i+\frac{1}{2},j,k}}\right) - \frac{1}{k_z}\Lambda_{\Delta z}\left(H^{n+1/2}_{y_{i+\frac{1}{2},j,k}}\right) \tag{5.146}$$

$$+\sum_{m=0}^{n}\left(Z^m_{0,y}\Lambda_{\Delta y}\left(H^{n-m+1/2}_{z_{i+\frac{1}{2},j,k}}\right) - Z^m_{0,z}\Lambda_{\Delta z}\left(H^{n-m+1/2}_{y_{i+\frac{1}{2},j,k}}\right)\right),$$

where $\delta_{\Delta t}$ is a second order in time central difference operator (5.147), $\Lambda_{\Delta u}$ is a spatial second order central difference operator (5.148), (5.149) and $Z^m_{0,u}$ is the discrete impulse response of ζ_u (5.150) (Roden and Gedney, 2000).

$$\delta_{\Delta t}\left(F^t_{u_{i,j,k}}\right) = \frac{F^{t+\frac{\Delta t}{2}}_{u_{i,j,k}} - F^{t-\frac{\Delta t}{2}}_{u_{i,j,k}}}{\Delta t} \tag{5.147}$$

$$\Lambda_{\Delta z}\left(F^t_{u_{i,j,k}}\right) = \frac{F^t_{u_{i,j,k+\frac{1}{2}}} - F^t_{u_{i,j,k-\frac{1}{2}}}}{\Delta z} \tag{5.148}$$

$$\Lambda_{\Delta y}\left(F^t_{u_{i,j,k}}\right) = \frac{F^t_{u_{i,j+\frac{1}{2},k}} - F^t_{u_{i,j-\frac{1}{2},k}}}{\Delta y} \tag{5.149}$$

$$Z^m_{0,u} = \int_{m\Delta t}^{(m+1)\Delta t} \zeta_u(\tau)d\tau$$

$$= -\frac{\sigma_u}{\epsilon_0\kappa_u^2}\int_{m\Delta t}^{(m+1)\Delta t} e^{-\left(\frac{\sigma_u}{\epsilon_0\kappa_u}+\frac{\alpha_u}{\epsilon_0}\right)\tau}d\tau \tag{5.150}$$

$$= p_u e^{-\left(\frac{\sigma_u}{\kappa_u}+\alpha_u\right)\frac{m\Delta t}{\epsilon_0}}$$

$$p_u = \frac{\sigma_u}{\sigma_u\kappa_u + \kappa_u^2\alpha_u}\left(e^{-\left(\frac{\sigma_u}{\kappa_u}+\alpha_u\right)\frac{\Delta t}{\epsilon_0}} - 1\right). \tag{5.151}$$

The summation in (5.146) is calculated recursively by taking advantage of the exponential nature of Z_0 (Luebbers et al., 1991).

From (5.146) and (5.150) it is evident that the convolution in each time step takes place from 0 to $(n+1)\Delta t$. The spatial derivatives are assumed to be constant at the intervals $[n\Delta t,\ (n+1)\Delta t]$ and they are equal with the value they have at $(n+1/2)\Delta t$. This approach for evaluating recursively the

convolution is known as TRC (Siushansian and Vetri, 1997) which is more accurate compared with the first order RC suggested by Luebbers et al. (1991) and rivals the accuracy (Siushansian and Vetri, 1997) of PLRC (Kelley and Luebbers, 1996). The drawback of CPML is not the order of accuracy of TRC, but the fact that the approximated convolution is not synchronised with the main FDTD algorithm. This is evident in (5.146), in which the time derivative of the electric flux as well as the spatial derivatives of the magnetic field are evaluated at $(n + 1/2)\Delta t$ (using a second order approximation), while the convolutions arising due to the presence of the PML are evaluated using TRC which is a second oder approximation (Siushansian and Vetri, 1997) at $(n + 1)\Delta t$.

From the above, Maxwell's equations using CPML can be re-written in a discretised form (using a second order accuracy in time) as

$$\frac{\partial \vec{D}}{\partial t}^{n+1/2} = \nabla_\kappa \times \vec{H}^{n+1/2} + \left(\nabla_\zeta \times \vec{H}\right)^{n+1} \tag{5.152}$$

$$\frac{\partial \vec{B}}{\partial t}^{n+1} = -\nabla_\kappa \times \vec{E}^{n+1} - \left(\nabla_\zeta \times \vec{E}\right)^{n+3/2}. \tag{5.153}$$

In order to synchronize both $\nabla_\zeta \times \vec{H}$ and $\nabla_\zeta \times \vec{E}$ with the main FDTD algorithm a semi-implicit scheme is used which employes a second order interpolation (in time) (Taflove, 2005),

$$\nabla_\zeta \times \vec{H}^{n+1/2} \approx \frac{\nabla_\zeta \times \vec{H}^n + \nabla_\zeta \times \vec{H}^{n+1}}{2} \tag{5.154}$$

$$\nabla_\zeta \times \vec{E}^{n+1} \approx \frac{\nabla_\zeta \times \vec{E}^{n+1/2} + \nabla_\zeta \times \vec{E}^{n+3/2}}{2}. \tag{5.155}$$

Substituting (5.154) and (5.155) into (5.152) and (5.153) respectively, results into

$$\frac{\partial \vec{D}}{\partial t}^{n+1/2} = \nabla_\kappa \times \vec{H}^{n+1/2} + \frac{\left(\nabla_\zeta \times \vec{H}\right)^{n+1} + \left(\nabla_\zeta \times \vec{H}\right)^{n}}{2} \tag{5.156}$$

$$\frac{\partial \vec{B}}{\partial t}^{n+1} = -\nabla_\kappa \times \vec{E}^{n+1} - \frac{\left(\nabla_\zeta \times \vec{E}\right)^{n+3/2} + \left(\nabla_\zeta \times \vec{E}\right)^{n+1/2}}{2} \tag{5.157}$$

The modified CPML saves in temporary variables the values of $\nabla_\zeta \times \vec{H}^n$ and $\nabla_\zeta \times \vec{E}^{n+1/2}$ and subsequently calculates $\nabla_\zeta \times \vec{H}^{n+1}$ and $\nabla_\zeta \times \vec{E}^{n+3/2}$ according to Roden and Gedney (2000). The second order semi-implicit approximations in (5.154), (5.155) can now be trivially calculated and added as correction

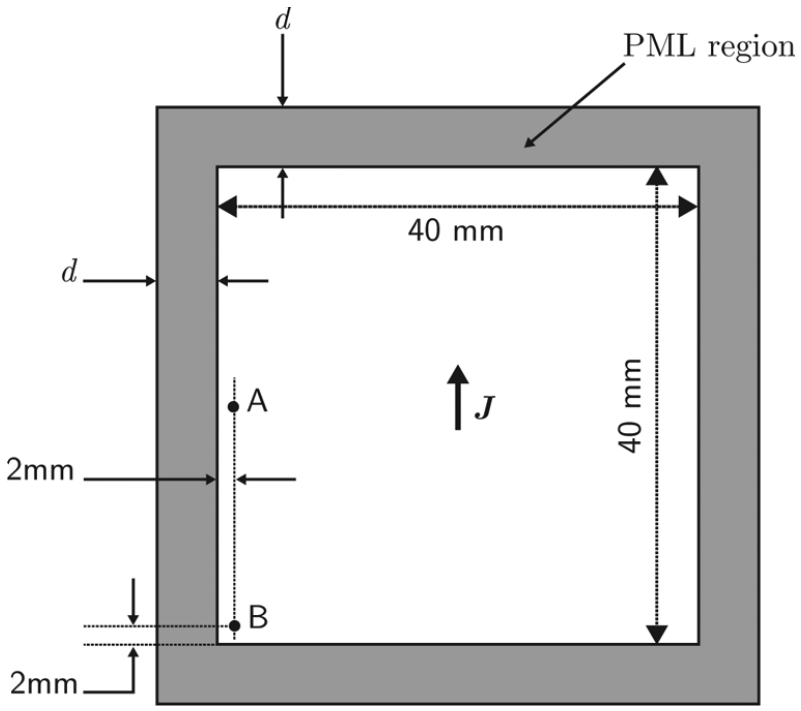

Figure 48: A y-directed current source is located at the centre of a 40×40 TE FDTD grid. The electric field E_y is probed at A and B points. The spatial step is $\Delta x = \Delta y = 1$ mm and the time step is 0.99 times the Courant limit. The thickness of the PML equals $d = 10$ mm (Taflove, 2005).

terms in the CPML-FDTD code. From the above it is evident that no additional variables are needed to be stored compared with the original CPML.

Numerical results

The performance of CPML with the proposed modification is validated through 2D and 3D numerical examples. The numerical experiments are similar to the ones used by Taflove (2005) and Giannopoulos (2008). The proposed algorithm i.e. semi-implicit CPML, is compared with the standard CPML in order to show how the suggested synchronisation affects the overall performance of the implemented CFS-PML. Semi-implicit CPML is also compared with the RIPML, which, as it is shown by Giannopoulos (2008) achieves a small increase in performance with respect to CPML.

In the first example a TE (H_z, E_y, E_x) FDTD is employed. The dimensions of the model are 40×40, the discretisation step equals to $\Delta x = \Delta y = 1$ mm (uniform along the grid) and the time step is 0.99 times the Courant limit. A

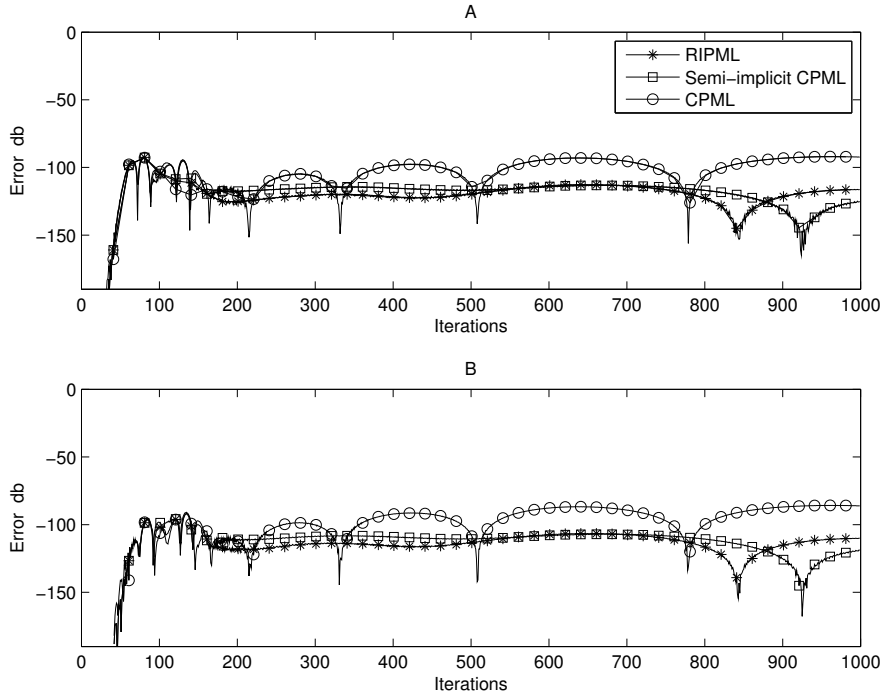

Figure 49: Error calculated from (5.159) using CPML, RIPML and semi-implicit CPML. A and B corresponds to the receiving points illustrated in Fig. 48.

current source is placed at the centre of the grid and the time variation of the source is equal with (Taflove, 2005)

$$I(t) = -2\frac{t - t_0}{t_w} e^{-\left(t - \frac{t_0}{t_w}\right)^2} \tag{5.158}$$

where $t_w = 26.53$ ps and $t_0 = 4t_w$. The electric field E_y is sampled at A and B points (see Fig. 48). The sampled E_y fields are compared to a reference solution and the error defined in (5.159) is calculated.

$$Error|_{i,j}^{n} = 20 \cdot \log_{10} \frac{||E|_{i,j}^{n} - E_{ref}|_{i,j}^{n}||}{E_{ref_{max}}|_{i,j}}. \tag{5.159}$$

Where $E|_{i,j}^{n}$ is the probed electrical field at grid points (i, j) and at n time step, $E_{ref}|_{i,j}^{n}$ is the reference solution and $E_{ref_{max}}|_{i,j}$ is the maximum absolute value of the reference solution.

The thickness of the PML is 10 Yee cells and the optimum value for σ_{max} is calculated using (Taflove, 2005)

$$\sigma_{max} = \frac{0.8(m + 1)}{Z \cdot dl} \tag{5.160}$$

where Z is the impedance of the medium, dl is the discretisation step and

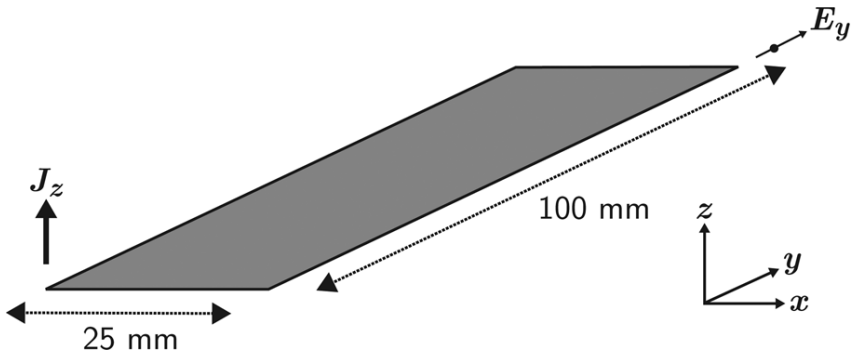

Figure 50: A z-directed Hertzian dipole over a PEC plate. The spatial step is $\Delta x = \Delta y = \Delta z = 1$ mm and the time step is 0.99 times the Courant limit. The thickness of the PML equals $d = 10$ mm. E_y is monitored in the opposite corner of the source's location, one Yee cell away from the PEC plate (Taflove, 2005).

$m = 3$ is the order of the polynomial function which is used to scale σ_u along the PML (Taflove, 2005). A constant value $\kappa_u = 1$ is applied along the FDTD grid. An inverse linear scaling is applied to α_u (Taflove, 2005) with $\alpha_{max} = 0.2$. Fig. 49 illustrates the error at the receiving points A and B (see Fig. 48) using CPML, RIPML and the semi-implicit CPML method. It is evident that there is an improvement in accuracy using semi-implicit CPML and RIPML compared with the CPML. The differences regarding the accuracy between RIPML and semi-implicit CPML are negligible. The main advantage of the proposed semi-implicit CPML formulation is the simplicity in implementing it into existing CPML codes.

In the second example the performance of the modified CPML is validated in the presence of evanescent waves. The dimensions of the 3D domain are $31 \times 106 \times 6$, the discretisation step is uniform along the domain and equals to $\Delta x = \Delta y = \Delta z = 1$ mm and the time step is 0.99 times the Courant limit. A $z-$directed Hertzian dipole is placed on top of the edge of a 25×100 mm PEC plate (Giannopoulos, 2008). The time evolution of the current source is given by (5.158) with $t_w = 53$ ps and $t_0 = 4t_w$ (Giannopoulos, 2008). The width of the PML is 10 Yee cells. The E_y field is probed at the opposite corner from the source's location, 1 mm away from the PEC plate (see Fig. 50). The values of the stretching function are $\kappa_u = 1$ (constant along the PML), σ_{max} is given by (5.160) with $m = 3$. A linear function is used to express α_u with $\alpha_{max} = 0.24$. Fig. 51 illustrates the error defined in (5.159) using CPML, semi-implicit CPML and RIPML. It is evident that synchronisation increases the overall performance of CPML. Again semi-implicit CPML and RIPML exhibit negligible differences in performance.

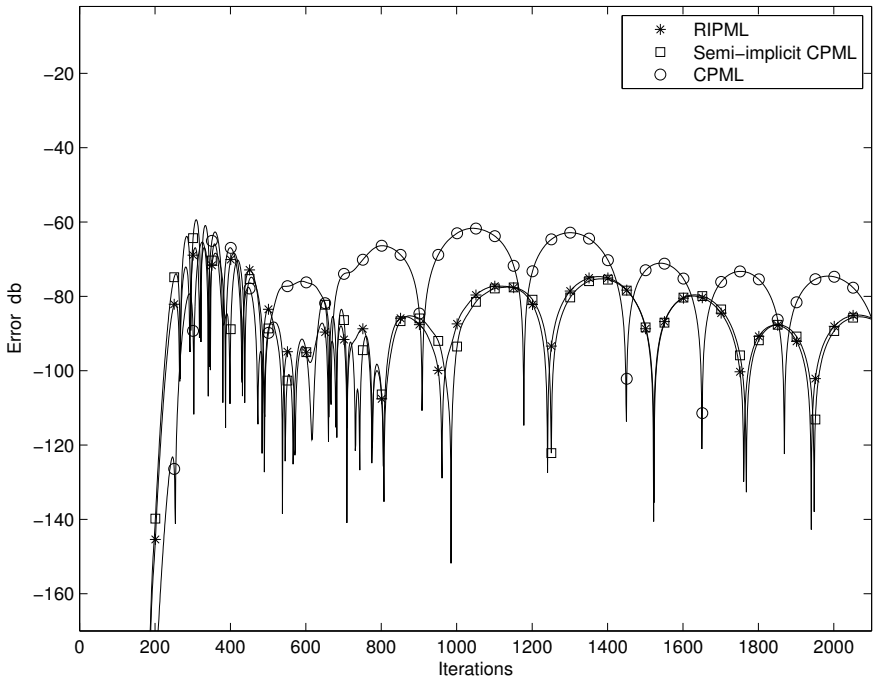

Figure 51: Calculated error (5.159) using semi-implicit CPML, CPML and RIPML for the case study described in Fig. 50.

6

NUMERICAL SCHEME FOR LANDMINE DETECTION

In the present chapter, a novel and realistic numerical framework for landmine detection using GPR is described. The numerical solver of the scheme is a 3D FDTD (2,2). Both PML (Giannakis and Giannopoulos, 2015) and dispersive media (Giannakis et al., 2014) are accurately and efficiently implemented in the numerical framework. Two detailed models of commercial-based bowtie GPR transducers are chosen for the simulations. Regarding the buried targets, three widely employed AP landmines, namely PMA-1, PMN and TS-50 are used. The validity of the modelled antennas and landmines are tested through comparison between numerical and real measurements. The modelled AP landmines are buried in a realistically simulated soil. The geometrical characteristics of the soil's inhomogeneity are modelled using fractal correlated noise which gives rise to Gaussian semivariograms often encountered in the field. Fractals are also employed in order to simulate the roughness of the soil's topography. Regarding the dielectric properties of the soil, a frequency-dependent complex electrical permittivity is used which relates both the speed and the attenuation of the electromagnetic waves with the soil's bulk density, sand particles density, clay fraction, sand fraction and volumetric water fraction. Debye functions are employed to approximate the complex electrical permittivity for a given frequency. Background features like vegetation and water puddles are also included in the models and it is shown that they can affect the performance of GPR for frequencies often used in demining (0.5-3 GHz).

6.1 INTRODUCTION

GPR has a wide range of applications (Daniels, 2004) and it has been extensively used for landmine detection (Daniels, 2006). The ability to detect plastic landmines and the greater depth range compared with metal detectors are some of the reasons why GPR is considered an attractive method for demining (Daniels, 2006). A better understanding of the scattering mechanisms within the ground can help us to increase the effectiveness of GPR and map its limitations. This can be achieved through numerical modelling which can give us an insight of how soil's characteristics can influence GPR. Numerical modelling can also be a practical tool for testing and comparing different antennas and processing algorithms in a variety of environments. In addition, a realistic numerical

scheme can be also employed for training purposes using machine learning. A multi-variable problem like demining using GPR, in order to be addressed using machine learning, requires a large number of data from a diverse set of scenarios (Giannakis et al., 2015). To our knowledge, the only plausible approach to obtain a diverse, equally distributed and adequately large dataset is through a realistic and accurate numerical scheme.

Numerical modelling for GPR is considered to be an alternative interpretation approach (Cassidy, 2007) and has been widely applied to a variety of GPR applications, amongst them are, Dense Non Aqueous Phase Liquids (DNAPL) detection (Carcione, 1996, Wilson et al., 2009), detection of geological targets like faults and caves (Hu et al., 2012, Ozturk and Drahor, 2010), tunnel inspections (Xianqi et al., 2009), assessing the location and condition of pipes (Cassidy and Milligton, 2009), assessing the condition of bridges (Belli et al., 2009, Diamanti and Giannopoulos, 2011), forensic applications (Hammon et al., 2000), mineral exploration (Sixin et al., 2011) and airborne GPR (Sixin and Yanqian, 2011). Regarding landmine detection, generic types of antennas over simple targets buried in both homogenous and inhomogeneous soils have been modelled by Gurel and Oguz (2000, 2001), Oguz and Gurel (2002) and Gurel and Oguz (2003). More advanced and realistic models for both antennas and targets are employed by Gonzalez-Huici et al. (2007) and Gonzalez-Huici (2012) in order to simulate and obtain single traces (A-Scans) which were subsequently used as a reference in an attempt to discriminate between landmines and false alarm targets.

As stated by Daniels (2006), a lot of antennas were validated in ideal conditions but their performance in real complex environments was found to differ significantly from the predicted one. Although PD can reach near 100% and PFA fall to near 0.01% at simple test sites, in realistic conditions, PD can fall to 50% and PFA can reach to 10% (Daniels, 2006). Based on that, numerical modelling should be able to simulate the behaviour of GPR in realistic and appropriately complex environments and not only in clinically simplified ones. Such simplifications give rise to predictable results which cannot be used to validate the performance of GPR in realistic conditions.

FDTD for detecting shallow buried targets like landmines has some unique characteristics emerging from the scale of the model and from the relatively high frequency content of the employed pulses. Namely, these characteristics are:

- High losses. This means that the imaginary part of the electrical permittivity which is directly related to the electromagnetic losses is a very crucial parameter and should neither be neglected nor simply defined.

- The antenna occupies a relative large volume in the modelled domain. This means that the antenna is not only related to the characteristics of the transmitted pulse (directivity, central frequency etc.) but it is also part of the model which contributes to the measured scattered field.
- Increased sensitivity to background characteristics. This means that soil inhomogeneity, rough surface, water puddles and vegetation are not negligible parameters and should be as accurately as possible incorporated into the models.

One of the most challenging problems regarding the numerical modelling of GPR is the implementation of the dielectric properties of soils. Simplistic models with a constant electrical permittivity plus a conductive term cannot accurately simulate soil's behaviour for the frequency range employed in demining. Dielectric properties of soils is a multi-parametric problem and no clear definition of a function which describes them has yet been derived.

Approximations of the dielectric properties of soils with multi-Debye relaxations (Clegg and Robinson, 2010, Giannakis et al., 2012, Kelley et al., 2007) is the most usual approach for implementing this type of dielectric properties into FDTD. Numerically evaluated fractional derivatives (Torres et al., 1996) or Pade approximations (Weedon and Rappaport, 1997) can also be used for implementing complex dielectric properties. Multi-Debye expansions however are more computationally efficient because it is straightforward to choose the frequency range for which the approximation will take place. By reducing the frequency range to the range of interest, the number of Debye poles needed for an adequate approximation is decreased which results in an overall decrease of the computational cost.

A number of authors have used multi-Debye functions to create simple models of homogenous soils (Atteia and Hussein, 2010, Bergmann et al., 1998, Carcione and Schoenberg, 2000, Xu and McMechan, 1997). Although these approaches simulate the dielectric properties of the specific soils correctly, homogenous models are still an oversimplification. A more inclusive definition is needed in order to be able to model different types of soils. In this work, the semi-empirical model described in chapter 4 is used. The semi-empirical model relates the dielectric properties of the soil with its bulk density, sand particles density, soil fraction, clay fraction and water volumetric fraction. This function can be approximated by a multi-Debye expansion and subsequently implemented into FDTD (Giannakis and Giannopoulos, 2015). By using this approach, different types of soils with different properties can be incorporated into the model as well as complex non-clinical media with a realistic statistical variation of properties like water fraction, clay fraction and so on.

Rough surface can have a significant effect to the overall performance of GPR especially when high frequencies are used (Daniels, 2004). Thus, an accurate numerical scheme should include a realistic representation of soil's topography. Fractals can express the earths topography with representative detail (Turcotte, 1987) for a wide range of scales. Due to that, fractal correlated noise (Turcotte, 1992) is chosen to describe the stochastic nature of soil's surface. Fractal correlated noise is also employed in an effort to describe soil's inhomogeneities. Evidence is given which support the premise that for the scales used in the current simulations, fractals give rise to semivariograms often encountered in real soils (Jabro et al., 2010, Rea and Knight, 1998, Rezaur et al., 2002, Yansui and Mikami, 2004).

Vegetation is a very important feature for the frequencies employed in demining and should neither be neglected nor simply defined. Both grass and roots are realistically incorporated into the suggested modelling scheme and it is shown that they affect the overall performance of GPR. A novel algorithm is proposed which generates the geometry of both grass and roots with representative detail into the FDTD model. The suggested algorithm creates the geometry of vegetation automatically having as inputs statistical characteristics like grass distribution, maximum height of grass, maximum depth of roots, standard deviation of the height of grass, standard deviation of the maximum depth of roots and properties related with the shape of the grass and roots. Regarding the dielectric properties of vegetation, a multi-Debye expansion is used to simulate the function suggested by Carlson (1967) and Tan (1981). This function expresses the complex electrical permittivity of vegetation with respect to its water weight based fraction. Water puddles are also incorporated into the numerical scheme in an effort to simulate humid environments.

Numerical modelling has been widely used for designing and optimising antennas, from complex antennas (Lee et al., 2004, Uduwawala, 2006) to more common, like bowties (Bourgeois and Smith, 1996, Caratelli et al., 2009, Klysz et al., 2004), dipoles (Bourgeois and Smith, 1997), vee dipoles (Montoya and Smith, 1996), spiral (McFadden and Scott, 2007) and horn antennas (Giannakis et al., 2014, Giannakis and Giannopoulos, 2014, Turk et al., 2007). FDTD has been successfully used to model generic types of antennas based on commercial ones (Klysz et al., 2006, Warren and Giannopoulos, 2011, 2012). Here, two models of bowtie GPR transducers are used which are based on the geometrical characteristics of the commercially available antennas GSSI 1.5 GHz and MALA 1.2 GHz as presented by Warren and Giannopoulos (2011). Both of the employed GPR antennas are designed mostly for engineering applications but because of their high frequency content and their availability for simple testing

have been chosen to illustrate the effectiveness of the proposed modelling framework for AP landmine detection.

The targets which are used in the simulations are accurate representations of the AP landmines PMA-1, PMN and TS-50. The geometry of the modelled AP landmines is based on dummy targets. The dielectric properties of the AP landmines are chosen such as the numerical and the real measurements of the scattered field in free space to be in good agreement.

6.2 SOIL MODELLING

Soil modelling consists of two parts, the first part has to do with the dielectric properties of the soil and the second deals with the soil's geometrical characteristics, i.e. soil's inhomogeneity and rough surface.

6.2.1 *Dielectric properties*

The dielectric model chosen for the numerical scheme is the semi-empirical model initially suggested by Dobson et al. (1985) and later modified by Peplinski et al. (1995). The semi-empirical model cannot be directly implemented in FDTD. A Particle Swarm Optimisation (PSO) (Kennedy and Eberhart, 1995) can be used in order to approximate both the real and the imaginary part of the dielectric model with a conductive term plus a multi-pole Debye function (6.1),

$$\epsilon_m \approx \epsilon_\infty + \frac{\sigma}{j\omega} + \sum_{p=1}^{N} \frac{\Delta\epsilon_p}{1 + j\omega t_{0,p}} \tag{6.1}$$

where N is the number of the Debye poles (Giannakis et al., 2014).

In order for FDTD to be stable, $\Delta\epsilon_p$ must be positive and $\epsilon_\infty \geq \epsilon_0$ (Kelley et al., 2007). By increasing the number of Debye poles, the approximation becomes more accurate, but for each extra Debye pole three additional variables for the electric fields are needed to be stored for each FDTD cell with dispersive dielectric properties. A balance between accuracy and computational cost must occur in order for the simulations to be both accurate and practical. For the frequency range of interest (0.5-3 GHz), a single Debye pole is an adequate approximation as shown in Fig. 52. Accurate approximations for wider range of frequencies require more Debye poles to be used which subsequently creates the need for more computational resources.

For the approximations illustrated in Fig. 52, a more practical approach, which doesn't employ any iterative optimisation schemes, is used in order to

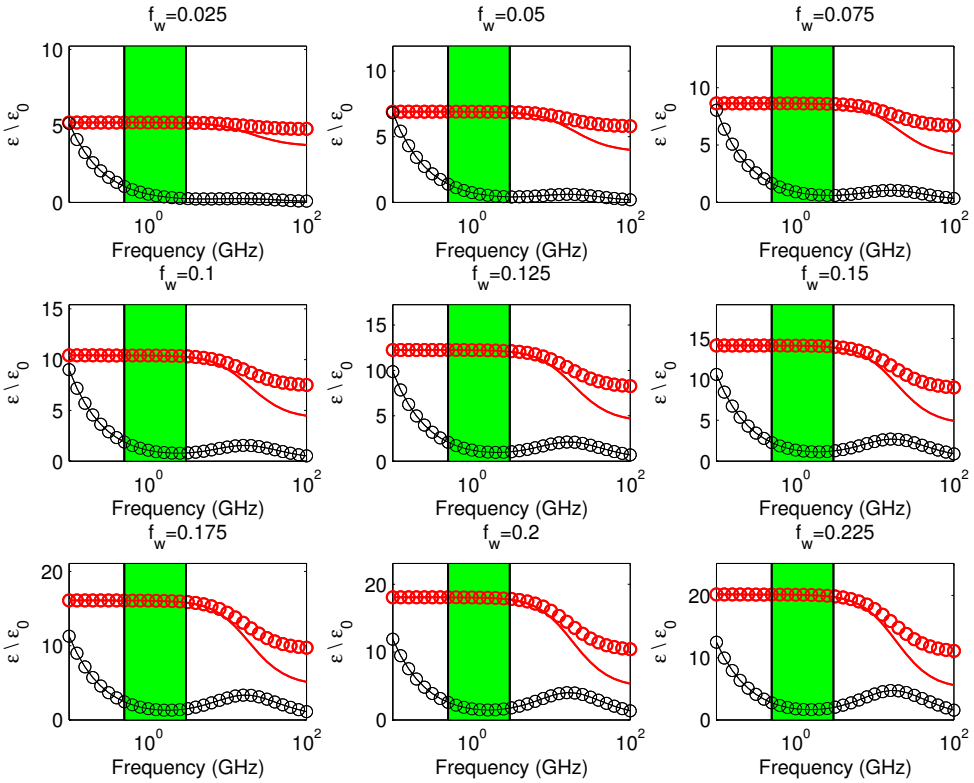

Figure 52: The semi-empirical model and the Debye approximations for both real (red) and imaginary (black) parts for soils with different water volumetric fractions (f_w). The soil's parameters are $S = 0.6$, $C = 0.4$, $\rho_b = 2$ gr/cm^3 and $\rho_s = 2.66$ gr/cm^3. The green area illustrates the frequency range of GPR for landmine detection.

approximate the semi-empirical model (Dobson et al., 1985) with an extended Debye model (Debye function plus conductive term). The semi-empirical model is described in (4.87)-(4.95) and can be rewritten in a more simple form as

$$\epsilon = \epsilon' - j f_w^{\frac{\beta''}{a}} \epsilon''_w + f_w^{\frac{\beta''}{a}} \frac{\sigma_f}{j\omega\epsilon_0} \frac{(\rho_s - \rho_b)}{\rho_s f_w} \tag{6.2}$$

where ϵ' is the real part of the semi-empirical model which is related to the soil's properties (4.87)-(4.95). Equation (6.2) is approximated with a single Debye pole plus a conductive term

$$\epsilon' - j f_w^{\frac{\beta''}{a}} \epsilon''_w + f_w^{\frac{\beta''}{a}} \frac{\sigma_f}{j\omega\epsilon_0} \frac{(\rho_s - \rho_b)}{\rho_s f_w} \approx \epsilon_{a,\infty} + \frac{\epsilon_{a,s} - \epsilon_{a,\infty}}{1 + j\omega t_{0,a}} + \frac{\sigma}{j\omega\epsilon_0}. \tag{6.3}$$

We first approximate the conductive term σ by equating the terms with divisor $\frac{1}{j\omega}$

$$\sigma = f_w^{\frac{\beta''}{a}} \sigma_f \frac{\rho_s - \rho_b}{\rho_s f_w}. \tag{6.4}$$

From (6.3) and (6.4) it is derived that the Debye function must approximate only the dipolar mechanisms of the semi-empirical model

$$\epsilon' - j f_w^{\frac{\beta''}{a}} \epsilon''_w \approx \epsilon_{a,\infty} + \frac{\epsilon_{a,s} - \epsilon_{a,\infty}}{1 + j\omega t_{0,a}}. \tag{6.5}$$

By further expanding (6.5), yields

$$\epsilon' - j f_w^{\frac{\beta''}{a}} \frac{\omega t_{0,w} \left(\epsilon_{w,s} - \epsilon_{w,\infty}\right)}{1 + \left(\omega t_{0,w}\right)^2} \approx \epsilon'_a - j \frac{\omega t_{0,a} \left(\epsilon_{a,s} - \epsilon_{a,\infty}\right)}{1 + \left(\omega t_{0,a}\right)^2}. \tag{6.6}$$

where ϵ'_a is the real part of ϵ_a. Equating the imaginary parts of (6.6) yields

$$f_w^{\frac{\beta''}{a}} \frac{\omega t_{0,w} \left(\epsilon_{w,s} - \epsilon_{w,\infty}\right)}{1 + \left(\omega t_{0,w}\right)^2} \approx \frac{\omega t_{0,a} \left(\epsilon_{a,s} - \epsilon_{a,\infty}\right)}{1 + \left(\omega t_{0,a}\right)^2}. \tag{6.7}$$

From Fig. 20 it is evident that the relaxation time t_0 is related to the frequency for which the imaginary part reaches its maximum value. Thus,

$$t_{0,w} = t_{0,a} \tag{6.8}$$

is a reasonable choice which is based on the fact that both the semi-empirical model and its approximation should have maximum imaginary parts at the same frequencies. Using the assumption $t_{0,w} = t_{0,a}$, yields

$$f_w^{\frac{\beta''}{a}} \left(\epsilon_{w,s} - \epsilon_{w,\infty}\right) \approx \epsilon_{a,s} - \epsilon_{a,\infty}. \tag{6.9}$$

From Fig. 20 it is derived that ϵ_s is the real electrical permittivity for zero frequency (static permittivity). By assuming that

$$\epsilon_{a,s} = \epsilon'(0), \tag{6.10}$$

we constrain the semi-empirical model and its approximation to have the same static permittivity. Since the real part of the semi-empirical model is basically

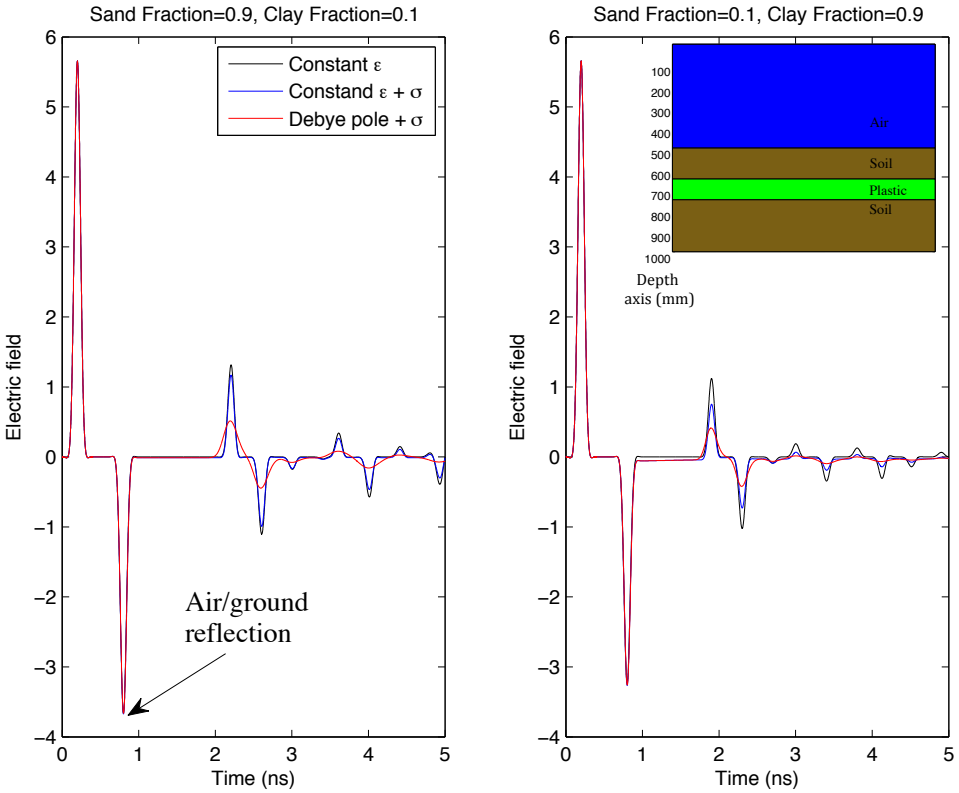

Figure 53: Resulting simulated traces using two different soils for the 1D model illustrated on the top right. In both soil models $\rho_s = 2.66$ g/cm^3, $\rho_b = 2$ g/cm^3, and $f_w = 0.2$. In the right plot $S = 0.1$, $C = 0.9$ and in the left $S = 0.9$, $C = 0.1$. Three different approaches are used for both soils to define their dielectric properties. With black, only a constant electrical permittivity is used. With blue, a constant electrical permittivity plus a conductive term is employed and with red, the full model (i.e. a Debye pole with a conductive term) is implemented.

constant below 3 GHz, by assuming $\epsilon_{a,s} = \epsilon'(0)$ we essentially approximate the real part of the semi-empirical model for frequencies below 3 GHz.

Lastly, from (6.9) and (6.10) it is derived that

$$\epsilon_{a,\infty} = \epsilon'(0) - f_w^{\frac{\beta''}{a}} \left(\epsilon_{w,s} - \epsilon_{w,\infty}\right). \tag{6.11}$$

To summarise, the semi-empirical model can be approximated with an extended Debye model (6.3) using (6.8), (6.10) and (6.11). Using this approach, the imaginary part of the semi-empirical model is simulated exactly using the extended Debye model. The real part is adequately approximated for the frequencies below 3 GHz.

In order to illustrate the importance of implementing the complete electromagnetic losses, a numerical experiment was performed in which a simple 1D

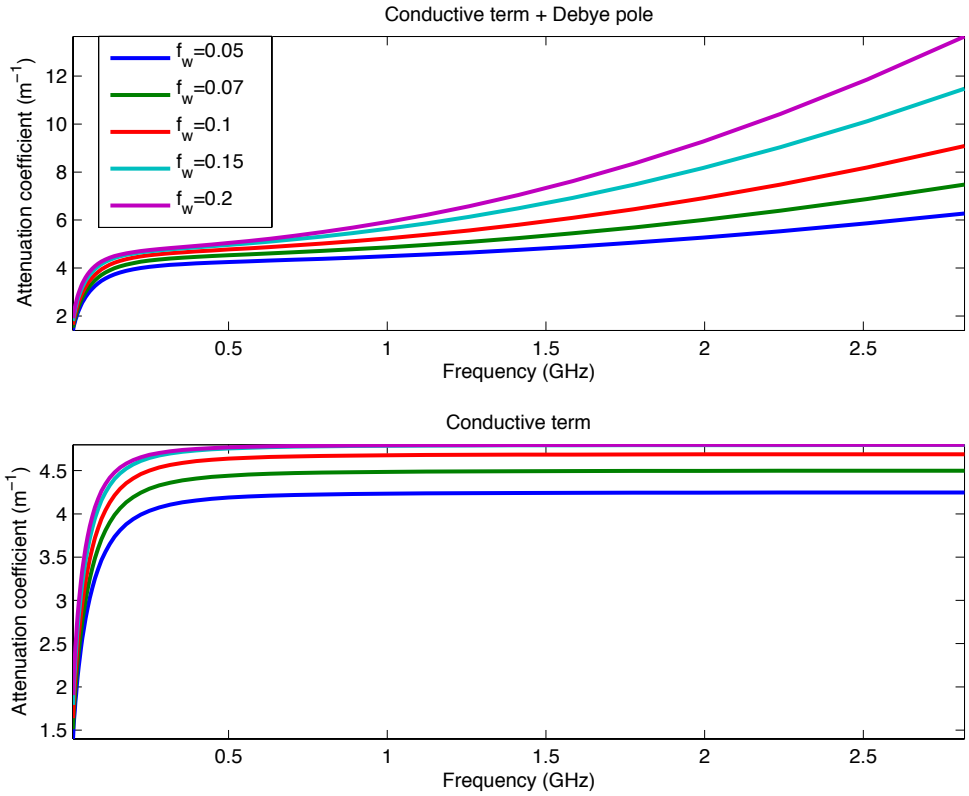

Figure 54: Electromagnetic losses of a plane wave propagating inside a soil with $\rho_s = 2.66$ g/cm^3, $\rho_b = 2$ g/cm^3, $S = 0.5$, $C = 0.5$ and for different water fractions f_w. In the first case the complete dielectric properties are accounted for, while in the second case only the conductive term is used.

model is simulated using FDTD. The model consists of four layers, namely air, soil, plastic and soil (see Fig. 53). The excitation source is a Gaussian-modulated sinusoidal pulse with central frequency 2 GHz and fractional bandwidth equals to four. The spatial discretisation equals $\Delta z = 1$ mm and the time step equals to the Courant limit for the 1D FDTD scheme ($\Delta t = 3.3$ ps) (Taflove and Hagness, 2000). The relative electrical permittivity of plastic is chosen to be $\epsilon_p = 3$. Regarding the soil, three different scenarios are tested. In the first one, a simple constant electrical permittivity is implemented without any electromagnetic losses. In the second one, a conductive term is added and in the third one, a Debye pole plus a conductive term are employed. Two different types of soils are tested, in the first case $\rho_s = 2.66$ g/cm^3, $\rho_b = 2$ g/cm^3, $S = 0.1$, $C = 0.9$ and $f_w = 0.2$. The second case is similar with the previous one with $S = 0.9$ and $C = 0.1$. Fig. 53 illustrates that the complete model (Debye pole plus conductive term) apart from decreasing the amplitude of the pulse, also lowers the central frequency of the scattering field which subsequently reduces the ability of the pulse to resolve small targets.

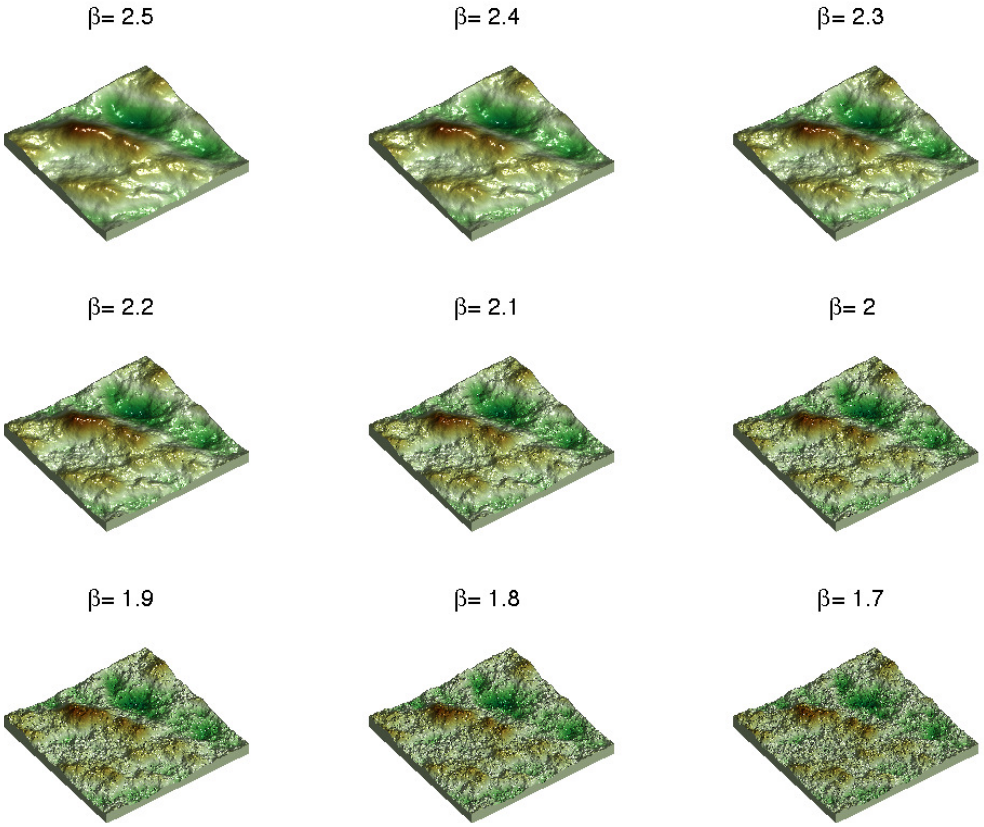

Figure 55: Fractal surface for different β. The latter is related with the fractal dimension with $\beta = -(2D - 7)$, where D is the fractal dimension (Turcotte, 1992).

The effects of soil's dipolar losses are clearly illustrated in Fig. 54. For low frequencies the dipolar losses due to water can be neglected since the losses can be adequately described using only the effects of ionic conductivity. As the frequency increases, dipolar losses become more dominant. From Fig. 54 it is evident that for the frequencies employed in demining, dipolar losses is the main source of electromagnetic losses.

Electromagnetic losses can have a significant effect to the overall signal to noise ratio as well as to the shape of the target's scattering field. From the above it is evident that simple definitions of the loss mechanisms within the soil using only a conductive term can result to an overestimation of GPR's performance. Thus, an accurate implementation of the dielectric properties is essential for a realistic and coherent numerical modelling scheme which aims to be used as a testbed for different processing algorithms and as a training platform for machine learning.

6.2.2 *Geometrical characteristics*

Fractals are scale invariant functions which can express the earths topography for a wide range of scales with sufficient detail (Turcotte, 1987). Fractals frequently arise in geology and as stated by Huang and Turcotte (1989), fractals are the reason why everyday objects are used for scale in geological related pictures. Fractal correlated noise for n dimensions can be generated through (Giannakis et al., 2016)

$$F\left(x_1, x_2 ... x_n\right) = \mathcal{F}^{-1}\left(R\left(k_1, k_2, ... k_n\right) \cdot \left(\sum_{i=1}^{n} k_i^2\right)^{-\frac{\beta}{2}}\right) \tag{6.12}$$

where F is the resulting fractal correlated noise, x_i is the ith dimension, R is the Fourier transform of a $n$ith-dimensional Gaussian noise, k_i is the ith dimension in the wavenumber's domain, β is a linearly-related term to the fractal dimension (Turcotte, 1992) and $\mathcal{F}^{-1}$ denotes the inverse Fourier transform symbol. Fig. 55 illustrates the resulting rough surface using fractal correlated noise. Decreasing β results to the increase of the roughness of the soil's surface.

Semivariogram (6.13) is a geostatistical tool which is used to describe correlation lengths and it is an attractive approach to describe the stochastic nature of soil's properties like water fraction, clay fraction and so on (Hillel, 1980)

$$\gamma(h) = \frac{1}{2V} \sum_{i=1}^{V} |z(i+h) - z(i)|^2. \tag{6.13}$$

Where h is the lag distance, z is the investigated property (water fraction, clay fraction, bulk density etc.) and V is the number of the observations for each lag length (h). Soil's properties usually follow exponential, spherical or Gaussian semivariograms (Jabro et al., 2010, Rezaur et al., 2002, Takahashi et al., 2012, 2014, Yansui and Mikami, 2004). In the proposed numerical framework, a fractal correlated noise (Turcotte, 1992) is used to describe the stochastic distribution of soil's properties. This approach is chosen because as it is stated by Burrough (1981) and Hillel (1980), a lot of soil-related environmental properties obey fractal laws. Apart from that, it is shown (see Fig. 57) that the distribution of an arbitrarily property using 3D fractals results to Gaussian semivariograms (6.14) (for the scales used for AP landmine detection)

$$\gamma(h) = (s-n)\left(1 - e^{\left(-\frac{h^2}{r^2 w}\right)}\right) + n_0. \tag{6.14}$$

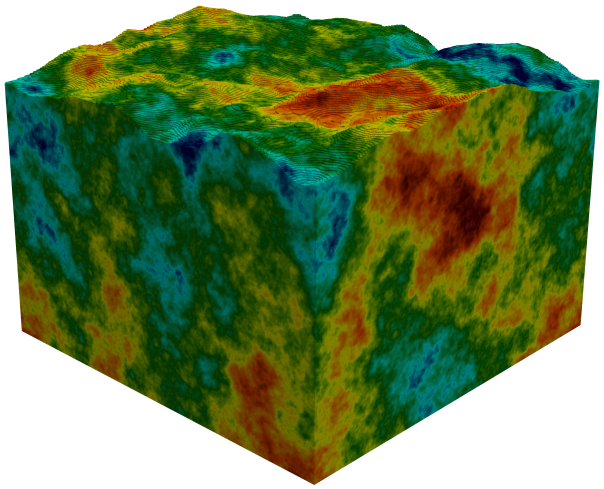

Figure 56: Stochastic distribution of an arbitrarily chosen property of the soil (e.g. water volumetric fraction, clay fraction, sand density and so on). The rough surface as well as the soil's property distribution is created using fractal correlating noise.

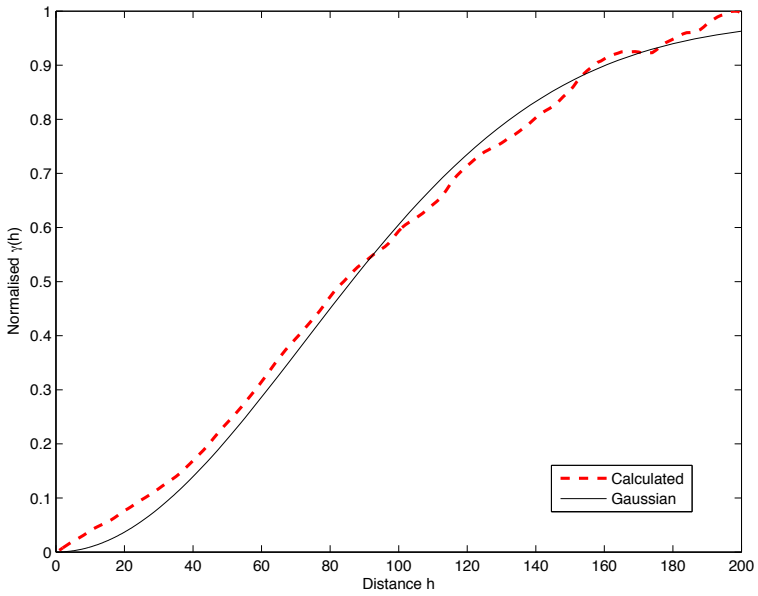

Figure 57: Calculated semivariogram (dots) and simulated Gaussian semivariogram (solid line) (6.14) of the arbitrarily chosen property of the soil shown in Fig. 56. The distance h is unit-less and represents the pixels in Fig. 56.

Where s is called sill and it is the value of the semivariogram when $h \to \infty$, r is called range and is the distance in which semivariogram starts to converge to the sill value, n_0 is the value of the semivariogram for $h = 0$ (nugget) and w is a constant which is equal with $1/3$.

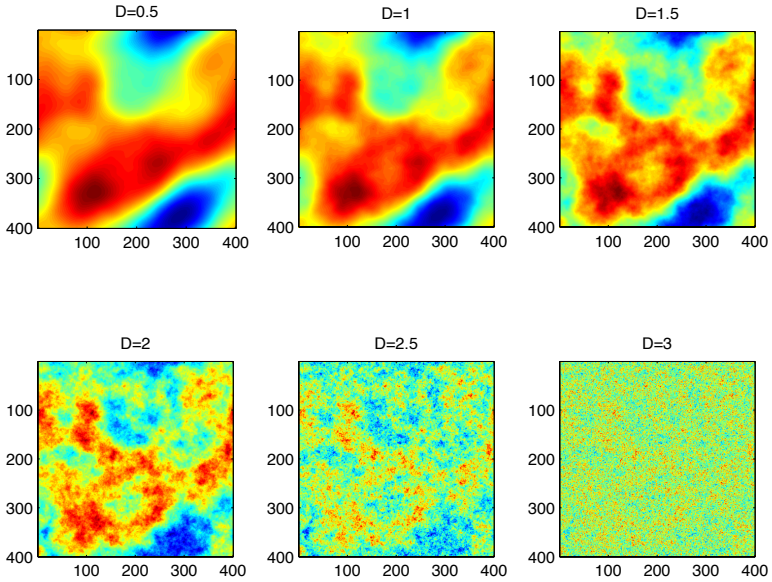

Figure 58: 2D fractals using different fractal dimensions D. For 2D fractals the fractal dimension equals with $D = 3.5 - \frac{\beta}{2}$ (Turcotte, 1992).

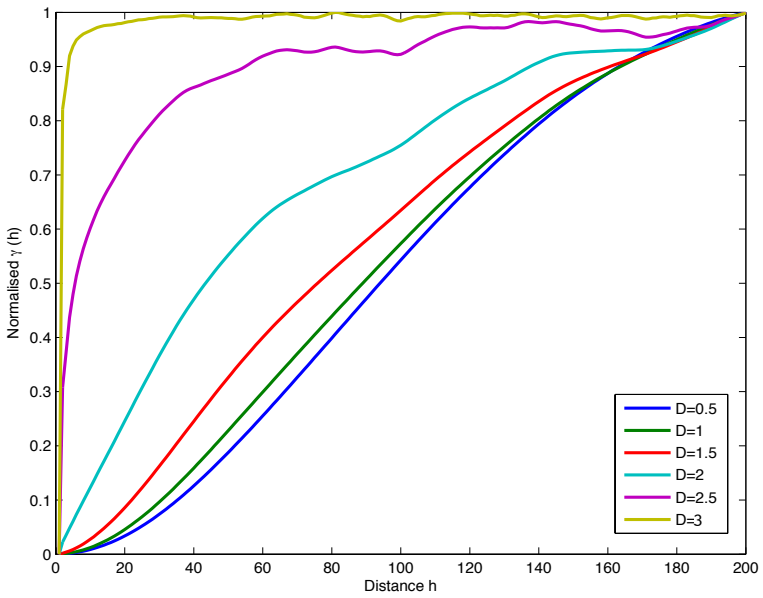

Figure 59: Calculated semivariograms for the fractals shown in Fig. 58.

Fig. 56 illustrates an example of a stochastic soil's property distribution (e.g. water volumetric fraction, clay fraction, sand density etc.) and rough surface created using fractal correlated noise. Fig. 57 shows the simulated Gaussian and the calculated semivariogram of the model shown in Fig. 56. A Gaussian semivariogram can simulate the calculated one with sufficiently accuracy which is an indicator of the reliability of the modelled soil. Changing the fractal dimension results to a different semivariogram. Fractals are capable

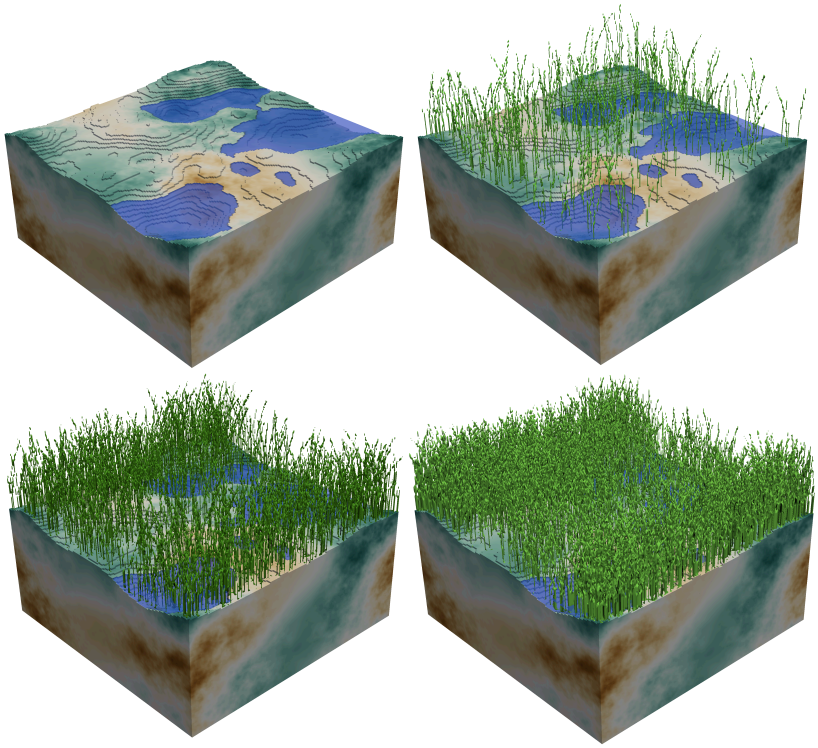

Figure 60: Modelled vegetation using the proposed method.

of simulating a wide range of Gaussian-like semivariograms, from un-corellated noise (flat semivariogram with $\gamma(h) \neq 0$ where $\gamma \in \mathbb{R}$) to homogenous media ($\gamma(h) = 0$ where $\gamma \in \mathbb{R}$). Fig. 58 illustrates 2D fractals using different fractal dimensions. Their resulting semivariograms are shown in Fig. 59.

6.3 VEGETATION MODELLING

AP landmines are shallow buried targets typically no more than 10 cm and their diameter is usually 10-20 cm. Therefore, in order for the AP landmines to be detectable, high frequency antennas are employed (0.5-3 GHz). The use of high frequency antennas leads to an increased sensitivity to small scale features such as grass and roots. In order to check the effects of vegetation to AP landmine detection using GPR, we propose an algorithm which models the geometry of vegetation using its statistical properties. The proposed algorithm works as follows:

- A 2D fractal is created and the summation of the fractal values is constrained to be equal to one. Each fractal value represents the probability of a blade of grass to exist in the corresponding coordinates of this value (x_c, y_c).

- For each blade of grass, a maximum height is picked based on a Gaussian distribution.
- The parametric equations of each blade of grass are (for $0 < t <$maximum height):

$$x = x_c + s_x \left(\frac{t}{b_x}\right)^2 \tag{6.15}$$

$$y = y_c + s_y \left(\frac{t}{b_y}\right)^2 \tag{6.16}$$

$$z = t \tag{6.17}$$

  where s_x and s_y can be 1 or -1 and they are randomly chosen. The constants b_x and b_y are random numbers based on a Gaussian distribution.
- For each blade of grass, a root is placed in the same coordinates (x_c, y_c) and a maximum depth for the root is picked based on a Gaussian distribution.
- The function which describes the geometry of the roots is a random walk in x and y coordinates as the depth increases linearly:

$$x_{i+1} = x_i + R_x \tag{6.18}$$

$$y_{i+1} = y_i + R_y \tag{6.19}$$

$$z_{i+1} = z_i - \Delta z \tag{6.20}$$

  where both R_x and R_y are random variables based on a Gaussian distribution and Δz is the depth discretisation step. The iterative procedure described in (6.18)-(6.20) continues until z reaches the value of the maximum depth of the root.

Fig. 60 illustrates the resulting (modelled) vegetation using the proposed method. Changing the statistical properties of the grass can result to a more sparse vegetation distribution, more synchronised blade orientation and so on.

Dielectric models of vegetation like leaves of corn (Ulaby and Jedlicka, 1984), stalks, trunks (El-Rayes and Ulaby, 1987, Ulaby and El-Rayes, 1987) alfalfa (Shrestha et al., 2007) and conifer trees (Franchois et al., 1998) have been

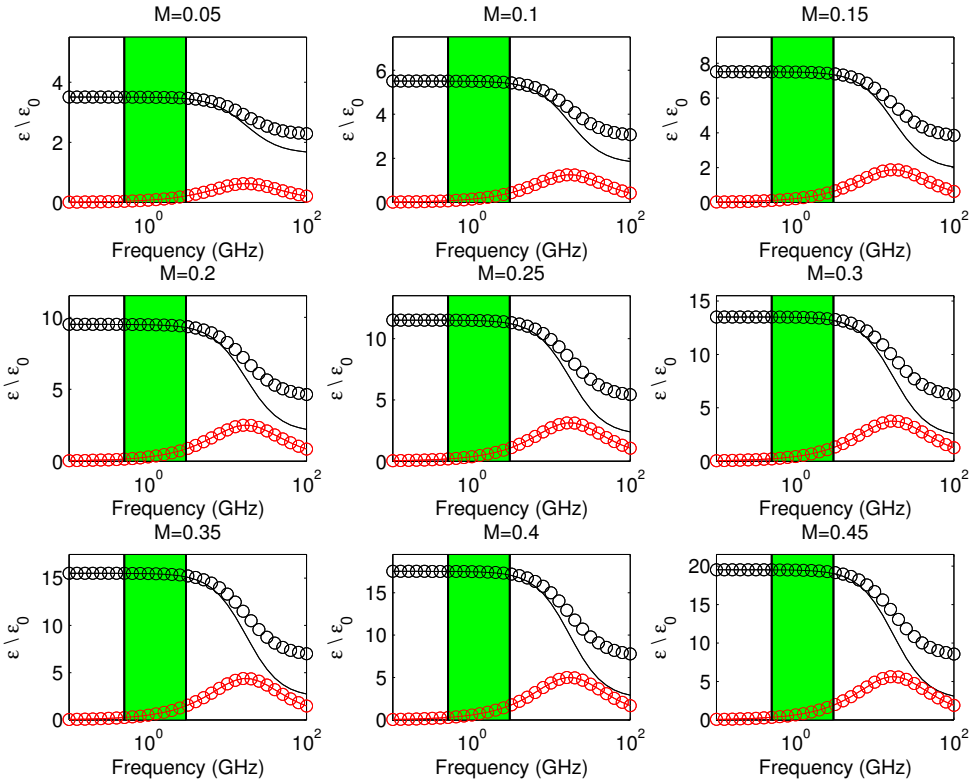

Figure 61: Electrical relative permittivity of grass and the Debye approximations for both real (black) and imaginary (red) parts for different water weight based fractions (M). The green area illustrates the frequency range employed in demining (0.5-3 GHz).

reported in the literature. In the present work the formula suggested by Carlson (1967) (Tan, 1981) is used to describe the dielectric properties of vegetation

$$\epsilon'_g - j\epsilon''_g = 1.5 + \left(\frac{\epsilon'_w}{2} - j\frac{\epsilon''_w}{3}\right) M, \tag{6.21}$$

where ϵ'_w is the real part of the electrical permittivity of the water, ϵ''_w is the imaginary part of water's permittivity, j is the imaginary unit ($j = \sqrt{-1}$) and M is the water content based on a weight basis (Tan, 1981).

This function relates the relative electrical permittivity of vegetation to the water weight based fraction and the dielectric properties of the water (6.21). The basic drawback of this model is that it is validated only for a single frequency (8.5 GHz). Extending the model to the frequency range of interest (0.5 - 3 GHz) results to an electrical permittivity which has a constant real part and an imaginary part which increases linearly with the frequency. This seems reasonable but as reported by Tan (1981) the extension of this model to other frequencies should be checked experimentally.

Similar to soil modelling, a PSO can be used to simulate equation (6.21) with a multi-Debye function (6.1). For the frequency range of interest (0.5-3 GHz), a single Debye pole can sufficiently approximate equation (6.21) for different water weight based fractions (M) as it is shown in Fig. 61. For the approximations in Fig. 61 a similar approach with the one followed for the soil's dielectric properties (6.2)-(6.11) is also employed here. By making the assumption that both the actual and the predicted dielectric properties have the same relaxation frequency and static electric permittivity results to a straightforward and efficient optimisation scheme. The optimised parameters for the Debye approximation are

$$t_{0,g} = t_{0,w} \tag{6.22}$$

$$\epsilon_{s,g} = 1.5 + \frac{M \cdot \epsilon_{s,w}}{2} \tag{6.23}$$

$$\epsilon_{\infty,g} = \epsilon_{s,g} + \frac{M \cdot (\epsilon_{s,w} - \epsilon_{\infty,w})}{3} \tag{6.24}$$

where $t_{0,g}$ is the relaxation time of grass, $t_{0,w}$ is the relaxation time of water, $\epsilon_{s,g}$ is the static permittivity of grass, $\epsilon_{s,w}$ is the static permittivity of water and $\epsilon_{\infty,g}$ and $\epsilon_{\infty,w}$ are the real permittivity of grass and water respectively.

6.4 ANTENNAS AND LANDMINES

A number of antenna units have been suggested to assist in demining and some of them have already been used in commercial systems. Table 1 shows a list of GPR systems suggested for demining. Both handheld and vehicle-based systems have been designed and successfully tested in real conditions. Modelling these types of antennas is particularly difficult due to confidentiality issues. For example, we know that the well known HSTAMIDS uses three antennas in a triangular arrangement (Tabony et al., 2010) but no specific information is available regarding the type of the antenna, impedance, absorbers and other important details that are needed in order to build a realistic numerical model of this transducer.

Apart from the systems outlined in Table 1, numerous antennas, designed to assist demining have been examined and analysed, namely, spiral antennas (Sato et al., 2005, Van Genderen et al., 2003), low dielectric conical horns (Teggatz et al., 2005), air-coupled wedge antennas (Savelyev et al., 2007), Vivaldi (Sato et al., 2003, 2005), horn-fed bowtie (Youn and Chen, 2005), dielectric rode antennas (Youn and Chen, 2005), vee dipoles (Nuzzo et al.,

Country	Program	Type	Maturity
Australia	HILDA	H	medium
	RRMNS	V	high
Belgium	HUDEM	H	low
Canada	ILDP	V	high
EU	GEODE	V	low
	LOTOS	V	low
	DEMINE	H	low
	MINEREC	H	low
	HOPE	H	low
	PICE	H	low
France	SALMANDER	V	medium
Germany	MMSR	V	medium
Israel	ELTA	V	high
Japan	MEXTSENCION	H	high
Sweden	PICE	H	medium
UK	MINETECT	H	high
	DCMC	H	medium
	MCMC	V	medium
USA	HSTAMIDS	H	high
	GSTAMIDS	V	low

Table 1: GPR systems for landmine detection. V and H stands for vehicle-based and handheld respectively (Tesfamariam, 2013).

2014), dielectric-filled TEM horn (Bart et al., 2000), ridged horn antennas (Panzner et al., 2010) and so on. In the same context, bowtie antennas have been also examined and successfully applied for landmine detection (Gonzalez-Huici et al., 2007, Gonzalez-Huici, 2012, Metwaly, 2007, Tesfamariam, 2013).

In the present thesis, two commercial based antennas are used to demonstrate the capabilities of the suggested numerical framework. Commercial antennas are particularly attractive for demonstration purposes, since they are easily available and well-known.

The GPR antennas used in the present thesis are bowtie antennas based on the geometrical characteristics of commercial GPR antennas, namely, the GSSI 1.5 GHz and the MALA 1.2 GHz (Warren and Giannopoulos, 2011, 2012) (see Fig. 62). Because of the central frequencies used, both of the antennas are suitable choices for demonstrating issues associated with GPR for AP landmine detection. The dielectric properties of the antennas as well as the input pulses and the impedances are chosen based on the Taguchi's optimisation which tries

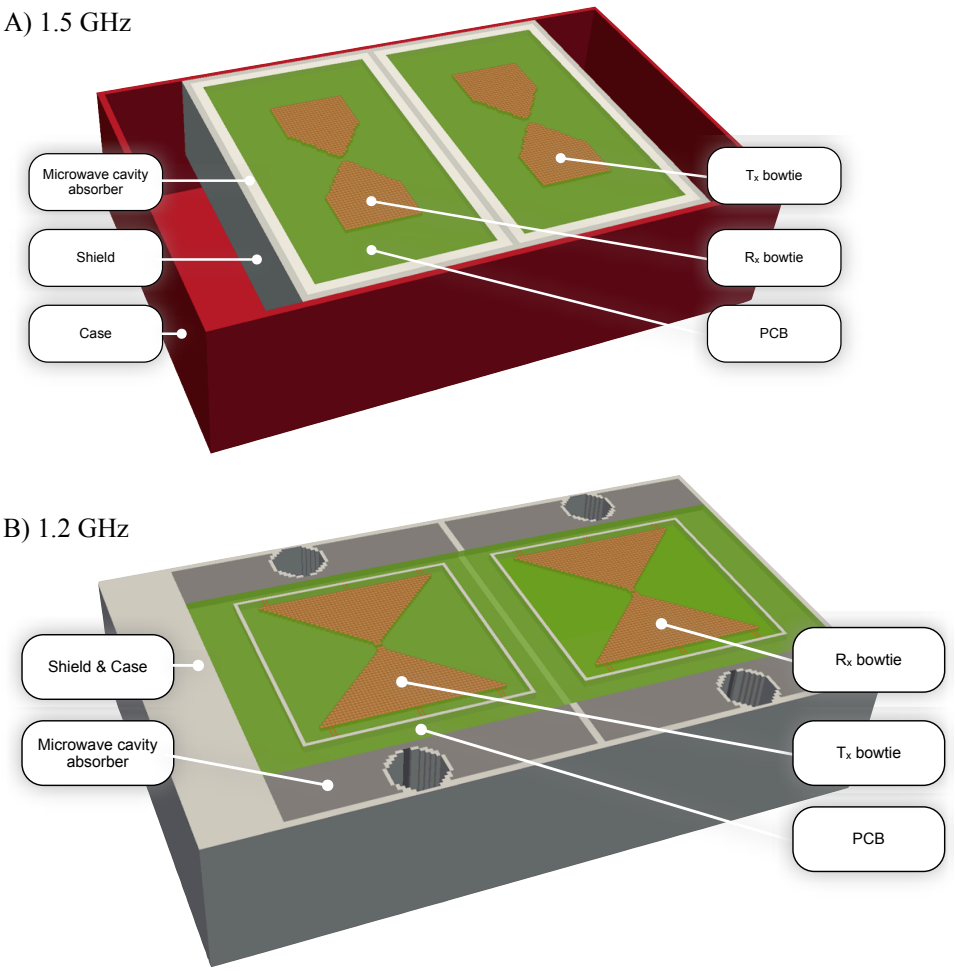

Figure 62: Modelled antennas, A) 1.5 GHz and B) 1.2 GHz (Warren and Giannopoulos, 2011).

to minimise the error between real and numerical measurements in free space (Warren, 2009, Warren and Giannopoulos, 2011, 2012).

The targets chosen for the simulations are the AP landmines PMA-1, PMN and TS-50. All of them are widely used and frequently found in minefields (Physicians for the Human Rights, 1993).

PMA-1 is a blast AP landmine with minimum metal content. It is manufactured in former Yugoslavia and was used in the Balkan area. Because of the metal fuse inside PMA-1, it is possible to be detected using metal detector, but there are also reported types of PMA-1 with plastic fuses. PMA-1 has 200 g of high explosive content (TNT) where the average is 50-100 g, therefore PMA-1 can destroy the whole foot or even the complete lower part of the victim's body. The dimensions of PMA-1 are, height: 30 mm, length: 140 mm, width: 65 mm. Fig. 63 shows the dummy AP landmine which was used to get the geometrical characteristics of PMA-1. Fig. 64 illustrates the modelled AP

Figure 63: Dummy landmines, A) PMN, B) PMA-1.

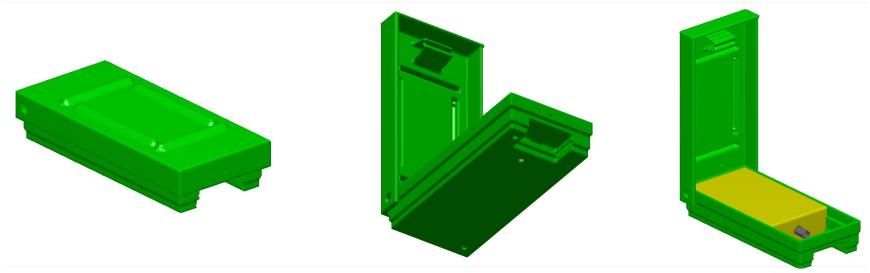

Figure 64: Modelled AP landmine PMA-1. Green is plastic ($\epsilon = 2.5$), grey is PEC and yellow is rubber ($\epsilon = 6$).

landmine. The discretisation step used for the model is $\Delta x = \Delta y = \Delta z = 1$ mm. Larger discretisation step can be applied in a straightforward manner with a simple interpolation.

PMN is one of the oldest landmines that are still in use (Physicians for the Human Rights, 1993). It is manufactured in Russia and it is one of the most widely employed landmines. Similarly to PMA-1, PMN has a large amount of high explosive (240 g TNT). Because of that, the majority of the victims are severely injured or killed. PMN is a palm shaped cylindrical blast AP landmine with minimum metal content. The dimensions of PMN are, height: 50 mm, diameter: 115 mm. Fig. 63 and 65 show the dummy and the modelled PMN, the discretisation step of the model is $\Delta x = \Delta y = \Delta z = 1$ mm.

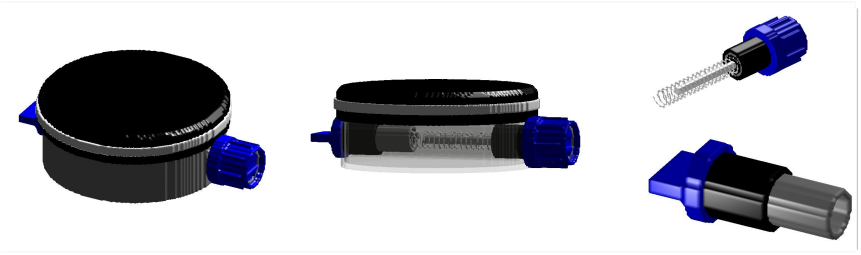

Figure 65: Modelled AP landmine PMN. The adapted side parts of the landmine are shown at the right of the image. The black top of the AP landmine is rubber ($\epsilon = 6$), the black pieces on the adapted parts is bakelite ($\epsilon = 3.5$), shiny grey is PEC, blue is plastic ($\epsilon = 3$), the grey parts of the landmine are also bakelite ($\epsilon = 3.5$) and the inside of the landmine is rubber ($\epsilon = 6$).

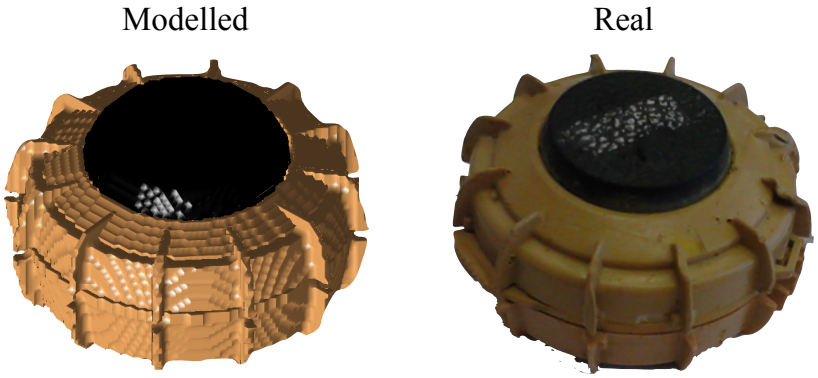

Figure 66: Modelled and real AP landmine TS-50. The black is plastic ($\epsilon = 5$), yellow is plastic ($\epsilon = 4$) and inside TNT is rubber ($\epsilon = 6$).

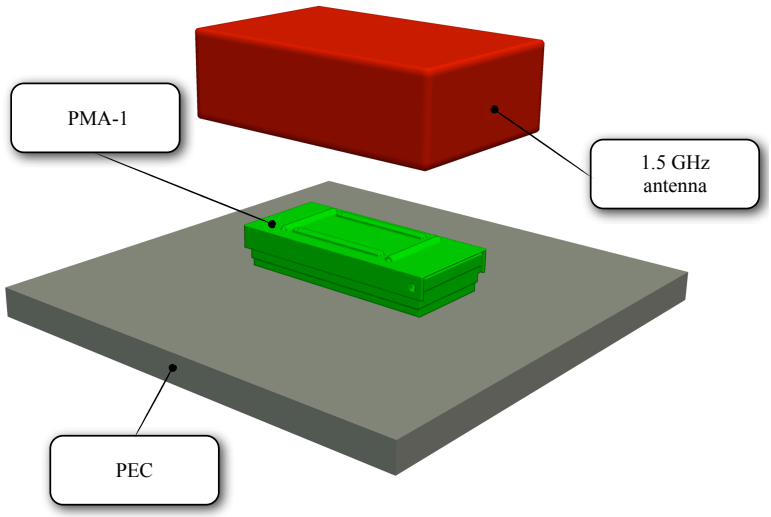

Figure 67: The 1.5 GHz antenna (red box) operates 10 cm above a PEC plate on which the PMA-1 is placed. The same experiment was also executed using PMN.

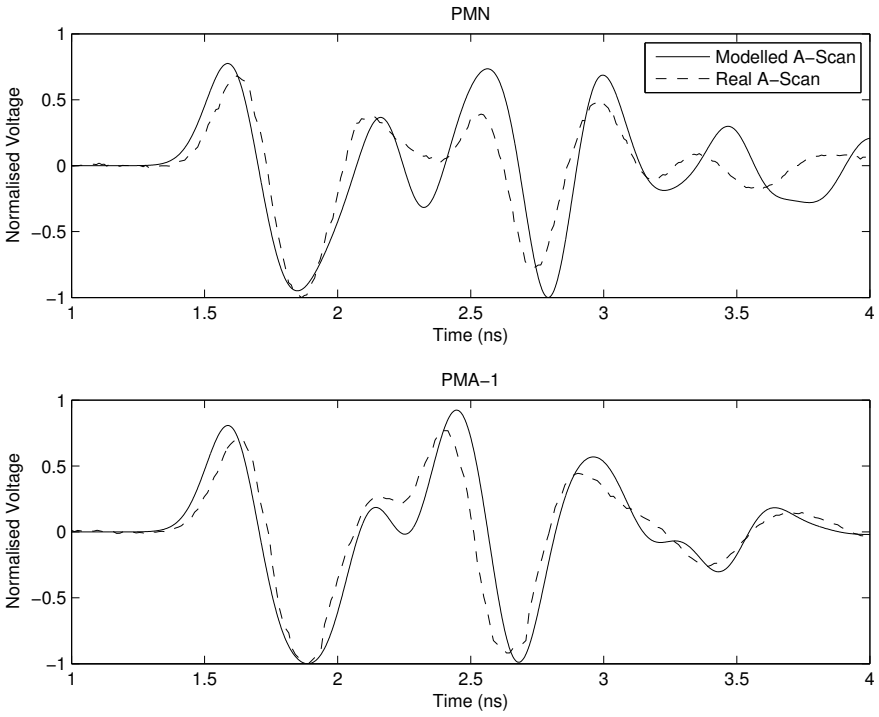

Figure 68: Numerical and measurent normalised A-Scans for the experiment described in Fig. 67 using both PMA-1 and PMN.

TS-50 is an italian manufactured AP landmine which has 50 g of TNT. Because of the low explosive content, TS-50 aims to injure the lower part of the legs. Its design allows TS-50 to operate also upside down. TS-50 has no metal content. Apart from the metal-free design of TS-50, another reason why it is hard to detect is its small size and the fact that no significant air gap exists inside the landmine. The dimensions of TS-50 are, diameter: 90 mm, height: 45 mm. Fig. 66 illustrates the modelled TS-50, the discretisation of the model is $\Delta x = \Delta y = \Delta z = 1$ mm.

The geometry of the AP landmines is expressed using polynomials and parametric equations, for more details see Appendix E. The dielectric properties of the modelled AP landmines are chosen such as the numerical and the real A-Scans of the experiment shown in Fig. 67 to be in good agreement. During the experiment both of the AP landmines are placed over a PEC plate and the antenna is placed at 10 cm height. The antenna unit chosen for the present experiment is the 1.5 GHz antenna. The reason for that is that higher frequency pulse contains more information about the detailed parts of the modelled AP landmines. Fig. 68 illustrates that the numerical and the measured normalised A-Scans are in good agreement which indicates that the AP landmines are realistically represented in the model.

6.5 SIMULATION RESULTS

For the simulations I used a customised version of gprMax (www.gprmax.com) (Giannopoulos, 2005), a free software which solves Maxwell's equations by using a second order (in both space and time) accuracy FDTD method (Yee, 1966). In all the models, the discretisation step is $\Delta x = \Delta y = \Delta z = 1$ mm and the time step is set to be equal to the Courant limit for the 3D FDTD scheme $\Delta t = 1.925$ ps (Taflove and Hagness, 2000). A small discretisation step increases the computational cost but is essential in order to represent the geometry of the model with adequate resolution. A small discretisation step is also needed in order to decrease the unnatural dispersion which occurs to small wavelengths due to numerical errors inherent to FDTD. Regarding the absorbing boundary conditions, a PML with 10 cells thickness is applied to all the simulations.

The computational requirements of the suggested scheme are related to the model's size, its dielectric properties and the maximum number of iterations. Dispersive soils have more computational requirements compared to non-dispersive media. In that context, a $1000 \times 400 \times 300$ model consisted entirely of dispersive media needs approximately 8 gigabyte of RAM. Using 6 processors and 12 gigabyte of RAM, the evaluation time for such a model is approximately 2 hours per trace (for 2500 iterations). The computational resources required for these kind of modelling problems are more than a conventional computer can offer if results are to be obtained in a reasonable time scale. To overcome this obstacle we have employed the Edinburgh Compute and Data Facility (ECDF), the cluster computer of The University of Edinburgh. A parallelised version of gprMax has allowed us to compute complete B-Scans in the same time that is needed for computing a single A-Scan on a single workstation.

6.5.1 *Vegetation*

In the present example, the effects of vegetation to the overall performance of GPR is examined. The model's dimensions are $1000 \times 250 \times 450$ mm, the surface is relatively smooth, the soil's properties are $\rho_s = 2.66$ g/cm^3, $\rho_b = 2$ g/cm^3, $C = 0.5$, $S = 0.5$ and the water volumetric fraction varies stochastically from $f_w = 0 - 0.25$. The height of grass varies from 20 to 130 mm and the roots from 20 to 200 mm. Three different scenarios are tested using both the antennas. In the first scenario, the water weight based fraction of the vegetation is equal to $M = 0.4$ (saturated grass and roots). In the second scenario, the water weight based fraction is $M = 0.1$ (dry grass and roots) and in the third scenario

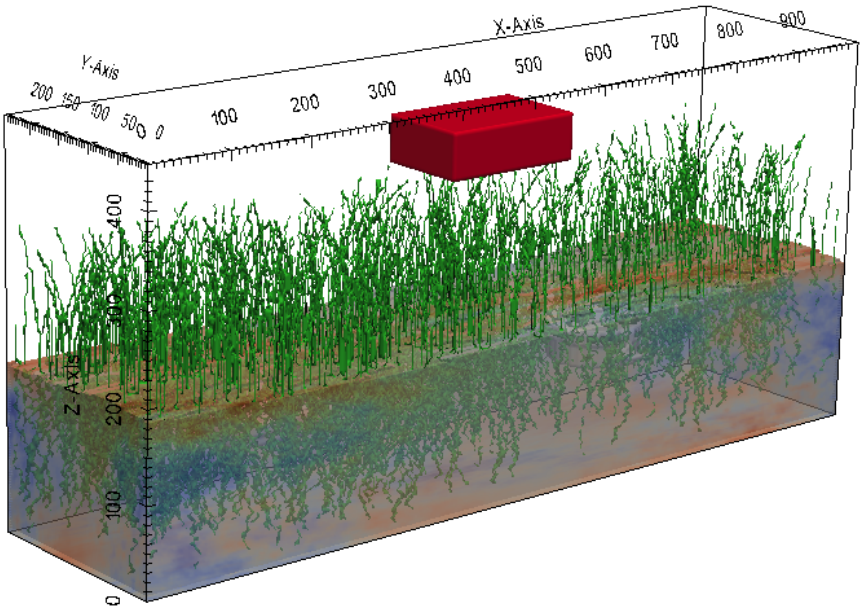

Figure 69: AP landmines PMN and PMA-1 buried in a complex soil with $f_w = 0 - 0.25$. Red colours depict the dry areas while with blue colours saturated areas are illustrated. The red box is the antenna unit. The axis are in mm.

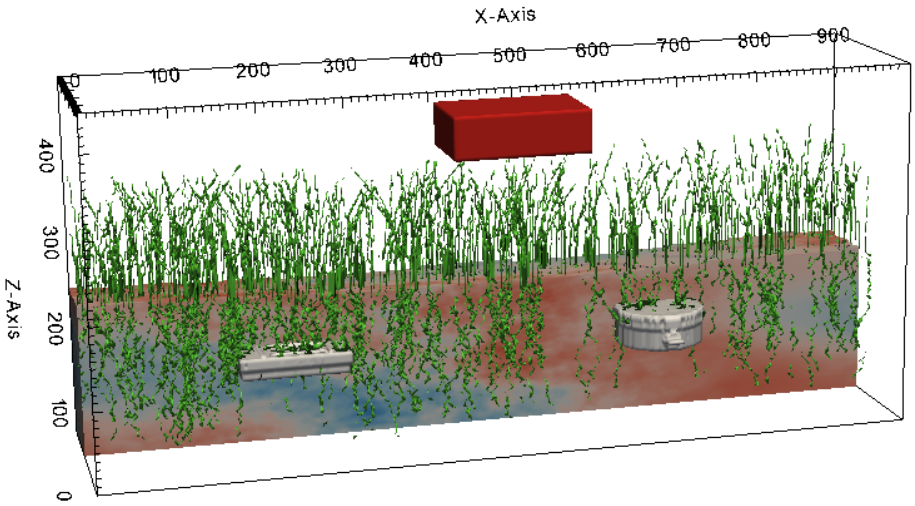

Figure 70: A slice parallel to the tomography line of the model shown in Fig. 69.

there is no vegetation. Fig. 69 and 70 illustrate the geometry of the model. The height of the antenna unit is approximately 160 mm above the ground and 20 mm above the grass. The depth of both landmines is approximately $50 - 70$ mm. The B-Scan is taken place along the x axis. The moving step of the antenna is 6 mm which results to a B-Scan consisted of 132 traces. Fig. 71 illustrates snapshots of different time steps using the 1.5 GHz antenna.

Fig. 72 shows the B-Scans and the normalised energy plots using the 1.5 GHz antenna. Only a quadratic gain is applied to the raw data. With and

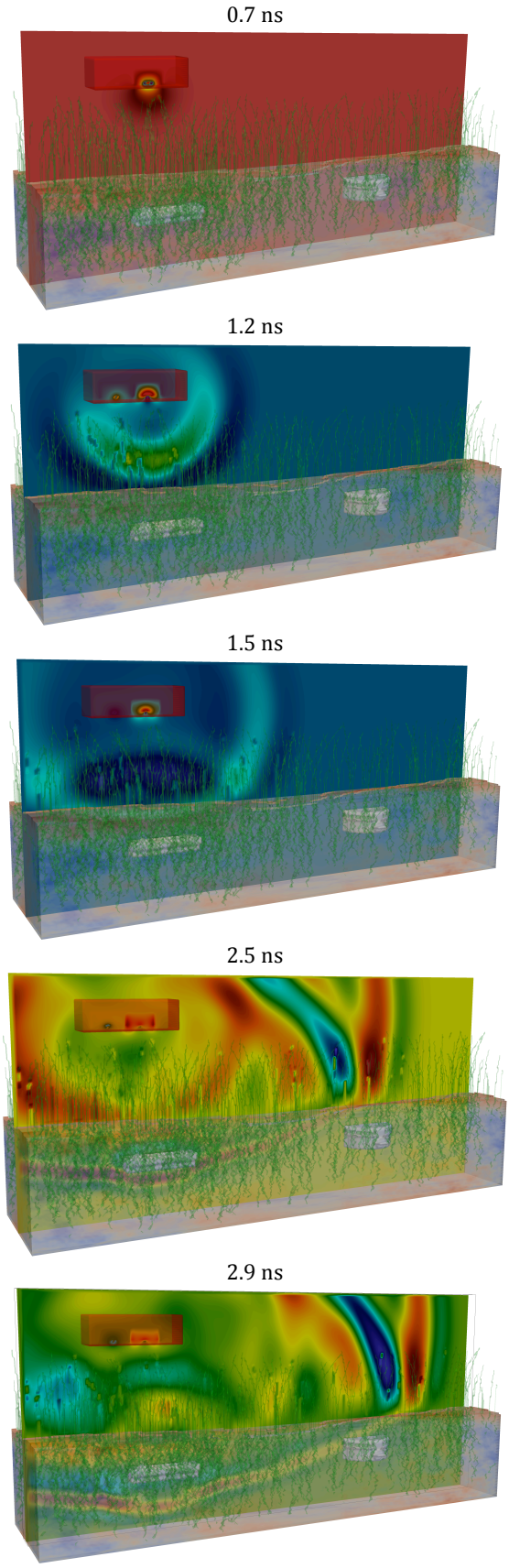

Figure 71: Snapshots of the model shown in Fig. 69 using the 1.5 GHz antenna. The fields in each snapshot are normalised so as the fields to be clearly visible. In the absence of normalisation the fields in the later snapshots would not be visible due to geometrical spreading of the energy and losses within the ground.

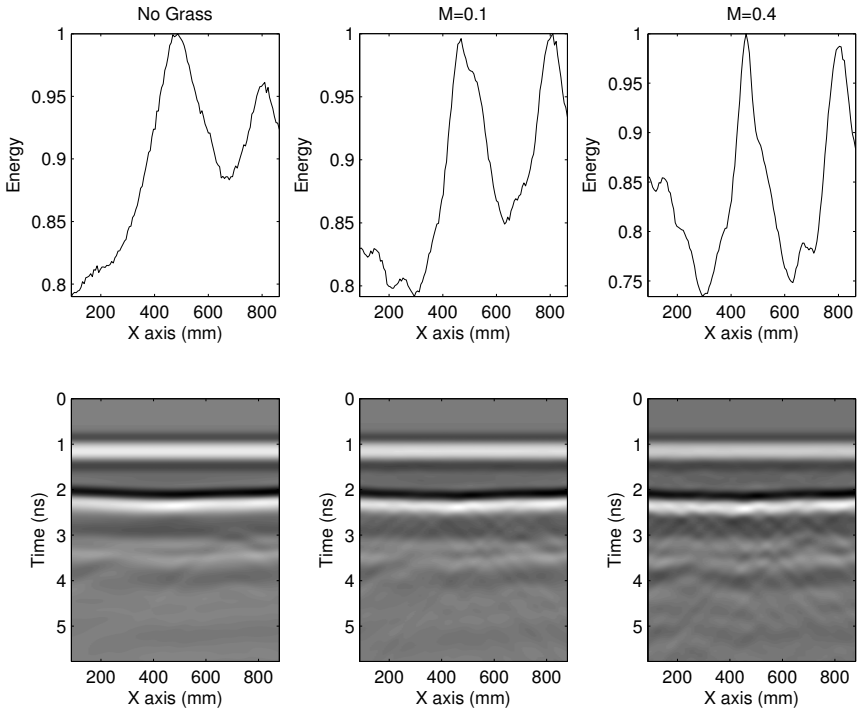

Figure 72: B-Scans and normalised energies of the model shown in Fig. 69 with and without vegetation. The vegetation's water weight based fraction equals $M = 0.1$ and $M = 0.4$. The 1.5 GHz antenna is used for the simulations. A quadratic gain is applied to the raw data. The X axis corresponds to the centre of the antenna unit in each trace.

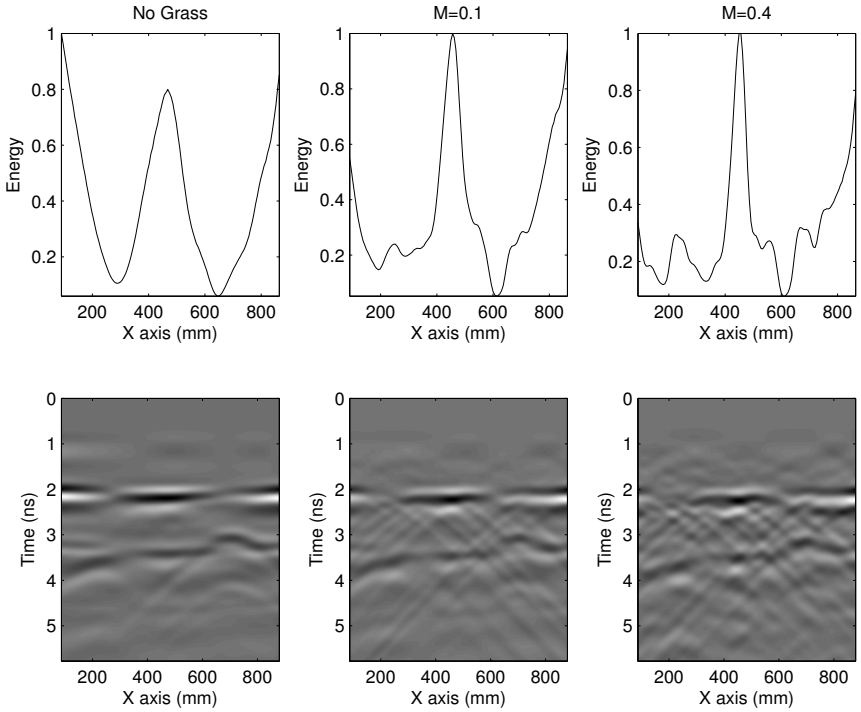

Figure 73: Similar with Fig. 72 using different processing scheme. A quadratic gain and average removal is applied to the raw data.

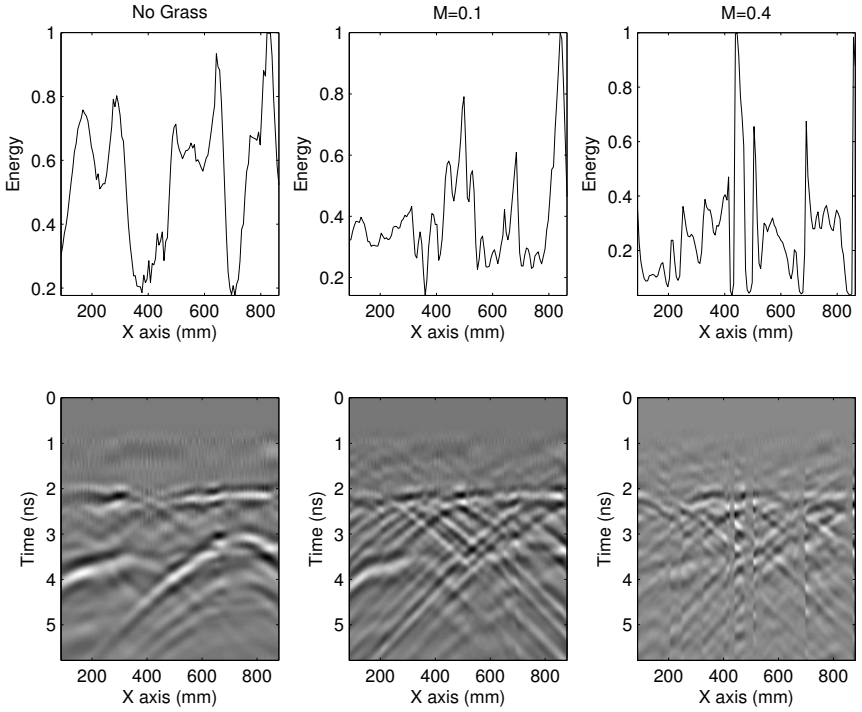

Figure 74: Similar with Fig. 72 using different processing scheme. A quadratic gain, an average removal and ASaS are applied to the raw data.

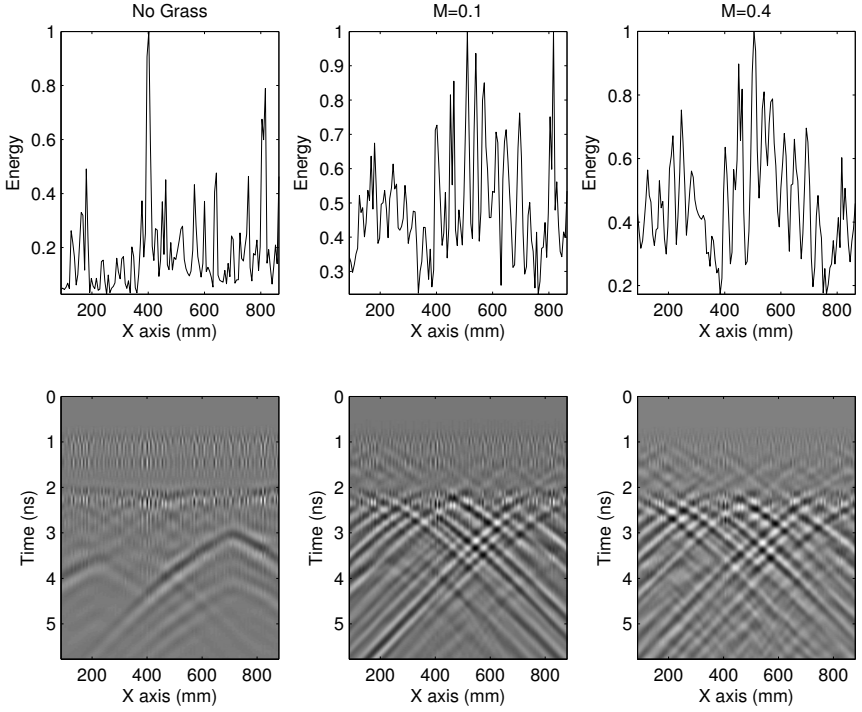

Figure 75: Similar with Fig. 72 using different processing scheme. A quadratic gain and a high frequency filter are applied to the illustrated B-Scans.

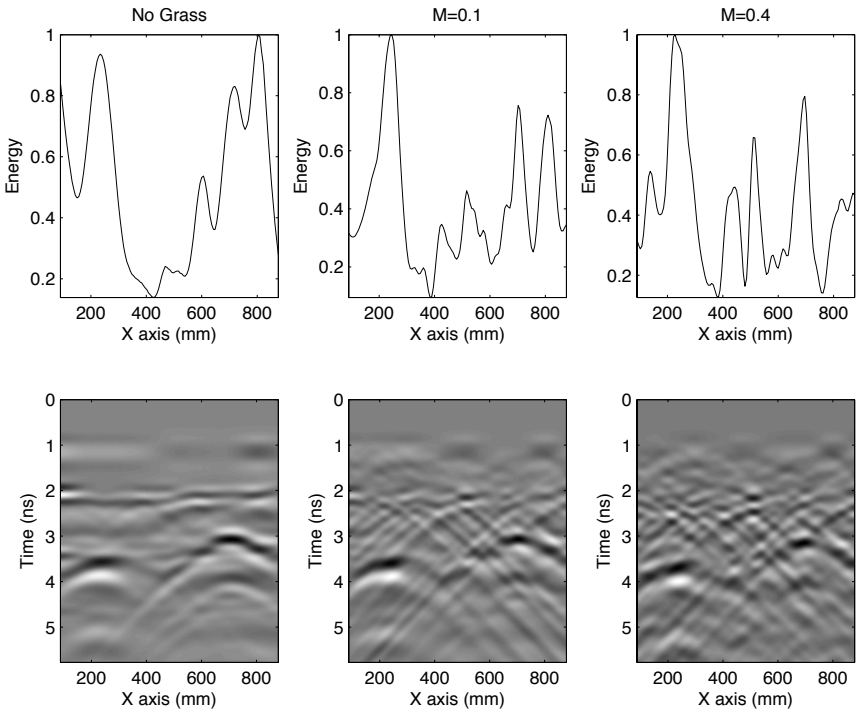

Figure 76: Similar with Fig. 72 using different processing scheme. A quadratic gain and subsequently an SVD (three dominant eigenvalues are filtered out) are applied to the illustrated B-Scans.

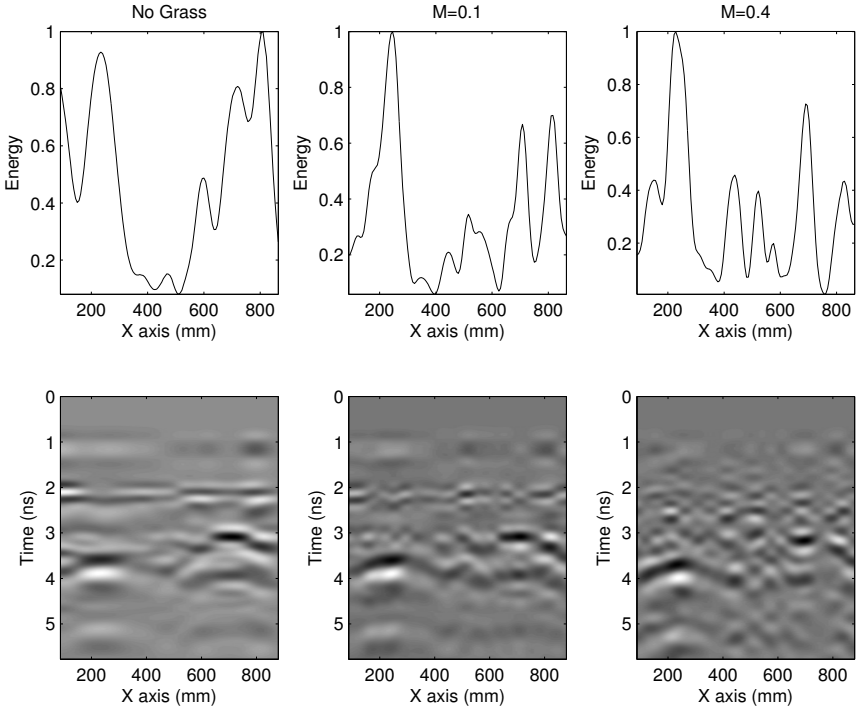

Figure 77: Similar with Fig. 72 using different processing scheme. A quadratic gain and subsequently an SVD (3-6 dominant values are plotted) are applied to the illustrated B-Scans.

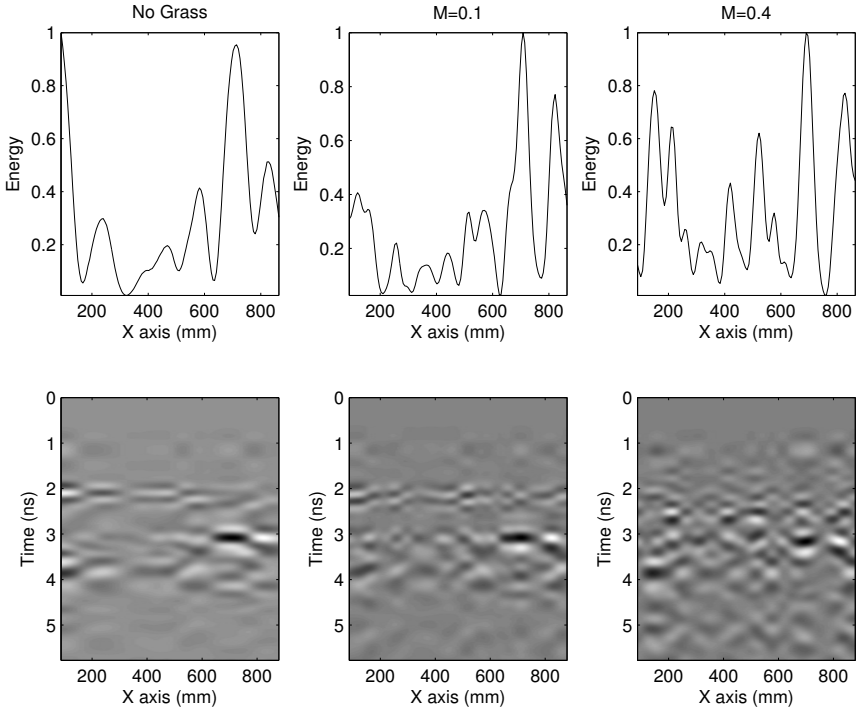

Figure 78: Similar with Fig. 72 using different processing scheme. A quadratic gain and subsequently an SVD (4-6 dominant values are plotted) are applied to the illustrated B-Scans.

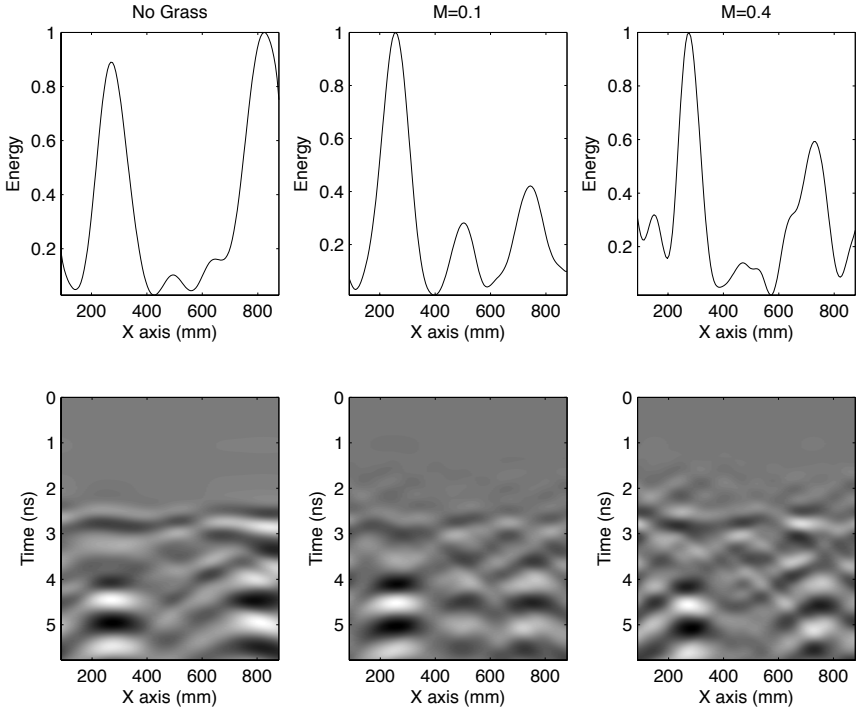

Figure 79: Similar to Fig. 76 using the 1.2 GHz antenna.

without vegetation both of the AP landmines are not reliably detected. When no vegetation is present, although high frequency clutter is absent, the fact that the antenna operates far from the ground makes the target's scattering fields "foggy" and weak. In Fig. 73 an average removal is applied to the data in an effort to remove the direct response and the ground reflection. Average removal does indeed make the image more readable by removing the direct response but, nonetheless, the AP landmines are depicted like a layer which is difficult to be interpreted as target (see Fig. 73 energy plots). In Fig. 74, an average removal is applied prior to ASaS in order to remove the smooth artefacts like the apparent layer discussed previously. The resulting B-Scans are readable in the absent of vegetation, but the performance of ASaS is not adequate when vegetation is present. Similar results are obtained when an F-K high frequency filter (see Fig. 75) is applied. The high frequency reflections from the blades of grass increase the Signal to Noise Ratio (SNR), thus decreases the performance of GPR.

Next, an SVD filter is applied to the data shown in Fig. 72. In Fig. 76, three dominant eigenvalues are filtered out in an effort to remove the high correlated trends of the B-Scan, which includes the direct response and the ground reflection. The performance of GPR for both with and without vegetation is adequately good although when the water weight based fraction of vegetation is high, the B-Scan becomes noisy which consequently results to a noisy energy plot. In Fig. 77 a by-pass SVD filter is applied, the 3-6 dominant eigenvalues are plotted in an effort to remove main trends and low correlated features like the reflections from the vegetation. Both AP landmines are clearly detectable even when saturated vegetation is present. SVD filtering must be used with cautious since a wrong range of eigenvalues may result to the elimination of the target's signature as it is illustrated in Fig. 78. In the present case, an SVD filter which keeps the 4-6 dominant eigenvalues results to the elimination of the PMA-1 signature even when vegetation is absent.

Using a lower frequency antenna results to the decrease of the vegetation's scattering field. Nonetheless, a low frequency pulse cannot resolve the AP landmines, which are relatively small targets. A balance between decreasing the unwanted reflections and increasing the targets response must be found for an effective performance. Using the 1.2 GHz antenna model produces equally unreliable results using, average removal, high frequency filter and ASaS. Filtering the 3 dominant eigenvalues (see Fig. 79) makes both AP landmines detectable with and without vegetation. Applying a by-pass SVD by keeping 3-6 dominant eigenvalues – similar to the procedure employed using the 1.5 GHz antenna – does not have major effects on the performance of GPR since

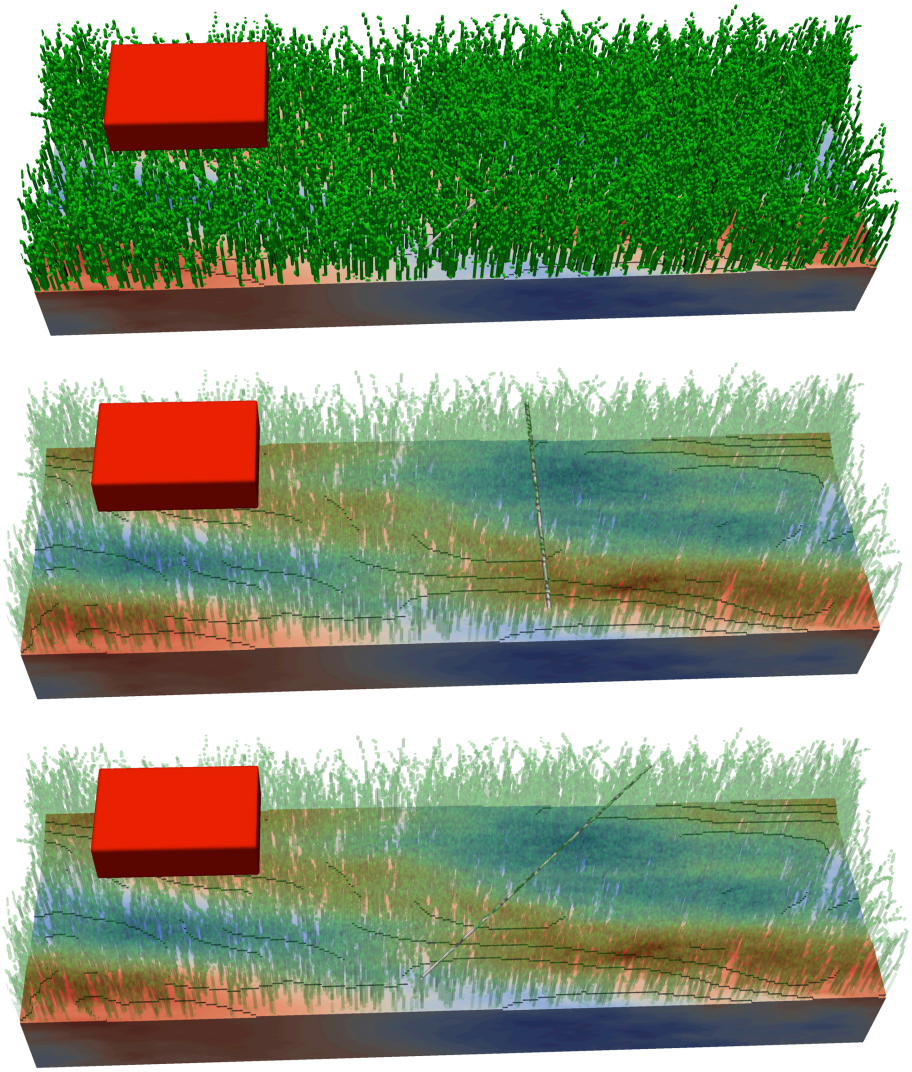

Figure 80: PEC cylinders with 3 mm diameter used to simulate hidden tripwires. Two cases are examined with different tripwire orientation with respect to the antenna polarisation.

high frequency features are absent due to the lower central frequency of the antenna.

The present case study shows that the simulated vegetation is not a negligible feature and it can affect the performance of GPR for the frequency range used for landmine detection (0.5-3 GHz). Nonetheless, Fig. 76, 77 and 79 illustrate that GPR has the potential to be effective in grassy environments in which vegetation removal is not trivial due to tripwires which may be present (Cameron et al., 1998). From Fig. 76 and 77 is evident that increasing the water based fraction of the vegetation results in an increase of the background noise. When the vegetation is completely dry, from (6.21) yields, that the real part of the relative permittivity of vegetation equals to $\epsilon_g = 1.5$. This makes the grass practically

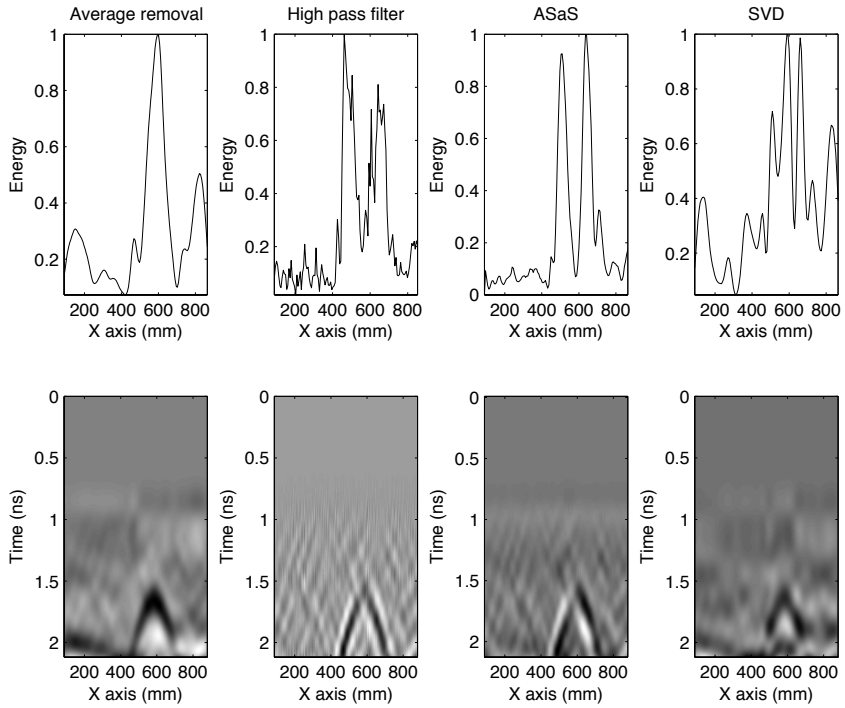

Figure 81: Resulting B-Scans from the model illustrated in Fig. 80. The tripwire is placed vertical to the antenna position. A quadratic gain and subsequently ground removal techniques are applied to the raw data.

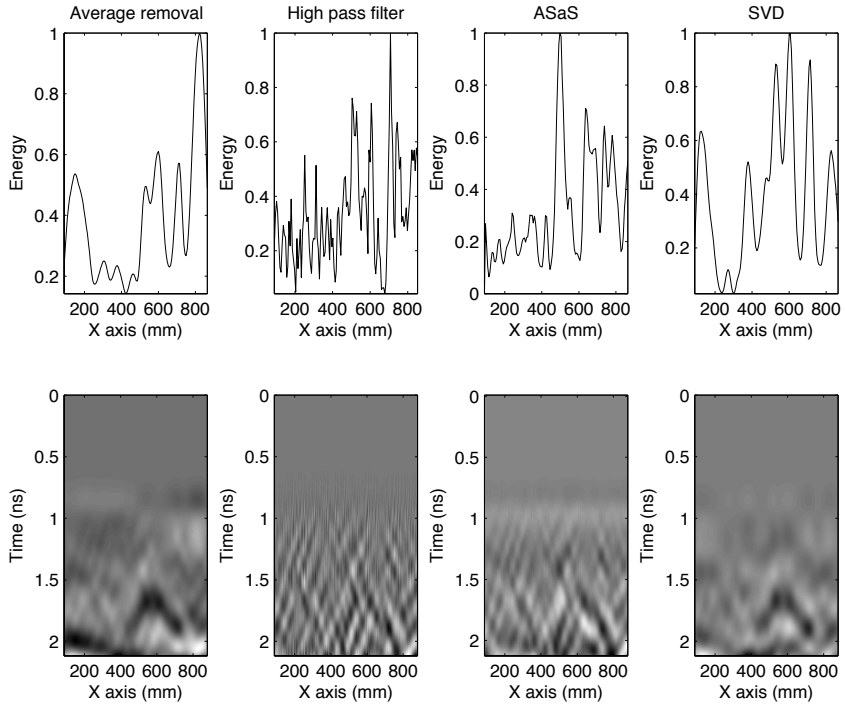

Figure 82: Similar with Fig. 81 with the tripwire being oriented 45^o with respect to the antenna position.

invisible to GPR assuming that roots with a zero water based fraction is the result of dry soil which will have relative electrical permittivity close to $\epsilon' = 2.5$.

Although SVD seems promising and clearly outperforms average removal, ASaS and F-K filter (see Fig .77), that is not always the case as it will be shown in the following section. This raises the issue of the limitations of processing algorithms and their applicability in diverse scenarios. Accurate numerical modelling can assist on mapping the limitations of a suggested antenna-processing couple and evaluating its performance in a wide range of synthetic, but nonetheless realistic data.

6.5.2 *Tripwires hidden in vegetation*

As mentioned earlier, hidden tripwires make vegetation-removal time-consuming and risky (Cameron et al., 1998). In the next example the effectiveness of GPR for detecting tripwires is examined. Fig. 80 illustrates the present model. The dimensions are $1000 \times 350 \times 400$, the water weight based fraction equals $M = 0.4$. The soil's properties are $\rho_s = 2.66$ g/cm^3, $\rho_b = 2$ g/cm^3, $C = 0.5$, $S = 0.5$ and the water volumetric fraction varies stochastically from $f_w = 0.2 - 0.3$ (saturated soil). The 1.5 GHz antenna is employed in the present example. The tripwires are modelled as PEC cylinders with 3 mm diameter.

Assuming plane wave solutions in the far field, Radzevicius and Daniels (2000) concluded that small diameter, with respect to the wavelength, PEC cylinders give larger scattering fields when the polarisation of the antenna is parallel to the main axis of the cylinder. Their predictions are backed up by experimental evidences (Radzevicius and Daniels, 2000). In the present example the results are as they were expected to be. The tripwire which is placed vertical to the antenna polarisation has larger scattering field which can be isolated from the background using average removal, high pass filter, ASaS and SVD (3-6 eigenvalues) (see Fig. 81). When the tripwire is at 45^o angle with respect to the polarisation of the antenna, the resulting scattering field is weak and cannot be reliably detected using high pass filter and ASaS (see Fig. 82). From the above it is evident that GPR has the potential to be used for tripwire detection taking into account the polarisation aspects of the problem.

6.5.3 *Soil's inhomogeneity*

In the previous example a case was made about how vegetation can affect and decrease the performance of GPR. Apart from vegetation, more often encounter features like soil's inhomogeneity can also result to false alarm targets and mask

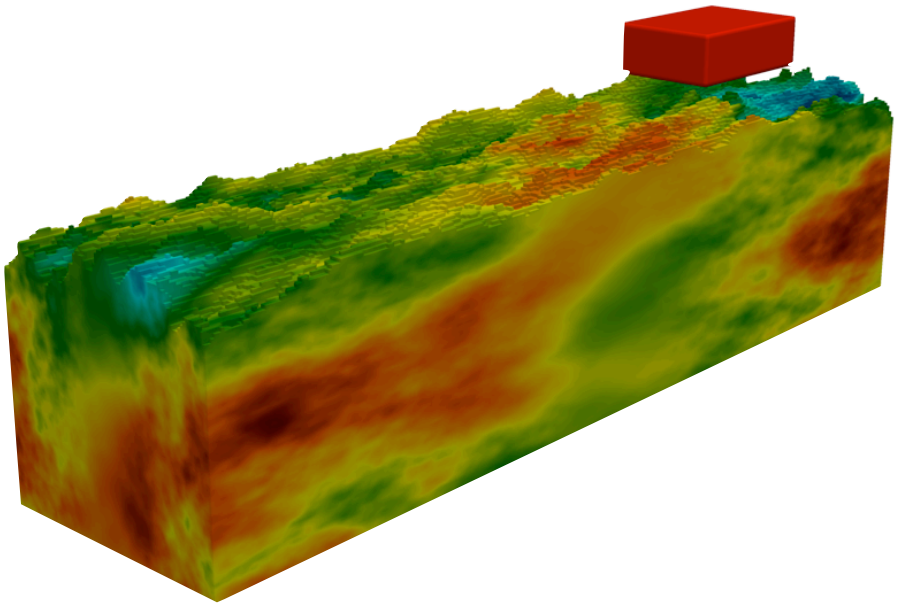

Figure 83: A complex medium with $\rho_s = 2.66$ g/cm^3, $\rho_b = 1.5$ g/cm^3, $C = 0.5$, $S = 0.5$ and water volumetric fraction which varies stochastically from $f_w = 0 - 0.25$. Three AP landmines (PMN, PMA-1 and TS-50) are placed in the centre of the model (see Fig. 84). The 1.5 GHz antenna is used for the simulations.

the landmine's scattering field (Giannakis et al., 2016). Most of the numerical modelling done so far (Gurel and Oguz, 2000, 2001, 2003, Oguz and Gurel, 2002) as well as real field experiments (Schofield et al., 2014) are taken place in simplified/clinical models. This overestimates the performance of GPR and gives a false impression of its abilities and limitations.

The dimensions of the models in this section are $1000 \times 250 \times 350$. The rough surface as well as soil's inhomogeneity modelled using fractal correlated noise. The properties of the soil are $\rho_s = 2.66$ g/cm^3, $\rho_b = 1.5$ g/cm^3, $C = 0.5$, $S = 0.5$ and the water volumetric fraction varies from $f_w = 0 - 0.25$. The antenna used is the 1.5 GHz and it is placed relatively close to the ground. In the first example, the three AP landmines (PMN, PMA-1 and TS-50) are placed in shallow depth in the centre of the model (see Fig. 83, 84). Raw modelled data with an additional quadratic gain (Fig. 85) clearly map the position of the AP landmines although the reflections from the inhomogeneity at 800 mm makes the energy based detection less reliable. Applying an average removal, decreases the energy from the false alarm (see Fig. 86). By further eliminating high correlated features using an SVD (3 dominant eigenvalues are filtered out) does not further improve the detection, on the contrary it decreases the scattering signature of the TS-50 (see Fig. 87). ASaS produces slightly better results (see Fig. 88) compared to average removal but the most

effective processing for the present case, as it is illustrated in Fig. 89, is the F-K high pass filter which seems to effectively decrease the energy from the false alarm target while preserving the landmine's signature.

Soil inhomogeneities can potentially mask the landmine's signature making the B-Scan difficult to interpret. Fig. 90 illustrate a similar model with the ones described previously. The AP landmine PMA-1 is buried in shallow depth in the centre of the model. Soil's inhomogeneities which occur in the model result to noisy and "foggy" B-Scans as it is illustrated in Fig. 91. F-K filter, SVD and ASaS failed to clear the image and enchase the target's signature.

Fig. 92 shows the last model which will be examined in this section. As it is illustrated in Fig. 92 no landmine is buried in order to get an insight on the nature of the false alarms which can occur due to the soil's inhomogeneity. The 1.5 GHz antenna model is used for the simulations. The resulting B-Scans using SVD, high pass filter and ASaS are shown in Fig. 93. A clear response is visible in the middle of the scan which is the result of the high humidity cluster shown in Fig. 92. First of all, it is clear – from the present but also from the previous examples – that not all inhomogeneities result to false alarms. The gradual change from a dry area to a saturated one results to losses and changes in the directivity patterns of the antenna but not clear reflections can occur from these kind of interfaces. Sudden changes in the permittivity and large size clusters can affect the reflection coefficients of the inhomogeneities. In the present example sudden changes which occur relatively near the surface results to a scattering field which might give the impression of an AP landmine.

One main feature of the scattering fields from the AP landmines is the long tail which follows the main response. This is due to the sharp deterministic boundaries of the landmines which result to reverberating reflections inside the landmine and between the surface and the top of the landmine. This long tail can be enhanced using a quadratic gain and that is the main reason why it is used and suggested in the present thesis. Scattering fields from soil's inhomogeneities do not follow this pattern as it is shown in Fig. 93.

Although long tail reflections from landmines can frequently encountered, there are cases in which long tail reflections are absent. Absence of reverberating reflections from landmine's scattering fields can happen due to various reasons, the most important of which are

- Large depth of the landmine, which decreases the reverberating reflection from the landmine-surface.
- Almost exposed landmine, which makes difficult for the pulse to resolve the gap between the surface and the landmine.

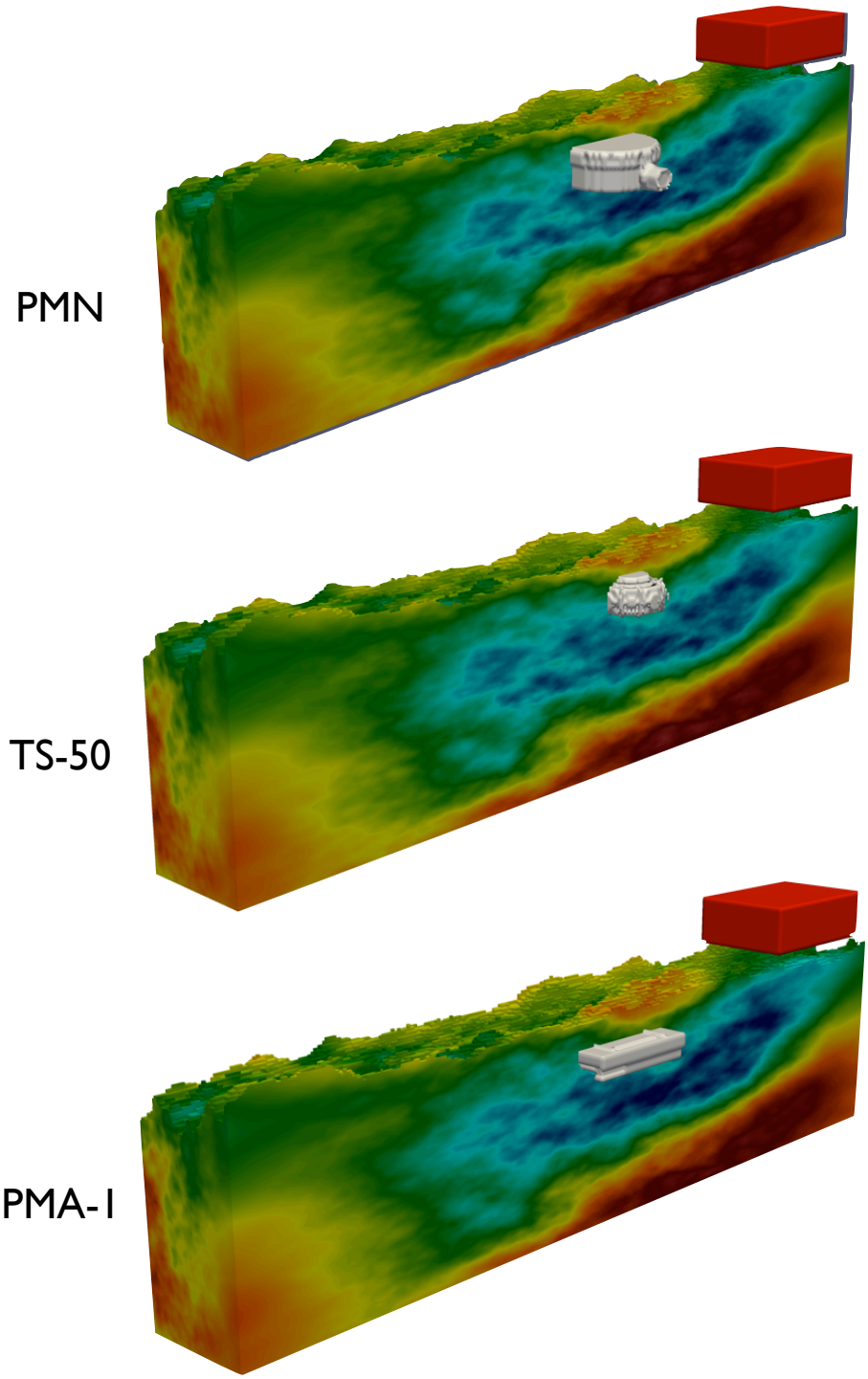

Figure 84: A slice of the model shown in Fig. 83. Three different scenarios are examined in which the three AP landmines PMN, PMA-1 and TS-50 are placed in shallow depth in the centre of the scan.

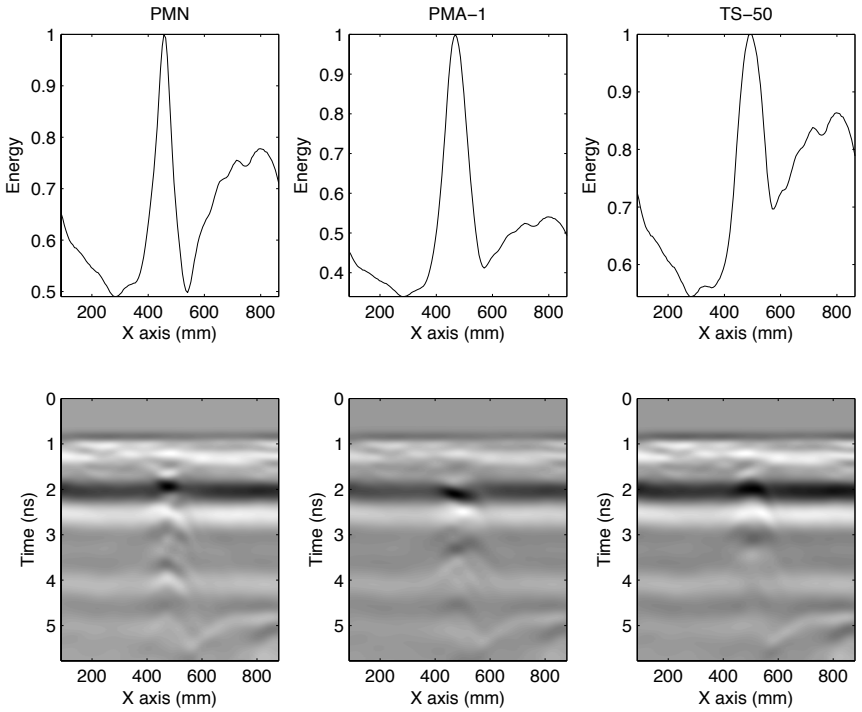

Figure 85: B-Scans of the models shown in Fig. 84. Only a quadratic gain is applied to the raw data.

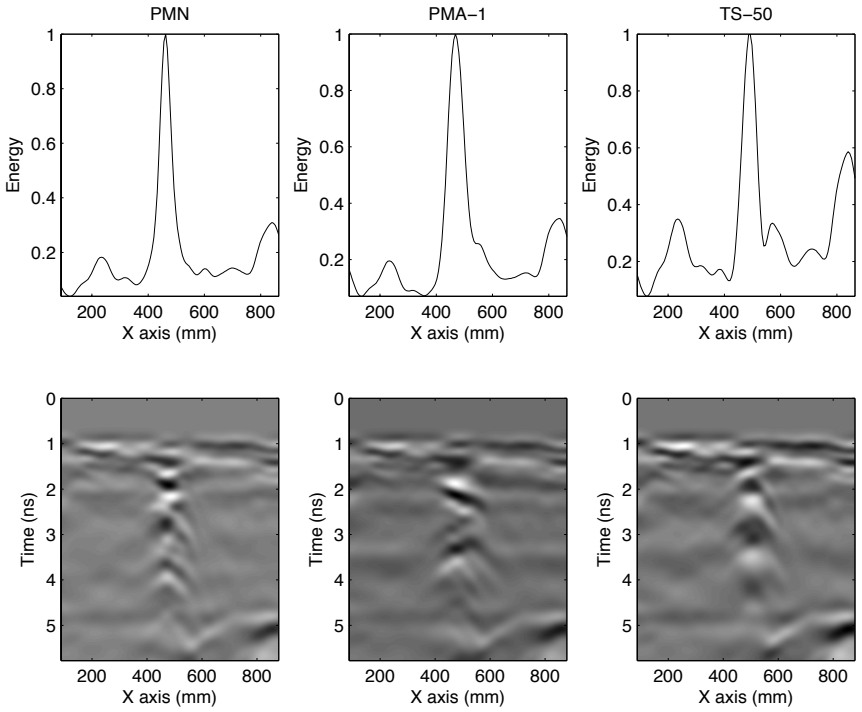

Figure 86: Similar with Fig. 85 using the average removal method.

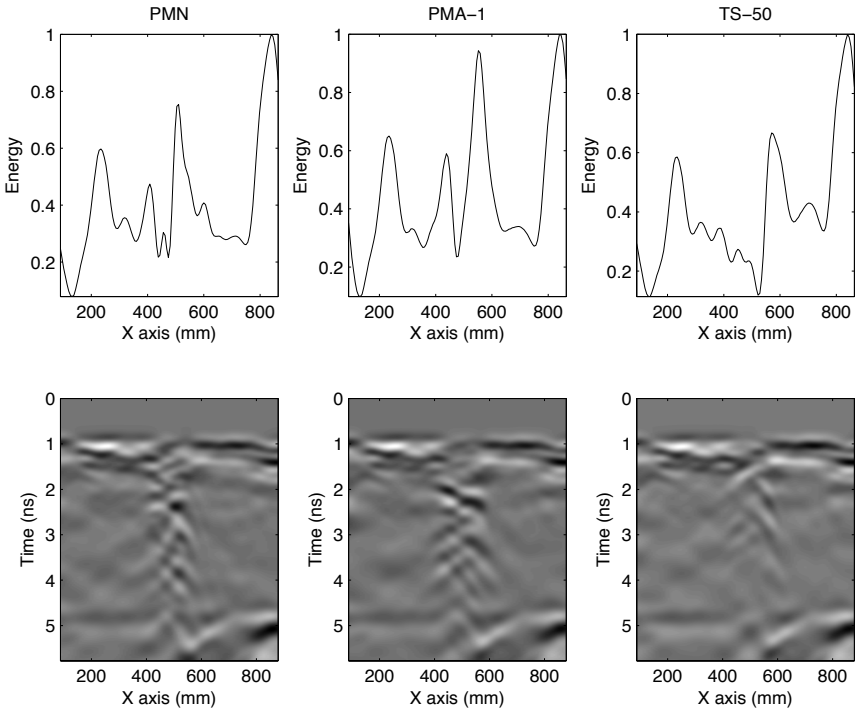

Figure 87: Similar with Fig. 85 using an SVD filter (3 dominant eigenvalues are filtered out).

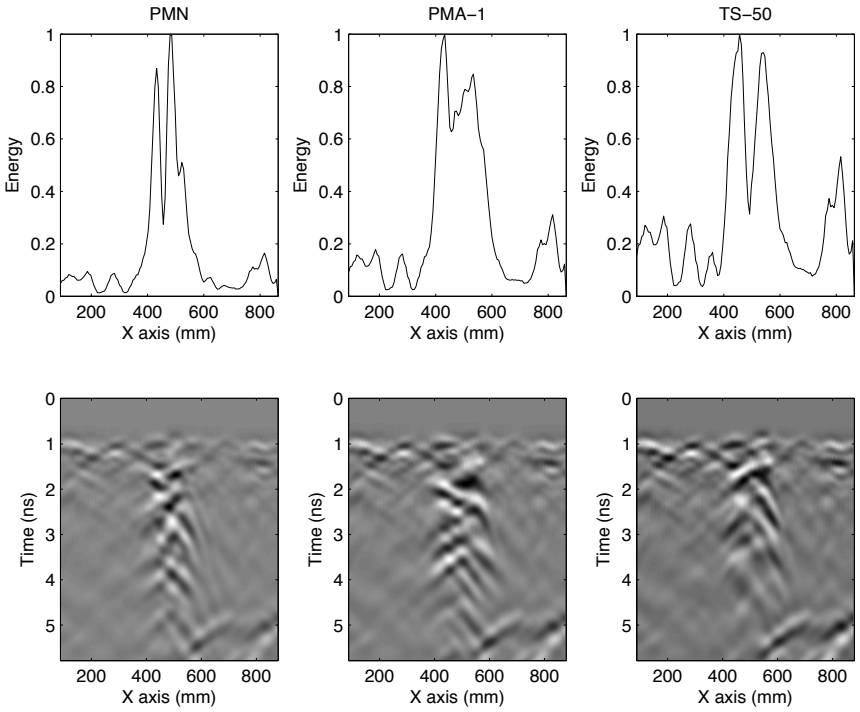

Figure 88: Similar with Fig. 85 using an ASaS filter.

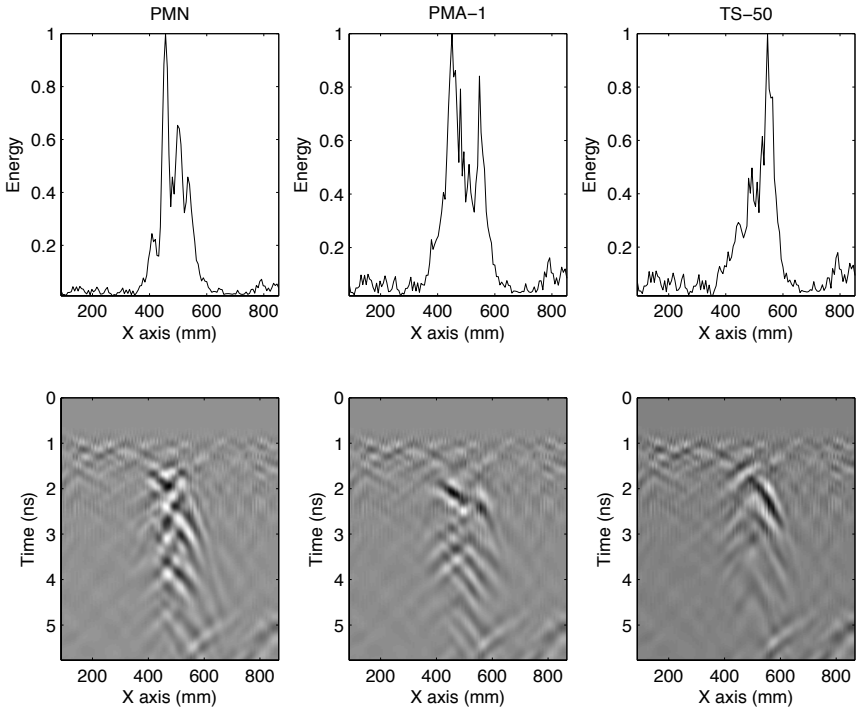

Figure 89: Similar with Fig. 85 using a high pass filter.

- Low velocity media, which results to small wavelengths which cannot clearly resolve the sharp boundaries of the targets.

The present section illustrates how soil's inhomogeneity can affect the performance of GPR. Regarding the processing methods, a high pass filter seems to surpass the performance of average removal, SVD and ASaS. It is interesting to note that the performance of F-K filter was rated last in the previous section. This furthers supports the premise that processing methods are case sensitive and their performance should be evaluated in a wide range of diverse scenarios. In addition, as it is clearly illustrated in Fig. 89, different targets result to different scattering fields. A numerical scheme which aims to provide training sets for machine learning should be able to predict the signatures of specific landmines and not generic simplified geometrical objects.

6.5.4 *Water puddles*

AP landmines can be found in a variety of environments like deserts, urban environments, jungles and so on (Daniels, 2006). Humid environments with saturated soils and water puddles is a common case in which AP landmines can be found e.g. Bosnia, Cambodia etc. (Daniels, 2006). In this section the effects of water puddles to the overall performance of GPR are going to be examined.

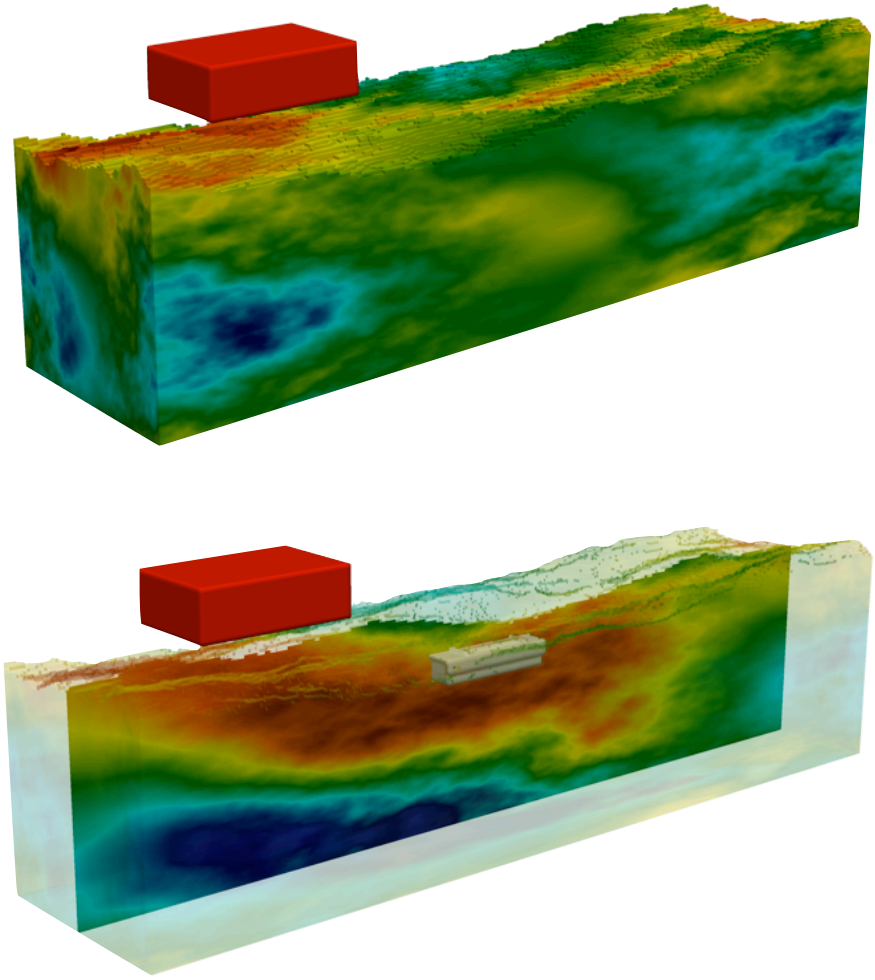

Figure 90: Buried AP landmine PMA-1 in a stochastically varied soil. The properties of the soil are $\rho_s = 2.66$ g/cm^3, $\rho_b = 1.5$ g/cm^3, $C = 0.5$, $S = 0.5$ and water volumetric fraction which varies from $f_w = 0 - 0.25$. The antenna unit used is the 1.5 GHz.

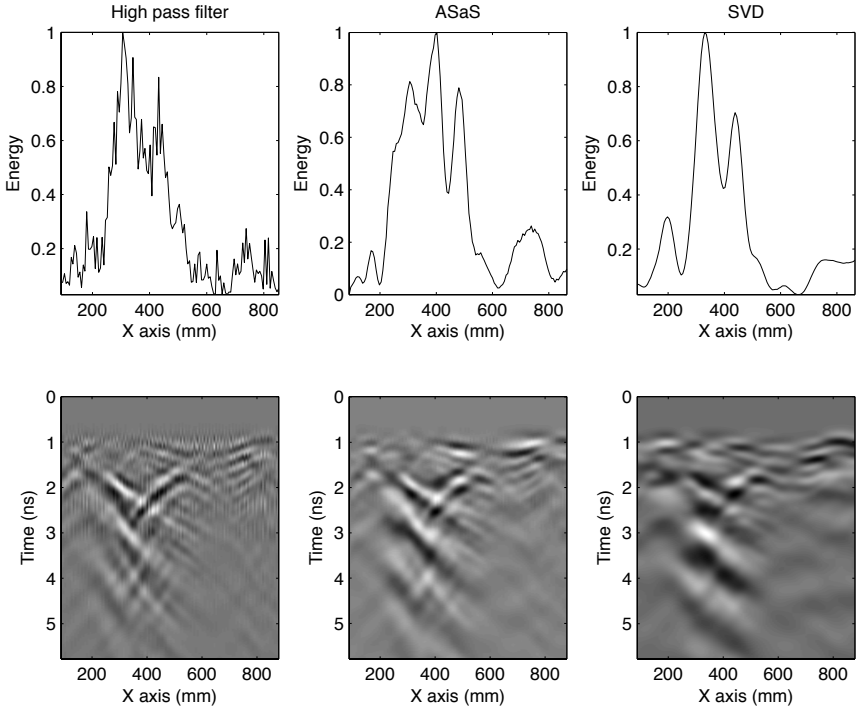

Figure 91: B-Scan using the 1.5 GHz antenna of the model shown in Fig. 90. A high pass filter, ASaS and an SVD (3 dominant eigenvalues are filtered out) are applied (apart from the quadratic gain). In all three cases the scattering signature of PMA-1 is masked from the response of the soil's inhomogeneities.

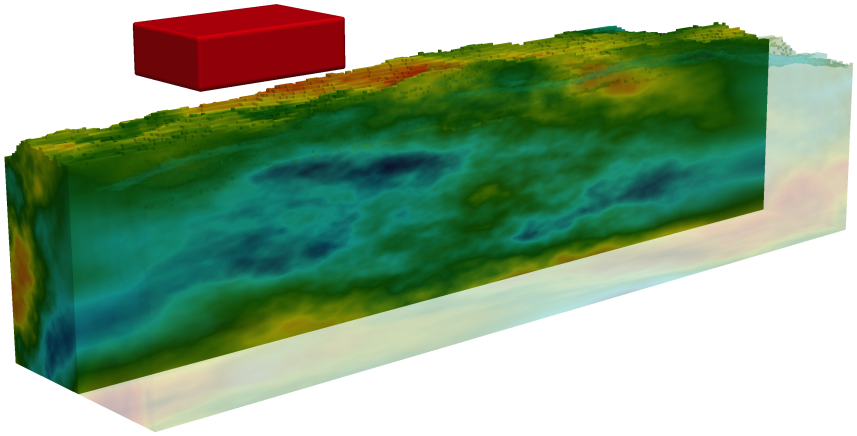

Figure 92: A complex medium with no targets buried within it. The properties of the soil are $\rho_s = 2.66$ g/cm^3, $\rho_b = 1.5$ g/cm^3, $C = 0.5$, $S = 0.5$ and water volumetric fraction varies from $f_w = 0 - 0.25$. The antenna unit used is the 1.5 GHz.

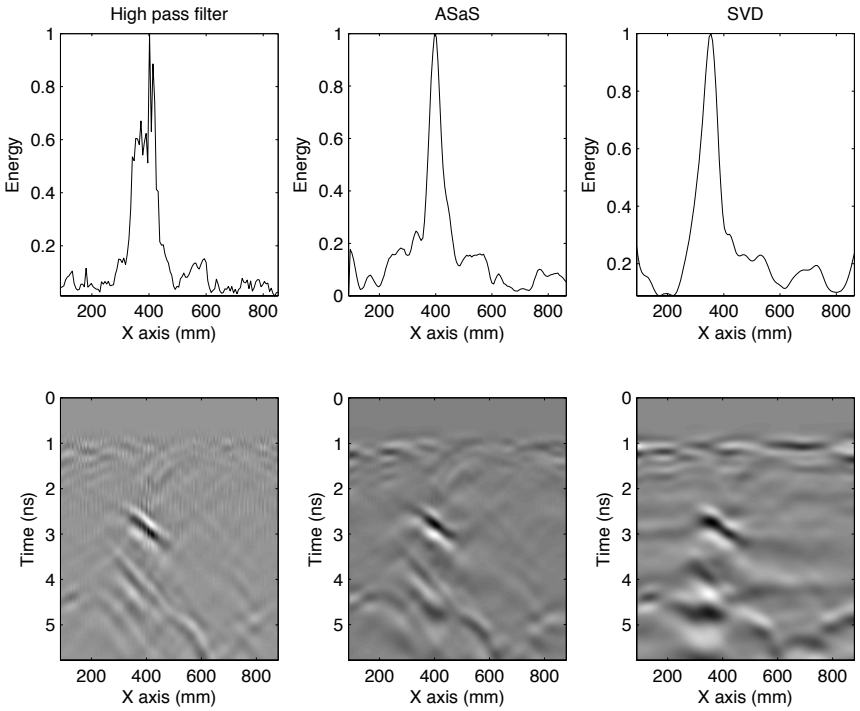

Figure 93: B-Scan using the 1.5 GHz antenna of the model shown in Fig. 92. A high pass filter, ASaS and an SVD (3 dominant eigenvalues are filtered out) are applied (after the quadratic gain). In all three cases a false alarm occurs (approximately) in the centre of the scan.

The dimensions of the model are $1000 \times 250 \times 450$ mm, the antennas are placed close to the ground surface (40 mm) and the AP landmines are buried at 60 mm depth. The soil is a homogenous saturated sand with $\rho_s = 2.66$ g/cm^3, $\rho_b = 2$ g/cm^3, $C = 0.5$, $S = 0.5$ and $f_w = 0.15$. Three different scenarios are examined in which water puddles are gradually increased (see Fig. 94). The complex relative electric permittivity of the water is a Debye function with $t_{0,w} = 5.8$ ps, $\epsilon_{w,s} = 80.1$ and $\epsilon_{w,\infty} = 4.9$ (Peplinski et al., 1995). Notice that only the dipolar relaxation of the water is employed in the simulations. The conductive term which is related to free ions (Stogryn, 1971) is neglected.

Water absorbs electromagnetic waves due to its ionic conductivity and its dipolar relaxation (Debye, 1929, Hill, 1969). Even pure-distilled water absorbs electromagnetic waves and the absorption is highly proportional to the frequency of the pulse. Fresh water (drinkable, lakes, rivers etc.) has salinity $S < 0.5$ ppt (particles per thousands). Using the formula suggested by Stogryn (1971) (4.73), (4.74), the conductivity of the water can be calculated with respect to the salinity (ppt) and the temperature. Subsequently we can analytically evaluate the losses of a monochromatic plane wave propagating inside water with different salinities. Fig. 95 illustrates the losses with respect to frequency,

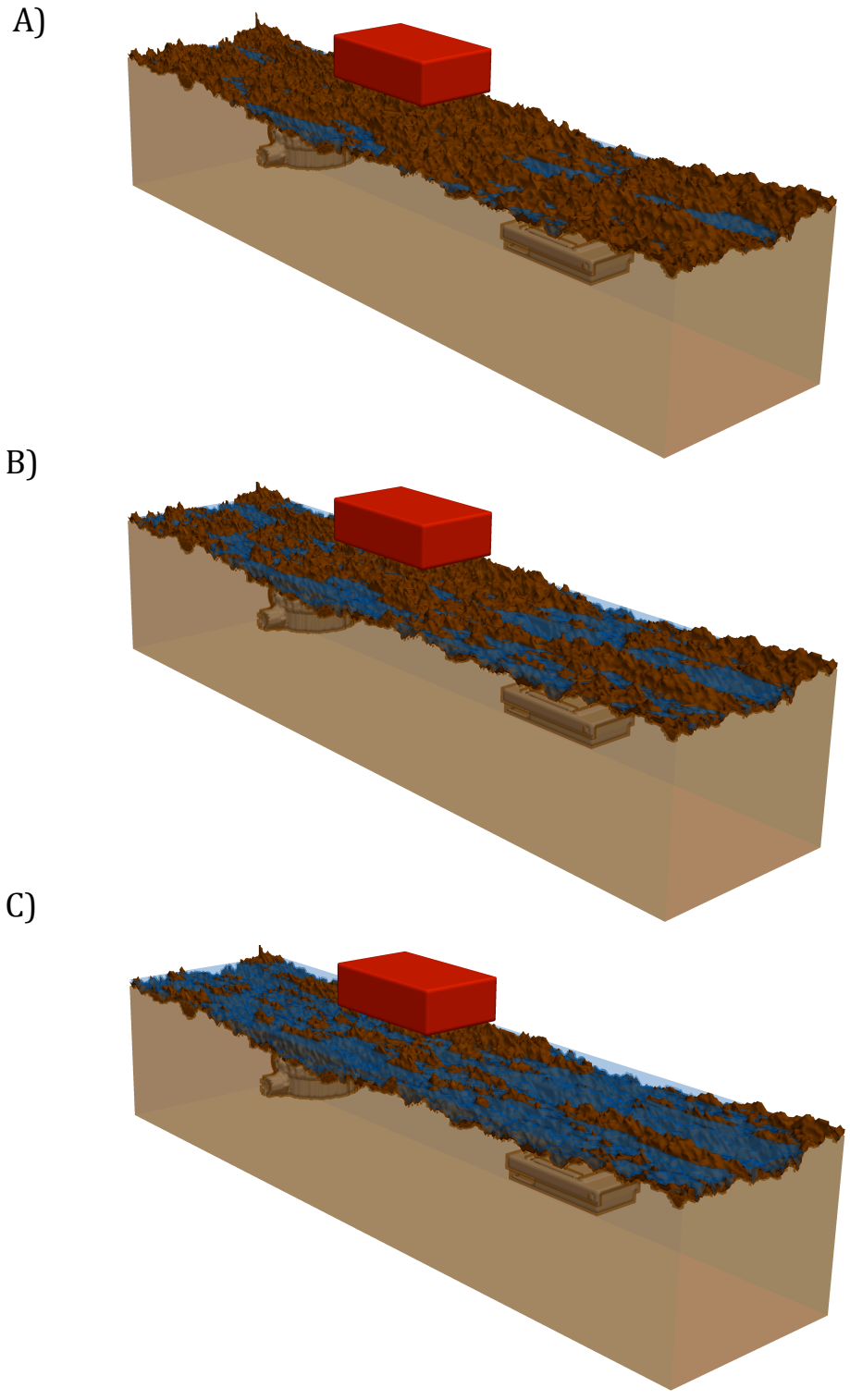

Figure 94: Water puddles with gradually increasing size over a homogenous saturated sand with fractal rough surface. The soil's properties are $\rho_s = 2.66$ g/cm^3, $\rho_b = 2$ g/cm^3, $C = 0.5$, $S = 0.5$ and $f_u = 0.15$.

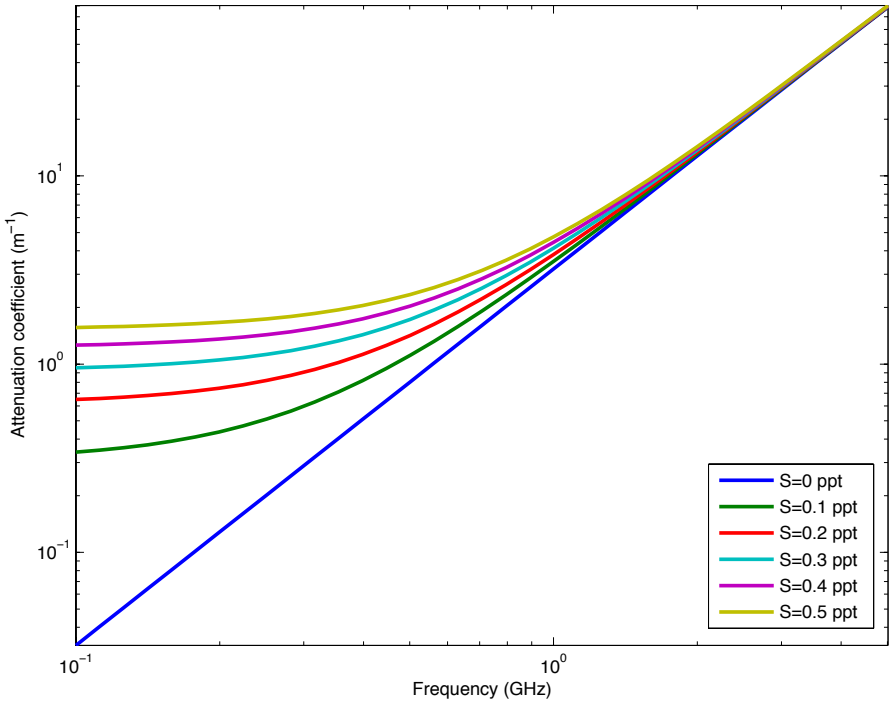

Figure 95: Electromagnetic losses of a monochromatic plane wave propagating inside water. S stands for salinity (ppt).

for different salinities S, ranging from $S = 0 - 0.5$ ppt ($T = 20$ C^o). It is evident that the predominant loss mechanism, for the range frequencies often used for landmine detection, is the water's dipolar relaxation. If high-salinity water needed to be modelled, the formula suggested by Stogryn (1971) (4.73)-(4.74) can be used in order to express conductivity with respect to temperature and particles per thousands (ppt).

Fig. 96-100 illustrate the resulting B-Scans using the 1.5 GHz antenna. In Fig. 96 only a quadratic gain is employed. The rough surface combined with water puddles make interpretation difficult although indications for the presence of two targets are readable through B-Scans. Increasing the size of water puddles further decreases the quality of detection using both B-Scan and energy based detection. In Fig. 97 the ASaS method is employed in order to decrease the ringing noise and the ground reflection. Both of the targets are detectable but nonetheless false alarms are also present due to the inability of ASaS to successfully remove the ground bounce. Fig. 98 illustrates the resulting B-Scans using an SVD filter by filtering out the three dominant eigenvalues. Similar to ASaS, false alarms are present and at the same time PMA-1 has a weak signature which makes its detection unreliable. Using a high pass filter (Fig. 99) produces similar results. Using an average removal, the most simple and straightforward approach, results to an easy to interpret and reliable results

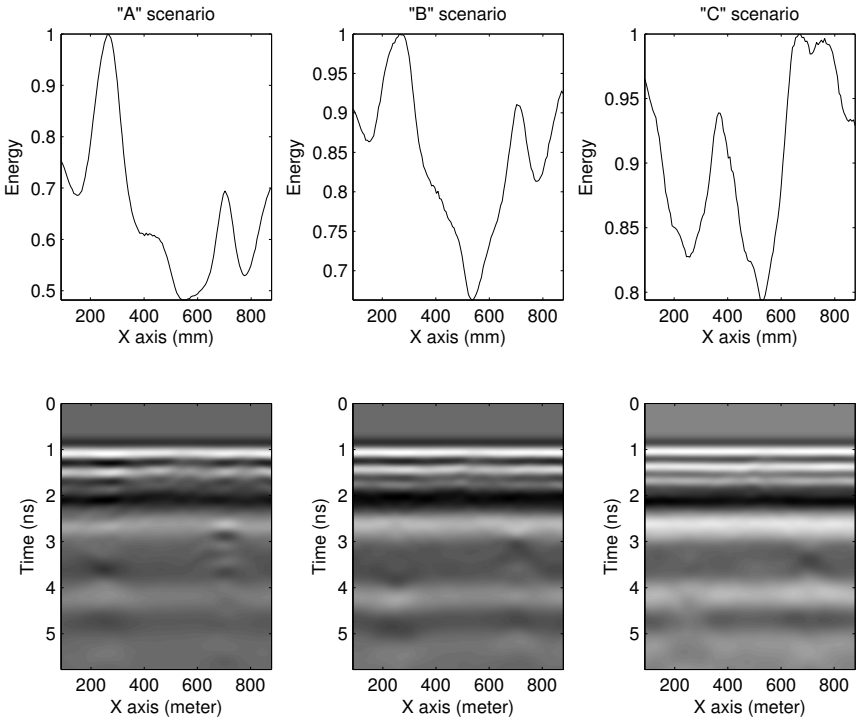

Figure 96: B-Scans of the models shown in Fig. 94 using the 1.5 GHz antenna. “A", “B" and “C" scenario corresponds to the gradual increase of the water puddles. A quadratic gain is applied to the raw data. The X axis corresponds to the center of the antenna unit.

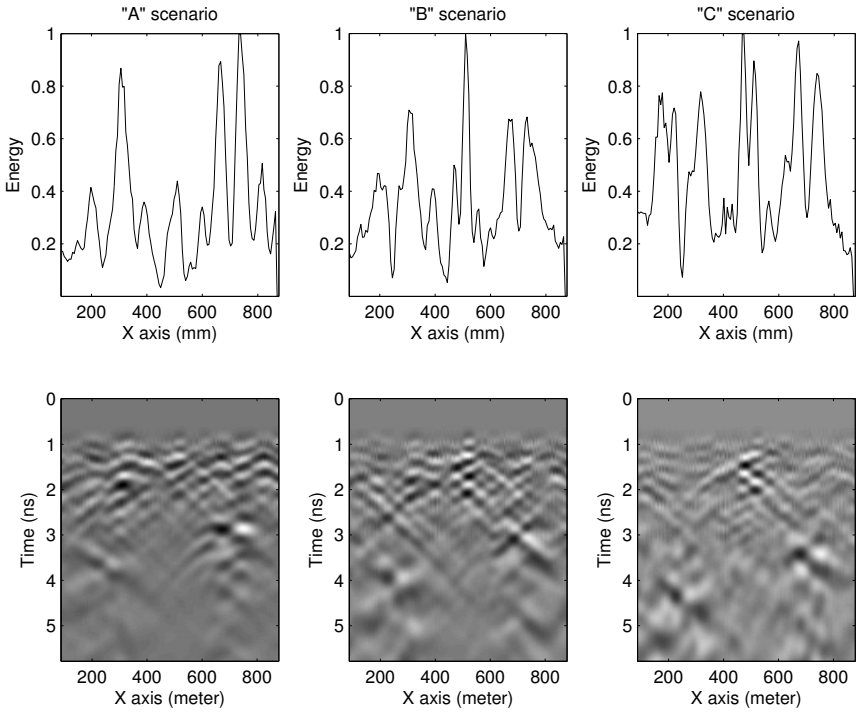

Figure 97: Similar with Fig. 96 using ASaS method.

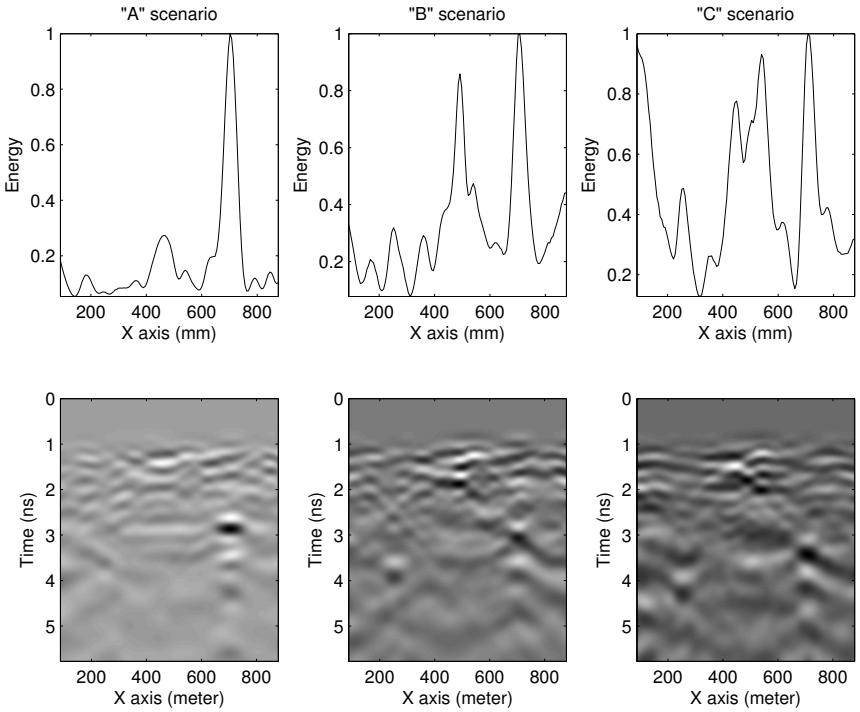

Figure 98: Similar with Fig. 96 using SVD filter (three dominant eigenvalues are filtered out).

using both B-Scans and energy based detection (as it is illustrated in Fig. 100). The 1.2 GHz model antenna is proven not effective for the present case study. The only approach with which the AP landmines are adequately depicted in the data is by using a high pass filter (see Fig. 101).

The above case study supports the premise that the performance of processing algorithms are case sensitive and their performance is related to both the environment and the antenna unit. Due to that, there are cases in which simple methods like average removal can outperform more sophisticated methods like ASaS.

Fig. 102 illustrates snapshots for different time steps for the “C" scenario (see Fig. 94) using the 1.5 GHz antenna. From Fig. 100 and 101 it is evident that the 1.5 GHz antenna gives more clear results compared to the 1.2 GHz antenna. The reason for that is because the high frequency content which is essential in order to get a clear reflection from the AP landmines is rapidly attenuating inside the water and inside the saturated sand. The 1.2 GHz antenna has a lower frequency content which manages to pass through the water but it cannot resolve the AP landmines. The already small high frequency content of the 1.2 GHz antenna is attenuated inside the water. Due to that, the pulse which finally reaches the AP landmines has a very low central frequency which makes the AP landmines undetectable. This is the reason why high pass filter works

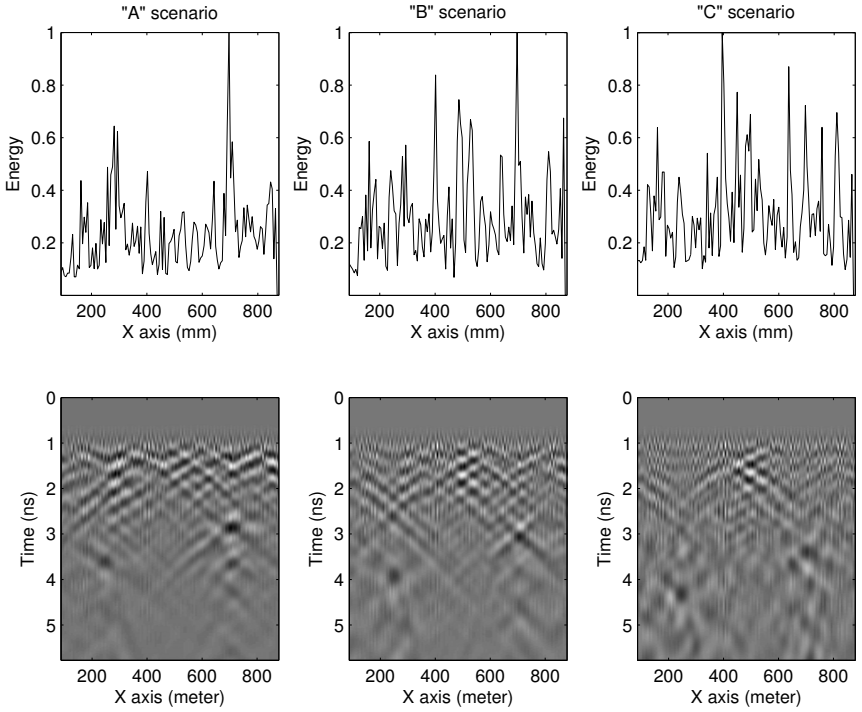

Figure 99: Similar with Fig. 96 using a high pass filter.

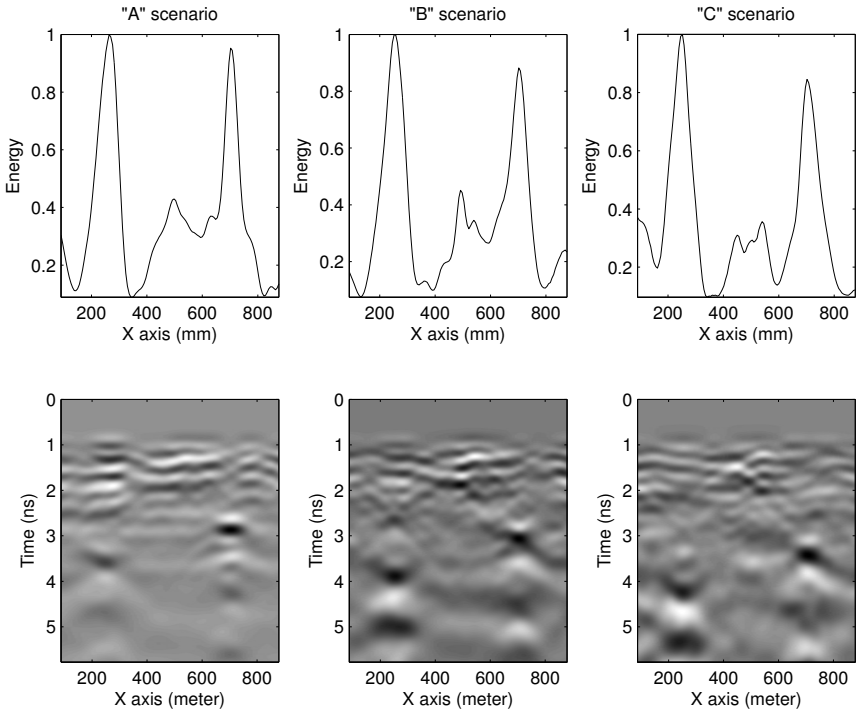

Figure 100: Similar with Fig. 96 using an average removal.

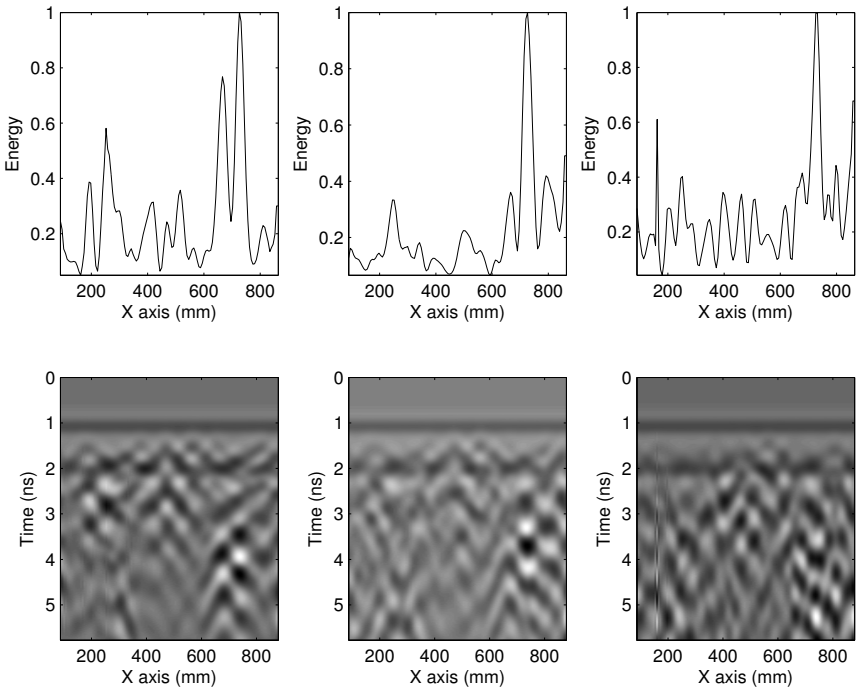

Figure 101: Similar to Fig. 100 using the 1.2 GHz antenna. Instead of average removal a high pass filter is applied.

better than the average removal using 1.2 GHz antenna (i.e. it enhances the high frequency content of the B-Scan). On the other hand the 1.5 GHz antenna has a larger amount of high frequency content which manages to pass through the water and get a clear reflection from the AP landmines. The reduction of the central frequency of the pulse due to the water puddles is illustrated in Fig. 100. In all the scenarios ("A", "B" and "C") the early reflections from the surface have a higher frequency content compared with the later reflections from the buried targets. As the size of the water puddles increases, the central frequency of the resulting scattering fields is also decreased. This is also due to the dipolar losses within the soils which are accurately implemented to the present numerical framework.

Due to the high dipolar losses of the water, no multi-interference phenomena neither waveguide effects (Strobach et al., 2013) occur within the water. The high frequency propagating modes of a thin dielectric slab, like water puddles, are rapidly attenuating inside water.

Fig. 100 presents an apparently peculiar result. The reflections from the AP landmines seem to increase in amplitude as the water puddles increase. In order to explain this, we plot the traces (A-Scans), when the 1.5 GHz antenna operates over the PMN, for all three scenarios (Fig. 103). An average removal is applied to the corresponding B-Scans and no gain is applied. From Fig. 103

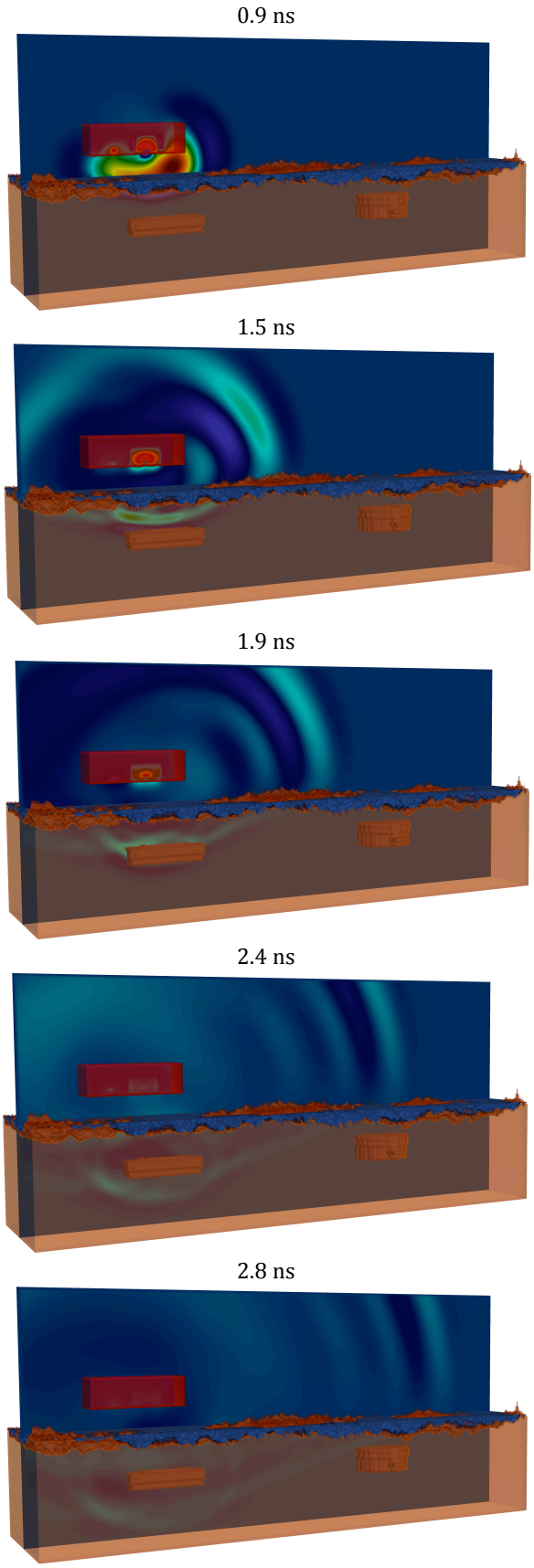

Figure 102: Snapshots of the model shown in Fig. 94 for the “C" scenario. The antenna which is used is the 1.5 GHz antenna. The fields in each snapshot are normalised so as the fields to be clearly visible. In the absence of normalisation the fields in the later snapshots would not be visible due to geometrical spreading of the energy and losses within the ground.

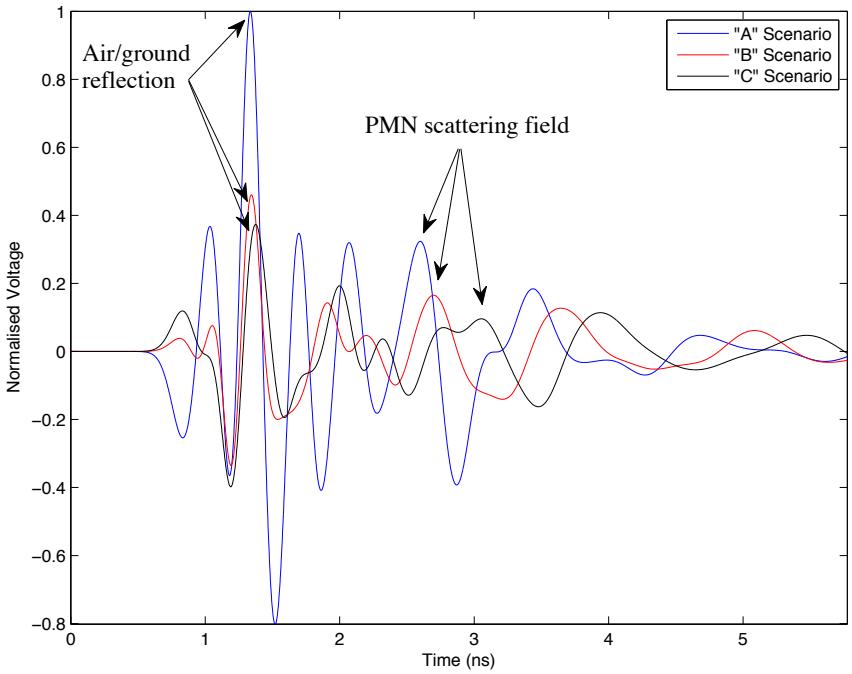

Figure 103: Traces (normalised to "A" scenario) over PMN of all the three scenarios explained in Fig. 94. An average removal is applied to all the B-Scans (no gain is applied). It is evident that both the reflections from PMN as well as the ground reflections (after average removal) are decreasing in amplitude when the water puddles are increasing.

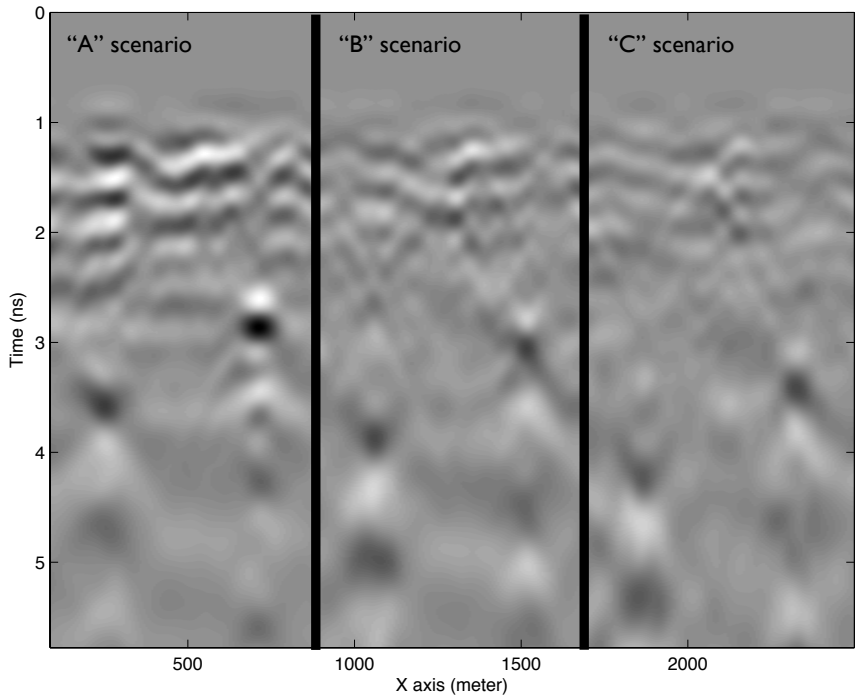

Figure 104: The B-Scans shown in Fig. 100 plotted right next to each other using the same colour scale. It is evident that both the ground bounce as well as the targets response is decreased as the size of the water puddles increase.

is evident that the reflections from PMN gets smaller as the water puddles increase. The same happens for the remains of the ground reflection. Because of that, although the scattering field from the AP landmines gets smaller, the contrast between the ground reflection and the scattering field from the targets is also decreased. This makes the reflections from the AP landmines more readable in the B-Scans due to the reduced clutter. This is highlighted in Fig. 104 in which the B-Scans shown in Fig. 100 are plotted together using the same colour scale.

The reason why the average removal works better in the present example, is because water puddles tend to create a flat surface which is easier to manipulate using ground removal techniques. Apart from that, the direct wave may couple with the reflections from the water, which have opposite sign, and reduce the overall early reflections. Also the central frequency of the pulse which enters the water puddles is decreased which makes it harder to resolve the roughness of the surface.

6.5.5 *Water puddles and vegetation*

In the present section, it is examined how GPR performs in complex environments. Saturated soils with water puddles as well as vegetation are incorporated into the model (Fig. 105). The examples resemble tropical-humid environments in which AP landmines are frequently found e.g. PMN has been extensively used at the Thai border in heavy-vegetated environments, i.e. jungles (Physicians for the Human Rights, 1993).

The dimensions of the model are $1000 \times 250 \times 450$. The modelled B-scans consist of 132 traces. In all the scenarios, the AP landmine PMA-1 is buried at approximately 50 mm depth (Fig. 105). The 1.5 GHz antenna is used for the simulations. The soil's properties are $C = 0.5$, $S = 0.5$, $\rho_s = 2.66$ gr/cm^3, $\rho_b = 2$ gr/cm^3 and the volumetric water fraction varies stochastically from $f_w = 0 - 0.22$. The water weight based fraction of the vegetation equals with $M = 0.4$.

In the first scenario, the antenna is placed at approximately 0.15 m above the ground. No vegetation, neither water puddles exist in this model. A relatively smooth surface and a stochastic variation of water volumetric fraction are the only sources of unwanted clutter. The resulting B-Scans are shown in Fig. 106. A quadratic gain is applied to the raw data and subsequently different processing approaches are used, namely, average removal, high pass filter, ASaS and SVD (3-6 eigenvalues are plotted). All the methods apart from average removal perform equally well with the ASaS to over-perform both high pass

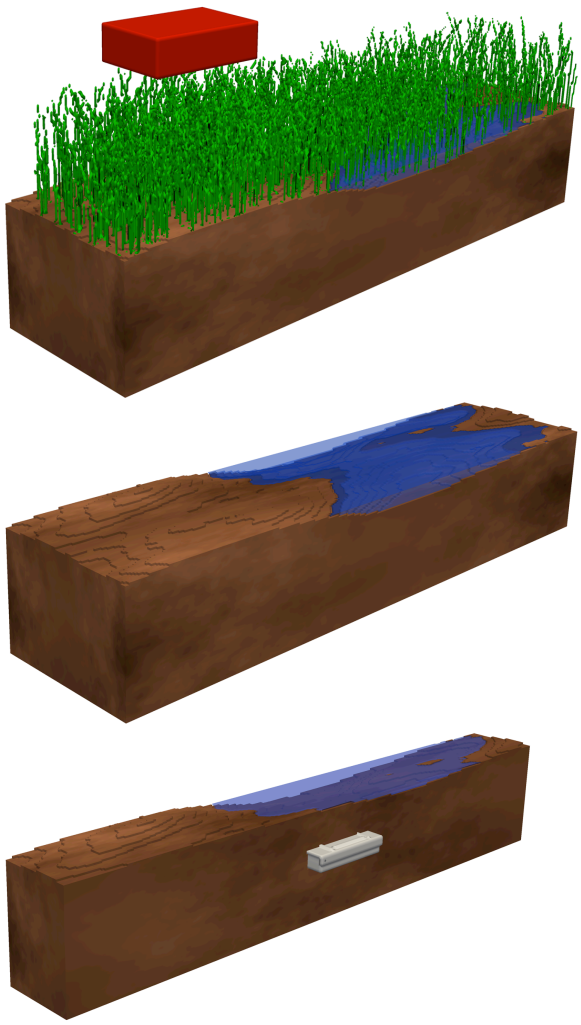

Figure 105: The soils properties are $C = 0.5$, $S = 0.5$, $\rho_s = 2.66\ gr/cm^3$, $\rho_b = 2\ gr/cm^3$ and the water volumetric fraction stochastically varies from $f_w = 0 - 0.22$. Water puddles as well as vegetation are implemented to the model. The 1.5 GHz antenna is used for the simulations.

filter and SVD (see the energy plots in Fig. 106). Fig. 107 shows the B-Scan when the antenna is placed near the ground at approximately 5 cm. It is evident that placing the antenna closer to the ground enhances the performance of GPR using all the aforementioned processing approaches.

In the second scenario water puddles have been added to the model. The antenna is placed relatively far from the ground. Fig. 108 shows the resulting B-Scans. The water puddles ($t_{0,w} = 5.8$ ps, $\epsilon_{w,s} = 80.1$ and $\epsilon_{w,\infty} = 4.9$) decrease the scattering signature of the AP landmines making the detection impossible for the present case, the specific antenna and for the processing approaches used. Placing the antenna closer to the ground, results to equally unreliable results (see Fig. 109).

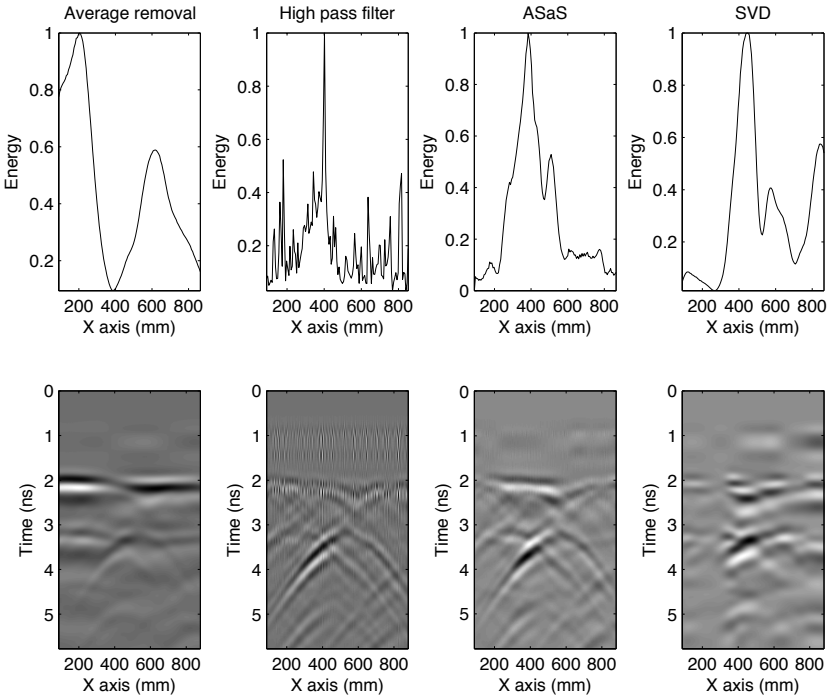

Figure 106: B-scans of the model shown at Fig. 105. No vegetation neither water puddles occur in the model. The antenna (1.5 GHz) is placed at approximately 0.15 m above the ground. An average removal, a high pass filter, ASaS and SVD (3-6 eigenvalues are plotted) are applied to the data (subject to a quadratic gain).

In the third scenario, only vegetation without water puddles is implemented into the model. Again, a quadratic gain and subsequently an average removal, high pass filter, ASaS and SVD (3-6 eigenvalues are plotted) are applied to the data. Using ASaS and SVD surpass the performance of average removal and high pass filter.

In the last scenario both vegetation and water puddles have been added to the model. The same processing approaches as previously are applied to the raw modelled data. The resulting B-Scans are heavily corrupted from high frequency clutter, due to the presence of grass, and ringing noise which gives the impression of an apparent layer. The ringing noise is due to the reverberating reflections between the ground and the antenna due to the fact that the antenna is placed far from the ground. The vegetation corrupts the ringing noise making it difficult to remove it using ground removal techniques.

In order to further explore the performance of GPR to complex environments, three additional cases are examined using both modelled antennas (1.5 and 1.2 GHz). In all of the cases, rough surface, water puddles and vegetation are implemented into the models. The dimensions of the models are $1000 \times 250 \times 450$, the properties of the soil are $\rho_s = 2.66$ g/cm^3, $\rho_b = 2$ g/cm^3, $C = 0.5$, $S = 0.5$

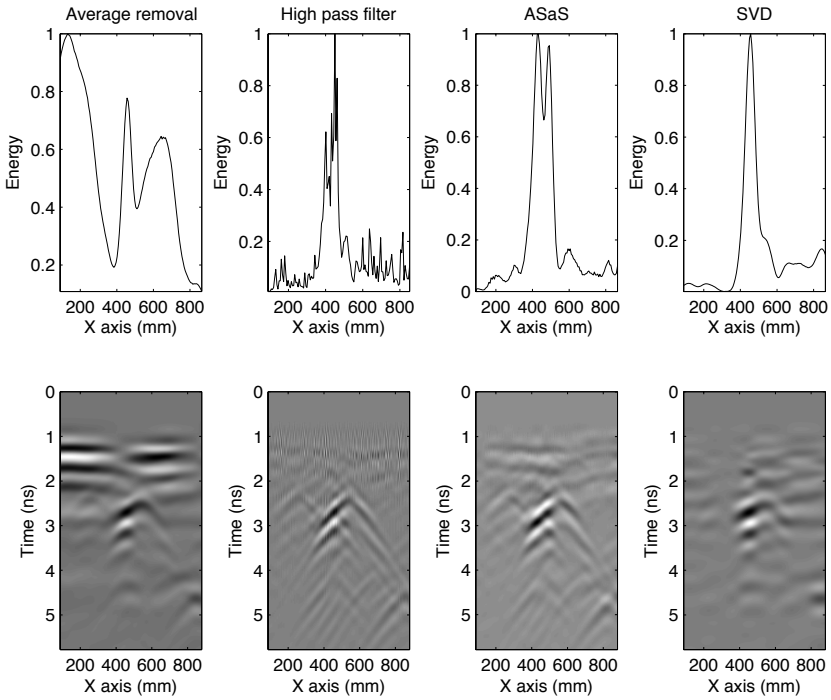

Figure 107: Similar to Fig. 106 with the antenna placed approximately 5 cm above the ground.

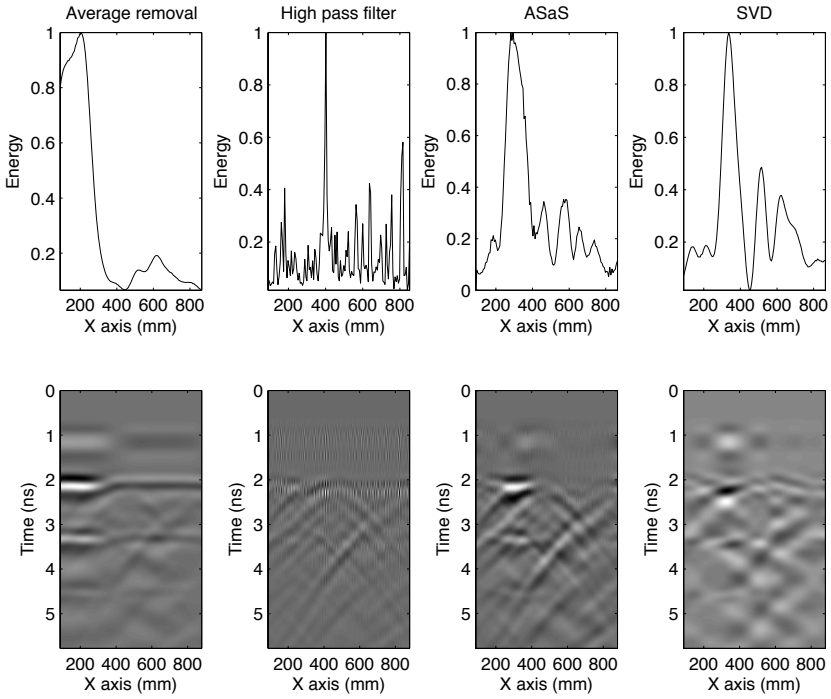

Figure 108: Similar to Fig. 106 adding water puddles.

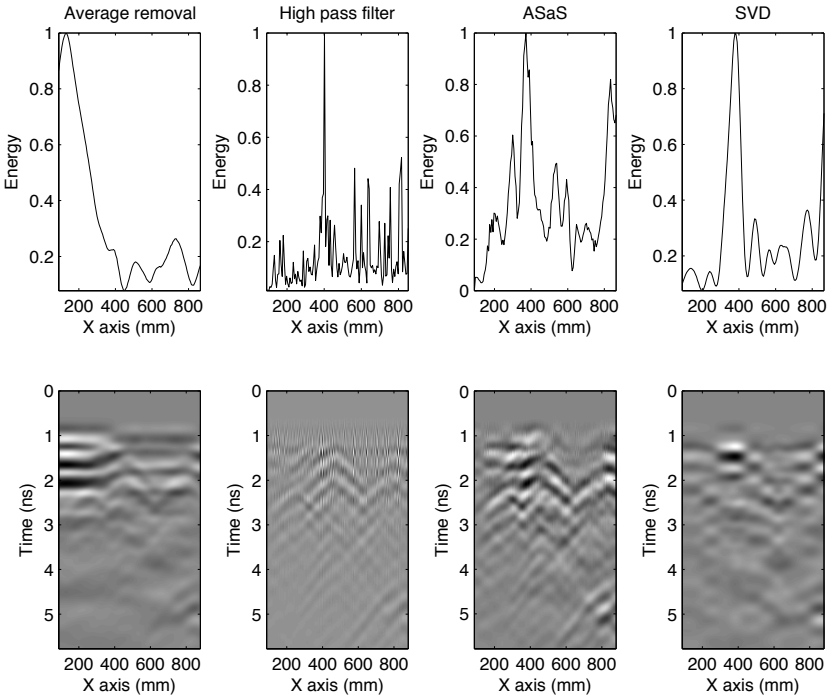

Figure 109: Similar to Fig. 108 placing the antenna approximately 5 cm above the ground.

and the water volumetric fraction varies stochastically from $f_w = 0 - 0.25$. The water weight based fraction of the vegetation equals to $M = 0.4$. In the first case, the AP landmine PMA-1 is buried in the centre of the model at 60 mm depth, in the second case, PMN is buried in the centre of the model also at 60 mm depth and in the the third case, no landmines are buried in order to investigate the false alarms which may occur (Fig. 112).

Fig. 113 and 114 show the B-Scans and the energy plots using the 1.5 GHz and the 1.2 GHz antenna models respectively. A quadratic gain and an SVD (four dominant eigenvalues are filtered out) are applied to the raw modelled data. Both of the antennas result to noisy and difficult to interpret B-scans. The 1.2 GHz antenna gives indications of PMN and PMA-1 but similar patterns in the B-Scan can be seen when no landmines are present in the model. This clearly illustrates the difficulties that GPR has in some truly complex environments. It is evident from these examples that a numerical scheme that aims to be used as a testbed for developing GPR antennas and advanced processing methods should be capable of producing difficult and challenging data sets like the ones presented in this section.

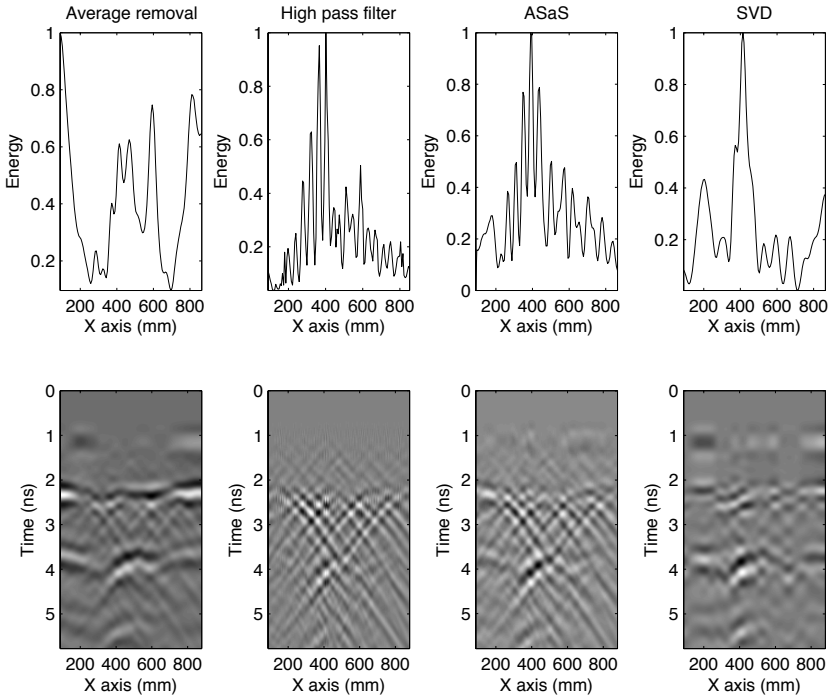

Figure 110: Similar to Fig. 106 adding vegetation.

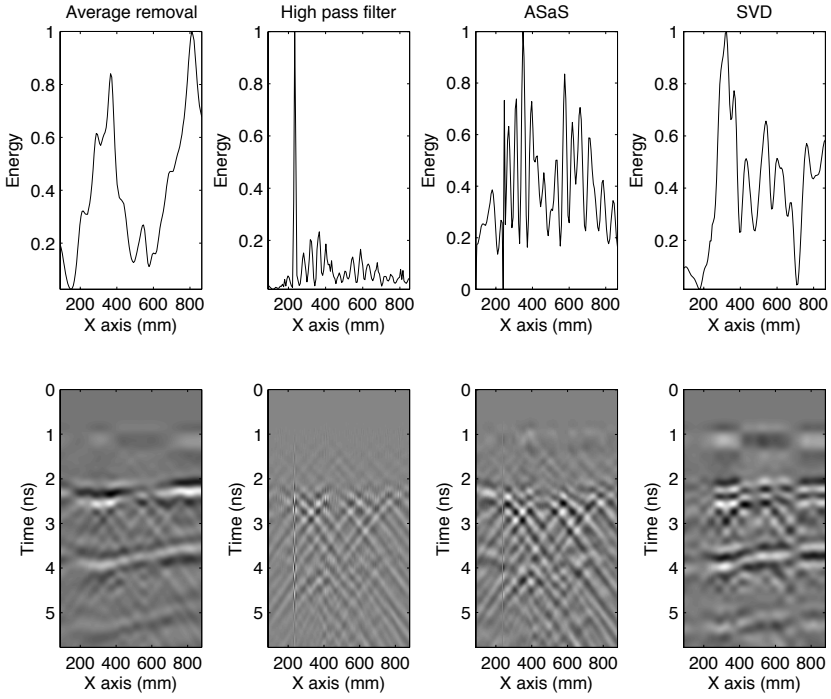

Figure 111: Similar to Fig. 106 adding vegetation and water puddles.

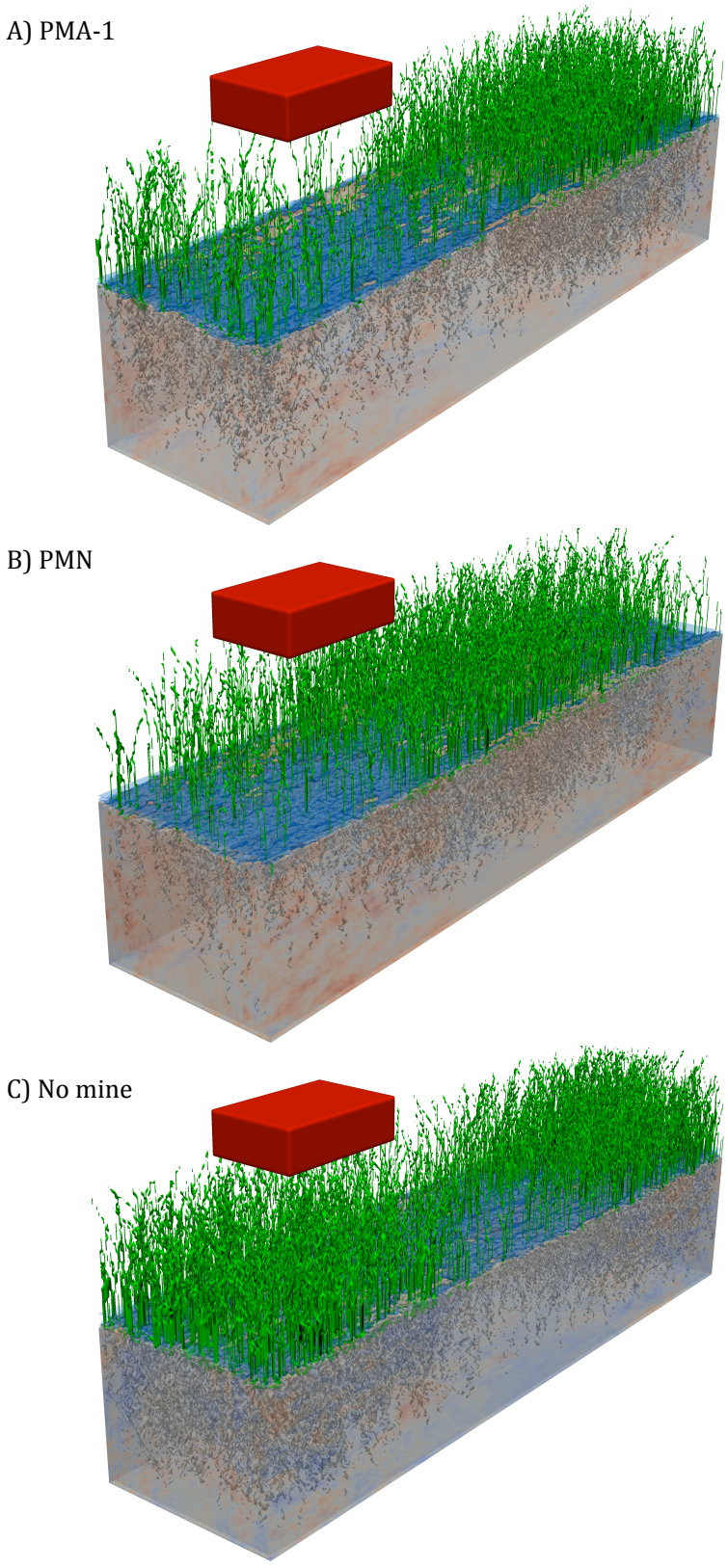

Figure 112: Three different complex media with a stochastically varied water volumetric fraction, rough surface, water puddles and vegetation. In “A" case the AP landmine PMA-1 is buried at the center of the model at approximately 60 mm depth. In “B" scenario, PMN is placed 60 mm (approximately) beneath the surface and in “C" no landmine is present.

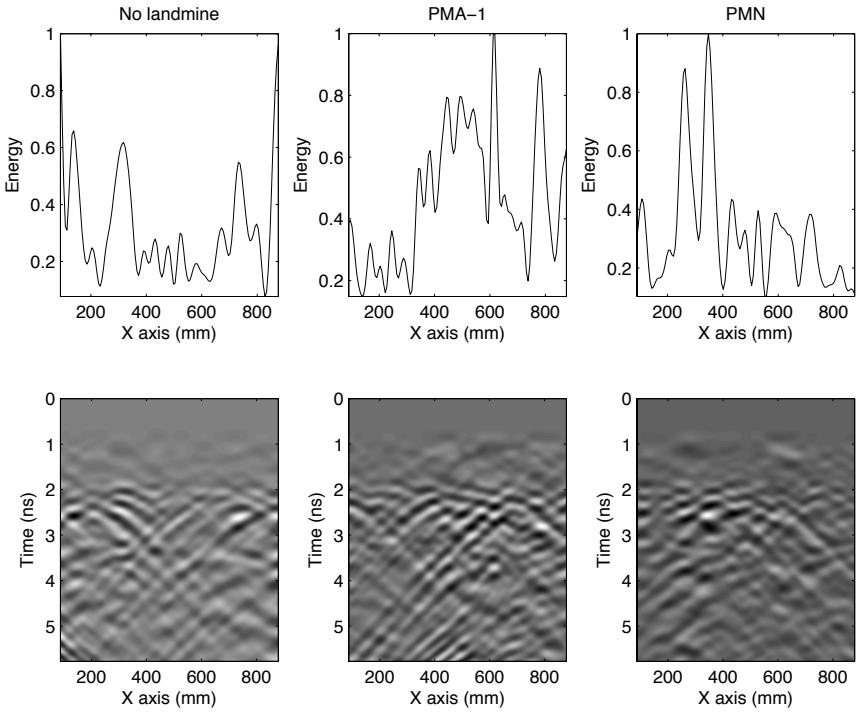

Figure 113: B-Scans and energy plots using the 1.5 GHz antenna for the cases shown in Fig. 112. A quadratic gain and subsequently an SVD (four dominant eigenvalues are filtered out) are applied to the raw data. The X axis corresponds to the center of the antenna unit.

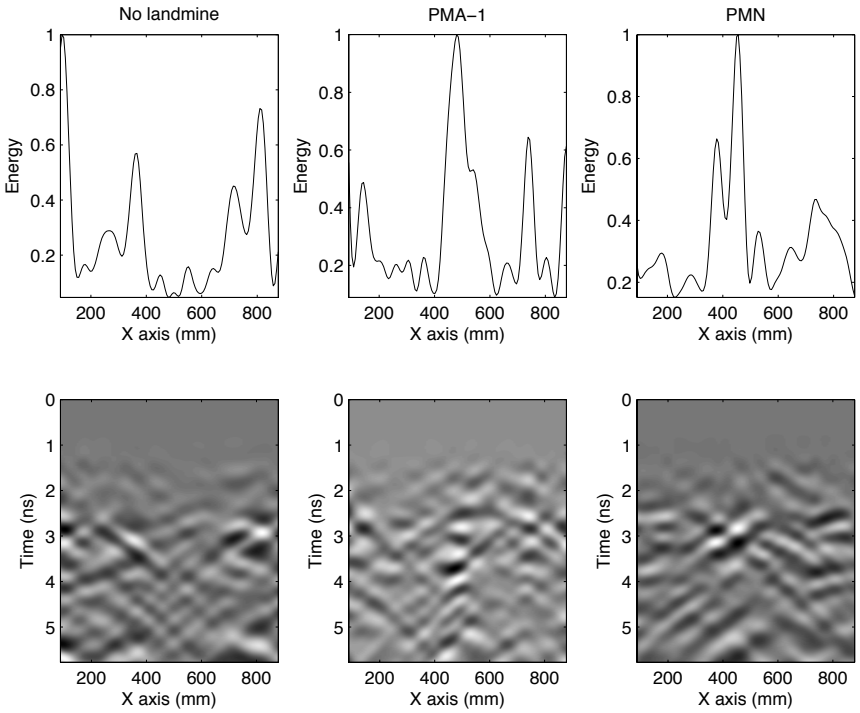

Figure 114: Same with Fig. 113 using the 1.2 GHz antenna.

7

NEURAL NETWORKS FOR AP LANDMINE DETECTION USING GPR

A case study is presented which aims to investigate the applicability of ANN to AP landmine detection using GPR. An essential requirement of ANN and of machine learning in general is a complete training set. A complete training set should include data from all possible scenarios. In the case of GPR for AP landmine detection, an adequate training set should consist of data from a diverse set of models with varying topography, soil's inhomogeneity, landmines, false alarm targets, heights of the antenna, depths of the landmines and so on. Previous attempts to apply machine learning for AP landmine detection, employed limited training sets, thus, they underestimated the capabilities of ANN. In the present study, a 2D FDTD (2,2) is used as a training platform for ANN. Although 2D is a simplification, nonetheless, is a computationally efficient approach for examining the performance of ANN subject to a complete training set. The results are promising and provide strong support for further expanding this approach to the more computationally expensive 3D case.

7.1 INTRODUCTION

Landmine detection using GPR is a unique and highly complicated problem. The high frequencies employed in GPR for AP landmine detection are rapidly attenuated in the presence of saturated soils. In addition, high frequency pulses give rise to unwanted clutter resulting from the soil's spatial heterogeneities and the rough surface of the soil. Furthermore, the antenna unit must operate in a small proximity to the ground which results to ringing noise due to the reverberating reflections between the antenna and the soil's surface. Unwanted clutter combined with losses and ringing noise decrease the SNR making detection difficult and in some cases unreliable.

Different approaches have been suggested in an effort to increase SNR and consequently the detectability of GPR (see Chapter 3). Here, it is interesting to mention a recent paper by Schofield et al. (2014), in which, migration is applied to data received using the well known handheld device MINEHOUND. The difficulties arising from the fact that no accurate positioning is available are highlighted. Schofield et al. (2014) suggest modifications in an effort to overcome these issues. Their approach is applied to anti-tank landmine detec-

tion and not AP. Also, it is interesting to quote a part of their conclusions which highlights the need for an accurate and inclusive testbed for validating processing algorithms:

" *Further research could include testing this method on more soil types and types of mine across various sites to improve the reliability of the algorithm. Also, it would be of interest to introduce clutter in the ground to see how well the algorithm will distinguish between clutter and the mines*" Schofield et al. (2014).

Demining using GPR can be roughly divided into two categories, handheld GPR and vehicle based GPR. Handheld devices have been extensively used for AP landmine detection while vehicle based GPR is primarily focused on anti-tank landmines (Daniels, 2008). Handheld devices are constrained, primarily due to technical difficulties, to operate without any accurate positioning system and to give real-time results while the antenna is moving (Daniels, 2008). It is apparent that a detection scheme like the one described above is based on individual A-traces rather than B-Scans or C-Scans:

" *Handheld landmine systems are more limited in the signal processing algorithms that can be applied because they usually only have a single transmit-receive antenna pair compared with vehicle based systems that use arrays of antennas and with only a few exceptions do not form an image.*" Daniels (2008).

In that context, extensive research has been done on processing frameworks which focus on single A-traces:

"*Research into target discrimination based on the analysis of A-scans by means of complex resonances, wavelets, time- frequency characteristics, Neural networks, fuzzy sets, Gaussian mixture models, order statistics, template matching, has been carried out...*" Daniels (2008).

In addition to the aforementioned constrains, GPR for AP landmine detection is a multi-parametric problem. Landmines can be found in deserts, urban environments, juggles and so on. It has been shown in chapter 6 that GPR's performance is case sensitive and no straightforward approach has yet to be defined. Different targets in different media using different antennas may result to substantially different results, making the inclusivity of any proposed processing approach questionable.

The non-linearity and the large diversity of the demining problem combined with the need for real time results makes machine learning a promising approach for both detection and classification (Bishop, 1996).

Azimi-Sadjadi et al. (1992), employed C-Scans measured from a specific minelane in an effort to train a feedforward neural net. PCA is also employed in order to reduce the dimensionality of the problem. Further results are given by Azimi-Sadjadi et al. (1994), in which different methodologies are applied in an effort to reduce the dimensions of the model and increase its training efficiency. Plett et al. (1997), used data from a single minelane as a training platform for ANN. In contrast with Azimi-Sadjadi et al. (1992, 1994), a simple trace is used in order to retain the applicability of the ANN to handheld devices in which accurate positioning is not available. B-Scans, after simple post-processing are used as inputs by Alauddin and Nath (2006), again the training set is measured at a single minelane. Yang and Bose (2005), proposed a hybrid complex valued ANN in order to use both the magnitude and the phase of eleven distinct frequencies (ranging from 0.8-1.2 GHz) as input functions. It is interesting to note that Yang and Bose (2005), suggests a step by step classification strategy. The latter, initially isolates targets from background and subsequently a classification takes place between those targets. Similar to the previous approaches a single minelane is employed as a training platform.

Labeled data, i.e. data accounted to a known state – presence or absence of a target – are expensive and not easily available (Haykin, 2009). This is the main reason why all the approaches discussed above are trained using data from a single minelane raising doubts about their inclusivity and their generalisation capabilities. In order to fully explore the potential of ANN to assist AP landmine detection, the training set must be representative of the whole feature space and not being biased to specific clinical minelanes. The present study examines the performance of ANN subject to an adequate and coherent database of modelled responses. These are synthetically calculated using a 2D FDTD (2,2) method. Although an ANN trained with a database based on 2D modelled responses is clearly not applicable to real field cases, nonetheless it can provide an estimation of the performance of ANN in a diverse set of different scenarios. The resulting ROC for the suggested ANN are promising, providing good reasons for support into further expanding this approach to the more computationally expensive 3D case.

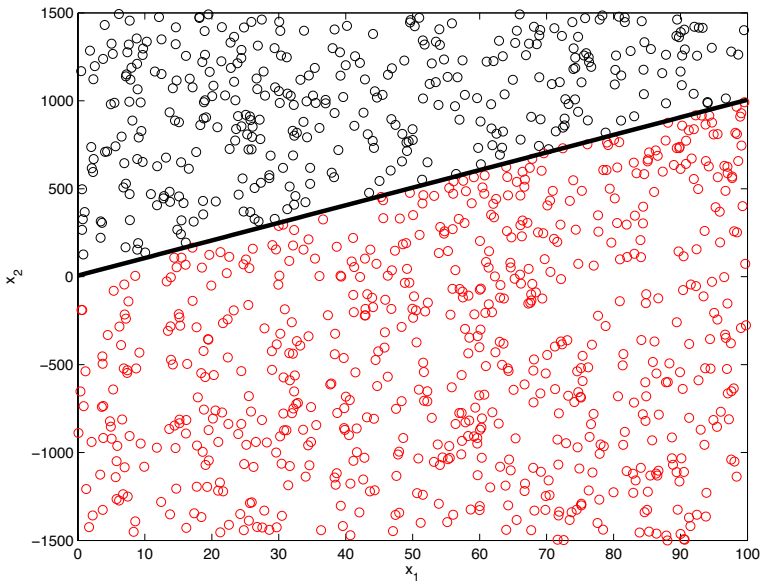

Figure 115: A classification problem which uses two parameters as inputs (x_1 and x_2). The input data are classified into two distinct groups, red and black.

7.2 NEURAL NETWORKS FOR PATTERN RECOGNITION.

A single layer ANN with two inputs (x_1 and x_2) is going to be described in order to illustrate how and why ANN can effectively address pattern recognition problems. Fig. 115 illustrates the present case study. It is evident that the boundary which separates the two distinct groups is a straight line. The data which fall under the line are classified as red and the ones above the straight line are classified as black. For mathematical convenience, the two groups are defined as zero and one. ANN for pattern recognition in their simplest form can be stated in mathematical notation as

$$g\left(w_0 + w_1 x_1 + w_2 x_2\right) \approx 1 \tag{7.1}$$

$$g\left(w_0 + w_1 x_1 + w_2 x_2\right) \approx 0 \tag{7.2}$$

$$g\left(z\right) = \frac{1}{1 + \exp\left(-uz\right)} \tag{7.3}$$

Equation (7.3) is called the sigmoid function and it is widely used in ANN. The reason for that is because it is a continuous function which can classify outputs into two groups, namely zero and one (Bishop, 1996) (see Fig. 116). Traditionally $u = 1$. Changing the u value rescales the problem with no

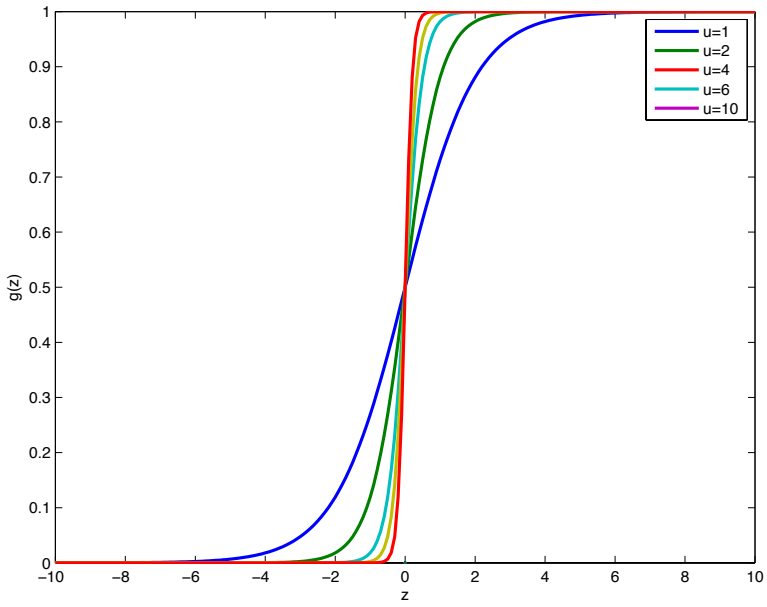

Figure 116: The sigmoid function for different u (7.3).

significant implication to ANN performance. If z is greater than zero, the output of the sigmoid function is approximately one otherwise is approximately zero. Supervised ANN for pattern recognition employ training sets i.e. sets of input data which correspond to known outputs. Subsequently, an optimisation is executed which tries to find the best weight vector ($\mathbf{w}$) which minimises the difference between the actual and the predicted outputs. The weight vector can then be applied to data with unknown outputs in order to classify them based on the so-called experience of ANN (Bishop, 1996). From Fig. 115 it can be shown that the optimised values for the unknowns in (7.1)-(7.3) are $w_0 = -6$, $w_1 = 1$ and $w_2 = -10$. Using the optimised weight vector, a classification between red and black can be made based on the input data x_1 and x_2. Notice that the line illustrated in Fig. 115 can be expressed as $w_1 \cdot x_1 = -w_2 \cdot x_2 - w_0$. Based on that, it is evident that a single layer ANN with two inputs tries to find the optimised line which separates two distinct groups.

The above ANN can only handle classification problems with linear boundaries (see Fig. 115) (Bishop, 1996). To address non-linear boundaries (see Fig. 117), more hidden layers and neurones must be added. Adding an extra neurone in (7.1)-(7.3) results to

$$g_1 \left(w_{0,1,1} + w_{1,1,1} x_1 + w_{2,1,1} x_2 \right) \tag{7.4}$$

$$g_2 \left(w_{0,1,2} + w_{1,1,2} x_1 + w_{2,1,2} x_2 \right) \tag{7.5}$$

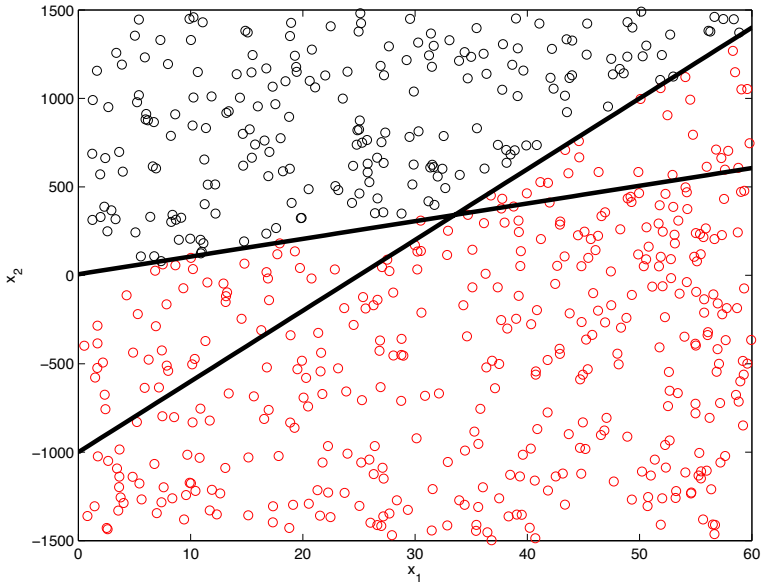

Figure 117: A classification problem with no linear boundaries.

$$y = g_3\left(w_{0,2,1} + w_{1,2,1}g_1 + w_{2,2,1}g_2\right) \tag{7.6}$$

If $y \approx 1$ then the data are classified as red and when $y \approx 0$ as black. The weights are defined as $w_{i,j,k}$ where i is the input parameter, j is the number of the layer and k indicates to what neurone the weight is associated with. The above problem can be represented graphically using neural nets (see Fig. 118). This type of representation is very popular to the ANN research community due to the fact that ANN are inspired by human brain and neural nets resembles brain activity (Haykin, 2009).

Adding a neurone to ANN, results to the introduction of an extra linear boundary (see Fig. 117). In order to make this more clear, a set of weights and biasses is derived (bias is the w_0, i.e. the weight which is directly implemented to the sigmoid function and is not applied to any input units) which can sufficiently classify the problem illustrated in Fig. 117. A set of parameters which can adequately perform the above classification are $w_{0,1,1} = -6$, $w_{1,1,1} = 1$, $w_{2,1,1} = -10$, $w_{0,1,2} = 1000$, $w_{1,1,2} = 1$, $w_{2,1,2} = -40$, $w_{0,2,1} = -150$, $w_{1,2,1} = 100$ and $w_{2,2,1} = 100$. By applying these weights, a logical problem arise. The latter states that if the inputs x_1 and x_2 lay above the two lines illustrated in Fig. 117, then the data are classified as red, otherwise the data are classified as black. Notice that the weights are associated with the straight lines illustrated in Fig. 117. The straight lines can be expressed as $w_{1,1,1} \cdot x_1 = w_{2,1,1} \cdot x_2 + w_{0,1,1}$ and $w_{1,1,2} \cdot x_1 = w_{2,1,2} \cdot x_2 + w_{0,1,2}$. If the data falls over the two straight lines then

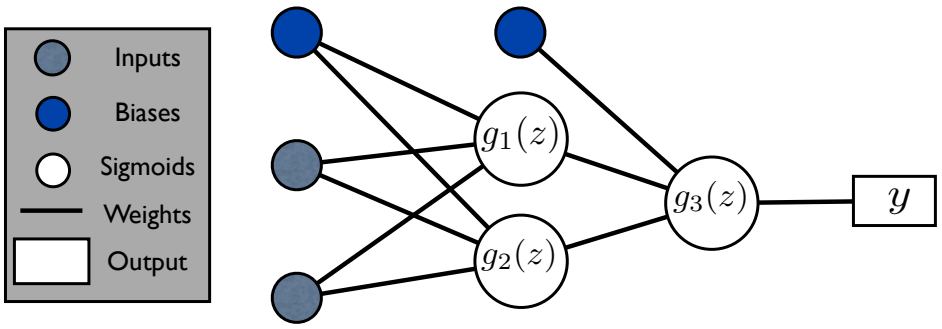

Figure 118: A two layered ANN with two inputs and two neurones.

both sigmoid functions of the first layer will give as output one. By further applying the weights of the second layer we basically scale the problem which now varies from -150 (when data falls under both lines), -50 (when data falls under one of the lines) and 50 (when both data falls over the two lines). By applying the last sigmoid function ($g_3(z)$) results to one if the data falls over the two lines and zero if not.

By introducing more neurones in the second layer, more complex boundaries (like circles) can be addressed (Bishop, 1996). Nonetheless, cases like the one illustrated in Fig. 119 can not be treated using two layered ANN. More hidden layers are required (Bishop, 1996) which subsequently result to a high dimensional optimisation problem difficult to be addressed due to the high number of local minima.

7.3 ERROR BACK-PROPAGATION ALGORITHM

The error back-propagation algorithm is an elegant approach to evaluate the derivatives necessary for the optimisation during the training of the feed forward ANN. Traditionally, the optimiser is the gradient-descent method, although, non-linear damped least squares (Levenberg-Marquardt least squares), Scaled Conjugate Gradiend-descent (SCG) method, Bayessian regularisation as well as global optimisers are also frequently used (Bishop, 1996, Haykin, 2009). Here, the error back-propagation algorithm using a gradient-descent method is described.

Let's assume a simple feed forward ANN with one layer, one sigmoid neurone $g(z)$ and an arbitrary number of inputs x_i. The error function is then defined as

$$E = \frac{1}{2}(y - t)^2 \tag{7.7}$$

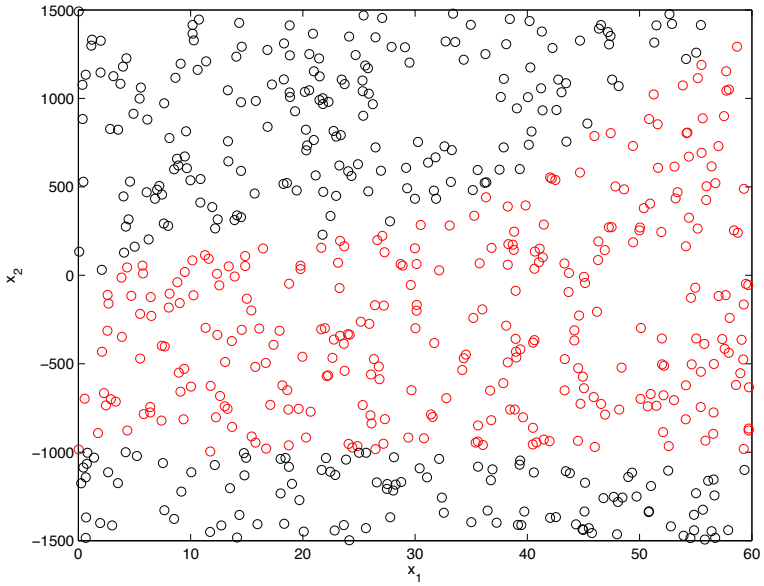

Figure 119: A classification problem which requires more than two hidden layers in order to be addressed (Bishop, 1996).

where t is the desired output and y is the actual output, zero or one. The fraction $\frac{1}{2}$ is used in order to be eliminated after differentiation (Bishop, 1996). The gradient-descent method tries to minimise (7.7) subject to an initial randomly selected set of weights and given inputs x_i. Iteratively, the weights are changing until the error (7.7) converges to a minimum. In each iteration the weights are recalculated according to

$$\mathbf{w}^{u+1} = \mathbf{w}^u - \beta \cdot \nabla E\left(\mathbf{w}^u\right) \tag{7.8}$$

$$\nabla E\left(\mathbf{w}\right) = \left[\frac{\partial E}{\partial w_1}, \frac{\partial E}{\partial w_2} ..... \frac{\partial E}{\partial w_n}\right] \tag{7.9}$$

where u is the iteration number, β is a constant that defines the optimisation step and ∇E is a vector which points towards the direction with the greatest rate of increase (Kreyszig, 1999). The error back-propagating algorithm calculates the derivatives in (7.9) using the chain rule

$$\frac{\partial E}{\partial w_i} = \frac{\partial E}{\partial g(z)} \frac{\partial g(z)}{\partial z(w)} \frac{\partial z(w)}{\partial w_i} \tag{7.10}$$

where

$$z = \sum_{i=1}^{n} w_i x_i. \tag{7.11}$$

From (7.11) it is easy to prove that

$$\frac{\partial z(w)}{\partial w_i} = x_i. \tag{7.12}$$

The derivative of the sigmoid function $g(z)$ with respect to z equals with

$$\frac{\partial g(z)}{\partial z(w)} = \frac{\exp\left(-z(w)\right)}{\left(1+\exp\left(-z(w)\right)\right)^2} = g(z)\left(1-g(z)\right). \tag{7.13}$$

In order to complete the evaluation of (7.10), the derivative $\frac{\partial E}{\partial g(z)}$ needs to be calculated. The latter is equal with

$$\frac{\partial E}{\partial g(z)} = \frac{\partial E}{\partial y} = y - t. \tag{7.14}$$

Substituting (7.12), (7.13) and (7.14) to (7.10) results to

$$\frac{\partial E}{\partial w_i} = (y-t)\left(1-g(z)\right)g(z)x_i. \tag{7.15}$$

Using equation (7.15), the gradient vector (7.9) and consequently $\mathbf{w}^{u+1}$ (7.8) can be evaluated in a straightforward manner. The same approach can be easily expanded to more complex neural nets with arbitrarily number of layers and neurones (Bishop, 1996, Haykin, 2009).

7.4 TRAINING SET

One of the most important aspects of ANN is the training database (Bishop, 1996). To our knowledge, no published work related to demining have ever focused on the quality of the training set. Limited data can result to a low resolution feature space. In addition, non-equally distributed (i.e. unbalanced between the number of data associated with the output patterns) can result to a low convergence rate and over-trained ANN biased to one pattern. To overcome this, Plett et al. (1997) replicated the traces associated with landmines in order to create a balanced training set. This brute approach manages to overcome issues related with the unbalanced data (low convergence etc.) but still the low resolution of the feature space remains.

As it is stated by the Hungarian mathematician Cornelius Lanczos

"A lack of information cannot be remedied by mathematical trickery."

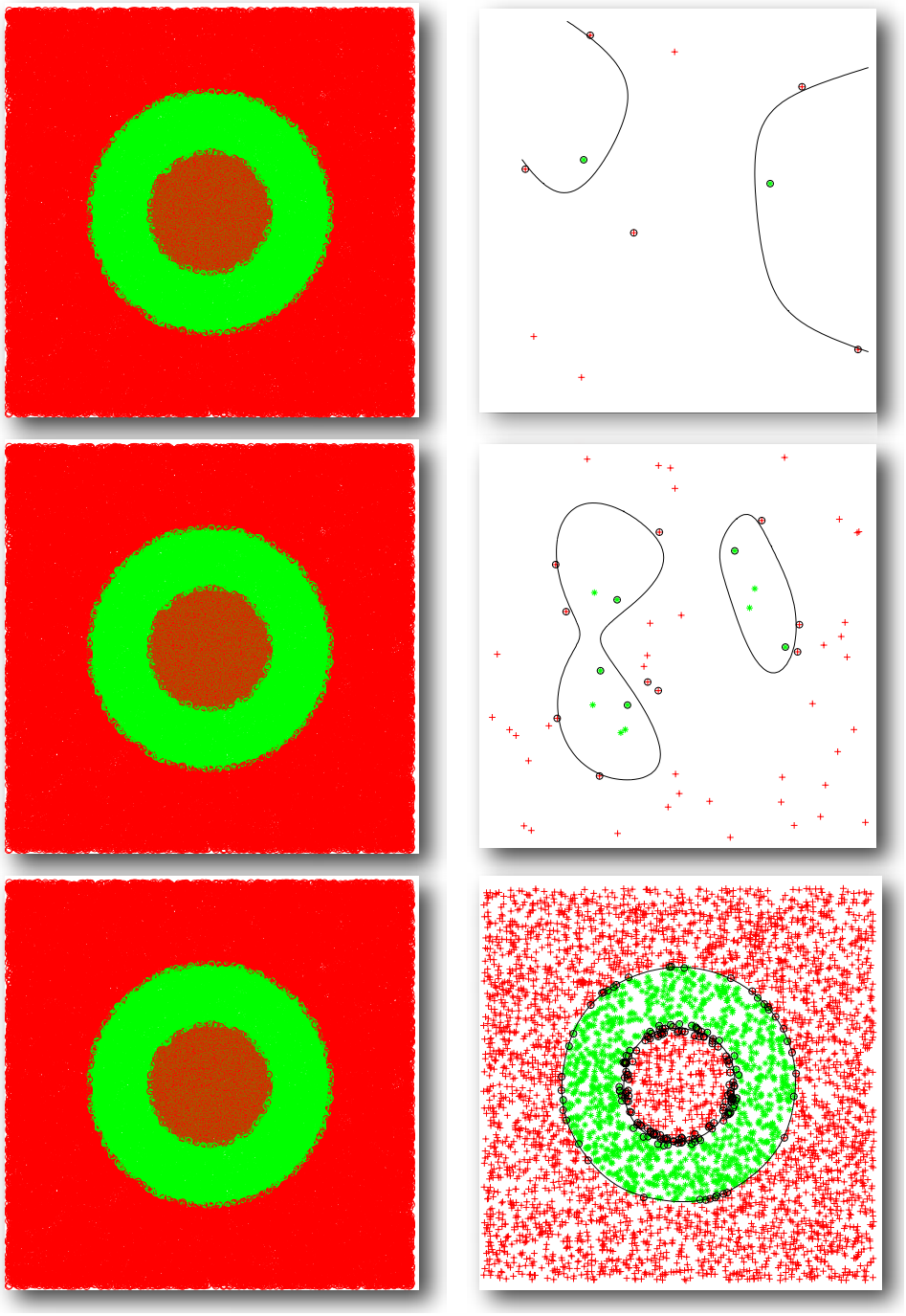

Figure 120: A classification problem consisted of two classes namely, red and green. The problem is two dimensional, i.e. has two inputs. Two homocentric circles draw the boundaries between the two classes. The left images are the true feature space while the right is the resolved feature space using different number of training data. An SVM with a Gaussian Kernel function is used for the present classification. Using limited number of training data, SVM can accurately classify the training set but can not be generalised to the whole feature space.

This is clearly illustrated in Fig. 120 in which different amount of training data are used in order to classify two classes namely, red and green. In the present example Support Vector Machines (SVM) using Gaussian Kernel function are employed for the classification (Haykin, 2009). It is evident that there is no possible way to address lack of information. A representative training sample is necessary in order to fully resolve the feature space illustrated in Fig. 120. Regarding AP landmine detection, a training set that includes all the realistically plausible cases must be employed if a reliable and universal detection scheme is to be developed. A realistic numerical framework can address this problem by providing a sufficient amount of data resulting from fully controlled scenarios.

The training set employed in the present study is evaluated using a 2D FDTD (2,2) method (Taflove, 2005). The numerical scheme used here is a 2D equivalent of the one described in chapter 6. The antenna is simulated as an ideal line source. The input pulse is a Gaussian modulated sinusoidal source with central frequency 1.2 GHz and fractional bandwidth equal to three. The targets used in the simulations are the AP landmines PMA-1 and PMN. Bullets are also added to the models in an effort to add false alarms and increase the complexity. Bullets are modelled as PEC objects. The discretisation step of the FDTD is uniform along the grid with $\Delta x = \Delta z = 1$ mm. The time step is equal to the Courant limit for the 2D case $\Delta t = 2.357$ ps. (Taflove, 2005).

The pre-processed inputs of the ANN are single traces (A-Scans) similar to Plett et al. (1997). The models dimensions are 350×350 mm and the source is placed at the centre of the model with a varying height. The model's fractal dimensions of the water's distribution, the roughness of the surface, the height of the transmitter, the existence or not of the landmines, the type and the depth of the landmines – if they are present in the model – and the number of possible bullets are randomly chosen in an effort to keep the training set equally distributed while increasing its size. With that approach, a diverse set of possible models is generated and subsequently is employed as a training set. The models vary in a realistic context, e.g. the static relative permittivity varies from $\epsilon = 2 - 25$ and so on. Fig. 121 and 122 illustrate a sample of the models used as a training platform for the ANN. The training set consists of 4000 traces from an equally distributed set of models which cover a wide aspect of possible scenarios. Notice that the landmines are always placed at the centre of the model. With that, we avoid the so called outliers (when the antenna is placed on top of the edge of the landmine) which seems to reduce the performance of ANN (Plett et al., 1997, Yang and Bose, 2005).

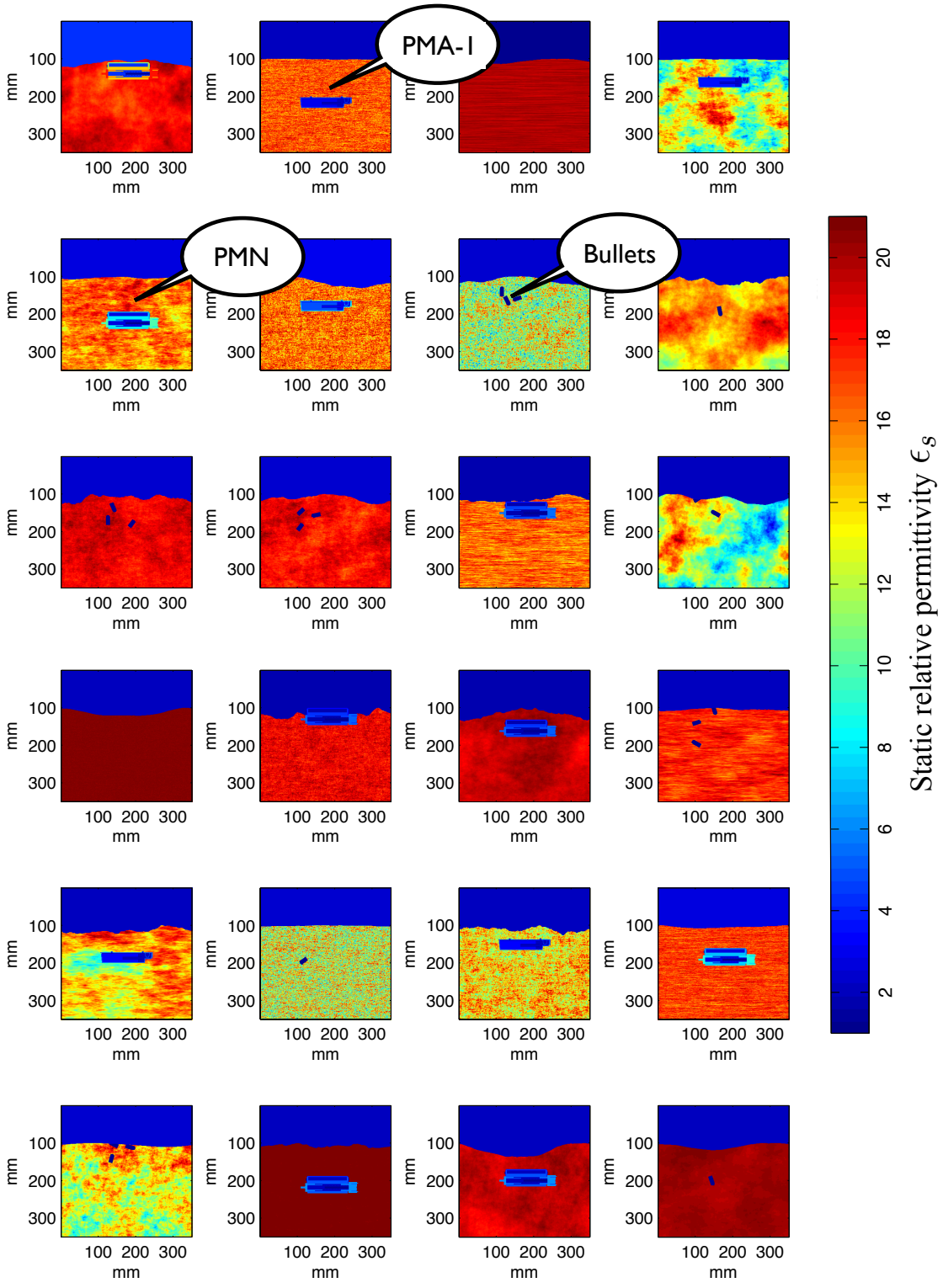

Figure 121: A sample of the models used to train ANN. The bullets are modelled as PEC.

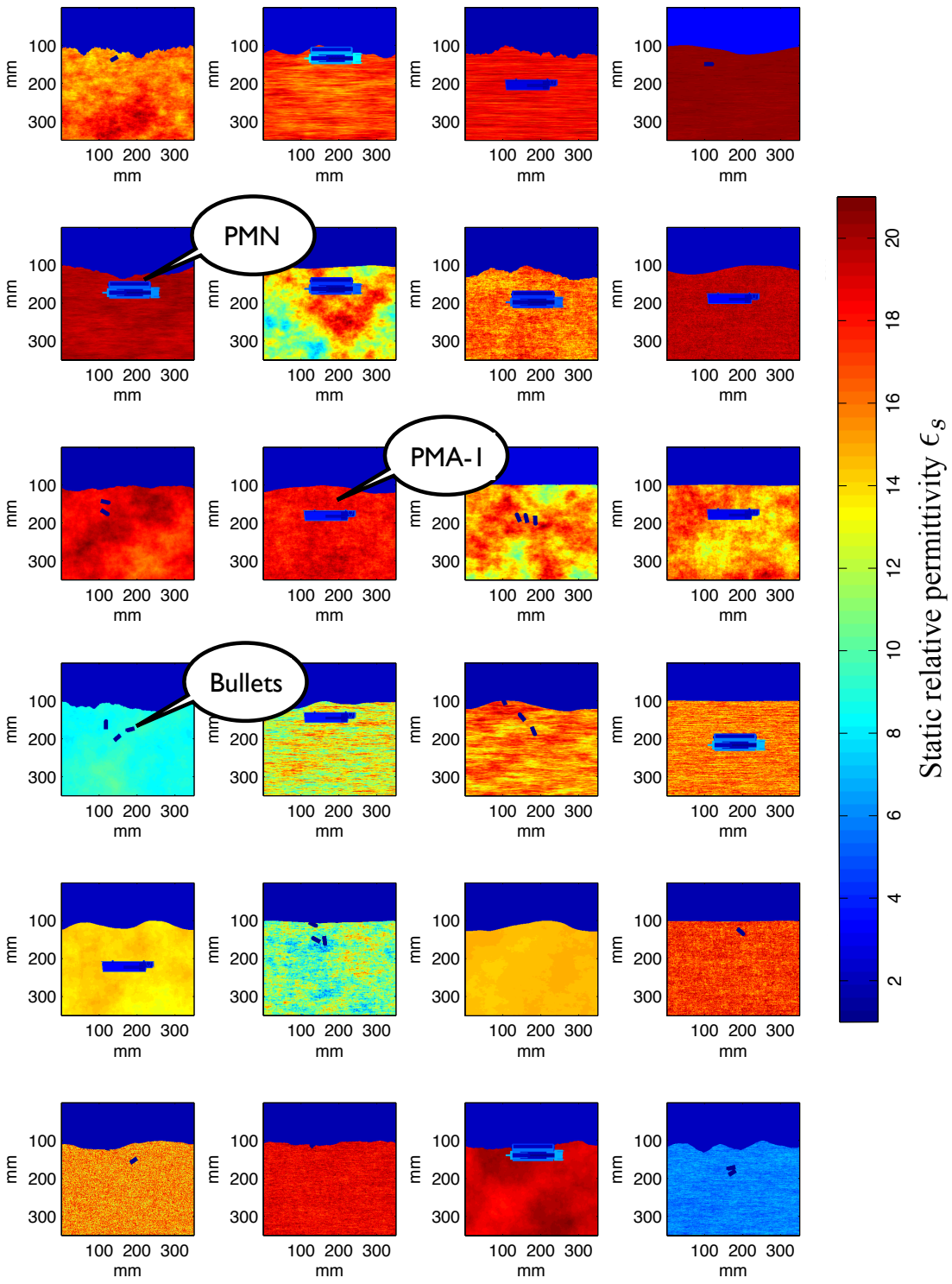

Figure 122: A sample of the models used to train ANN. The bullets are modelled as PEC.

7.5 PRE-PROCESSING

Apart from the quality of the training data, another equally important parameter of ANN is the pre-processing. The raw data contain all the information available, nonetheless, this information is not easily accessible to ANN. Pre-processing address this problem by making the input data more readable, thus, increasing the resolution of the feature space.

In the present study, a processing scheme based on deterministic deconvolution is applied for the classification between PMA-1 and PMN. Initially, the free-space response is subtracted from the raw data in an effort to eliminate the direct wave. Subsequently, a deterministic deconvolution is applied with which the reflectivity of the model is retrieved

$$R(\omega) = \frac{D(\omega) - F(\omega)}{F(\omega) + e^2} = \frac{P(\omega)}{F(\omega) + e^2} \tag{7.16}$$

where R is the reflectivity, F is the direct response, D is the raw data, P is the data after the removal of the direct response and e is a damping factor which aims to overcome instabilities due to possible divisions by zero (ω indicates that the operations in (7.16) take place in frequency domain). Lastly, a moving average filter is employed in order to remove the unnatural high-frequency content of the reflectivity due to deconvolution artefacts.

The procedure described above is used for the classification between the AP landmines PMA-1 and PMN. For classification between AP landmines and non-landmines, it is shown that reflectivity leads to misleading results. Thus, another pre-processing approach is employed to detect landmines against false alarm targets. Ten traces which contain information from false alarms (soil's inhomogeneity, bullets and rough surface) are randomly selected. Then, the matrix $\mathbf{G} = [\mathbf{g}_1,\ \mathbf{g}_2,\ ...\ \mathbf{g}_{10}]$ is defined, where $\mathbf{g}_q$ is the $q$ith randomly selected trace. Subsequently, we approximate the background clutter with a linear combination of the randomly selected traces

$$\mathbf{w} = \left(\mathbf{G}^T\mathbf{G}\right)^{-1}\mathbf{G}^T\mathbf{P} \tag{7.17}$$

$$\mathbf{Q} = \mathbf{P} - \mathbf{G}\cdot\mathbf{w} \tag{7.18}$$

where $\mathbf{P} = [P(1),\ P(2),\ ...\ P(N)]^T$ is the raw data after removing the direct response and $\mathbf{w} = [w(1),\ w(2), ...\ w(10)]^T$ is the weight vector. The predicted clutter is subsequently subtracted from $\mathbf{P}$. The new trace $\mathbf{Q} = [Q(1),\ Q(2),\ ...\ Q(N)]^T$ is the input used to discriminate between AP land-

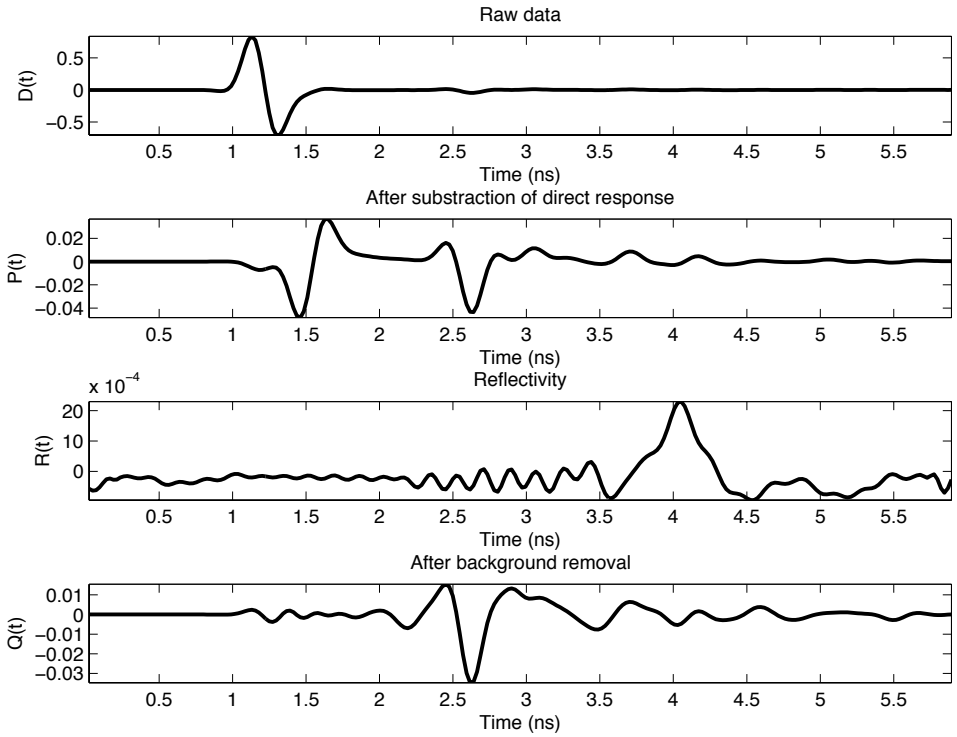

Figure 123: Data collected over a PMN landmine. The first image illustrates the raw data, in the second image the free-space response is subtracted, in the third the smoothed reflectivity (see (7.16)) is calculated and in the fourth the clutter-reduced A-Scan is illustrated (see (7.17) and (7.18)).

mines and false alarms. Fig. 123 illustrates an example of how the raw data are transformed to reflectivity – for inter landmine classification – and to a clutter-reduced A-Scan for isolating landmines from false alarms. Notice that no gain is used in the present framework, since through trial and error it was found that did not substantially affect the performance of ANN.

7.6 NEURAL NETWORKS STRUCTURE

A three-layered ANN (Bishop, 1996, Jain et al., 1996) structure is used in the proposed classification scheme. Through trial and error, it was found, that increasing the complexity of the neural structure did not increase the performance of ANN. A three-layered ANN, with 50 and 30 neurones respectively, was found to maximise the performance without introducing unnecessary complexity which might lead to over fitting (Haykin, 2009). The optimisation employed in the training process is the scaled conjugate gradient method (Moller, 1993). The synthetically evaluated dataset is consisted of 4000 different A-Scans resulting from 4000 different and diverse models. The database is divided into three parts, 60 % of the data are used for training purposes, 20 %

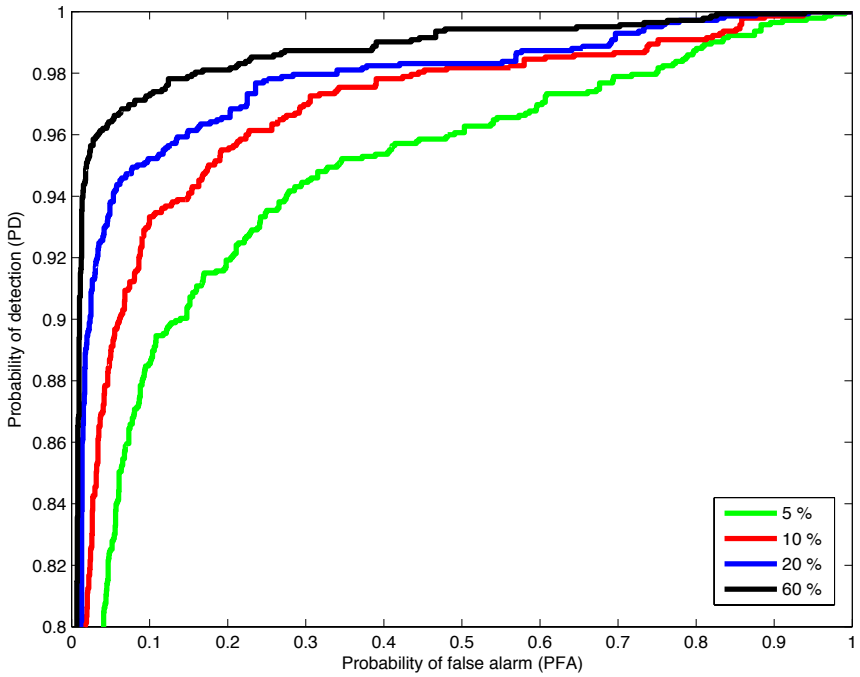

Figure 124: ROC curves using 5 %, 10 % , 20 % and 60 % of the data as training set. The targets of interest are the AP landmines PMN, PMA-1. Scattering fields from bullets, soil's inhomogeneity, rough surface etc. are classified as false alarm targets. A linear combination of ten randomly selected traces is employed in an effort to decrease the clutter from the input data (after the direct response is removed).

of the data are used for testing the ANN performance after the training process and 20 % are used for validation purposes (Bishop, 1996, Haykin, 2009). The training process is supervised, thus, its up to the user to define the targets of interest.

A step by step strategy, similar to the one suggested by Yang and Bose (2005)), is employed in the present classification scheme. Initially, a classification between AP landmines and false alarms isolates the traces of interest which are subsequently further examined in an effort to identify the type of the buried target. Through that, the complexity of the feature space is decreased making detection and classification more accurate. The ANN used in each step are supervised accordingly. Fig. 124 and 125 illustrate the ROC curves for each step. It is evident that increasing the size of the training set while retaining its inclusivity increases the performance of ANN, especially when classification between similar targets (PMA-1 and PMN) is to be achieved. The ROC curves are calculated using the test set, i.e. 20 % of the initial data which were not used during the training process.

Two 2D case studies are examined in order to illustrate the performance of the suggested classification scheme. In the first case study (see Fig. 126), both

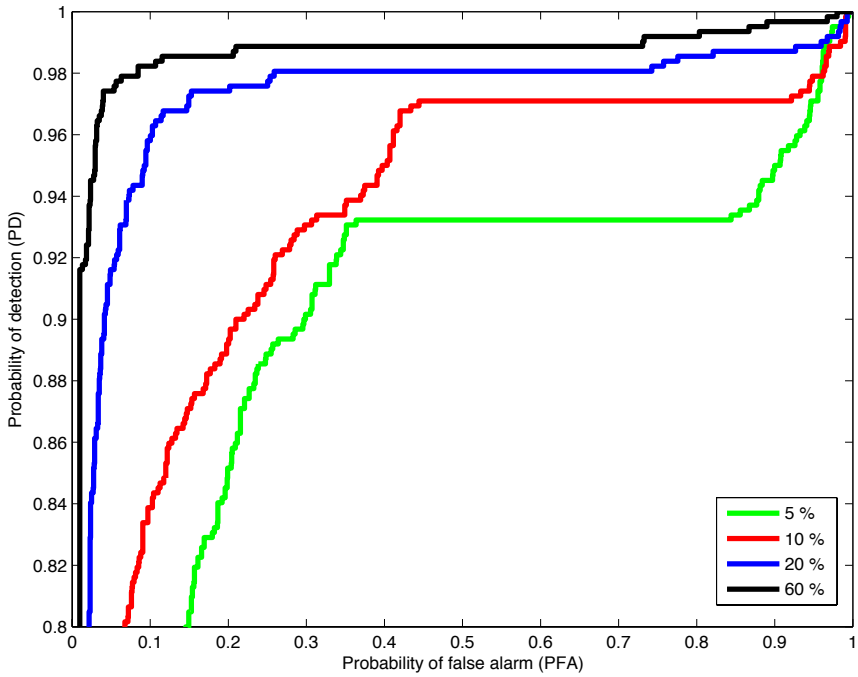

Figure 125: ROC curves using 5 %, 10 % , 20 % and 60 % of the data as training set. The data contains only A-Scans from PMA-1 and PMN buried in a diverse set of media. The pre-processing consists of a deterministic deconvolution (7.16) (after the direct response is removed).

the AP landmines PMA-1 and PMN are employed. Bullets are also added in an effort to increase the complexity of the model. The soil as well as the rough surface varies stochastically obeying a fractal law (see Chapter 6). The electric permittivity is a frequency depended function simulated with a conductive term and a Debye function (Giannakis et al., 2014, Giannakis and Giannopoulos, 2015). The static relative electrical permittivity varies stochastically from $\epsilon = 5 - 25$. The classification scheme uses the clutter-reduced responses of the traces in order to isolate the AP landmines over the false alarm targets. Subsequently, the traces which are classified as AP landmines are further examined. The reflectivity of the aforementioned traces is used in order to identify the type of the AP landmine. In the present examples our objective is to detect PMA-1. The outputs of the suggested scheme in each trace can be either zero or one (landmines or no-landmines, PMN or PMA-1), the value 0.9 is chosen as threshold, the traces which fall below 0.9 are neglected as no targets of interest. As it is shown in Fig. 126, landmines are successfully detected against false alarm targets. In addition, the proposed detection framework proved to be capable of distinguishing between similar targets like PMA-1 and PMN. Fig. 126 shows that PMA-1 is successfully detected and identified over false alarms and PMN.

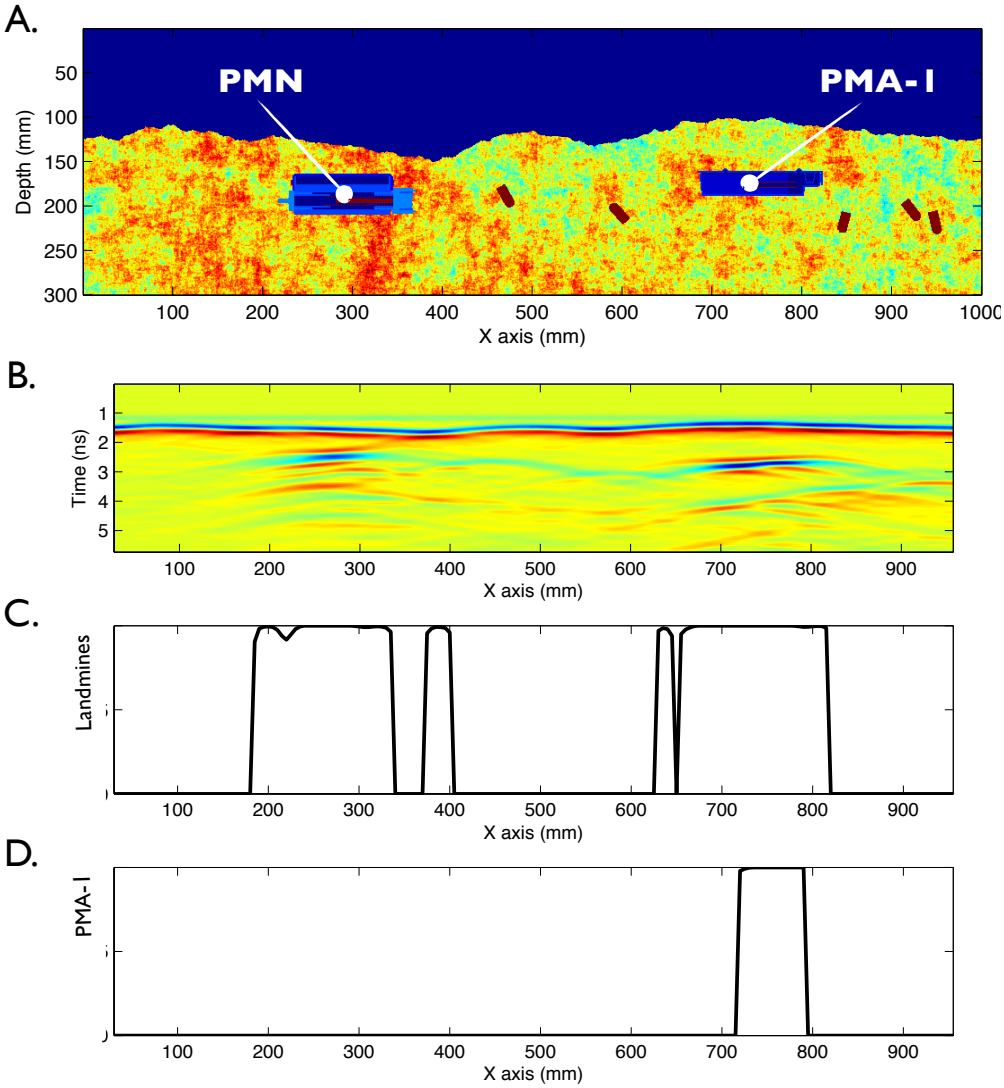

Figure 126: A) A 2D model with a stochastic variation of soil's properties and rough surface. Both AP landmines (PMA-1 and PMN) as well as bullets are buried along the x axis. B) B-Scan after the removal of the direct response (no gain is applied). C) Classification between landmines and false-alarms (soil's inhomogeneity and bullets). Both AP landmines are successfully detected. D) The traces which were categorised as landmines are further examined in order to specifically detect PMA-1.

In the second example (see Fig. 127), the AP landmine PMA-1 is buried in a stochastic medium with static relative permittivity which varies from $\epsilon = 5 - 15$ (higher velocity compared with the example illustrated in Fig. 126). Bullets are also implemented into the model. Again, the suggested detection scheme successfully detects the buried AP landmines as well as identify their type (in the present case PMA-1).

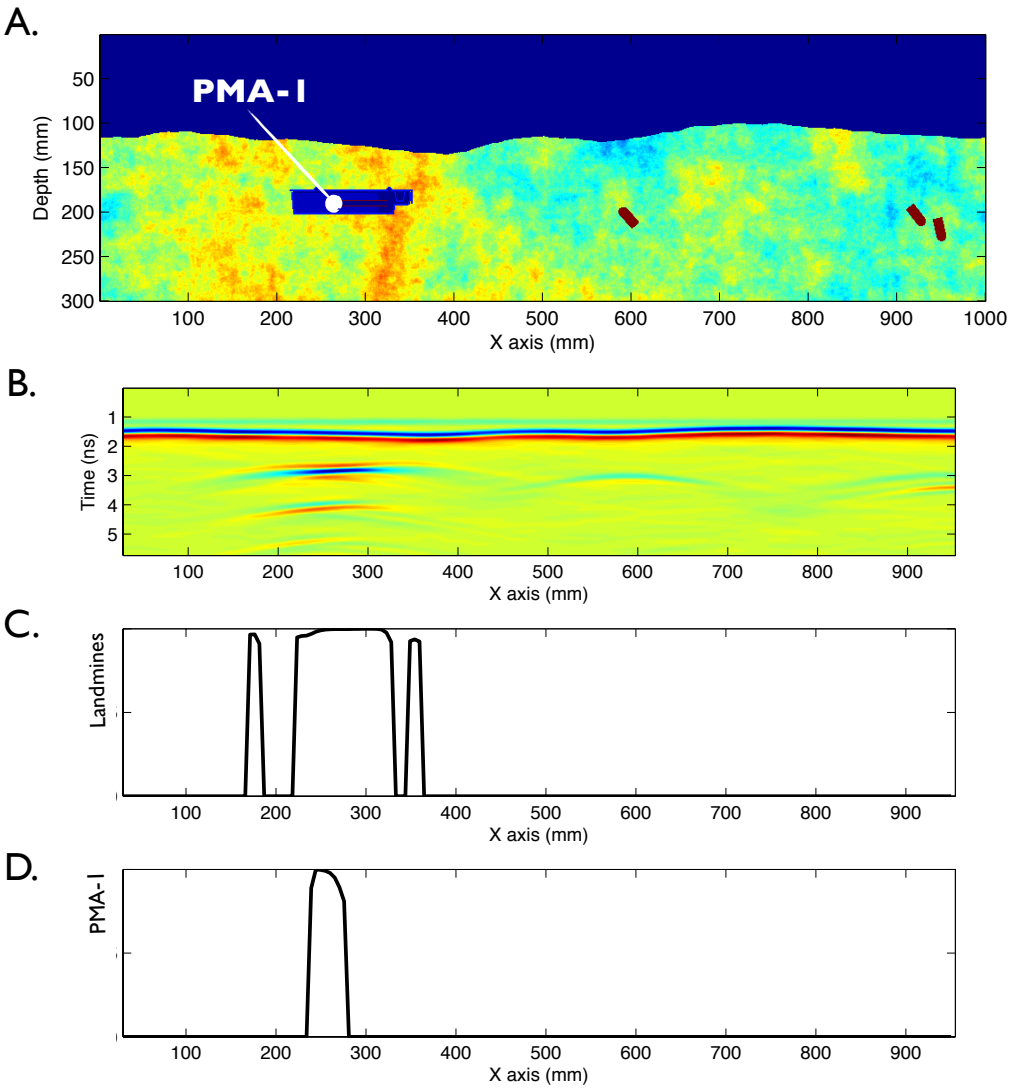

Figure 127: Similar with Fig. 126 using a higher velocity model. The AP landmine PMA-1 and three bullets are shallow buried along the x axis. Again, PMA-1 is successfully detected and identified.

7.7 DISCUSSION

In the present chapter the potential use of machine learning to assist GPR for AP landmine detection is presented. The theoretical concepts behind supervised learning and in particular ANN are outlined and a detection framework is presented which respects the constrains emerging from the nature of the problem i.e. no accurate positioning available, real time processing is required and the detection framework should be effective in a wide range of different environemnts. In that context, the tuned ANN use a single A-Scan as input from which the presence and the type of the AP landmine is given as an output in real time. Due to computational constrains a 2D case study is examined in

order to explore the capabilities of ANN to detect and classify using a single A-Scan.

Supervised learning uses given inputs which correspond to known outputs in order to unravel the underlying relationship between them. Thus, the quality of the training set is highly important and extra effort should be given on obtaining an equally distributed, representative and well-labelled data set. Labelled data are usually expensive and in the case of GPR for landmine detection the training set should include thousands or data from a diverse set of different soils with different topography, soil's properties, depth of the landmine, height of the antenna, false alarm targets and so on. It is apparent that obtaining a good quality training set experimentally is a time-consuming and expensive procedure. This is the reason why previous approaches employed training sets from limited mine lanes which resulted to overtrained detection frameworks only applicable to the specific mine lanes (Azimi-Sadjadi et al., 1992, 1994, Plett et al., 1997, Yang and Bose, 2005). This results from the fact that the target's scattering field is highly affected from the soil's parameters. For example, larger wavelengths occur in saturated soils which are capable to resolve the detailed structures of the target in contrast to small wavelengths which occur in dry soils. In addition, saturated soils result to higher losses which furthermore decrease the overall SNR. Rough surfaces can substantially affect the directivity pattern of the antenna and decrease the performance of the clutter-removal techniques. In the same context, soil's heterogeneities can direct the waveform and increase the resulting clutter. All the above are correlated to each other and affected by the depth of the target as well as the frequencies used and the height of the antenna (Giannakis et al., 2016). In a problem as complicated as the one described above, using a limited training set from a specific soil type, will result to an unreliable detection scheme, since not adequate information is available in order for machine learning to unravel the underlying pattern behind the scattering fields emerging from AP landmines.

Numerical modelling can provide an equally distributed, representative labelled data set if computational resources are available. As it is presented in Chapter 6, the medium can be parametrized using the above inputs

- Sand fraction.
- Bulk density of soil.
- Sand particle's density.
- Type of landmine.
- Burial depth of the landmine.

- Number of false alarm targets.
- Coordinates of false alarm targets.
- Minimum water volumetric fraction.
- Maximum water volumetric fraction.
- Fractal dimension of water volumetric fraction.
- Maximum absolute deviation of the surface.
- Fractal dimension of soil's surface (roughness).

The fact that the soil can be parametrized using a limited number of inputs gives the ability to generate a coherent and representative training set by randomly varying the inputs above. In the present chapter, it is shown that ANN subject to a representative training set can both detect and classify in real time using a single A-Scan. The present detection framework can be applied to a wide range of realistically possible cases as it is shown in Fig. 124 and 125. The importance of the training set is illustrated in Fig. 124 and 125 in which the amount of training data are clearly related to the PD and the PFA. Notice that in Fig. 125 it is shown that ANN can adequately classify between similar targets (PMN and PMA-1) in a wide range of different environments. Nonetheless when only 5 % of the data are employed for training purposes the resulting PD can fall to 0.5 for PFA 0.1.

From the present 2D case study, strong indications are given which support the premise that a single A-Scan contains adequate information regarding the presence and the type of the target. Supervised machine learning can be used in order to teach the system to detect patterns in A-Scans associated with specific types of AP landmines. To do that, a coherent training set should be employed in order to resolve the high non-linear feature space of the problem. This can be achieved by using an accurate and straightforwardly parametrized numerical framework as presented in Chapter 6.

8

CONCLUSIONS AND RECOMMENDATIONS

The aim of this chapter is to provide an outline of the outputs of each previous chapter individually and combine them into a coherent summary and conclusions of the thesis. In addition, recommendations for further research are also provided.

8.1 CONCLUSIONS

The main aim of this thesis that was achieved was to develop and present a realistic numerical scheme for numerical modelling of GPR for AP landmine detection. The reason for developing such a numerical scheme was to be able to be employed as a powerful tool for designing antennas, for evaluating the performance of different processing approaches and for obtaining datasets which can be subsequently applied for training purposes in machine learning. Once a detailed numerical modelling approach is developed appropriate simplifications can be sought at a later stage as they can be introduced only if they are deemed not to affect the overall model's performance.

GPR has been widely used for detecting AP landmines and UXO. Different antennas as well as processing approaches have been suggested through the years. Validation and mapping the limitations of GPR systems is a time consuming and expensive procedure which involves tests in mine lanes with different soil conditions and targets. Numerical modelling can assist to overcome this problem by providing a practical platform for designing and optimising antennas as well as testing processing algorithms to a diverse set of media. In order to do so, the numerical scheme must be accurate and reliable, avoiding simplifications and superficial approaches.

AP landmines are relatively small (10 cm approximately) shallow-buried (no more than 10 cm depth) targets. Due to that, the GPR systems employed for landmine detection use high frequency antennas which are usually operate within a small proximity to the ground. The above, classify the problem as a high-frequency near field GPR application. In contrast to civil engineering applications, AP landmine detection takes place in a large range of diverse scenarios which include homogenous and inhomogeneous media, soil's with rough surface, with or without vegetation, water puddles, different targets in different depths, different antennas and so on. An inclusive numerical scheme

must be able to implement the aforementioned features as realistically and accurately as possible and to deal with the issues which arise from the non-uniqueness of the problem. These issues are:

- Accurate model of the antenna. The antennas operate close to the ground which means that they contribute to the scattering field and give rise to ringing noise which must be accurately simulated. Apart from that, an accurate implementation of the directivity of the antenna is essential for predicting the performance of different GPR systems.
- Landmines can be buried in a large range of stochastically varied soils. Accurate simulation of the geometry of the soil is highly important.
- Rough surface reduces the effectiveness of ground removal techniques which subsequently results to the increase of the PFA. Thus, an accurate implementation of the roughness of the surface must be included in the numerical scheme.
- Soil dielectric properties and specifically the electromagnetic losses of the ground must be accurately implemented. GPR for landmine detection is a high frequency problem which is affected from the resulting dipolar relaxation from the water fraction of the soils. The dispersive properties of the soils must be accurately and fully implemented.
- Features like water puddles and vegetation must be included due to the high frequency content of the antennas. Vegetation and water puddles contribute to the scattering field and reduce the performance of GPR. Thus, it is important these features to be included in a valid and reliable numerical scheme.
- Each AP landmine has unique features and details which make it differ from the others. Training sets employed in machine learning algorithms must accurate simulate the targets characteristics if a classification between targets is to be achieved.

One of the most important characteristic of the numerical scheme is the numerical solver. Different methods for numerically evaluate Maxwell's equations have been suggested and a detailed review is given in Chapter 5. The numerical solver must deals with issues of GPR for landmine detection, namely,

- The numerical solver must operate in time-domain. Time-domain solvers are attractive choices for wide-frequency applications like GPR. The main reason for this, is that all the employed frequencies can be evaluated with a simple execution.

- Frequency depended dielectric properties must be accurately implemented.
- Numerical errors must be kept to a minimum and a balance between accuracy and computational resources is necessary. Numerical artefacts from the boundaries must be minimised as well.

8.1.1 *Computational tools*

FDTD was the method of choice in the present thesis. The reasons for that were discussed in Chapter 5. The most important of them are the time domain nature of FDTD, its computational efficiency and its ability to implement dispersive media. The computational tools which were developed in an effort to improve the performance of FDTD are the following:

- Two novel piecewise linear recursive convolution approaches for implementing dispersive properties in FDTD are proposed (Giannakis and Giannopoulos, 2014). The suggested methods are proven to be more accurate compared with PLRC, complex-conjugate and TRC with no additional computational cost.
- A time-synchronised PML is suggested which reduces the errors associated with the boundary conditions (Giannakis and Giannopoulos, 2015). The present method increases the accuracy while retaining the computational efficiency.

All the methods above are not applicable only to GPR applications. Without any further modification they can be easily applied to any problem related to numerical modelling using FDTD.

8.1.2 *Numerical framework*

Using an accurate and powerful numerical solver is not enough for a coherent and realistic modelling. Implementing both the geometry and the dielectric properties of the model is highly important and necessary in order for the numerical scheme to be reliable and valid. The suggested numerical scheme can be summarised as follows (Giannakis et al., 2014, 2015):

- Fractals are used to model the rough surface since it has been proven that fractals can simulate Earth's topography sufficiently for a wide range of scales. (Turcotte, 1987).

- Fractals are also used to simulate the distribution of the soil's properties and has been proven (see Chapter 6) that give rise to semivariograms frequently found in the field.
- A semi-empirical model suggested by Peplinski et al. (1995) is used to describe the dielectric properties of soils. The semi-empirical model defines the dielectric properties with respect to soil's characteristics like sand fraction, clay fraction, water volumetric fraction, sand's density and bulk density.
- For the frequency range of interest (0.5-3 GHz), a simple Debye function can adequately simulate the semi-empirical model. Debye function is accurately implemented using the novel piecewise linear approaches explained in Chapter 5 (Giannakis and Giannopoulos, 2014).
- A novel algorithm which builds the geometry of vegetation (both grass and roots) is suggested. The dielectric properties of vegetation are simulated with a single Debye pole.
- Water puddles are also included in the model. A single Debye pole is employed in order to describe the dielectric properties of the fresh water, a conductive term can be trivially added in case that brackish or salty water are needed to be modelled.
- Commercial based generic antennas are employed in the simulations (Warren, 2009).
- Accurate models of AP landmines are included in the suggested numerical scheme. The modelled targets are validated through comparisons between measurements and synthetic data.

The above numerical scheme can be used to evaluate processing methods in an inexpensive and practical manner. In the present thesis, widely used processing methods have been trialled to a wide range of diverse environments. Average removal, F-K filter, SVD and ASaS are tested using synthetically calculated but nonetheless realistic data. The interesting output of this comparison is that processing algorithms are case sensitive. Hence, there are no "silver-bullet" approaches which can be applied effectively to all conditions. This raises the question on how processing methods should be evaluated and makes a strong positive argument on how numerical modelling can assist on providing a synthetic, but nonetheless, realistic platform for evaluating and mapping the limitations of processing approaches.

8.1.3 *Artificial neural networks*

Numerical modelling can be used to create large datasets for a wide range of scenarios. A question arises, if these datasets can be used as training sets for machine learning. In Chapter 7, strong indications are given which support the premise that ANN are capable of sufficiently decreasing the PFA, subject to an adequate and equally distributed data set (Giannakis et al., 2015). A practical and sustainable way to train ANN is through numerical modelling. The main obstacles of this approach are the computational demands and the need for an accurate model of the antenna unit which requires either close collaboration with GPR system manufacturers or creation and design of bespoke GPR systems.

8.2 RECOMMENDATIONS

The research contacted in the present thesis is part of a continuous effort to assist AP landmine detection through numerical modelling. Further research should focus on increasing the reliability of the numerical framework and subsequently apply it to demining related problems.

Regarding FDTD, higher order schemes can be used in order to increase the accuracy and the frequency range of the models (Kantartzis and Tsiboukis, 2006). Sub-grids can also be employed when smaller discretisation steps are locally needed. In addition, when lower frequencies are used (e.g. for anti-vehicle landmine detection), efficient methods can be applied (Giannakis et al., 2012) in order to implement the Cole-Cole relaxation mechanisms of the soils (see Chapter 4).

Apart from FDTD, improvements can be made on the model itself. Vegetation's dielectric properties can be improved by employing a more reliable and inclusive function. This function can be calculated experimentally, similarly to the procedure used to extract the semi-empirical model (Peplinski et al., 1995). Regarding the targets, more landmines can be implemented into the numerical framework in an effort to create a more complete library of targets aimed to be used for evaluating GPR systems and for training purposes in machine learning. In addition rusty objects can be modelled using an effective electric permittivity (Cassidy and Milligton, 2009) in an effort to include false alarm targets into the models. Muddy water can be also implemented into the model using a bulk permittivity approximation which will relate the permittivity of the muddy water to the permittivity of its elements (water, soil) and their corresponding fraction. Lastly, tilted antennas can be included in the numerical

framework. Modelling a tilted antenna using FDTD is a challenging task due to the fact that thin planar PEC surfaces can not be adequately and realistically resolved in a discretised grid. In addition, due to the fact that the fields are not collocated, modelling tilted impressed sources as a vector summation is not theoretically robust and fine tuning is necessary in order to model the desired excitation source. To overcome the above, the tilted antenna can be implemented indirectly by rotating the model instead of the antenna.

Although strong indications are given about the capabilities of ANN subject to an adequate training set, nonetheless, the suggested approach must be expanded to 3D models and tested in real field conditions. An accurate antenna model is necessary before moving towards this direction.

Last but not least, all the above must be implemented into a user-friendly package which can be used by a wide range of researchers without the need for a strong background to numerical modelling (Warren et al., 2015).

A

UPDATE EQUATIONS FOR THE FDTD METHOD

Yee's algorithm is applied to Maxwell's equations, notice that all the fields can be explicitly evaluated using their previous-step values.

$$
\begin{aligned}
E_x\Big|_{i,j+\frac{1}{2},k+\frac{1}{2}}^{n+\frac{1}{2}} = & \left(\frac{1 - \frac{\sigma_{i,j+\frac{1}{2},k+\frac{1}{2}} \Delta t}{2\epsilon_{i,j+\frac{1}{2},k+\frac{1}{2}}}}{1 + \frac{\sigma_{i,j+\frac{1}{2},k+\frac{1}{2}} \Delta t}{2\epsilon_{i,j+\frac{1}{2},k+\frac{1}{2}}}} \right) E_x\Big|_{i,j+\frac{1}{2},k+\frac{1}{2}}^{n-\frac{1}{2}} \\
& + \left(\frac{\frac{\Delta t}{\epsilon_{i,j+\frac{1}{2},k+\frac{1}{2}}}}{1 + \frac{\sigma_{i,j+\frac{1}{2},k+\frac{1}{2}} \Delta t}{2\epsilon_{i,j+\frac{1}{2},k+\frac{1}{2}}}} \right) \frac{H_z\Big|_{i,j+1,k+\frac{1}{2}}^{n} - H_z\Big|_{i,j,k+\frac{1}{2}}^{n}}{\Delta y} \\
& - \left(\frac{\frac{\Delta t}{\epsilon_{i,j+\frac{1}{2},k+\frac{1}{2}}}}{1 + \frac{\sigma_{i,j+\frac{1}{2},k+\frac{1}{2}} \Delta t}{2\epsilon_{i,j+\frac{1}{2},k+\frac{1}{2}}}} \right) \frac{H_y\Big|_{i,j+\frac{1}{2},k+1}^{n} - H_y\Big|_{i,j+\frac{1}{2},k}^{n}}{\Delta z} \\
& - \left(\frac{\frac{\Delta t}{\epsilon_{i,j+\frac{1}{2},k+\frac{1}{2}}}}{1 + \frac{\sigma_{i,j+\frac{1}{2},k+\frac{1}{2}} \Delta t}{2\epsilon_{i,j+\frac{1}{2},k+\frac{1}{2}}}} \right) J_{Sx}\Big|_{i,j+\frac{1}{2},k+\frac{1}{2}}^{n}
\end{aligned}
\tag{A.1}
$$

$$
\begin{aligned}
E_y\Big|_{i-\frac{1}{2},j+1,k+\frac{1}{2}}^{n+\frac{1}{2}} = & \left(\frac{1 - \frac{\sigma_{i-\frac{1}{2},j+1,k+\frac{1}{2}} \Delta t}{2\epsilon_{i-\frac{1}{2},j+1,k+\frac{1}{2}}}}{1 + \frac{\sigma_{i-\frac{1}{2},j+1,k+\frac{1}{2}} \Delta t}{2\epsilon_{i-\frac{1}{2},j+1,k+\frac{1}{2}}}} \right) E_y\Big|_{i-\frac{1}{2},j+1,k+\frac{1}{2}}^{n-\frac{1}{2}} \\
& + \left(\frac{\frac{\Delta t}{\epsilon_{i-\frac{1}{2},j+1,k+\frac{1}{2}}}}{1 + \frac{\sigma_{i-\frac{1}{2},j+1,k+\frac{1}{2}} \Delta t}{2\epsilon_{i-\frac{1}{2},j+1,k+\frac{1}{2}}}} \right) \frac{H_x\Big|_{i-\frac{1}{2},j+1,k+1}^{n} - H_x\Big|_{i-\frac{1}{2},j+1,k}^{n}}{\Delta z} \\
& - \left(\frac{\frac{\Delta t}{\epsilon_{i-\frac{1}{2},j+1,k+\frac{1}{2}}}}{1 + \frac{\sigma_{i-\frac{1}{2},j+1,k+\frac{1}{2}} \Delta t}{2\epsilon_{i-\frac{1}{2},j+1,k+\frac{1}{2}}}} \right) \frac{H_z\Big|_{i,j+1,k+\frac{1}{2}}^{n} - H_z\Big|_{i-1,j+1,k+\frac{1}{2}}^{n}}{\Delta x} \\
& - \left(\frac{\frac{\Delta t}{\epsilon_{i-\frac{1}{2},j+1,k+\frac{1}{2}}}}{1 + \frac{\sigma_{i-\frac{1}{2},j+1,k+\frac{1}{2}} \Delta t}{2\epsilon_{i-\frac{1}{2},j+1,k+\frac{1}{2}}}} \right) J_{Sy}\Big|_{i-\frac{1}{2},j+1,k+\frac{1}{2}}^{n}
\end{aligned}
\tag{A.2}
$$

$$
\begin{aligned}
E_z\Big|_{i-\frac{1}{2},j+\frac{1}{2},k+1}^{n+\frac{1}{2}} &= \left(\frac{1-\frac{\sigma_{i-\frac{1}{2},j+\frac{1}{2},k+1}\Delta t}{2\epsilon_{i-\frac{1}{2},j+\frac{1}{2},k+1}}}{1+\frac{\sigma_{i-\frac{1}{2},j+\frac{1}{2},k+1}\Delta t}{2\epsilon_{i-\frac{1}{2},j+\frac{1}{2},k+1}}}\right) E_z\Big|_{i-\frac{1}{2},j+\frac{1}{2},k+1}^{n-\frac{1}{2}} \\
&+ \left(\frac{\frac{\Delta t}{\epsilon_{i-\frac{1}{2},j+\frac{1}{2},k+1}}}{1+\frac{\sigma_{i-\frac{1}{2},j+\frac{1}{2},k+1}\Delta t}{2\epsilon_{i-\frac{1}{2},j+\frac{1}{2},k+1}}}\right) \frac{H_y\Big|_{i,j+\frac{1}{2},k+1}^{n} - H_y\Big|_{i-1,j+\frac{1}{2},k+1}^{n}}{\Delta x} \\
&- \left(\frac{\frac{\Delta t}{\epsilon_{i-\frac{1}{2},j+\frac{1}{2},k+1}}}{1+\frac{\sigma_{i-\frac{1}{2},j+\frac{1}{2},k+1}\Delta t}{2\epsilon_{i-\frac{1}{2},j+\frac{1}{2},k+1}}}\right) \frac{H_x\Big|_{i-\frac{1}{2},j+1,k+1}^{n} - H_x\Big|_{i-\frac{1}{2},j,k+1}^{n}}{\Delta y} \\
&- \left(\frac{\frac{\Delta t}{\epsilon_{i-\frac{1}{2},j+\frac{1}{2},k+1}}}{1+\frac{\sigma_{i-\frac{1}{2},j+\frac{1}{2},k+1}\Delta t}{2\epsilon_{i-\frac{1}{2},j+\frac{1}{2},k+1}}}\right) J_{Sz}\Big|_{i-\frac{1}{2},j+\frac{1}{2},k+1}^{n}
\end{aligned}
\tag{A.3}
$$

$$
\begin{aligned}
H_x\Big|_{i-\frac{1}{2},j+1,k+1}^{n+1} &= \left(\frac{1-\frac{\sigma^*_{i-\frac{1}{2},j+1,k+1}\Delta t}{2\mu_{i-\frac{1}{2},j+1,k+1}}}{1+\frac{\sigma^*_{i-\frac{1}{2},j+1,k+1}\Delta t}{2\mu_{i-\frac{1}{2},j+1,k+1}}}\right) H_x\Big|_{i-\frac{1}{2},j+1,k+1}^{n} \\
&+ \left(\frac{\frac{\Delta t}{\mu_{i-\frac{1}{2},j+1,k+1}}}{1+\frac{\sigma^*_{i-\frac{1}{2},j+1,k+1}\Delta t}{2\mu_{i-\frac{1}{2},j+1,k+1}}}\right) \frac{E_y\Big|_{i-\frac{1}{2},j+1,k+\frac{3}{2}}^{n+\frac{1}{2}} - E_y\Big|_{i-\frac{1}{2},j+1,k+\frac{1}{2}}^{n+\frac{1}{2}}}{\Delta z} \\
&- \left(\frac{\frac{\Delta t}{\mu_{i-\frac{1}{2},j+1,k+1}}}{1+\frac{\sigma^*_{i-\frac{1}{2},j+1,k+1}\Delta t}{2\mu_{i-\frac{1}{2},j+1,k+1}}}\right) \frac{E_z\Big|_{i-\frac{1}{2},j+\frac{3}{2},k+1}^{n+\frac{1}{2}} - E_z\Big|_{i-\frac{1}{2},j+\frac{1}{2},k+1}^{n+\frac{1}{2}}}{\Delta y} \\
&- \left(\frac{\frac{\Delta t}{\mu_{i-\frac{1}{2},j+1,k+1}}}{1+\frac{\sigma^*_{i-\frac{1}{2},j+1,k+1}\Delta t}{2\mu_{i-\frac{1}{2},j+1,k+1}}}\right) M_{Sx}\Big|_{i-\frac{1}{2},j+1,k+1}^{n+\frac{1}{2}}
\end{aligned}
\tag{A.4}
$$

$$
\begin{aligned}
H_y\Big|_{i,j+\frac{1}{2},k+1}^{n+1} &= \left(\frac{1-\frac{\sigma^*_{i,j+\frac{1}{2},k+1}\Delta t}{2\mu_{i,j+\frac{1}{2},k+1}}}{1+\frac{\sigma^*_{i,j+\frac{1}{2},k+1}\Delta t}{2\mu_{i,j+\frac{1}{2},k+1}}}\right) H_y\Big|_{i,j+\frac{1}{2},k+1}^{n} \\
&+ \left(\frac{\frac{\Delta t}{\mu_{i,j+\frac{1}{2},k+1}}}{1+\frac{\sigma^*_{i,j+\frac{1}{2},k+1}\Delta t}{2\mu_{i,j+\frac{1}{2},k+1}}}\right) \frac{E_z\Big|_{i+\frac{1}{2},j+\frac{1}{2},k+1}^{n+\frac{1}{2}} - E_z\Big|_{i-\frac{1}{2},j+\frac{1}{2},k+1}^{n+\frac{1}{2}}}{\Delta x} \\
&- \left(\frac{\frac{\Delta t}{\mu_{i,j+\frac{1}{2},k+1}}}{1+\frac{\sigma^*_{i,j+\frac{1}{2},k+1}\Delta t}{2\mu_{i,j+\frac{1}{2},k+1}}}\right) \frac{E_x\Big|_{i,j+\frac{1}{2},k+\frac{3}{2}}^{n+\frac{1}{2}} - E_x\Big|_{i,j+\frac{1}{2},k+\frac{1}{2}}^{n+\frac{1}{2}}}{\Delta z} \\
&- \left(\frac{\frac{\Delta t}{\mu_{i,j+\frac{1}{2},k+1}}}{1+\frac{\sigma^*_{i,j+\frac{1}{2},k+1}\Delta t}{2\mu_{i,j+\frac{1}{2},k+1}}}\right) M_{Sy}\Big|_{i,j+\frac{1}{2},k+1}^{n+\frac{1}{2}}
\end{aligned}
\tag{A.5}
$$

$$
\begin{aligned}
H_z\Big|_{i,j+1,k+\frac{1}{2}}^{n+1} &= \left(\frac{1-\frac{\sigma^*_{i,j+1,k+\frac{1}{2}}\Delta t}{2\mu_{i,j+1,k+\frac{1}{2}}}}{1+\frac{\sigma^*_{i,j+1,k+\frac{1}{2}}\Delta t}{2\mu_{i,j+1,k+\frac{1}{2}}}}\right) H_z\Big|_{i,j+1,k+\frac{1}{2}}^{n} \\
&+ \left(\frac{\frac{\Delta t}{\mu_{i,j+1,k+\frac{1}{2}}}}{1+\frac{\sigma^*_{i,j+1,k+\frac{1}{2}}\Delta t}{2\mu_{i,j+1,k+\frac{1}{2}}}}\right) \frac{E_x\Big|_{i,j+\frac{3}{2},k+\frac{1}{2}}^{n+\frac{1}{2}} - E_x\Big|_{i,j+\frac{1}{2},k+\frac{1}{2}}^{n+\frac{1}{2}}}{\Delta y} \\
&- \left(\frac{\frac{\Delta t}{\mu_{i,j+1,k+\frac{1}{2}}}}{1+\frac{\sigma^*_{i,j+1,k+\frac{1}{2}}\Delta t}{2\mu_{i,j+1,k+\frac{1}{2}}}}\right) \frac{E_y\Big|_{i+\frac{1}{2},j+1,k+\frac{1}{2}}^{n+\frac{1}{2}} - E_y\Big|_{i-\frac{1}{2},j+1,k+\frac{1}{2}}^{n+\frac{1}{2}}}{\Delta x} \\
&- \left(\frac{\frac{\Delta t}{\mu_{i,j+1,k+\frac{1}{2}}}}{1+\frac{\sigma^*_{i,j+1,k+\frac{1}{2}}\Delta t}{2\mu_{i,j+1,k+\frac{1}{2}}}}\right) M_{Sz}\Big|_{i,j+1,k+\frac{1}{2}}^{n+\frac{1}{2}}
\end{aligned}
\tag{A.6}
$$

B

PLRC ORDER OF ACCURACY

PLRC (Kelley and Luebbers, 1996) tries to numerically evaluate the following integral

$$\int_{n\Delta t}^{(n+1)\Delta t} e^{Q_s(t-\tau)}\vec{E}d\tau \tag{B.1}$$

subject to a linear constrain for the electric field. In the following we preset a proof about the approximately second order accuracy of this assumption of linearity:

By applying the integration by parts rule to the convolution yields:

$$e^{Q_s^{(n+1)\Delta t}}\int_{n\Delta t}^{(n+1)\Delta t} e^{-Q_s\cdot\tau}\vec{E}d\tau = -\frac{e^{Q_s(n+1)\Delta t}}{Q_s}\int_{n\Delta t}^{(n+1)\Delta t}\frac{\partial e^{-Q_s\tau}}{\partial\tau}\vec{E}d\tau = \tag{B.2}$$

$$= -\frac{e^{Q_s(n+1)\Delta t}}{Q_s}\left(e^{-Q_s\cdot\tau}\vec{E}|_{n\Delta t}^{(n+1)\Delta t} + \frac{1}{Q_s}\int_{n\Delta t}^{(n+1)\Delta t}\frac{\partial\vec{E}}{\partial\tau}\frac{\partial e^{-Q_s\tau}}{\partial\tau}d\tau\right) = \tag{B.3}$$

$$= -\frac{e^{Q_s(n+1)\Delta t}}{Q_s}\left(e^{-Q_s\cdot\tau}\vec{E}|_{n\Delta t}^{(n+1)\Delta t} + \frac{1}{Q_s}\left(e^{-Q_s\tau}\frac{\partial\vec{E}}{\partial\tau}|_{n\Delta t}^{(n+1)\Delta t} - \int_{n\Delta t}^{(n+1)\Delta t}\frac{\partial^2\vec{E}}{\partial\tau^2}e^{-Q_s\cdot\tau}d\tau\right)\right) = \tag{B.4}$$

$$= -\frac{e^{Q_s(n+1)\Delta t}}{Q_s}\left(e^{-Q_s\cdot\tau}\vec{E}|_{n\Delta t}^{(n+1)\Delta t} + \frac{1}{Q_s}\left(e^{-Q_s\tau}\frac{\partial\vec{E}}{\partial\tau}|_{n\Delta t}^{(n+1)\Delta t} + \frac{1}{Q_s}\left(e^{-Q_s\tau}\frac{\partial^2\vec{E}}{\partial\tau^2}|_{n\Delta t}^{(n+1)\Delta t} + ...\right)\right)\right). \tag{B.5}$$

If we continue with this kind of analysis, the convolution is expressed in higher order (n) derivatives of the electric field multiplied by terms of the form of $\frac{1}{Q_s^n}$. Assuming that $1/Q_s < 1$, (which is the common scenario) the order of accuracy of the approximation to the convolution can be found by taking the last term in equation (B.5) as terms with derivatives higher than $n > 2$ are multiplied by $1/Q_s^n < 1/Q_s^{n-1}$. That means that the errors related with higher order derivatives ($n > 2$) of the electric field are of smaller order when compared with the errors related to the second derivative of the electric field. This is because they are multiplied with the term $1/Q_s^n$ where n is the order of the derivative and $1/Q_s^n < 1/Q_s^{n-1}$. So, we assume that the derivatives higher than the second ($n = 2$) are zero, i.e. we isolate the term with the higher order of error assuming a piecewise linear behaviour of the electric field.

$$Error \approx -\frac{e^{Q_s(n+1)\Delta t}}{Q_s^2}\int_{n\Delta t}^{(n+1)\Delta t}\frac{\partial^2\vec{E}}{\partial\tau^2}e^{-Q_s\cdot\tau}d\tau \tag{B.6}$$

$$\approx -\frac{e^{Q_s(n+1)\Delta t}}{Q_s^3}\frac{\partial^2\vec{E}}{\partial t^2}\left(e^{-Q_s(n+1)\Delta t}-e^{-Q_s n\Delta t}\right) \tag{B.7}$$

$$\approx -\frac{1}{Q_s^3}\frac{\partial^2\vec{E}}{\partial t^2}\left(1-e^{Q_s\Delta t}\right) \tag{B.8}$$

By expressing the term $\left(1-e^{Q_s\Delta t}\right)$ using a series expansion yields :

$$Error \approx \frac{1}{Q_s^3}\frac{\partial^2\vec{E}}{\partial t^2}\left(\frac{(Q_s\Delta t)}{1}+\frac{(Q_s\Delta t)^2}{2}+\frac{(Q_s\Delta t)^3}{3!}+\frac{(Q_s\Delta t)^4}{4!}.....\right) \tag{B.9}$$

With $Q_s\Delta t<1$ (which again is the most common scenario), the terms with higher order can be neglected.

$$Error \approx \frac{\Delta t}{Q_s^2}\frac{\partial^2\vec{E}(t)}{\partial t^2} \tag{B.10}$$

The term $1/Q_s$ has more or less the same order of magnitude with Δt (in most of the applications), so $1/Q_s^2$ usually is smaller than Δt. So, the order of accuracy of the convolution is higher than second order but approximately is considered to be at least a second order accuracy.

The error related with the numerical evaluation of the convolution is related to the time step (Δt), to the term $1./Q_s$ and to the second derivative $\frac{\partial^2\vec{E}}{\partial t^2}$ which in turn are related to the frequency content of the propagating pulse and the overall resolution of the model.

C

ADE INTERPRETATION OF POLARISATION DENSITY METHOD

Transforming (5.60) into the frequency domain yields

$$\vec{R}_s(\omega) = \frac{-\frac{W_s}{Q_s}}{1-\frac{j\omega}{Q_s}}\vec{E}(\omega). \tag{C.1}$$

Multiplying both sides of (C.1) with $1-\frac{j\omega}{Q_s}$ yields

$$\vec{R}_s(\omega) - \frac{j\omega}{Q_s}\vec{R}_s(\omega) = -\frac{W_s}{Q_s}\vec{E}(\omega) \tag{C.2}$$

which on the time domain is equal to

$$\vec{R}_s - \frac{1}{Q_s}\frac{\partial \vec{R}_s}{\partial t} = -\frac{W_s}{Q_s}\vec{E}. \tag{C.3}$$

We solve this differential equation for each time interval $n\Delta t - (n+1)\Delta t$ separately assuming that the electric field is a first order polynomial in each interval. The initial condition for such an ODE is $\vec{R}_s = \vec{R}_s^{n\Delta t}$ for $a\Delta t = 0$ ($\alpha \in [0\ \ 1]$).

So, for each time interval we have

$$\vec{R}_s^{(n+\alpha)\Delta t} - \frac{1}{Q_s}\frac{\partial \vec{R}_s^{(n+\alpha)\Delta t}}{\partial(\alpha\Delta t)} = -\frac{W_s}{Q_s}\left(\vec{E}^{n\Delta t} + \frac{\vec{E}^{(n+1)\Delta t} - \vec{E}^{n\Delta t}}{\Delta t}\alpha\Delta t\right). \tag{C.4}$$

Taking the Laplace transform of (C.4) yields

$$\vec{LP}_s^{(n+\alpha)\Delta t} - \frac{1}{Q_s}\left(S \cdot \vec{LP}_s^{(n+\alpha)\Delta t} - \vec{R}_s^{n\Delta t}\right) == -\frac{W_s}{Qs}\left(\frac{\vec{E}^{n\Delta t}}{S} + \frac{\vec{E}^{(n+1)\Delta t} - \vec{E}^{n\Delta t}}{\Delta t \cdot S^2}\right)$$

(C.5)

where $\vec{LP}_s^t = \mathcal{L}(\vec{R}_s^t)$, $\vec{R}_s^t = \mathcal{L}^{-1}(\vec{LP}_s^t)$ and $\mathcal{L}(\frac{\partial \vec{R}_s^t}{\partial t}) = S \cdot \vec{LP}_s^t - \vec{R}_s^0$, where $S \in \mathbb{C}$. Rearranging terms in (C.5) and solving for $\vec{LP}_s^{(n+\alpha)\Delta t}$ gives

$$\vec{LP}_s^{(n+a)\Delta t} = \frac{\vec{R}_s^{n\Delta t}}{(S - Q_s)} + + W_s \left(\frac{\vec{E}^{n\Delta t}}{S(S - Q_s)} + \frac{\vec{E}^{(n+1)\Delta t} - \vec{E}^{n\Delta t}}{\Delta t \cdot S^2 (S - Q_s)} \right). \quad \text{(C.6)}$$

From Laplace transform theory (Poularikas, 1996) we know that

$$\mathcal{L}^{-1} \left(\frac{1}{S - Q_s} \right) = e^{Q_s \alpha \Delta t} \quad \text{(C.7)}$$

$$\mathcal{L}^{-1} \left(\frac{1}{S(S - Q_s)} \right) = -\frac{1}{Q_s}(1 - e^{Q_s \alpha \Delta t}) \quad \text{(C.8)}$$

$$\mathcal{L}^{-1} \left(\frac{1}{S^2(S - Q_s)} \right) = -\frac{\alpha \Delta t}{Q_s} - \frac{1}{Q_s^2}(1 - e^{Q_s \alpha \Delta t}). \quad \text{(C.9)}$$

Transforming (C.6) back to time domain using (C.7), (C.8) and (C.9) we obtain (5.78). Therefore, one can easily arrive at exactly the same update equations as presented in section 5.4.1 for the polarisation density method (Giannakis and Giannopoulos, 2014).

D

ADE INTERPRETATION OF CURRENT DENSITY METHOD

Transforming (5.90) into the frequency domain yields

$$\vec{T}_s(\omega) = \frac{-\frac{W_s}{Q_s}}{1-\frac{j\omega}{Q_s}} j\omega\vec{E}(\omega). \tag{D.1}$$

Multiplying both sides of (D.1) with $1-\frac{j\omega}{Q_s}$ gives

$$\vec{T}_s(\omega) - \frac{j\omega}{Q_s}\vec{T}_s(\omega) = -\frac{W_s}{Q_s} j\omega\vec{E}(\omega). \tag{D.2}$$

By transforming (D.2) to time domain a first order differential equation is obtained

$$\vec{T}_s - \frac{1}{Q_s}\frac{\partial\vec{T}_s}{\partial t} = -\frac{W_s}{Q_s}\frac{\partial\vec{E}}{\partial t}. \tag{D.3}$$

In order to solve this equation subject to the assumption that the derivative of the electric field is constant in each time interval and without making any assumptions about the nature of T_s, we use a power series method (Kreyszig, 1999). First we define $\vec{T}_s$ in the interval $n\Delta t-(n+1)\Delta t$ as an infinity order polynomial (*i.e.* a power series)

$$\vec{T}_s = \sum_{k=0}^{\infty} \vec{v}_k(\alpha\Delta t)^k \tag{D.4}$$

where $\vec{v}_k$ are vectors and $\alpha \in [0\ \ 1]$. Substituting (D.4) to (D.3) yields

$$\sum_{k=0}^{\infty} \vec{v}_k(\alpha\Delta t)^k - \frac{1}{Q_s}\sum_{k=1}^{\infty} k\cdot\vec{v}_k(\alpha\Delta t)^{k-1} = -\frac{W_s}{Q_s}\frac{\partial\vec{E}}{\partial t}. \tag{D.5}$$

Equation (D.5) can be written in a more practical form as

$$\vec{v}_0 - \frac{\vec{v}_1}{Q_s} + \sum_{k=1}^{\infty} (\alpha \Delta t)^k \left(\vec{v}_k - \frac{\vec{v}_{k+1}(k+1)}{Q_s} \right) = -\frac{W_s}{Q_s} \frac{\partial \vec{E}}{\partial t}. \tag{D.6}$$

This method is applied in each time interval separately so, the right term can be considered as constant. The initial condition of this differential equation in each time interval is $\vec{T}_s = \vec{T}_s^{n\Delta t}$ for $a\Delta t = 0$. From that initial condition and (D.4) can be easily shown that $\vec{v}_0 = \vec{T}_s^{n\Delta t}$.

From (D.6) by equating the coefficients of the same power of $a\Delta t$ on the left and right side yields

$$\vec{v}_0 - \frac{\vec{v}_1}{Q_s} = -\frac{W_s}{Q_s} \frac{\partial \vec{E}}{\partial t} \tag{D.7}$$

$$\vec{v}_1 = \left(\frac{W_s}{Q_s} \frac{\partial \vec{E}}{\partial t} + \vec{T}_s^{n\Delta t} \right) Q_s. \tag{D.8}$$

If we define $\vec{Y} = \left(\frac{W_s}{Q_s} \frac{\partial \vec{E}}{\partial t} + \vec{T}_s^{n\Delta t} \right)$ then

$$\vec{v}_1 = \vec{Y} Q_s, \tag{D.9}$$

$$-\frac{2\vec{v}_2}{Q_s} + \vec{v}_1 = 0, \quad \vec{v}_2 = \frac{\vec{v}_1 Q_s}{2} = \frac{\vec{Y} Q_s^2}{2} \tag{D.10}$$

$$-\frac{3\vec{v}_3}{Q_s} + \vec{v}_2 = 0, \quad \vec{v}_3 = \frac{\vec{v}_2 Q_s}{3} = \frac{\vec{v}_1 Q_s^2}{3!} = \frac{\vec{Y} Q_s^3}{3!}. \tag{D.11}$$

Repeating the process in a similar way for all the coefficients we derive the inclusive formula for $k = 1, 2, 3, 4...$

$$\vec{v}_k = \frac{\vec{Y}(Q_s)^k}{k!} = \left(\frac{W_s}{Q_s} \frac{\partial \vec{E}}{\partial t} + \vec{T}_s^{n\Delta t} \right) \frac{(Q_s)^k}{k!}. \tag{D.12}$$

Substituting (D.12) to (D.4) and using the initial condition (*i.e.* $v_0 = \vec{T}_s^{n\Delta t}$) yields

$$\vec{T}_s = \vec{T}_s^{n\Delta t} \left(1 + \sum_{k=1}^{\infty} \frac{(Q_s \alpha \Delta t)^k}{k!} \right) + \frac{W_s}{Q_s} \frac{\partial \vec{E}}{\partial t} \sum_{k=1}^{\infty} \frac{(Q_s \alpha \Delta t)^k}{k!}. \tag{D.13}$$

The Maclaurin series for $e^{Q_s a \Delta t}$ is given by

$$e^{Q_s \alpha \Delta t} = 1 + \sum_{k=1}^{\infty} \frac{(Q_s \alpha \Delta t)^k}{k!}. \tag{D.14}$$

Using (D.14), (D.13) and a central difference scheme for the derivative of the electrical field in time in (D.13) we derive (5.92). As a result, one can then easily arrive at exactly the same update equations as presented in section 5.4.2 for the current density density method (Giannakis and Giannopoulos, 2014). From (D.4), it is clear that no simplifications are made about the order of $\vec{T}_s$ in the interval $n\Delta t - (n+1)\Delta t$.

E

GEOMETRICAL REPRESENTATION OF AP LANDMINES

Polynomials and parametric equations are employed in an effort to mathematically express the geometry of the dummy AP landmines. Subsequently 3D models are constructed based on the aforementioned functions. In all the models the discretisation step is uniform along the grid and equals to $\Delta x = \Delta y = \Delta z = 1$ mm.

E.1 PMA-1

Initially the main part of PMA-1 is generated (see Fig. 128). The base of the main core is linearly increasing with height along both X and Y axis. The relative permittivity of the plastic is equal with $\epsilon = 2.5$.

```
clear
clc
close all

%Define the (0,0,0)-(Cx,Cy,Cz) coordinates of the landmine
    model
Cx=10;
Cy=10;
Cz=1;

%Define the relative permittivities of plastic and rubber
plast=2.5
wax=6

%For computational efficiency we predefine the 3D grid.
P(1:1:160,1:1:70,1:1:50)=0;

%Define the X-Y boundaries of the bottom cap of the PMA-1
axx=Cx;
bxx=Cx+130;
ayy=Cy;
byy=Cy+55;
```

```
%As the z increases the X-Y boundaries are linearly
    increasing
for z=1:1:25
y=(0.1*(z-1));
ay=ayy-y;
by=byy+y;

x=(0.1*(z-1));
ax=axx-x;
bx=bxx+x;

P(round(ax):1:round(bx),round(ay):1:round(by),Cz+z)=plast;
end
```

The same procedure is repeated choosing smaller initial boundaries in order to fill the inner part of the main core with air (see Fig. 129).

```
%The boundaries are reduced by 2 mm
axx=Cx+2;
bxx=Cx+130-2;
ayy=Cy+2;
byy=Cy+55-2;

%Notice that z starts from 3 mm
for z=3:1:25
y=(0.1*(z-1));
ay=ayy-y;
by=byy+y;

x=(0.1*(z-1));
ax=axx-x;
bx=bxx+x;

P(round(ax):1:round(bx),round(ay):1:round(by),Cz+z)=1;
end
```

Subsequently five circular holes are added at the main core. The radius of the holes are 1.7 mm and they are irregularly placed along the bottom surface and on the sides of PMA-1 (see Fig. 130). The distance between two points is calculated by evaluating the norm of their vector difference. For example the distance between $(x_1,\ y_1)$ and $(x_2,\ y_2)$ is equal with $||\vec{X_1} - \vec{X_2}||$ where $\vec{X_1} = [x_1,\ y_1]$ and $\vec{X_2} = [x_2,\ y_2]$.

```
%Define the width of the holes
z=1:1:3;
%Define the center (ps) and the radius (Ra) of the first
    hole
ps=[7,7];
Ra=1.7;

%Generate the first hole

for i=1:1:20
 for j=1:1:20
 ps1=[i,j];
 if norm(ps - ps1) < Ra;
 P(Cx+i,Cy+j,Cz+z)=0;
 end
 end
end

%Define the center of the second hole (all the holes have
    the same radius)
ps=[123,48];

for i=115:1:130
 for j=30:1:55
 ps1=[i,j];
 if norm(ps - ps1) < Ra;
 P(Cx+i,Cy+j,Cz+z)=0;
 end
 end
end

%Define the center of the third hole
ps=[104.5,30];

for i=100:1:125
  for j=20:1:35
  ps1=[i,j];
  if norm(ps - ps1) < Ra;
  P(Cx+i,Cy+j,Cz+z)=0;
  end
  end
end

%Define the centre of the fourth and fifth hole
```

```
ps=[3,20];

for z=1:1:30
  for i=1:1:50
  ps1=[i z];
  if norm(ps-ps1)<Ra
  P(Cx+round(i),:,Cz+round(z))=0;
  end
  end
end
```

A trapezoidal figure is added to the plastic case (see Fig. 131). Notice that the air inside the landmine is flagged as one in contrast with the air outside the landmine which is flagged as zero. This is a practical way to add landmines to an already modelled medium. When zero is present no changes are applied to the medium.

```
ayy=15;
for z=13:-1:1
%The X-Y boundaries of the rectangular shape are linearly
   decrease as z increases
ay=ayy + (14-z)*(0.16667);
y=(0.1*(z-1));
P(Cx+round(130+y:-1:112+y),Cy+round(27-ay:1:27+ay),...
   Cz+z)=plast;

%Fill the rectangular shape with zeros. Zeros is a flag
   for leaving the medium as is when adding the landmine
   to an already modelled soil
if z<12
 ay=(ayy-1) + (14-z)*(0.16667);
 y=(0.1*(z-1));
 P(Cx+3+round(130+y:-1:112+y),Cy+round(27-ay:1:27+ay),...
     Cz+z)=0;
end
end
```

NExt, the wax is incorporated into the model (see Fig. 132). The relative permittivity of the wax equals $\epsilon = 6$. Subsequently a hollow PEC cylinder is added inside the wax (see Fig. 133). The PEC is arbitrarily chosen to be denoted by the number minus two.

```
%Define the X-Y boundaries of the bottom base of the wax
```

```
axx=Cx+2;
bxx=Cx+130-2;
ayy=Cy+2;
byy=Cy+55-2;

%As the z increases the X-Y boundaries are linearly
   increasing
for z=3:1:24
y=(0.1*(z-1));
ay=ayy-y;
by=byy+y;

y=(0.1*(z-1));
ax=axx-y;
bx=bxx+y;

P(round(ax):1:Cx+95,round(ay):1:round(by),Cz+z)=wax;
end

%Define the center of the PEC cylinder
ps=[55/2 25/2];

for j=55/2-10:1:55/2+10
 for z=25/2-10:1:25/2+10
 ps1=[j,z];
 %Create the PEC cylinder
 if norm(ps1 - ps)<3.5
 P(Cx+105:-1:65,Cy+round(j),Cz+round(z))=-2;
 end
 %Make the cylinder hollow
 if norm(ps1 - ps)<2.5
 P(Cx + 130-25:-1:130-25-40,Cy+ round(j),Cz+round(z))=1;
 end

 end
end
```

With the above code, the bottom part of PMA-1 is completed. For the upper part, we start by constructing its side parts. Furthermore, two additional holes are incorporated synchronised with the two side holes of the bottom part (see Fig. 134).

```
%Generate the sides of the top part of the landmine
P(Cx+(-4:1:134),Cy+(-4:1:-2),Cz+(13:1:27))=plast;
```

```
P(Cx+(-4:1:134),Cy+62+(-5:1:-3),Cz+(13:1:27))=plast;
P(Cx+[133 134],Cy+(-4:1:59),Cz+(13:1:27))=plast;
P(Cx+(-4:1:134),Cy+(-4:1:59),Cz+[27 28])=plast;

%Add two holes to the side parts
ps=[3,20];
for z=1:1:30
 for i=1:1:50
 ps1=[i z];

 if norm(ps-ps1)<1.7
 P(Cx+round(i),Cy+[-5:1:-3,62+(-5:1:-3)],Cz +round(z))=0;
 end

 end
end
```

Next, a firth order polynomial is employed in an effort to mathematically express the curvy feature illustrated in Fig. 135. The coefficients of the polynomial are given in the following code.

```
%The polynomial's coefficients
coe=[5.554e-16,-2.336e-12,3.695e-09,-2.707e
   -06,0.000875,-0.0703,0.5381];

%Realisation of the polynomial
x=1:1:1401;
n=length(coe);
yr=zeros(1,1401);
for i=1:n;
 yr=yr+coe(i).*x.^(n-i);
end

%Implementation of the polynomial surface into the model
ii=0;
for i=127:-0.01:113;
ii=ii+1;
z=27-yr(ii);
P(round(Cx+i),Cy+[18:1:37],Cz+round(z))=plast;
end
```

Lastly, the curvy surfaces on the top of PMA-1 are incorporated into the model (see Fig. 136). The strategy followed in order to do so, is to implement

a cylinder and add two semi-spheres at each end.

```
%Implement the curvy surfaces on the top part of PMA-1
PS=[26,27.5];
for z=17.5:0.1:37.5;
 for i=16:1:36;
  PS1=[i z];

  if z>27;
   if norm(PS - PS1)<3.5;
   P(round(Cx+i),round(Cy+(5:1:51)),round(Cz+z))=plast;
   end
  end

  if norm(PS - PS1)<2;
  P(round(Cx+i),round(Cy+(7:1:48)),round(Cz+z))=1;
  end

 end
end

lk=[26,27.5,54];
for j=44:1:55;
 for z=27.5:0.1:37.5;
  for i=16:1:36
  lk1=[i,z,j];

  if norm(lk - lk1)<3.5;
  P(round(Cx+i),round(Cy+j-5),round(Cz+z))=plast;
  end

  if norm(lk - lk1)<2;
  P(round(Cx+i),round(Cy+j-5),round(Cz+z))=1;
  end

  end
 end
end

lk=[26,27.5,10];
for j=1:1:10;
 for z=27.5:0.1:37.5;
  for i=16:1:36
  lk1=[i,z,j];
```

```
  if norm(lk - lk1)<3.5;
  P(round(Cx+i),round(Cy+j-5),round(Cz+z))=plast;
  end

  if norm(lk - lk1)<2;
  P(round(Cx+i),round(Cy+j-5),round(Cz+z))=1;
  end

  end
 end
end

PS=[108,27.5];
for z=17.5:0.1:37.5;
 for i=96:1:116;
  PS1=[i z];

  if z>27;
   if norm(PS - PS1)<3.5;
   P(round(Cx+i),round(Cy+(5:1:51)),round(Cz+z))=plast;
   end
  end

  if norm(PS - PS1)<2;
  P(round(Cx+i),round(Cy+(7:1:48)),round(Cz+z))=1;
  end

 end
end

lk=[108,27.5,54];
for j=44:1:55;
 for z=27.5:0.1:37.5;
  for i=96:1:116
  lk1=[i,z,j];

  if norm(lk - lk1)<3.5;
  P(round(Cx+i),round(Cy+j-5),round(Cz+z))=plast;
  end

  if norm(lk - lk1)<2;
  P(round(Cx+i),round(Cy+j-5),round(Cz+z))=1;
  end
```

```
  end
 end
end

lk=[108,27.5,10];
for j=1:1:10;
 for z=27.5:0.1:37.5;
  for i=96:1:116
  lk1=[i,z,j];

  if norm(lk - lk1)<3.5;
  P(round(Cx+i),round(Cy+j-5),round(Cz+z))=plast;
  end

  if norm(lk - lk1)<2;
  P(round(Cx+i),round(Cy+j-5),round(Cz+z))=1;
  end

  end
 end
end

PS=[11.5,27.5];
for z=17.5:0.1:37.5;
 for j=1:1:21.5;
  PS1=[j z];

  if z>27;
   if norm(PS - PS1)<3.5;
   P(round(Cx+(36:1:98)),round(Cy+j-5),round(Cz+z))=plast;
   end
  end

  if norm(PS - PS1)<2;
  P(round(Cx+(36:1:98)),round(Cy+j-5),round(Cz+z))=1;
  end

 end
end

PS=[52.5,27.5];
for z=17.5:0.1:37.5;
 for j=41:1:62.5;
  PS1=[j z];
```

```
  if z>27;
   if norm(PS - PS1)<3.5;
   P(round(Cx+(36:1:98)),round(Cy+j-5),round(Cz+z))=plast;
   end
  end

  if norm(PS - PS1)<2;
  P(round(Cx+(36:1:98)),round(Cy+j-5),round(Cz+z))=1;
  end

 end
end

lk=[36,28,6.5];
for j=1:1:30;
 for z=20:1:40;
  for i=26:1:46;
  lk1=[i,z,j];

  if norm(lk - lk1)<3.5;
  P(round(Cx+i),round(Cy+j),round(Cz+z))=plast;
  end

  if norm(lk - lk1)<2;
  P(round(Cx+i),round(Cy+j),round(Cz+z))=1;
  end

  end
 end
end

lk=[100,28,6.5];
for j=1:1:30;
 for z=20:1:40;
  for i=86:1:106;
  lk1=[i,z,j];

  if norm(lk - lk1)<3.5;
  P(round(Cx+i),round(Cy+j),round(Cz+z))=plast;
  end

  if norm(lk - lk1)<2;
  P(round(Cx+i),round(Cy+j),round(Cz+z))=1;
  end
```

```
  end
 end
end

lk=[36,28,47.5];
for j=41:1:70
 for z=20:1:40
  for i=26:1:46
  lk1=[i,z,j];

  if norm(lk - lk1)<3.5;
  P(round(Cx+i),round(Cy+j),round(Cz+z))=plast;
  end

  if norm(lk - lk1)<2;
  P(round(Cx+i),round(Cy+j),round(Cz+z))=1;
  end

  end
 end
end


lk=[100,28,47.5];
for j=41:1:70
 for z=20:1:40
  for i=86:1:106
  lk1=[i,z,j];

  if norm(lk - lk1)<3.5;
  P(round(Cx+i),round(Cy+j),round(Cz+z))=plast;
  end

  if norm(lk - lk1)<2.;
  P(round(Cx+i),round(Cy+j),round(Cz+z))=1;
  end

  end
 end
end
```

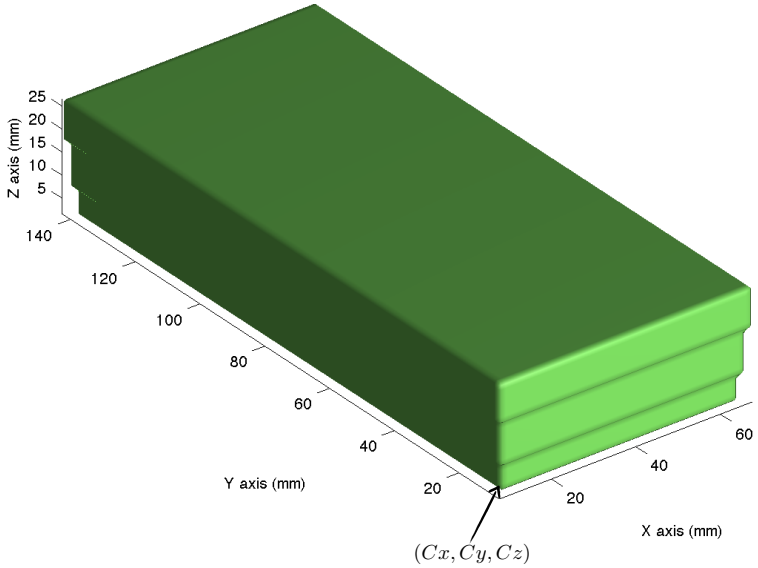

Figure 128: Modelling the plastic base of PMA-1, Cx, Cy and Cz denotes the origin of the PMA-1 (x, y, z).

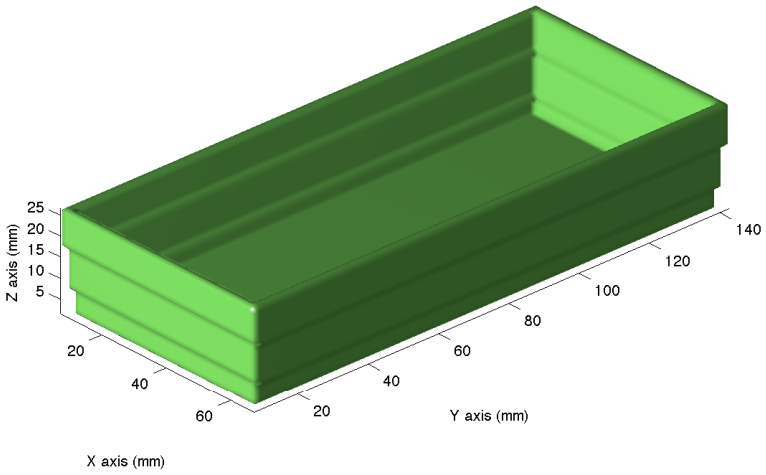

Figure 129: The inner part of the main core is filled with air.

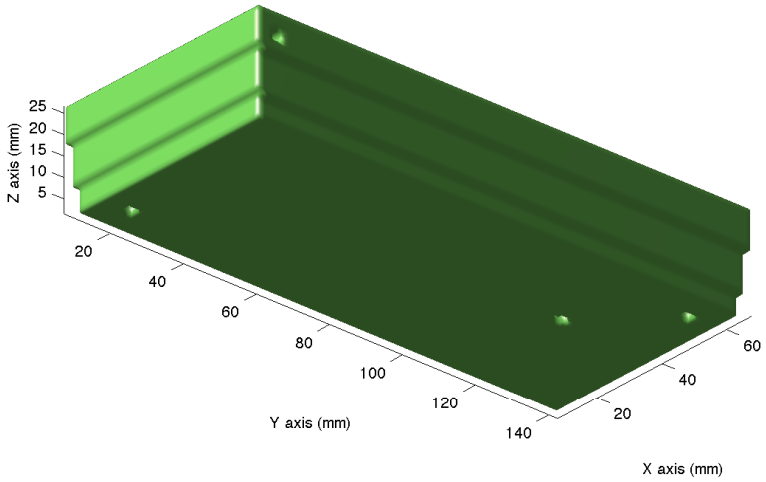

Figure 130: Five circular holes (one is not visible) are added to the main plastic core.

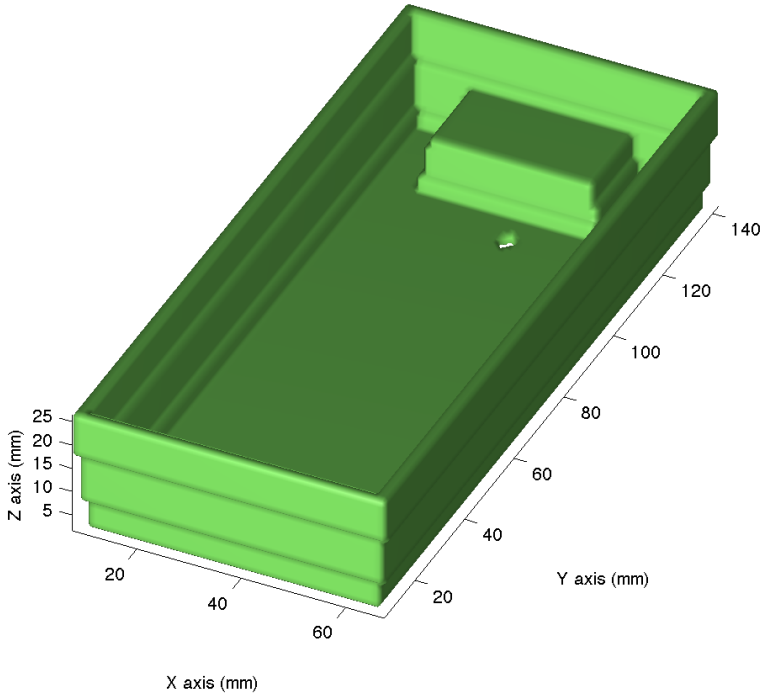

Figure 131: A trapezoidal feature is added to the plastic base.

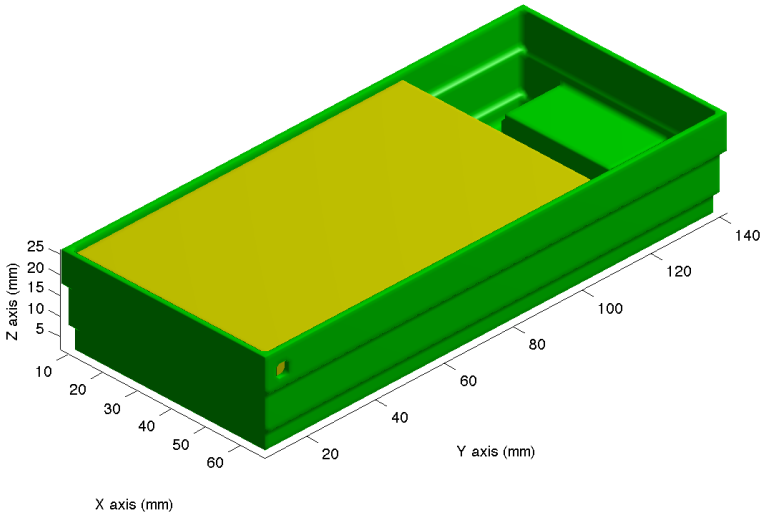

Figure 132: The wax is illustrated with yellow colour. The relative permittivity of the wax equals with $\epsilon_w = 6$.

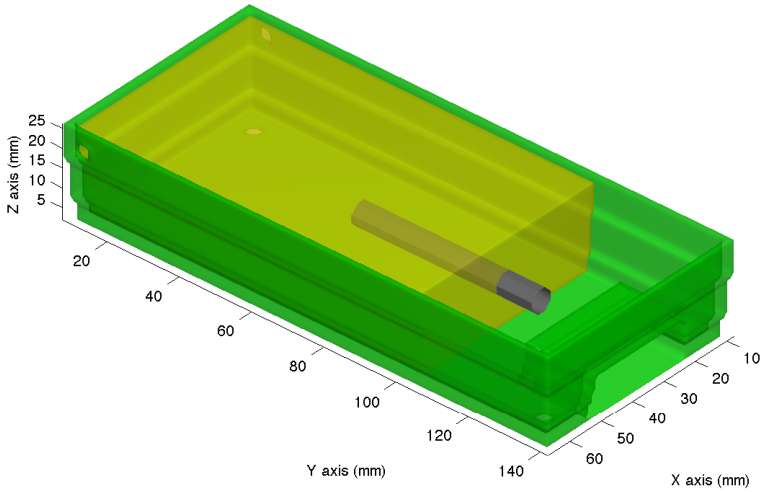

Figure 133: A hollow PEC cylinder illustrated with grey colour is added to the model.

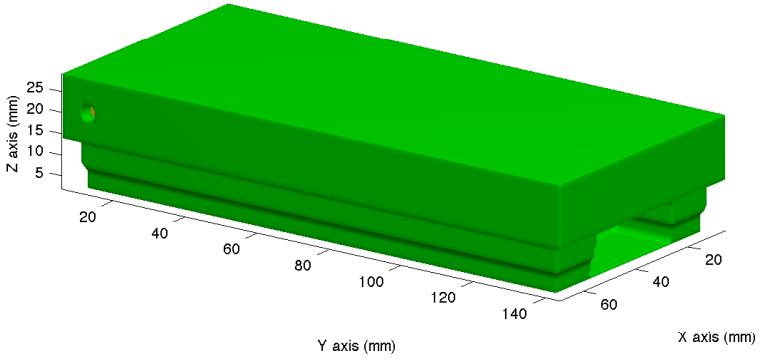

Figure 134: The sides of the upper part are implemented to the model. Two holes are added synchronised with the ones on the bottom part.

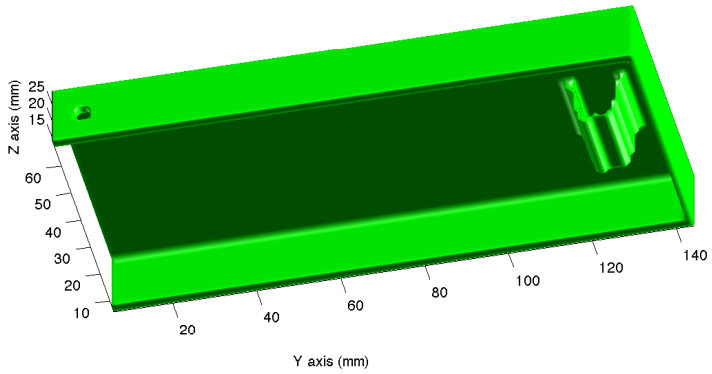

Figure 135: A polynomial surface is used in order to implement the illustrated curvy feature to the top part of PMA-1.

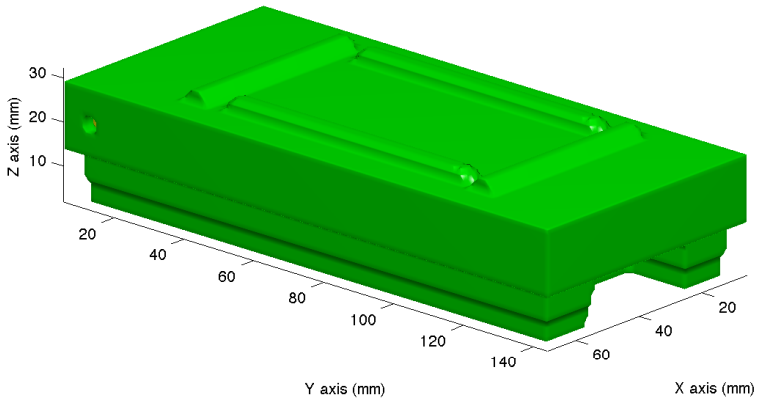

Figure 136: The complete model of PMA-1.

E.2 PMN

The main cylinder of PMN is initially generated (see Fig. 137). The cylinder is filled with wax which resembles TNT with respect to dielectric properties ($\epsilon = 6$). The main core is made of plastic ($\epsilon = 3.5$).

```
clear
clc
close all

%Define the center of the landmine
or=[60 80 15];
or2=[or(1) or(2)];

%Define the relative electric permittivities
grey=3.5;
wax=6;
b_r=6;
pec=-2;
black=3;
blue=3;

%Pre-define the 3D grid
F2(1:1:140,1:1:165,1:1:50)=0;

%Create the main cyllinder which is filled with wax
for i=1:0.5:180
 for j=1:0.5:180
 P=[i j];
 if norm(P-or2)<53.5
 F2(round(i),round(j),2:45)=grey;
 end
 if norm(P-or2)<51.5
 F2(round(i),round(j),35:45)=1;
 end
 if norm(P-or2)<51.5
 F2(round(i),round(j),4:35)=wax;
 end
 end
end
```

Next an inner cylinder which passes through the main core of PMN is created (see Fig. 138). The cylinder is made of plastic ($\epsilon = 3$) and it is filled with air.

```
%Define the center of the inner cylinder
or2=[or(1),17];
%Generate the inner cylinder and fill it with air
for i=1:0.5:180
 for z=4:0.5:35
 P=[i,z];
 if norm(P-or2)<11
 F2(round(i),round(or(2)-54:1:54+or(2)),round(z))=grey;
 end
 if norm(P-or2)<=9
 F2(round(i),round(or(2)-54:1:54+or(2)),round(z))=1;
 end
 end
end
```

Subsequently the top part of PMN is created. The top part is made of rubber ($\epsilon = 3$) and it is surrounded by a PEC ring.

```
%Generate the top part of PMN
for i=1:0.5:180
 for j=1:0.5:180
 P=[i j];
 %Generate the main body of the top part
 if norm(P-or2)<56 & norm(P-or2)>54;
 F2round(i),round(j),44:-1:44-15)=b_r;
 end
 %Generate the smooth curvy ending on the top
 for k=0:2;
 if norm(P-or2)<55.5-k
 F2(round(i),round(j),45+k)=b_r;
 end
 end
 %Surround the rubber part with a PEC ring
 if norm(P-or2)<57 & norm(P-or2)>55 ;
 % Pec ring - optional to omit
 F2(round(i),round(j),40:-1:40-5)=pec;
 end
 end
end
```

PMN has two adapted parts which are placed at each side of the inner cylinder. The following code generates the geometry of the first one (see Fig. 140).

```
%Generate the homocentric cyllinders of the first adaptor
for i=1:0.1:180
 for z=3:0.1:34
 P=[i,z];
 if i<100;
  if norm(P-or3)<9 & norm(P-or3)>=7 ;
  F2(round(i),or2(2)-54:1:or2(2)-34,round(z))=black;
  end
  if norm(P-or3)<=7 & norm(P-or3) >= 6;
  F2(round(i),or2(2)-54:1:or2(2)-14,round(z))=grey;
  end
 end
 if norm(P-or3)<11.5
 F2(round(i),or2(2)-54:-1:or2(2)-59,round(z))=blue;
 end
 end
end

%Generate the curvy surface at the end of the first
   adaptor
for j=or2(2)-59:-0.5:or2(2)-71
 for i=or2(1)-10:0.5:or2(1)+10
 F2(round(i),round(j),17-2:1:17+2)=blue;
 end
end
ii=6
for j=or2(2)-59:-0.5:or(2)-61
 ii=ii-1;
 F2(or2(1)-10:1:or2(1)+10,round(j),17-ii:1:17+ii)=blue;
end
```

Lastly, the second adaptor, referred as the "complex" one, is generated. Similar to the first adaptor, homocentric cylinders are employed to model the main parts of the adaptor. In addition, a helix function, expressed parametrically, is used to simulate the PEC spring.

```
%Generate the homocentric cylinders of the complex adaptor
for i=or2(1)-15:0.1:or2(1)+15
 for z =3:0.1:34
 PD=[i,z];
 if norm(PD-or3)<14
 F2(round(i),or2(2)+56:1:or2(2)+63,round(z))=blue;
 end
 if norm(PD-or3)<12
```

```
 F2(round(i),or2(2)+64:1:or2(2)+81,round(z))=blue;
 end
 if norm(PD-or3)<10
 F2(round(i),or2(2)+79:1:or2(2)+81,round(z))=0;
 end
 if norm(PD-or3)<10 & norm(PD - or3)>9
 F2(round(i),or2(2)+64:1:or2(2)+78,round(z))=grey;
 end
 if norm(PD-or3)<9
 F2(round(i),or2(2)+36:1:or2(2)+56,round(z))=black;
 end
 if norm(PD-or3)<7
 F2(round(i),or2(2)+36:1:or2(2)+56,round(z))=grey;
 end
 if norm(PD-or3)<5
 F2(round(i),or2(2)+36:1:or2(2)+56,round(z))=grey;
 end
 if norm(PD-or3)<2
 F2(round(i),or2(2)-7:1:or2(2)+56,round(z))=pex;
 end
 end
end

%Create the top part of the complex adaptor
for i=or2(1)-9:0.1:or2(1)+9
 for z = 17-2:0.1:17+2
 F2(round(i),or2(2)+56+8+14:1:or2(2)+56+8+15,round(z))=0;
 end
end
for i=or2(1)-3:0.1:or2(1)+3
 for z = 10-1:0.1:10+1
 F2(round(i),or2(2)+56+8+14:1:or2(2)+56+8+15,round(z))=0;
 end
end
for R=14:-0.01:11;
 for th=0:45:360;
 xx=R*sind(th);
 zz=R*cosd(th);
 F2(or2(1)+round(xx),or2(2)+65:or2(2)+78,17+round(zz))...
    =blue;
 end
end

%Using a parametric representation of a helix to express
   the pec spring
```

```
R=4.5;
for t=0:0.5:24*360;
 xx=R*cosd(t);
 zz=R*sind(t);
 yy=(3.2/360)*t;
 F2(or2(1)+round(xx),or2(2)+56-round(yy),17+round(zz))=pec
end
```

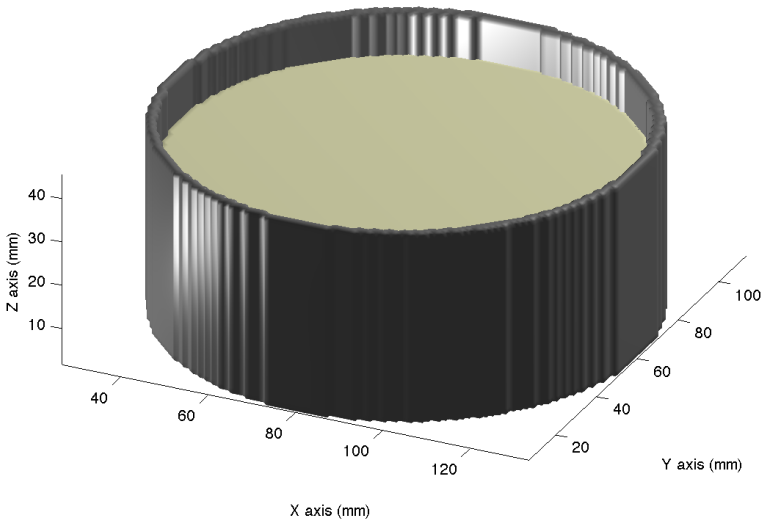

Figure 137: The main cylinder of PMN filled with wax.

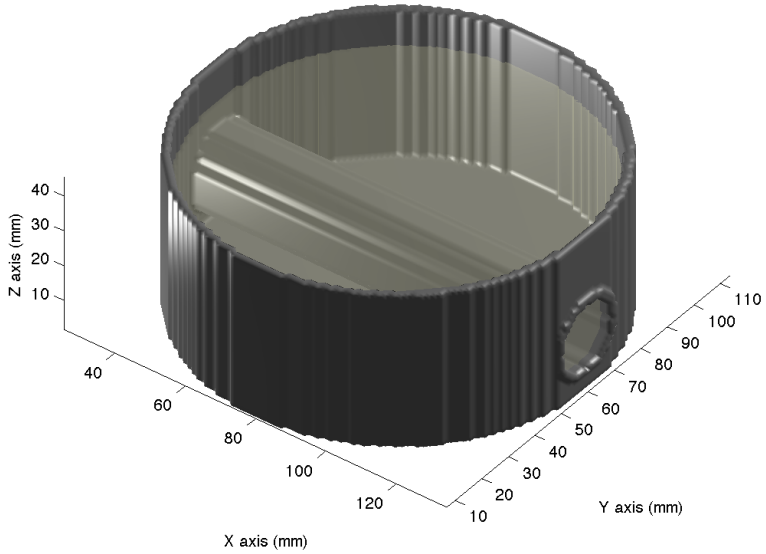

Figure 138: The inner cylinder which passes through the main core of PMN.

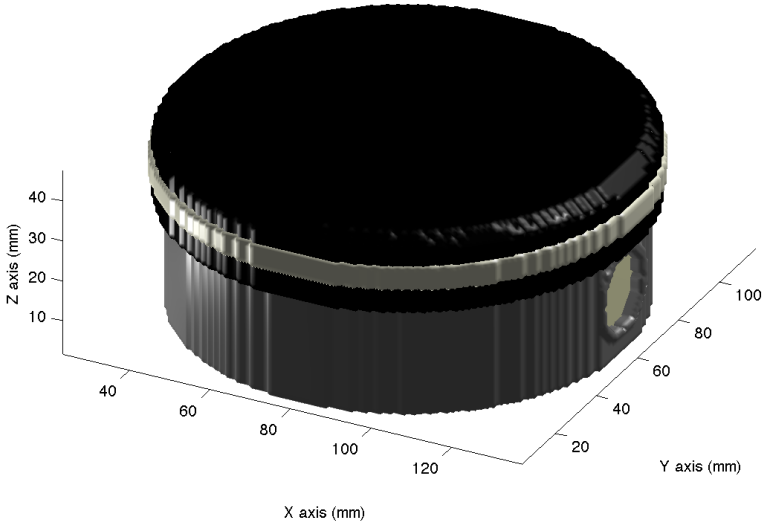

Figure 139: The top part of PMN is made of rubber and it is surrounded by a PEC ring.

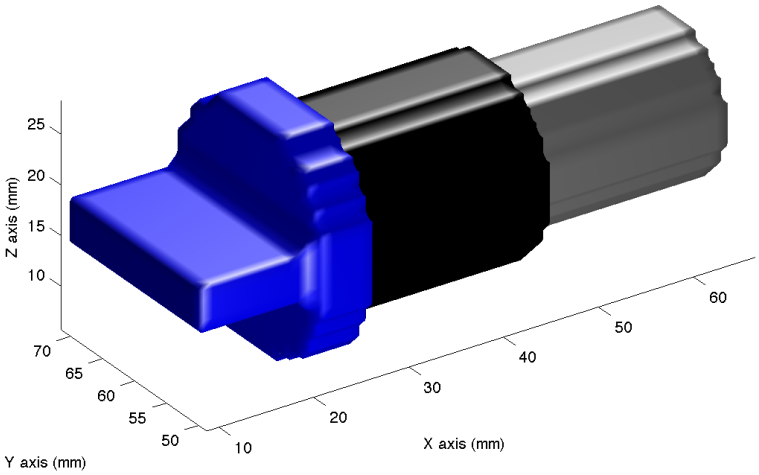

Figure 140: The first adapted part of PMN.

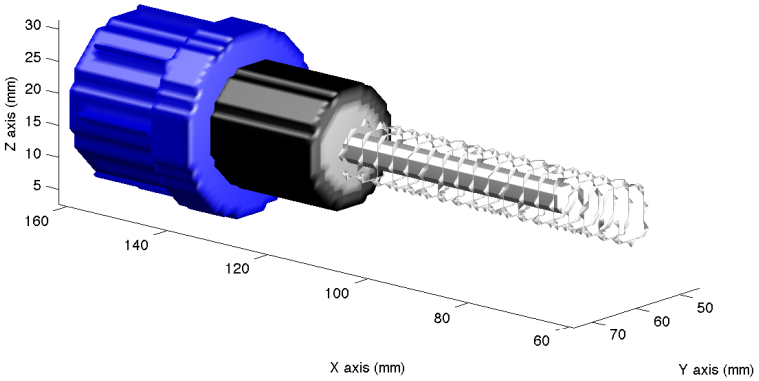

Figure 141: The second adapted part of PMN.

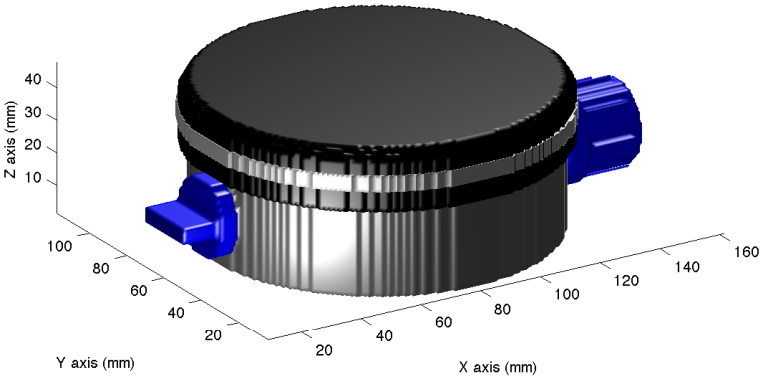

Figure 142: Complete model of PMN.

E.3 TS-50

Firstly, the bottom part of TS-50 is generated. The bottom part of TS-50 consists of a hollow cylindric shape accompanied by twelve wing-like features distributed equally around the centre of TS-50 (see Fig. 143). Regarding the dielectric properties, the bottom part consists of plastic ($\epsilon = 4$) and wax ($\epsilon = 6$).

```
clear
clc
close all

%Define the center of the TS-50 (x,y)
center=[50 50];

%Predefine the 3D matrix
HB=zeros(100,100,40);
HBx=zeros(100,100,40);

%Define the dielectric properties of TS-50
plastic=4;
plastic_black=5;
wax=6;

%Implement the "wing" shaped features at the bottom of TS
    -50
for i=30:30:360;
 for k=3:1:19;
 RR=((k-2).*(10^31.8)).^(1/20);
  for R=20:0.05:round(RR)-1;
   for ii=i:1:i+2;
   x=center(1) + R*sind(ii);
   y=center(2) + R*cosd(ii);
   HB(round(x),round(y),k)=3;
   end
  end
 end
end


%Generate the main part of the bottom part of TS-50
FB=37.5;
for k=5:1:23
 for i=1:1:100;
  for j=1:1:100;
```

```
  n=[i j];

  if norm(n-center) < FB;
  HB(i,j,k)=plastic;
  end

  if k>8
   if norm(n-center) < FB-3
   HB(i,j,k)=1;
   end
  end

  if k>5
   if norm(n-center) < 33
   HB(i,j,k)=wax;
   end
  end

  if k<6
   if norm(n-center) < 18
   HB(i,j,k)=0;
   end
  end
  end
 end
 FB=FB+0.17;
end
```

Subsequently the upper part of TS-50 is created. The main core of the upper part is created similar to the bottom part. In addition a conical shape and the pressure button are incorporated into the model (see Fig. 144).

```
%A similar procedure for generating the bottom part of TS
   -50 is followed here to generate the upper part.
   Subsequently the resulting matrix is flipped upside
   down.
FB=37.5;
for i=30:30:360
 for k=3:1:19;
 RR=((k-2).*(10^31.8)).^(1/20);
  for R=20:0.05:RR-1;
   for ii=i:1:i+2;
   x=center(1) + R*sind(ii);
   y=center(2) + R*cosd(ii);
```

```
   HBx(round(x),round(y),k)=plastic;
   end
  end
 end
end

for k=7:1:19
 for i=1:1:100;
  for j=1:1:100;
  n=[i j];
   if norm(n-center) < FB;
   HBx(i,j,k)=plastic;
   end

   if k>8
    if norm(n-center) < FB-6
    HBx(i,j,k)=1;
    end
   end

  end
 end
FB=FB+0.17;
end

%Here the HBx matrix is flipped upside down
for i=1:1:100;
 HV(:,:)=HBx(:,i,:);
 HBB(:,i,:)=fliplr(HV);
end
HB=HB+HBB;
clear HBB HV

%Generate the conical shape on the top part of TS-50
RR=36;
for k=34:1:40;
RR=RR-2;
 for i=1:0.25:100;
  for j=1:0.25:100;
  n=[i j];
   if norm(n-center)<RR;
   HB(round(i),round(j),k:1:k+1)=plastic;
   end
  n=[i j];
   if k<40
```

```
    if norm(n-center)<RR-3;
    HB(round(i),round(j),k:1:k+1)=1;
    end
   end
  end
 end
end

%Create the black pressure buttom of TS-50
RR=25;
for k=38:1:44;
RR=RR-0.5;
 for i=1:0.5:100;
  for j=1:0.5:100;
  n=[i j];
   if norm(n-center)<RR;
   HB(round(i),round(j),round(k):1:round(k)+1)=plastic_
       black;
   end
  end
 end
end
```

Lastly, the features occur inside the upper body of the TS-50 are generated (see Fig. 145). These features are made of plastic and they are simulated using toruses, cylinders and radial lines. Fig. 146 illustrates the final model of TS-50 after merging the upper and the bottom parts.

```
%Generate the torus shapes insode TS-50
RR=40;
for i=1:0.5:100;
 for j=1:0.5:100;
 n=[i j];
  if norm(n-center)<RR;
  HB(round(i),round(j),19:22)=plastic;
  end
 n=[i j];
  if norm(n-center)<RR-6;
  HB(round(i),round(j),19:22)=1;
  end
 end
end
RR=20;
for i=1:0.5:100;
 for j=1:0.5:100;
```

```
 n=[i j];
  if norm(n-center)<RR;
  HB(round(i),round(j),27:-1:20)=plastic;
  end
  if norm(n-center)<RR-3;
  HB(round(i),round(j),21:-1:20)=1;
  end
 end
end
RR=35;
for i=1:0.5:100;
 for j=1:0.5:100;
 n=[i j];
  if norm(n-center)<RR;
  HB(round(i),round(j),27:1:31)=plastic;
  end
  if norm(n-center)<RR-12;
  HB(round(i),round(j),27:1:30)=1;
  end
 end
end

%Generate the cylindrical legs inside TS-50
R=30;
for i=40:40:360
 for ii=i:1:i+1;
  x=center(1) + R*sind(i);
  y=center(2) + R*cosd(i);
  HB(round(x)-1:1:round(x)+1,round(y)-1:round(y)
      +1,27:-1:23)=plastic;
 end
end

%Create the radial lines inside TS-50
for i=11.25:11.25:360
 for ii=i:1:i+1;
  for R=20:0.1:25;
   x=center(1) + R*sind(ii);
   y=center(2) + R*cosd(ii);
   HB(round(x),round(y),27:1:31)=plastic;
  end
 end
end
```

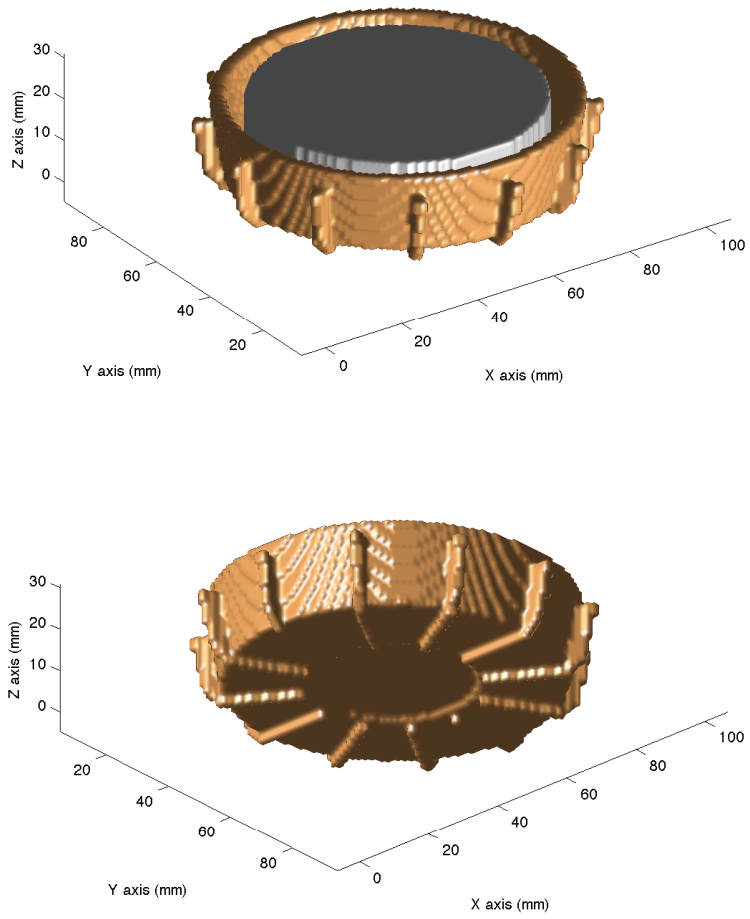

Figure 143: The bottom part of TS-50 filled with wax.

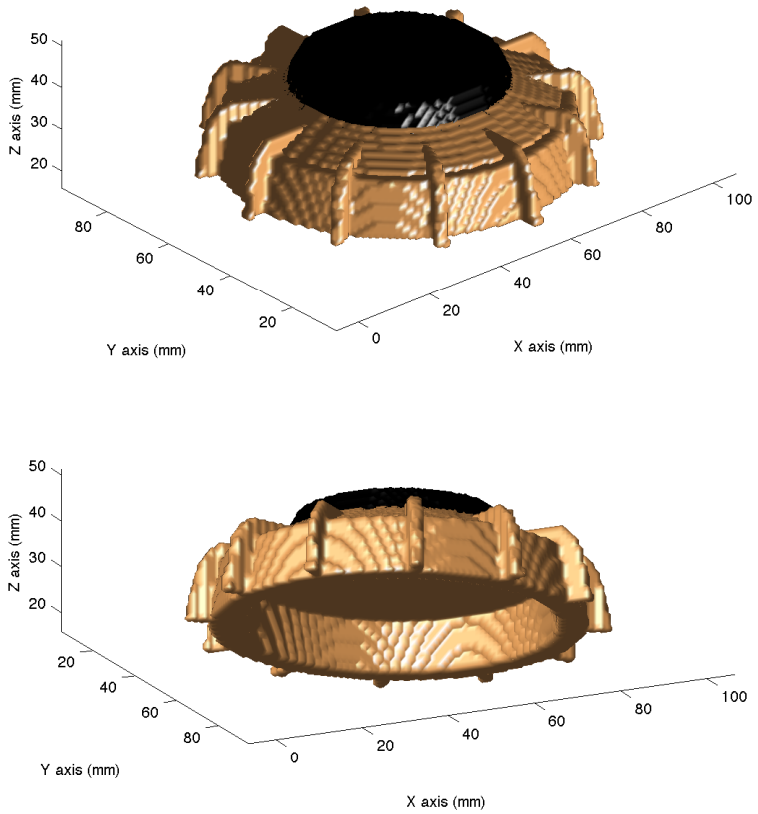

Figure 144: The upper part of TS-50.

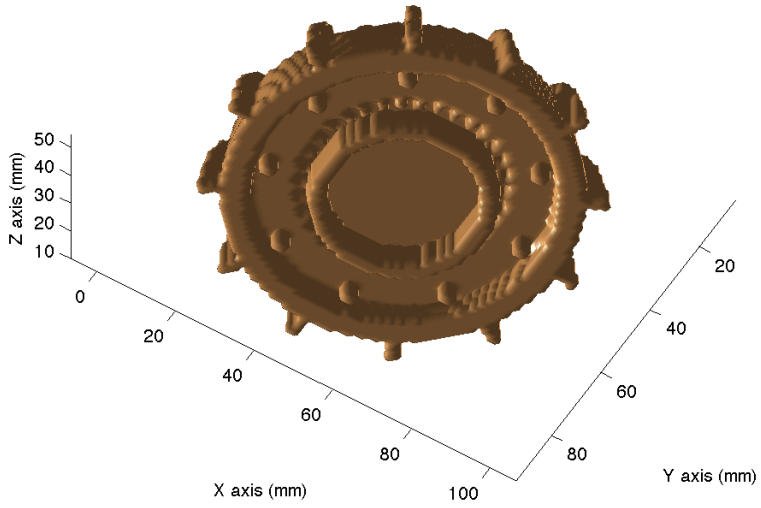

Figure 145: The inner parts of the top body of TS-50.

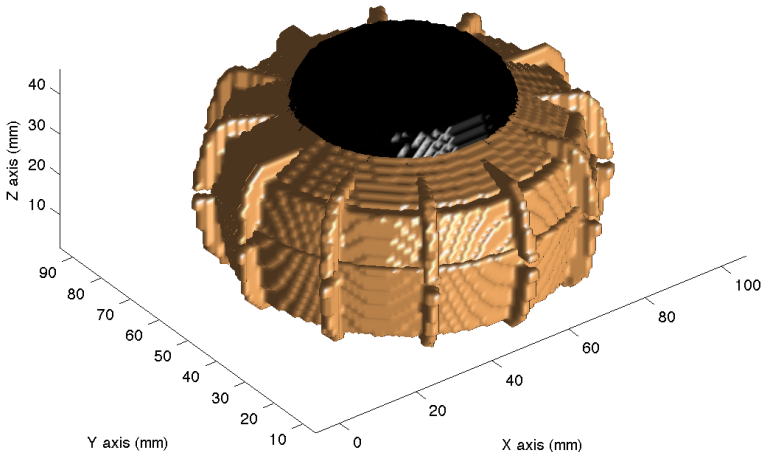

Figure 146: The complete model of TS-50 after merging the upper and the bottom part.

Abarbanel, S., Gottlieb, D. and Hesthaven, J. S., (2002), "Long time behaviour of the perfectly matched layer equations in computational electromagnetics," *Journal of Scientific Computation*, volume 17, number 14, pages 405-422. (Cited on page 101.)

Abraham, J. K., Vinoy, K. J., Tellakula, R. and Varadan, V. K., (2003), "Tailoring the dielectric properties of meta materials," *IEEE International Microwave Symposium Digest*, volume 3, pages 1837-1840. (Cited on page 45.)

Acheroy, M., (2007), "Mine action: status of sensor technology for close-in and remote detection of anti-personnel mines," *Near Surface Geophysics*, volume 5, pages 43-55. (Cited on pages 10 and 14.)

Alauddin, B. M. and Nath, B., (2006), "Anti-personnel mine detection and classification using GPR image," *IEEE 18th International Conference on Pattern Recognition*, pages 1082-1085. (Cited on page 173.)

Alawneh I., (2004), *Modeling of the backscatter behaviour of typical antipersonnel mines by computer simulations and experimental tests*, PhD thesis submitted at the Fakultat fur Elektrotechnik ind Informationstechnik an der Ruhr-Universitat Bochum. (Cited on page 3.)

Alsunaidi, M. A. and Al-Jabr, A. A., (2009), "A general ADE-FDTD algorithm for the simulation of dispersive structures," *IEEE Photonics Technology Letters,* volume 21, number 12, pages 817-819. (Cited on page 83.)

Annan, A., P., (1999), "Practical processing of GPR data," *Sensors and Software Inc. Mississauga*, Canada. (Cited on page 24.)

APOPO (2006), a Belgian research organisation that was initiated in response to the global landmine problem. http://www.apopo.org/. (Cited on page 14.)

Atteia, G. E., Hussein, K. F. A., (2010), "Realistic model of dispersive soils using PLRC-FDTD with applications to GPR systems," *Progress In Electromagnetics Research PIER*, volume 26, pages 335-359. (Cited on pages 83 and 115.)

Azimi-Sadjadi, M. R., Poole, D. E., Sheedvash, S., Sherbondy, K. D. and Stricker, A., (1992), "Detection and classification of buried dielectric anomalies using a separated aperture sensor and a neural network discriminator,"

IEEE Transactions on Instrumental Measurements, volume 41, number 1, pages 137-143. (Cited on pages 173 and 190.)

Azimi-Sadjadi and Stricker, A., (1994), "Detection and classification of buried dielectric anomalies using neural networks-further results," *IEEE Transactions on Instrumental Measurements*, volume 43, number 1, pages 34-39. (Cited on pages 173 and 190.)

Balanis, C., (1989), *Advanced Engineering Electromagnetics*, Wiley New York. (Cited on pages 18, 33, 38, 42, 43, 44, 45, 65, and 104.)

Bano, M., (2004), "Modelling of GPR waves for lossy media obeying a couplex power law of frequency for dielectric permittivity," *Geophysical Prospecting*, volume 41, pages 11-26. (Cited on page 48.)

Bart, S., Plasman, Y., Piette, M., Marc, P., Acheroy, J. and Vorst, A. V., (2000), "Laboratory UWB GPR system for land mine detection," *Proc. SPIE 4084, Eighth International Conference on Ground Penetrating Radar*, . (Cited on pages 4 and 130.)

Becache, E., Petropoulos, P. G., and Gedney, S. G., (2004), "On the long-time behaviour of unsplit perfectly matched layers," *IEEE Transactions on Antennas and Propagation*, volume 52, number 5, pages 1335-1342. (Cited on page 101.)

Belli, K., Rappaport, C. M., He, Z. and Wadia-Fascetti S., (2009), "Effectiveness of 2-D and 2.5-D FDTD ground-penetrating radar modeling for bridge-deck deterioration evaluated by 3-D FDTD," *IEEE Transactions on Geoscience and Remote Sensing*, volume 47, number 11, pages 3656-3663. (Cited on page 114.)

Berenger, J. P., (1994), "A perfectly matched layer for the absorption of electromagnetic waves," *Journal of Computational Physics,* volume 114, pages 185-200. (Cited on pages 100 and 102.)

Berenger, J. P., (1999), "Evanescent waves in PML's: origin of the numerical reflection in wave-structure interaction problems," *IEEE Transactions on Antennas and Propagation*, volume 47, number 10, pages 1497-1503. (Cited on page 101.)

Berenger, J. P., (2000), "Numerical reflection of evanescent waves by PMLs: origin and interpretation in the FDTD case, expected consequences to other finite methods," *International Journal of Numerical Modelling for Electronic Networks Devices Fields*, volume 13, pages 103-114. (Cited on page 101.)

Berenger, J. P., (2007), *Perfectly Matched Layer (PML) for Computational Electromagnetics*, 1st edition, Morgan and Claypool publishers. (Cited on pages 100 and 101.)

Bergmann, T., Robertsson, J. O. A. and Holliger, K., (1998), "Finite-difference modelling of electromagnetic wave propagation in dispersive and attenuating media," *Geophysics*, volume 63, pages 856-867. (Cited on pages 83 and 115.)

Birchak, R. J., Gardner, G. C., Hipp, E. J. and Victor, M. J., (1974), "High dielectric constant microwave probes for sensing soil moisture," *Proceedings of the IEEE*, volume 62, number 1, pages 93-98. (Cited on pages 51 and 53.)

Bishop, M., C., (1996), *Neural Networks for Pattern Recognition*, Oxford University Press. (Cited on pages xxviii, 173, 174, 175, 177, 178, 179, 185, and 186.)

Blindow, N., Salat, C., and Casassa, G., (2012), "Airborne GPR sounding of deep temperate glaciers, Examples from the Northern Patagonian Icefield," *14th International Conference on Ground Penetrating Radar (GPR)*, pages 664-669. (Cited on page 1.)

Bostanudin, F. J. N., (2013), *Computational Methods for Processing Ground Penetrating Radar Data*, PhD thesis submitted at the University of Portsmouth. (Cited on page 26.)

Bourgeois, J. R., Smith, G. S., (1996), "A fully three-dimensional simulation of a ground-penetrating radar: FDTD theory compared with experiment," *IEEE Transactions on Geoscience and Remote Sensing*, volume 34, number 1, pages 36-44. (Cited on pages 3 and 116.)

Bourgeois, J. M, Smith, G. S., (1997), "A complete electromagnetic simulation of a ground penetrating radar for mine detection: theory and experiment," *IEEE Antennas and Propagation Society International Symposium*, volume 2, pages 986-989. (Cited on pages 3 and 116.)

Boyarskii, D. A., Tikhonov, V. V. and Komarova, N. Y., (2002), "Model of dielectric constant of bound water in soil for applications of microwave remote sensing," *Progress In Electromagnetics Research*, volume 35, pages 251-269. (Cited on pages xx, 56, 57, and 58.)

Bradford, J. H., (2007), "Frequency-dependent attenuation analysis of ground-penetrating radar data," *Geophysics*, volume 72, number 3, pages j7-j16. (Cited on pages 54 and 57.)

Bristow, C. S., (2004), "GPR in sediments: recent advances in stratigraphic applications," *10th International Conference on Ground Penetrating Radar*, pages 569-572. (Cited on page 18.)

Brown, W. F., (1956), "Dielectrics," *in Encyclopedia of Physics*, volume 17, Berlin: Springer, 1956. (Cited on page 53.)

Burrough, P. A., (1981), "Fractal dimensions of landscapes and other environmental data," *Nature*, volume 294, pages 240-242. (Cited on page 123.)

Buyukozturk, O., (1998), "Imaging of concrete structures," *in NDT& E International*, volume 31, pages 233-243. (Cited on page 1.)

Brunzell, H., (1999), "Detection of shallowly buried objects using impulse radar," *IEEE Transactions on Geoscience and Remote Sensing*, volume 37, number 2, pages 875-886. (Cited on pages 22 and 28.)

(2014) http://www.cmac.gov.kh/userfiles/file/ten-years.pdf. (Cited on pages xviii and 10.)

Cameron, M. A., Lawson, R. J. and Tomlin, B. W., (1998), *To Walk Without Fear: The Global Movement to Ban Landmines*, Oxford University Press, USA, First Edition. (Cited on pages xviii, 7, 8, 9, 10, 11, 12, 13, 14, 143, and 145.)

Campell, M. J. and Ulricks, J., (1969), *Journal of Geophysical Research*, volume 74, pages 5867-5881. (Cited on page 49.)

Caratelli, D., Yarovoy, A. and Ligthart, L. P., (2009), "Accurate FDTD modelling of resistively-loaded bow-tie antennas for GPR applications," *IEEE 3rd European Conference on Antennas and Propagation*, pages 2115-2118. (Cited on page 116.)

Carcione, J. M., (1996), "Ground-penetrating radar: Wave theory and numerical simulations in lossy anisotropic media," *Geophysics*, volume 61, pages 1664-1677. (Cited on page 114.)

Carcione, J. M. and Schoenberg M. A., (2000), "3-D ground-penetrating radar simulation and plane-wave theory in anisotropic media," *Geophysics*, volume 65, pages 1527-1541. (Cited on page 115.)

Carlson, N. L., (1967), "Dielectric constant of vegetation at 8.5 GHz," Technical Report 1903-5, Electroscience Lab., Ohio State University, Columbus. (Cited on pages 116 and 128.)

Cassidy, N. J., (2007), "A review of practical numerical modelling methods for the advanced interpretation of ground-penetrating radar in near-surface environments," *Near Surface Geophysics*, volume 5, pages 5-21. (Cited on pages 2 and 114.)

Cassidy, N., (2008), "Introduction to GPR,", *Workshop at the 12th International Conference on Ground Penetrating Radar*, . (Cited on pages xviii and 18.)

Cassidy, N. J. and Millington, T. M., (2009), "The application of finite-difference time-domain modelling for the assessment of GPR in magnetically lossy materials," *Journal of Applied Geophysics*, volume 67, pages 296-308. (Cited on pages 114 and 197.)

Cassidy, N., (2009), "Ground Penetrating Radar Data Processing Modelling and Analysis", *in Ground Penetrating Radar Theory and Applications*, Elsevier, Amsterdam, pages 141-176. (Cited on pages 24 and 27.)

Causley, M. F., and Petropulos, P. G. (1967), "On the Time-Domain Response of Havriliak-Negami Dielectrics", *IEEE Transactions on Antennas and Propagation*, volume 61, number 6, pages 3182-3189. (Cited on page 48.)

Chen, Q., Katsurai, M. and Aoyagi, P. H., (1998), "An FDTD formulation for dispersive media using a current density", *IEEE Trans. Antennas Propag.*, volume 46, number 11, pages 1739-1746. (Cited on page 83.)

Chew, W. C. and Weedon, W. H., (1994), "A 3-D perfectly matched medium form modified Maxwell's equations with streched coordinates," *IEEE Microw. Opt. Technol. Lett.,* volume 7, number 13, pages 599-604. (Cited on pages 100 and 102.)

Church, P., McFee, J. E., Gagnon, S., and Wort, P., (2006), "Electrical impedance tomographic imaging of buried landmines," *IEEE Trans. Geosci. Remote Sens.*, volume 44, number 9, pages 2407-2420. (Cited on page 16.)

Claudio, B., Bertrand, G., Frederic, G., Pierre-Yves, P. and Olivier, C., (1998), "Ground penetrating radar and imaging metal detector for antipersonnel detection," *Journal of Applied Geophysics*, volume 40, pages 59-71. (Cited on page 14.)

Clegg, J. and Robinson, M. P., (2010), "A genetic algorithm used to fit Debye functions to the dielectric properties of tissues", *IEEE Congress on Evolutionary Computation (CEC)* pages 1-8. (Cited on pages 82, 84, and 115.)

Cole, K. S., and Cole, R. H., (1941), "Dispersion and absorption in dielectrics, alternating current characteristic", *Journal of Chemical Physics*, volume 9, pages 341-351. (Cited on page 47.)

Conyers, L. B. and Goodman, D., (1997), *Ground-Penetrating Radar, An Introduction for Archaeologists*, AltaMira Press, A Division of Sage Publications, Inc. (Cited on page 18.)

Crank, J. and Nicolson, P., (1947). "A practical method for numerical evaluation of solutions of partial differential equations of the heat-conduction type', *Proccedings of the Cambringe Society of Philosophy.*, volume 43, pages 50-67. (Cited on pages 65 and 67.)

Cummer, S. A., (2003), "A simple, nearly perfectly matched layer for general electromagnetic media," *IEEE Microw. and Wireless Comp. Lett.*, volume 13, number 3, pages 128-130. (Cited on page 100.)

Daniels, D. J. (2004), *Ground penetrating radar*, IEE, 2nd edition, The University of Michigan. (Cited on pages 5, 16, 17, 18, 27, 61, 113, and 116.)

Daniels, D. J., (2006), A review of GPR for landmine detection, *International Journal of Sensing and Imaging*, volume 7, number 3, pages 90-123. (Cited on pages 1, 11, 113, 114, and 151.)

Daniels, D. J., (2008), A review of landmine detection using GPR, *European Radar Conference, EuRAD*, pages 280-283. (Cited on pages 23 and 172.)

Daniels, D. J., Braunstein, J. and Nevard, M., (2014), "Using MINEHOUND in Cambodia and Afghanistan," *The Journal of ERW and Mine Action*, issue 18.2. (Cited on pages xviii, 15, 16, and 24.)

Davies, E., (1990), *Machine Vision: Theory, Algorithms and Practicalities*, Academic Press. (Cited on page 27.)

Davis, J. L. and Annan, A. P., (1977), "Electromagnetic detection of soil moisture: Progress report 1," *Canadian Journal of Remote Sensing*, volume 1, pages 76-86. (Cited on page 54.)

Debye, P., (1929), *Polar Molecules*, Chemical Catalogue Co.. (Cited on pages 45 and 154.)

Diamanti, N. and Giannopoulos, A., (2011), "Employing ADI-FDTD sub-grids for GPR numerical modelling and their application to study ring separation in brick masonry arch bridges," *Near Surface Geophysics,* voume 9, pages 245-256. (Cited on page 114.)

Dobson, M. C., Kouyate, F. and Ulabe, F. T., (1984), "A reexamination of soil textural effects on microwave emission and backscattering," *IEEE Transactions on Geoscience and Remote Sensing*, volume GE-22, pages 530-536. (Cited on pages 4, 62, and 63.)

Dobson, M. C., Ulaby, F. T., Hallikainen, M. T. and El-Rayes, M.A., (1985), "Microwave dielectric behaviour of wet soil–part II: Deielctric mixing models," *IEEE Transactions on Geoscience and Remote Sensing*, volume 23, number 1, pages 35-46. (Cited on pages 49, 59, 60, 63, 117, and 118.)

Drossaert, F. H. and Giannopoulos, A., (2007), "A non-split complex frequnecy-shifted PML based on recursive integration for FDTD modeling of elastic waves," *Geophysics*, volume 72, number 2, pages T9-T17. (Cited on page 100.)

El-Rayes, M. A. and Ulaby, F. T., (1987), "Microwave dielectric spectrum of vegetation-part I: Experimental observations," *IEEE Transactions on Geoscience and Remote Sensing*, volume GE-25, number 5, pages 541-549. (Cited on page 127.)

Everett, M. E., (2013), *Near-Surface Applied Geophysics*, Cambridge University Press. (Cited on page 17.)

Fa, W., (2013), "Simulation for ground penetrating radar (GPR) study of the subsurface structure of the Moon," *Journal of Applied Geophysics*, volume 99, pages 98-108. (Cited on page 18.)

Fan, G. X. and Liu, Q. H., (2000), "An FDTD algorithm with perfectly matched layers for general dispersive media," *IEEE Transactions on Antennas and Propagation*, volume 48, number 5, pages 637-646. (Cited on pages 83, 84, and 85.)

Fang, J., (1989), *Time Domain Finite Difference Computation for Maxwell's Equations*, PhD thesis, University of California, Berkeley, 1989. (Cited on pages 65 and 82.)

Feynman, P., (1964), *Lectures on Physics, the Electromagnetic Field*, Addison-Wesley Publishing Company, inc. (Cited on pages 33 and 35.)

Franchois, A., Pineiro, Y. and Lang, R. H., (1998), "Microwave permittivity measurements of two conifers," *IEEE Transactions on Geoscience and Remote Sensing*, volume 36, number 5, pages 1384-1395. (Cited on page 127.)

Furse, C., (2006), "A survey of phased arrays for medical applications," *Applied Computational Electromagnetic Society Journal*, volume 21, pages 365-379. (Cited on page 67.)

Gabriel, C., (1996), "Compilation of the Dielectric Properties of Body Tissues at RF and Microwave Frequencies',' *Brooks Air Force Tech. Rep. AL/OE-TR-1996-0037.* (Cited on page 82.)

Garcia, S. G., Lee, T. W. and Hagness, S. C., (2002), "On the accuracy of the ADI-FDTD method," *IEEE Antennas and Wireless Propagation Letters*, volume 1, number 1, pages 31-34. (Cited on page 67.)

Garrett, J., and Fear, E., (2014), "Stable and Flexible Materials to Mimic the Dielectric Properties of Human Soft Tissues," *IEEE Antennas and Wireless Propagation Letters*, volume 13, pages 599-602. (Cited on page 45.)

Gedney, S. D., (1996), "An anisotropic perfectly matched layer-absorbing medium for the truncation of FDTD lattices," *IEEE Transactions on Antennas and Propagation*, volume 44, number 12, pages 1630-1639. (Cited on page 100.)

Gedney, S. D., (2006), *Introduction to the Finite-Difference Time-Domain (FDTD) Method for Electromagnetics*, 1st edition, Morgan and Claypool publishers. (Cited on pages 65, 67, 79, 100, and 101.)

Gedney, S. and Zhao, B., (2010), "An auxiliary differential equation formulation for the complex-frequency shifted PML," *IEEE Transactions on Antennas and Propagation*, volume 58, number 3 pages 838-847. (Cited on page 101.)

Giannakis, I., Giannopoulos, A. and Davidson, N., (2012), "Incorporating dispersive electrical properties in FDTD GPR models using a general Cole-Cole dispersion function," *14th International Conference on Ground Penetrating Radar*, pages 232-236. (Cited on pages 57, 83, 84, 115, and 197.)

Giannakis, I., Giannopoulos, A. and Pajewski, L., (2014), "Numerical Modelling of Ground Penetrating Radar Antennas," *EGU General Assembly*, Vienna. (Cited on page 116.)

Giannakis, I., Giannopoulos, A. and Davidson, N., (2014), "Realistic modelling of ground penetrating radar for landmine detection using FDTD," *15th International Conference on Ground Penetrating Radar (GPR)*, pages 983-989. (Cited on pages 63, 113, 117, 187, and 195.)

Giannakis, I. and Giannopoulos, A., (2014), "Realistic Modelling of High Frequency Ground Penetrating Radar for Near Surface Applications," *19th European Meeting of Environmental and Engineering Geophysics*, Athens. (Cited on page 116.)

Giannakis, I. and Giannopoulos, A., (2014), "A novel piecewise linear recursive convolution approach for dispersive media using the Finite-Difference Time-Domain method," *IEEE Transactions on Antennas and Propagations,* volume 62, number 5, pages 2669-2678. (Cited on pages 195, 196, 206, and 209.)

Giannakis, I. and Giannopoulos, A., (2015), "Time-synchronised convolutional perfectly matched layer for improved absorbing performance in FDTD," *IEEE Antennas and Wireless Propagation Letters,* early access available. (Cited on pages 113, 115, 187, and 195.)

Giannakis, I., Giannopoulos, A., Warren, C. and Davidson, N., (2015), "An accurate FDTD numerical modelling framework of ground penetrating radar for landmine detection," *IEEE Journal of Selected Topics in Applied Earth Observations and Remote Sensing,* accepted for publication.. (Cited on page 195.)

Giannakis, I., Giannopoulos, A., Warren, C. and Davidson, N., (2015), "Numerical modeling and neural networks for landmine detection using ground penetrating radar," *8th International Workshop on Advanced Ground Penetrating Radar,* Florence, Italy.. (Cited on pages 114 and 197.)

Giannakis, I., Giannopoulos, A. and Yarovoy, A., (2016), "Model-based evaluation of signal to clutter ratio for landmine detection using ground penetrating radar," *IEEE Transactions on Geoscience and Remote Sensing,* volume PP, number 99, pages 1-10. (Cited on pages 123, 146, and 190.)

Giannopoulos, A., (1997), *The Investigation of Transmission-Line Matrix and Finite Difference Time-Domain Methods for Forward Problem of Ground Probing Radar*, PhD thesis submitted at the University of York. (Cited on pages 3 and 65.)

Giannopoulos, A., (2005), "Modeling ground penetrating radar by GprMax," *Constructions and Buildings Materials*, volume 19, pages 755-762. (Cited on pages 2 and 135.)

Giannopoulos, A., (2008), "An improved new implementation of complex frequency shifted PML for the FDTD method," *IEEE Transactions on Antennas and Propagation*, volume 56, number 9, pages 2995-3000. (Cited on pages 100, 101, 106, 109, and 111.)

Giovanneschi, F., Gonzalez-Huici, M. A. and Uschkerat, U., (2013), "A parametric analysis of time and frequency domain GPR scattering signatures from buried landmine-like targets," *Proceesings of SPIE - The international Society for Optical Engineering,* volume 8709. (Cited on page 3.)

Gonzalez-Huici, M. A., Uschkerat, U. and Hoerdt, A., (2007), "Numerical simulation of electromagnetic-wave propagation for land mine detection using GPR," *IEEE International Geoscience and Remote Sensing Symposium*, pages 4957-4960. (Cited on pages 4, 114, and 130.)

Gonzalez-Huici, M. A., (2012), "A strategy for landmine detection and recognition using simulated GPR responses," *14th International Conference on Ground Penetrating Radar (GPR)*, pages 871-876. (Cited on pages 4, 114, and 130.)

Gonzalez-Huici, M. A., (2013), "Accurate Ground Penetrating Radar Numerical Modeling for Automatic Detection and Recognition of Antipersonnel Landmines," Ph.D thesis, Mathematisch-Naturwissenschaftlichen Fakultät der Rheinischen Friedrich-Wilhelms-Universität Bonn. (Cited on pages 19 and 20.)

Gonzalez-Huici, M. A., Catapano I. and Soldovieri, F., "A comparative study of GPR reconstruction approaches for landmine detection," *IEEE Journal of Selected Topics in Applied Earth Observations and Remote Sensing*, volume 7, number 12, pages 4869-4878 (Cited on page 23.)

Gooneratne, C. P., Mukhopahyay, S. C. and Gupta, G. S., (2004), "A review of sensing technologies for landmine detection: Unmanned vehicle based approach," *2nd International Conference on Autonomous Robots and Agents*, Palmerston North, New Zealand. (Cited on pages 10, 14, and 16.)

Grant, E. H., Buchanan, T. J. and Cook, H. K., (1957), "Dielectric behaviour of water at microwave frequencies," *Journal of Chemical Physics*, volume 26, number 1, pages 156-161. (Cited on page 49.)

Gregoire, C. and Hollender, F., (2004), "Discontinuity characterisation by the inversion of the spectral content of ground-penetrating radar (GPR) reflections–Application of the Jonscher model," *Geophysics*, volume 69, number 6, pages 1414-1424. (Cited on pages 48 and 58.)

Groenenboom, J. and Yarovoy, A., (2002), "Data processing and imaging in GPR system dedicated for landmine detection," *Subsurface Sensing Technology Applications,* volume 3, number 4, pages 387-402 (Cited on page 22.)

Guo, X. M., Guo, Q. X., Zhao, W. and Yu, W. H., (2012), "Parallel FDTD simulation using NUMA acceleration technique," *Progress In Electromagnetics Research Letters*, volume 28, pages 1-8. (Cited on page 66.)

Gurel, L. and Oguz, U., (2000), "Three-dimensional FDTD modelling of a ground-penetrating radar," *IEEE Transactions on Geoscience and Remote Sensing*, volume 38, number 4, pages 1513-1521. (Cited on pages 4, 114, and 146.)

Gurel, L. and Oguz, U., (2001), "Simulations of ground-penetrating radars over lossy and heterogeneous grounds," *IEEE Transactions on Geoscience and Remote Sensing*, volume 39, number 6, pages 1190-1197. (Cited on pages xviii, 3, 4, 114, and 146.)

Gurel, L. and Oguz, U., (2003), "Optimisation of the transmitter-receiver separation in the ground-penetrating radar," *IEEE Transactions on Geoscience and Remote Sensing*, volume 51, number 3, pages 362-370. (Cited on pages 4, 114, and 146.)

Han, M., Dutton, R. W. and Shanhui, F., (2006), "Model dispersive media in finite-difference time-domain method with complex-conjugate pole-residue pairs", *IEEE Microwave and Wireless Components Letters,* volume 16, number 3, pages 119-121. (Cited on pages 83, 84, 85, and 94.)

Hai, L., Takahashi, K. and Sato, M., (2014), "Measurement of dielectric permittivity and thickness of snow and ice on a Brackish Lagoon using GPR," *IEEE Journal of Selected Topics in Applied Earth Observations and Remote Sensing*, volume 7, number 3, pages 820-827. (Cited on page 18.)

Hammon, W. S., McMechan, G. A. and Zeng, X., (2000), "Forensic GOR: finite-difference simulations of responses from buried human remains," *Journal of Applied Geophysics*, volume 45, pages 171-186. (Cited on page 114.)

Havriliak, S. and Negami, S., (1967), "A complex plane representation of dielectric and mechanical relaxation processes in some polymers," *Polymer*, volume 8, pages 161-210. (Cited on pages 47 and 48.)

Havykin Simon, (2009), *Neural Networks and Learning Machines*, Pearson Education, Third edition. (Cited on pages 173, 176, 177, 179, 181, 185, and 186.)

Higdom, R. L., (1986), "Absorbing boundary conditions for difference approximations to the multi-dimensional wave equation," *Mathematics of Computation*, volume 47, pages 437-459. (Cited on page 100.)

Hill, N. E., Vaughan, W. E., Price, A. H. and Davies, M., (1969), *Dielectric Properties and Molecular Behaviour*, Van Nostrand Reinhold Company. (Cited on pages 57 and 154.)

Hillel, D., (1980), *Environmental Soil Physics*, Academic Press. (Cited on page 123.)

Ho, K. C., Carin, L., Gader, P. D. and Wilson, J. N., (2008), "An investigation of using the spectral characteristics from ground penetrating radar for landmine/clutter discrimination," *IEEE Geoscience and Remote Sensing*, volume 46, number 4, pages 1177-1191. (Cited on page 3.)

Hoekstra, P. and Delaney, A., (1974), "Dielectric properties of soils at UHF and microwave frequencies," *Journal of Geophysical Research*, volume 79, number 11, pages 1699-1708. (Cited on pages 45 and 49.)

Horst, R., Pardalos, P. M. and Thoai, N. V., (2000), *Introduction to Global Optimization*, Second Edition, Kluwer Academic Publishers. (Cited on page 81.)

HRW and PHR, (1993), "Landmines: A Deadly Legacy," Library of Congress Catalog Card Number: 93 80418. (Cited on page 9.)

Hu, R., Lu, L. and Wang, S., (2012), "The numerical simulation study on ground penetrating radar detection of the typical adverse geological structure," *14th International Conference on Ground Penetrating Radar (GPR)*, pages 243-247. (Cited on page 114.)

Huang, J. and Turcotte, D. L., (1989), "Fractal mapping pf digitised images: Application to the topography of Arizona and comparisons with synthetic images," *Journal of Geophysical Research*, volume 94, number B6, pages 7491-7495. (Cited on page 123.)

International Committee of the Red Cross (ICRC), (1996), *Anti-personnel landmines: friend or foe? A study of the military use and effectiveness of anti-personnel mines,* Geneva: ICRC. (Cited on pages 9, 10, and 12.)

Ingham, A. E. and Vaughan, R. C., (1990), *The Distribution of Prime Numbers*, Cambringe University Press. (Cited on page 71.)

Ireland, D. and Abbosh, A., (2013), "Modeling Human Head at Microwave Frequencies Using Optimised Debye Models and FDTD Method", *IEEE Transactions on Antennas and Propagation*, volume 61, number 4, pages. 2352-2355. (Cited on page 82.)

Jabro, J. D., Stevens, W. B., Evans, R. G. and Iversen, W. M., (2010), "Spatial variability and correlation of selected soil properties in the AP horizon of a CRP grassland," *Applied Engineering in Agriculture*, volume 26, pages 419-428. (Cited on pages 116 and 123.)

Jain, A. K., Mao, J. and Mohiuddin, K. M., (1996), "Artificial neural networks: a tutorial," *IEEE Computer,* volume 29, number 3, pages 31-44. (Cited on page 185.)

Jin, J. M., (2002), *The Finite Element Method in Electromagnetics*, and ed. New York: John Wiley and Sons. (Cited on pages 65 and 66.)

Jonscher, A. K., (1977), "The 'universal' dielectric response," *Nature*, volume 267, pages 673-679. (Cited on page 48.)

Joseph, R. M., Hagness, S. C. and Taflove, A., (1991), "Direct time integration of Maxwell's equations in linear dispersive media with absorption for scattering and propagation of femtosecond electromagnetic pulses," *Optics Lett.*, volume 16, pages 1412-1414. (Cited on page 83.)

Kaatze, U. and Uhlendorf, V., (1981), "The dielectric properties of water at microwave frequencies," *Zeitchrift Physikalische Chemie Neue Folge*, volume 126, pages 151-165. (Cited on page 49.)

Kaneko, M. A., Fukushim, E. F. and Endo, G., (2014), "A discrimination method for landmines and metal fragments using metal detectors," *The Journal of ERW and Mine Action.* Issue 18.1. (Cited on page 1.)

Kantartzis, V. and Tsiboukis, T. D., (2006), *Higher Order FDTD Schemes for Waveguide and Antenna Structures*, 1st edition, Morgan and Claypool publishers. (Cited on pages 82 and 197.)

Kashiwa, T. and Fukai, I., (1990), "A treatment by the FD-TD method of the dispersive characteristics associated with electronic polarization," *Microwave Optical Technology Letter*, volume 3, number 6, pages 203-205. (Cited on page 83.)

Kelley, D. F. and Luebbers, R. J., (1996), "Piecewise linear recursive convolution for dispersive media using FDTD", *IEEE Transactions on Antennas and Propagation*, volume 44, number 6, pages 792-797. (Cited on pages 83, 86, 87, 94, 101, 108, and 203.)

Kelley, D. F., Destan, T. J. and Luebbers, R. J., (2007), "Debye function expansions of complex permittivity using a hybrid particle swarm-least squares optimisation approach," *IEEE Transactions on Antennas and Propagation*, volume 55, number 7, pages 1999-2005. (Cited on pages 115 and 117.)

Kelley, D. F., Destan, T. J. and Luebbers, R. J., (2007), "Debye Function Expansions of Complex Permittivity Using a Hybrid Particle Swarm-Least

Squares Optimization Approach", *IEEE Transactions on Antennas and Propagation*, volume 55, number 7, pages 1999-2005. (Cited on page 84.)

Kennedy, J. and Eberhart, R. C., (1995), "Particle swarm optimization," *IEEE International Conference on Neural Networks*, volume 4, pages 1942-1948. (Cited on page 117.)

Kim, J. H, Cho, S. J. and Yi, M. J., (2007), "Removal of ringing noise in GPR data by signal processing," *Geosciences Journal*, volume 11, pages 75-81. (Cited on pages 24 and 27.)

Kjartansson, E., (1979), "Constant Q-wave propagation and attenuation," *Journal of Geophysical Research*, volume 84, pages 4737-4748. (Cited on page 48.)

Klein, L. A. and Swift, C. T., (1977), "An improved model for the dielectric constant of sea water at microwave frequencies," *IEEE Transactions on Antennas and Propagation*, volume 25, number 1, pages 104-111. (Cited on pages 50 and 51.)

Klysz, G., Balayssac, J. P., Laurens, S. and Ferrieres, X., (2004), "Numerical FDTD simulation of the direct wave propagation of a GPR coupled antenna," *10th International Conference on Ground Penetrating Radar (GPR)*, volume 1, pages 45-48. (Cited on page 116.)

Klysz, G., Ferrieres, X., Balayssac, J. P. and Laurens, S., (2006), "Simulation of direct wave propagation by numerical FDTD for a GPR coupled antenna," *NDT & E International*, volume 39, number 4, pages 338-347. (Cited on page 116.)

Knuth, D., (1998), Teach Calculus with Big O, *Notices of the American Mathematical Society*, volume 45, page 687. (Cited on page 68.)

Kong, S. C. and Choi, Y. W., (2009), "Finite-Difference Time-Domain (FDTD) model for traveling-wave photodetectors," *Journal of Computational and Theoretical Nanoscience*, volume 6, pages 2380-2387. (Cited on page 67.)

Kopal, Z., (1955), *Numerical Analysis*, Chapman & Hall LTD. (Cited on page 69.)

Koppenjan, J., Streeton, M., Hua, L., Michael, L., Ono, S. and Nevada, B., (2004), "Advanced signal analysis for forensic applications of ground penetrating radar," *10th International Conference on Ground Penetrating Radar (GPR)*, pages 443-446. (Cited on page 1.)

Kowalczyk, S., Lukasiak, D. and Zukowska, K., (2014), "Ground penetrating radar survey in the central and eastern part of the Calowanie Fen, Central Poland," *15th International Conference on Ground Penetrating Radar (GPR)*, pages 1011-1016. (Cited on page 18.)

Kraus, J., (1991), *Electromagnetics*, WCB/McGraw-Hill. (Cited on pages 34, 35, 36, 37, and 42.)

Kreyszig, E., (1999), *Advanced Engineering Mathematics*, Wiley, 8th edition 1999. (Cited on pages 25, 34, 35, 38, 40, 49, 68, 103, 178, and 207.)

Kunz, K., (1957), *Numerical Analysis*, McGraw-Hill Bokk Company, INC. (Cited on page 67.)

Kuzuoglu, M. and Mittra, R., (1996), "Frequency dependence of the constitutive parameters of causal perfectly matched anisotropic absorbers," *IEEE Microwave and Guided Wave Letters*, volume 6, number 12, pages 447-449. (Cited on pages 101 and 106.)

Lambot, S., Slob, E. and Vereecken, H., (2007), "Fast evaluation of zero-offset Grenn's function for layered media with application to ground-penetrating radar," *Geophysical Research Letters*, volume 34, pages L21405. (Cited on page 65.)

Lane, J. A. and Saxton, J. A., (1952), "Dielectric dispersion in pure polar liquids at very high ratio frequencies. III. The effect of electrolytes in solution," *Proceedings of Royal Society*, volume 213, pages 531-545. (Cited on pages 49 and 50.)

Landmine Monitor Report, (2007), "Mine Action Funding", International Campaign to Ban Landmines. (Cited on pages xviii and 14.)

Lazebnik, M., Okoniewski, M., Booske, J. H. and Hagness, S. C., (2007), "Highly Accurate Debye Models for Normal and Malignant Breast Tissue Dielectric Properties at Microwave Frequencies," *IEEE Microwave and Wireless Component Letteres*, volume 17, number 12, pages 822-824. (Cited on page 82.)

LCD3, The World Bank, http://data.worldbank.org/data-catalog/landmine-database, December 2014. (Cited on pages xviii, 9, and 11.)

Letter to President Clinton, (1996). *New York TImes*, A9. (Cited on page 12.)

Lee, K., Chen, C. C., Teixeira, F. L. and Lee, K. H., (2004), "Modelling and investigation of a geometrically complex UWB GPR antenna using FDTD,"

IEEE Transactions on Antennas and Propagation, volume 52, number 8, pages 1983-1991. (Cited on page 116.)

Lee, J. F., Lee, R. and Cangellaris, A. C., (1997), *Time-domain finite-element methods*, Artech House. (Cited on page 65.)

Li, J. and Dai, J., (2006), "Z-Transform implementation of the CFS-PML for arbitrary media," *IEEE Microwave Component Letters*, volume 16, number 8, pages 437-439. (Cited on page 101.)

Li, J., Guo, L. X., Jiao, Y. C. and Wang, R., (2013), "Composite Scattering of a Plasma-Coated Target Above Dispersive Sea Surface by the ADE-FDTD Method," *IEEE Geoscience and Remote Sensing Letters*, volume 10, number 1, pages 4-8. (Cited on page 82.)

Liao, Z. P., Wong, H. L., Yang, B. P. and Yuan, Y. F., (1984), "A transmitting boundary for transient wave analyses," *Scientia Sinica*, (series A), volume XXVII, pages 1063-1076. (Cited on page 100.)

Liebe, H. J., Hufford, G. A. and Manabe, T., (1991), "A model for the complex permittivity of water at frequencies below 1 THz," *International Journal of Infrared and Millimeter Waves*, volume 12, number 7, pages 659-675. (Cited on page 49.)

Lin, Z. and Thylen, L., (2009), "On the Accuracy and Stability of Several Widely Used FDTD Approaches for Modelling Lorentz Dielectrics," *IEEE Transactions on Antennas and Propagations*, volume 57, number 10, pages 3378-3381. (Cited on page 83.)

Lin, H., Pantoja, M. F., Angulo, L. D., Alvarez, J., Martin, R. G. and Garcia, S. G., (2012), "FDTD Modelling of Graphene Devices Using Complex Conjugate Dispersion Material Model", *IEEE Microwave and Wireless Component Letters*, volume 22, number 12, pages 612-614. (Cited on pages 84 and 94.)

Liu, G. H., (1997), "The pseudo spectral time-domain (PSTD) method: A new algorithm for solutions of Maxwell's equations", *IEEE Antennas and Propagation Society International Symposium*, Montreal, Canada, volume 45, pages 430-442. (Cited on page 65.)

Liu, S., Yuan, N. and Mo, J., (2003), "A novel FDTD formulation for dispersive media," *IEEE Microwave and Wireless Component Letters,* volume 13, number 5, pages 187-189. (Cited on page 83.)

Liu, S., Liu, S. Q. and Liu, S. B., (2010), "Finite-difference time-domain algorithm for plasma based on trapezoidal recursive convolution technique,"

Journal of Infrared Millimeter TeraHz Waves, volume 31, number 5, pages 620-628. (Cited on page 82.)

Lopera, O. and Milisavljevic, N., (2007), "Prediction of the effects of soil and target properties on the antipersonnel landmine detection performance of ground-penetrating radar: A Colombian case study", *Journal of Applied Geophysics*, volume 63, pages 13-23. (Cited on pages 3 and 4.)

Luebbers, R. J., Hunsberger, F. P., Kunz, K. S., Standler, R. B. and Schneider, M., (1990), "A frequency-dependent finite-difference time-domain formulation for dispersive materials," *IEEE Transactions on Electromagnetic Compatibility,* volume 32, number 3, pages 222- 227. (Cited on pages 83 and 93.)

Luebbers, R. J., Hunsberger, F. and Kunz, K. S., (1991), "A frequency-dependent finite-difference time-domain formulation for transient propagation in plasma," *IEEE Transactions on Antennas and Propagation*, volume 39, number 1, pages 29-34. (Cited on pages 83, 101, 107, and 108.)

Luebbers, R. J. and Hunsberger, F., (1992), "FDTD for Nth-order dispersive media," *IEEE Transactions on Antennas and Propagation*, volume 40, number 11, pages 1297-1301. (Cited on pages 83 and 95.)

Luebbers, J. R. and Kunz, K., (1993), *The Finite Difference Time Domain Method for Electromagnetics.* Boca Raton, FL: CRC Press. (Cited on pages 44, 45, 46, 47, 65, and 98.)

Malmberg, C. G. and Maryott, A. A., (1956), "Dielectric constant of water from 0^o to 100^o C," *Journal of Research of the National Bureau of Standards*, volume 56, number 1, pages 1-7. (Cited on page 50.)

Matzier, C., (1998), "Microwave permittivity of dry sand," *IEEE Geoscience and Remote Sensing Letters*, volume 36, number 1, pages 317-319. (Cited on page 83.)

Maxwell, J. C., (1865), *A Dynamical Theory of the Electromagnetic Field*, Martino Publishing. (Cited on page 42.)

Mayordomo, A. M. and Yarovoy, A., (2008), "Optimal background subtraction in GPR for humanitarian demining," *Proccedings of the 5th European Radar Conference*, Amsterdam, The Netherlands, pp. 48-51 (Cited on page 22.)

McFadden, M. and Scott, W. R., (2009), "Numerical modelling of a spiral-antenna GPR system," *IEEE International Geoscience and Remote Sensing Symposium*, volume 2, pages 109-112. (Cited on page 116.)

Meles, G. A., (2011), *New Developments in Full Waveform Inversion of GPR Data*, D.Sc thesis, ETH Zurich. (Cited on page 17.)

Merwe, A. and Gupta, I., "A novel signal processing technique for clutter reduction in GPR measurements of small, shallow landmines," *IEEE Transactions on Geoscience and Remote Sensing*, volume 38, number 6, pages 2627-2637. (Cited on page 22.)

Metwaly, M., (2007), "Detection of metallic and plastic landmines using GPR and 2-D resistivity techniques," *Natural Hazards and Earth Systems Sciences,* volume 7, pages 755-763. (Cited on pages 4, 16, and 130.)

Moller, M. F., (1993), "Scaled conjugate gradient algorithm for fast supervised learning," *Neural Networks*, volume 6, pages 525-533.. (Cited on page 185.)

Montoya, T. P. and Smith, G. S., (1996), "Resistively-loaded Vee antennas for short-pulse ground penetrating radar," *IEEE Antennas and Propagation Society International Symposium*, volume 3, pages 2068-2071. (Cited on page 116.)

Moxley, F. I., Chuss, D. T. and Dai, W., (2013), "A generalised finite-difference time-domain scheme for solving nonlinear Schrodinger equations," *Computer Physics Communications*, volume 184, pages 1834-1841.. (Cited on page 66.)

Mur, G., (1981), "Absorbing boundary conditions for the finite-dofference approximation of the time-domain electromagnetic field equations," *IEEE Transactions of Electromagnetic Compatibility*, volume 23, pages 377-382. (Cited on page 100.)

Namiki, T., (1999), "A new FDTD algorithm based on alternating0direction implicit method," *IEEE Transactions on Microwave Theory and Techniques*, volume 47, pages 2003-2007. (Cited on pages 65 and 67.)

Negri, S. and Quarta, T. A. M., (2012), "Ground penetrating radar survey for civil engineering applications: Results from the test site," *14th International Conference on Ground Penetrating Radar*, pages 835-839. (Cited on page 17.)

Neuman, J. V. and Richtmyer, R. D., (1950), "A method for the numerical calculation of hydrodynamic shocks," *Journal of Applied Physics*, volume 21, pages 232-237. (Cited on page 66.)

Nishimoto, M., Ueno. S. and Kimura, Y., (2006), "Feature extraction from GPR data for identification of landmine-like objects under rough ground surface," *Journal of Electromagnetic Waves and Applications*, volume 20, number 12, pages 1577-1586. (Cited on page 4.)

Nuzzo, L., Alli, G., Guidi, R., Cortesi, N., Sarri, A. and Manacorda, G., (2014), "A new densely-sampled Ground Penetrating Radar array for landmine detection," *15th International Conference on Ground Penetrating Radar*, pages 969-974. (Cited on pages 4 and 129.)

Oguz, U. and Gurel, L., (2002), "Frequency responses of ground-penetrating radars operating over highly lossy grounds," *IEEE Transactions on Geoscience and Remote Sensing*, volume 40, number 6, pages 1385-1394. (Cited on pages 4, 114, and 146.)

Okoniewski, M., Mrozowski, M. and Stuchly, M. A., (1997), "Simple treatment of multi-term dispersion in FDTD',' *IEEE Microwave Guided Wave Letters,* volume 7, number 5, pages 121-123. (Cited on page 83.)

Ozturk, C. and Drahor, M. G., (2010), "Synthetic GPR modelling studies on shallow geological properties and its comparison with the real data," *13th International Conference on Ground Penetrating Radar (GPR)*, pages 1-4. (Cited on page 114.)

Pajewski, L., Benedetto, A., Derobert, X., Giannopoulos, A., Loizos, A., Manacorda, G., Marciniak, M., Plati, C., Schettini, G. and Trinks, I., (2013), "Applications of Ground Penetrating Radar in civil engineering - COST action TU1208," *7th International Workshop on Advanced Ground Penetrating Radar*, pages 1-6. (Cited on page 17.)

Panzner, B., Jostingmeier. A. and Omar., A., (2010), "A compact double-ridged horn antenna for ground penetrating radar applications," *7th International Workshop on Advanced Ground Penetrating Radar*, pages 1-6. (Cited on pages 4 and 130.)

Park, K., Park, S., Kim, K. and Hee Ko, K., (2013) "Multi-feature based detection of landmines using ground penetrating radar," *Progress In Electromagnetic Research*, volume 134, pages 455-474. (Cited on page 22.)

Peplinski, N. R., Ulaby, F. T. and Dobson M. C., (1995), "Dielectric properties of soils in the 0.3-1.3 GHz range," *IEEE Transactions on Geoscience and Remote Sensing*, volume 33, number 3, pages 803-807. (Cited on pages xx, 60, 61, 62, 63, 64, 117, 154, 196, and 197.)

Peplinski, N. R., Ulaby, F. T. and Dobson, M. C., (1995), "Corrections to dielectric properties of soils in the 0.3-1.3 GHz range," *IEEE Transactions on Geoscience and Remote Sensing*, volume 33, number 6, pages 1340. (Cited on page 60.)

Peterson, A. F., Ray, S. L. and Mittra, R., (1998), *Computational Methods for Electromagnetics*, New York: IEEE Press. (Cited on page 65.)

Phuong, T. A., Mahmoudzadeh Ardekani, M. R. and Lambot, S., (2012), "Coupling of dielectric mixing models with full-wave ground-penetrating radar signal inversion for sandy-soil-moisture estimation," *Geophysics*, volume 77, number 3, pages H33-H44. (Cited on pages 50 and 56.)

Physicians for the Human Rights, (1993), *Landmines, A deadly Legacy*, Human Rights Watch. (Cited on pages 131, 132, and 163.)

Pieraccini, M., Bicci, A., Mecatti, D., Macaluso, G. and Atzeni, C., (2009), "Propagation of Large Bandwidth Microwave Signals in Water," *IEEE Transactions on Antennas and Propagation*, volume 57, number. 11, pages. 3612-3618. (Cited on page 82.)

Plett, G. L., Doi, T. and Torrieri, D., (1997), "Mine detection using scattering parameters and an artificial neural network," *IEEE Transactions of Neural Networks*, volume 8, number 6, pages 1456-1467. (Cited on pages 173, 179, 181, and 190.)

Poularikas, A. D., (1996), *The Transforms and Applications Handbook*, First edition, Boca Raton: CRC Press LLC. (Cited on pages 90 and 206.)

Radzevivious, S. J. and Daniels, J. J., (2000), "Ground penetrating radar polarisation and scattering from cylinders," *Journal of Applied Geophysics*, volume 45, pages 111-125. (Cited on page 145.)

Random House Dictionary, (2012), "Land mine," *Random House, Inc.* (Cited on page 7.)

Rea, J. and Knight, R., (1998), "Geostatistical analysis of ground-penetrating radar data: A means of describing spatial variation in the subsurface," *Water resources research,* volume 34, pages 329-339. (Cited on page 116.)

Rezaur, R. B., Rahardjo, H. and Leong, E. C., (2002), "Spatial and temporal variability of pore-water pressures in residual soil slopes in a tropical climate," *Earth Surface Processes and Landforms*, volume 27, pages 317-338. (Cited on pages 116 and 123.)

Riaz, M. M., Ghafoor, A., (2013), "Ground penetrating radar image enhancement using singular value decomposition," *IEEE International Symposium in Circuits and Systems (ISCAS)*, pages 2388-2391. (Cited on page 24.)

Riaz, M. M., Ghafoor, A. and Sreeram, V., (2013), "Fuzzy C-means and principal component analysis based GPR image enhancement," *IEEE Radar Conference (RADAR)*, pages 1-4. (Cited on page 26.)

Roden, J., Gedney, S., (2000), "Convolution PML (CPML): an efficient FDTD implementation of the CFS-PML for arbitrarily media," *Microwave Optical Technology Letters,* volume 27, pages 334-339. (Cited on pages 101, 107, and 108.)

Roth, F., Genderen, P. and Verhaegen, M., (2005), "Convolutional models for buried target characterisation with ground penetrating radar," *IEEE Transactions on Antennas and Propagation*, volume 53, number 1, pages 3799-3810. (Cited on page 3.)

Sadiku, M. N. O., (2000), *Numerical techniques in electromagnetics* , 2nd edition, CRC press. (Cited on page 65.)

Sato, M., Guangyou, F. and Zhaofa, Z., (2003), "Landmine detection by a broadband GPR system," *IEEE Geoscience and Remote Sensing Symposium*, volume 2, pages 758-760. (Cited on pages 4 and 129.)

Sato, M., Xuan, F. and Fujiwara, J., (2007), "Handheld GPR and MD sensor for landmine detection," *IEEE Antennas and Propagation Society International Symposium*, volume 3B, pages 18-21. (Cited on pages 4 and 129.)

Sato, M., Takahashi, K and Fujiwara, J., (2007), "Hand held dual sensor ALIS and its evaluation test in Cambodia," *Geoscience and Remote Sensing Symposium*, pages 18-21. (Cited on page 16.)

Savelyev, A., Yarovoy, A. and Ligthart, L., (2007), "Experimental evaluation of an array GPR for landmine detection," *European Radar Conference EuRAD*, pages 220-223. (Cited on pages 4 and 129.)

Schroder, C. T. and Scott, W. R., (2000), "A finite-difference model to study the elastic-wave interactions with buried landmines," *IEEE Transactions on Geoscience and Remote Senssing*, volume 38, number 4, pages 1505-1512. (Cited on page 16.)

Schneider, J. B. and Wagner, C. L., (1999), "FDTD Dispersion revisited: faster-then-light propagation," *IEEE Transactions of Microwave and Guided Wave Letters*, volume 9, number 2, pages 623-650. (Cited on page 81.)

Schofield, J., Daniels, J. and Hammerton, P., (2014), "A multiple migration and stacking algorithm designed for land mine detection" *IEEE Transactions*

on Geoscience and Remote Sensing, volume 52, number 11, pages 6983-6988. (Cited on pages 23, 146, 171, and 172.)

Semenov, S. Y., (1995), "Comparative modelling of water saline and myocardium dielectric properties in the microwave spectrum," *IEEE 25th Microwave Conference*, volume 2, pages 852-855. (Cited on page 45.)

Sengwa, R. J. and Soni, A., (2006), "Low-frequency dielectric dispersion and microwave dielectric properties of dry and water-saturated limestones of the Jodhpur region," *Geophysics*, volume 71, number 5, pages G269-G277. (Cited on page 58.)

Shutko, M. A. and Reutov, E. M., (1982), "Mixture formulas applied in estimation of dielectric and radiative characteristics of soils and grounds at microwave frequencies," *IEEE Transactions on Geoscience and Remote Sensing*, volume GE-20, number 1, pages 29-32. (Cited on pages 55 and 56.)

Shibayama, J., Ando, R., Nomura, A., Yamauchi, J. and Nakano, H., (2009), "Simple Trapezoidal Recursive Convolution Technique for the Frequency-Dependent FDTD Analysis of a Drude-Lorentz Model," *IEEE Photonic Technology Letters,* volume 21, number 2, pages 100-102. (Cited on page 83.)

Shrestha, B. L., Wood, H. C. and Sokhansanj, S., (2007), "Modelling of vegetation permittivity at microwave frequencies," *IEEE Transactions on Geoscience and Remote Sensing*, volume 45, number 2, pages 342-348. (Cited on page 127.)

Sixin, L., Junjun. W., Junfeng. Z. and Zhaofa, Z., (2011), "Numerical simulations of borehole radar detection for metal ore," *IEEE Transactions on Geoscience and Remote Sensing*, volume 8, number 2, pages 308-312. (Cited on page 114.)

Sixin, L. and Yanqian, F., (2011), "Airborne GPR: Advances and numerical simulation," *IEEE International Geoscience and Remote Sensing Symposium*, pages 3397-3400. (Cited on page 114.)

Siushansian, R. and Lo Vetri, J., (1997), "Efficient evaluation of convolution integrals arising in FDTD formulations of electromagnetic dispersive media," *Journal of Electromagnetic Waves Applications*, volume 11, number 1, pages 101-117. (Cited on pages 83, 94, 101, and 108.)

Sommerfeld, A., (1909), "Propagation of waves in wireless telegraphy," *Annual Physics*, volume 28, pages 665-736. (Cited on page 65.)

Speiser, D., (2008), *Discovering the Principles of Mechanics*. Birkhauser. (Cited on page 39.)

Sreenivas, K., Venkatartnam, L. and Narasimha rao, P. V., (1994), "Dielectric properties of salt affected soils," *International Journal of Remote Sensing*, volume 16, pages 641-649. (Cited on pages 51 and 54.)

Stiefel, E. L., (1963), *An Introduction to Numerical Mathematics*, New York Academic Press London. (Cited on pages 70 and 71.)

Stogryn, A., (1971), "Equations for calculating the dielectric constant of saline water," *IEEE Transactions of Antennas and Propagation*, volume MTT-19, pages 733-736. (Cited on pages 50, 154, and 156.)

Strobach, E., Harris, B. D., Dupuis, J., C. and Kepi, A., W., (2013), "Waveguide properties recovered from shallow diffractions in common offset GPR," *Journal of Geophysical Research*, volume 118, pages 39-50. (Cited on page 160.)

Sullivan, D. M., (1992), "Frequency-dependent FDTD methods using Z transforms," *IEEE Transaction on Antennas and Propagation*, volume 40, number 10, pages 1223-1230. (Cited on page 83.)

Sullivan, D. M., (1994), "The use of Z transform theory for numerical simulation of dispersive and non-linear materials with the FDTD method," *Antennas and Propagation Society International Symposium*, volume 3, pages 1450-1453. (Cited on page 83.)

Tabony, J., Carlson, D. O., Duvoisin, H. A. and Torres-Rosario, J., (2010), "Detection of bulk explosives using the GPR only portion of the HSTAMIDS system," *Proceedings of SPIE*, col 7664. (Cited on page 129.)

Taflove, A. and Brodwin, M. E., (1975), "Numerical solution of steady-state electromagnetic scattering problems using the time-dependent Maxwell's equations," *IEEE Transactions of Microwave Theory and Techniques*, volume 23, pages 54-56. (Cited on pages 77 and 78.)

Taflove, A., (1980), "Application of the finite-difference time-domain method to sinusoidal steady state electromagnetic penetration problems," *IEEE Transactions on Electromagnetic Compatibility*, volume 22, pages 191-202.. (Cited on page 66.)

Taflove, A. and Hagness, S. C., (2000), *Computational electrodynamics, the finite-difference time-domain method*, and ed. Norwood, MA: Artech House. (Cited on pages 35, 66, 67, 83, 121, and 135.)

Taflove, A. and Hagness, S., (2005), *Computational Electromagnetics: The Finite-Difference Time-Domain Method*. Artech House Norwood, MA, 3rd edition. (Cited on pages xxii, 45, 46, 47, 65, 77, 78, 79, 80, 81, 100, 102, 108, 109, 110, 111, and 181.)

Taflove, A., Oskooi, A. and Johnson, G., (2013), "Advances in FDTD Computational Electrodynamics," *IEEE Transactions of Antennas and Propagation*, volume 45, number 3, pages 430-442. (Cited on page 65.)

Taherian, M. R., Kenyon, W. E. and Safinya, K. A., (1990), "Measurement of dielectric response of water-saturated rocks," *Geophysics*, volume 55, number 12, pages 1530-1541. (Cited on page 58.)

Takahashi, K., Igel, J. and Preetz, H., (2012), "Modelling of GPR clutter caused by soil heterogeneity" *International Journal of Antennas and Propagation*, volume 2012, Article ID 643430, 7 pages, 2012. doi:10.1155/2012/643430. (Cited on page 123.)

Takahashi, K., Igel, J., Preetz, H. and Sato, M., (2014), "Influence of heterogeneous soils and clutter in the performance of ground-penetrating radar for landmine detection" *IEEE Transactions on Geoscience and Remote Sensing*, volume 52, number 6, pages 3464-3472. (Cited on page 123.)

Takayama, Y. and Klaus, W., (2002), "Reinterpretation of the auxiliary differential equation method for FDTD," *IEEE Microwwave and Wireless Component Letters,* volume 12, number 3, pages 102-104. (Cited on page 83.)

Tan, H. S., (1981), "Microwave measurements and modelling of the permittivity of tropical vegetation samples," *Applied Physics*, volume 25, pages 351-355. (Cited on pages 116 and 128.)

Taoufik, B., Jamal, E. R., Francois, B. and Gerald, B., (2008), "Application of Jonscher model for the characterisation of the dielectric permittivity of concrete," *Journal of Physics D: Applied Physics*, volume 41. (Cited on page 48.)

Teggatz, A., Jonstingmeier, T. and Omar, A., S., (2005), "Detection of buried objects such as landmines using a forward impulse radiating antenna (IRA)," *IEEE Antennas and Propagation Society International Symposium*, volume 2A, pages 627-630. (Cited on pages 4 and 129.)

Teixeira, F. L. and Chew, W. C., (1995), "PML-FDTD in cylindrical and spherical coordinates," *IEEE Microwave Guided Wave letters,* volume 43, pages 1460-1463. (Cited on page 100.)

Teixeira, F. L., Chew, W. C., Straka, M., Oristaglio, M. L. and Wang, T., (1998), "Finite-difference time- domain simulation of ground penetrating radar on dispersive, inhomogeneous, and conductive soils", *IEEE Transactions on Geoscience and Remote Sensing*, volume 36, pages 1928-1937. (Cited on page 83.)

Tesfamariam, G. T., (2013), *Signal Processing Techniques for Landmine Detection Using Impulse Ground Penetrating Radar*, PhD thesis submitted at Elektotechnik ind Informationstechnik der Technischen Universitat Darmstadt. (Cited on pages 4, 27, and 130.)

Topp, G. C., Davis, J. L. and Annan, A. P., (1980), "Electromagnetic determination of ski water content: measurements in coaxial transmission lines," *Water Resources Research*, volume 16, number 3, pages 574-582. (Cited on pages xx, 54, 55, 62, and 64.)

Torres, F., Vaudon, P. and Jecko, B., (1996), "Application of fractional derivatives to the FDTD modelling of pulse propagation in a Cole-Cole dispersive medium," *Microwave Optical Technology Letters*, volume 13, number 5, pages 300-304. (Cited on page 115.)

Trabelsi, S. and Nelson, S., (2006), "Temperature-dependent behaviour of dielectric proper ties of bound water in grain at microwave frequencies," *Measurement Science and Technology*, volume 17, pages 2289-2293. (Cited on page 57.)

Turcotte, D. L., (1987), "A fractal interpretation of topography and geoid spectra on the Earth, Moon, Venus and Mars," *Journal of Geophysical Research*, volume 92, number B4, pages E597- E601. (Cited on pages 116, 123, and 195.)

Turcotte, D. L., (1992), *Fractals and chaos in geology and geophysics*, The Press Syndicate of the University of Cambridge. (Cited on pages xxiii, 116, 122, 123, and 125.)

Turk, A. S., Sahinkaya, D. A., Sezgin, M. and Nazli, H., (2007), "Investigation of convenient antenna designs for ultra-wide band GPR systems," *4th International Workshop on Advanced Ground Penetrating Radar (GPR)*, pages 192-196. (Cited on page 116.)

Uduwawala, D., (2006), "Modeling and investigation of planar parabolic dipoles for GPR applications: A comparison with bow-tie using FDTD," *Journal of Electromagnetic Waves and Applications*, volume 20, pages 227-236. (Cited on page 116.)

Uduwawala, D., Norgren, M. and Fuks, P., (2005), "A complete FDTD simulation of a real GPR antenna system operating above lossy and dispersive grounds," *Progress In Electromagnetics Research PIER*, volume 50, pages 209-229. (Cited on page 83.)

Ulaby, F. T. and Jedlicka, R. P., (1984), "Microwave dielectric properties of plant materials," *IEEE Transactions on Geoscience and Remote Sensing*, vol. GE-22, number 4, pages 406-415. (Cited on page 127.)

Ulaby, F. T. and El-Rayes, M. A., (1987), "Microwave dielectric spectrum of vegetation - Part II: Dual-dispersion model," *IEEE Transactions on Geoscience and Remote Sensing*, volume GE-25, number 5, pages 550-557. (Cited on page 127.)

UN Secretary-General, (1994), *Assistance in mine clearance*, document A/49/357. (Cited on pages 9 and 14.)

US Army, (1956), *The Law of Land Warfare*, Field Manual 27-10, volume 19. (Cited on page 12.)

US Defence Intelligence Agency and US Army Foreign Science and Technology Center, (1992), "Landmines Warfare–Trends and Projections," DST-1160S-019. (Cited on page 7.)

Van Genderen, P., Nicolaescu, I. and Zijderverd, J., (2003), "Some experience with the use of spiral antennas for a GPR for landmine detection," *Proceedings of the International Radar Conference*, pages 219-223. (Cited on pages 4 and 129.)

Vial, A., Grimault, A. S., Macias, D., Barchiesi, D. and Chapelle, M. D., (2005), "Improved analytical fit of gold dispersion. Application to the modelling of extinction spectra with a finite- difference time-domain method," *Physical Review B*, volume 71, number 8. (Cited on page 83.)

VonHippel, A. R., (1954), *Dielectric Materials and Apllications*, MIT press, Cambridge, Mass. (Cited on page 49.)

Warren, C., (2009), *Numerical modelling of high-frequency Ground-Penetrating Radar antennas*, PhD thesis, Department of Infrastructure and Environment, The University of Edinburgh. (Cited on pages 5, 19, 131, and 196.)

Warren, C., Giannopoulos, A., (2011), "Creating finite-difference time-domain models of commercial ground-penetrating radar antennas using Taguchi's optimisation method," *Geophysics*, volume 76, number 2, pages G37-G47. (Cited on pages xxiii, 5, 116, 130, and 131.)

Warren, C., Giannopoulos, A., (2012), "Investigation of the directivity of a commercial ground-penetrating radar antenna using a finite-difference time-domain antenna model," *14th International Conference on Ground Penetrating Radar (GPR)*, pages 226-231. (Cited on pages 5, 116, 130, and 131.)

Warren, C., Giannopoulos, A. and Giannakis, I., (2015), "An advanced GPR modelling framework, the next generation of gprMax," *8th International Workshop on Advanced Ground Penetrating Radar*, Florence. (Cited on page 198.)

Wang, T. and Oristaglio, M. L., (2000), "3-D simulation of GPR surveys over pipes in dispersive soils," *Geophysics*, volume 65, number 5, pages 1560-1568. (Cited on page 83.)

Weedon, W. H. and Rappaport, C. M., (1997), "A general method for FDTD modelling of wave propagation in arbitrary frequency-dispersive dielectrics," *IEEE Transactions on Antennas and Propagation*, volume 45, pages 401-410. (Cited on pages 83 and 115.)

Wilson, V., Power, C., Giannopoulos, A., Gerhard, J. and Grant, G., (2009), "DNAPL mapping by ground penetrating radar examined via numerical simulation," *Journal of Applied Geophysics*, volume 69, pages 140-149. (Cited on page 114.)

Wu., R., Clement, A., Li., J., Larsson, E. G., Bradley, M., Habersat, J. and Maksymonko, G., (2001), "Adaptive ground bounce removal," *IEEE Electronics Letters,* volume 37, number 20, pages 1250-1252. (Cited on page 22.)

Xianqi, H., Ziqiang, Z., Guangyin, L. and Qunyi, L., (2009), "The FDTD modeling of GPR for tunnel inspection," *IEEE International Conference on Information Engineering and Computer Science,* pages 1-4. (Cited on page 114.)

Xiaoxian, Z., McMechan, G. A. and Xu, T., (2000), "Synthesis of amplitude-versus-offset variations in ground-penetrating radar data," *Geophysics*, Volume 65, number 1, pages 113-125. (Cited on page 57.)

Xu, T., McMechan, G. A., (1997), "GPR Attenuation and its numerical simulation in 2.5 Dimensions," *Geophysics*, volume 62, number 1, pages 403-414. (Cited on page 115.)

Yale University Press, (1961), *The Papers of Benjamin Franklin.* (Cited on page 35.)

Yang, C-C. and Bose, N. K., (2005), "Landmine detection and classification with complex-valued hybrid neural network using scattering parameters dataset," *IEEE Transactions on Neural Networks*, volume 16, pages 743-753. (Cited on pages 173, 181, 186, and 190.)

Yansui Liu, Q. F. and Mikami, M., (2004), "Geostatistical analysis of soil moisture variability in grassland," *Journal of Arid Environments*, volume 58, pages 357-372. (Cited on pages 116 and 123.)

Yee, K., (1966), "Numerical solution of initial boundary equations in isotropic media," *IEEE Transactions on Antennas and Propagation*, volume 14, pages 302-307. (Cited on pages 65, 66, 67, 74, 80, 81, and 135.)

Youn, H and Chen, C-C, (2005), "Special GPR antenna developments for landmine and UXO surveys," *IEEE Antennas and Propagation International Symposium*, volume 3B, pages 100-103. (Cited on pages 4 and 129.)

Young, J. L. and Nelson, R. O., (2001), "A summary and systematic analysis of FDTD algorithms for linearly dispersive media," *IEEE Transactions on Antennas and Propagation*, volume 43, number 1, pages 61-126. (Cited on page 83.)

Zahn, M., Ohki, Y., Fenneman, D. B., Gripshover, R. J. and Gehman, V. H., (1986), "Dielectric properties of water/ethylene glycol mixtures for use in pulsed power system design," *Proceedings of the IEEE*, volume 74, number 9, pages 1182-1221. (Cited on page 45.)

Zhuansun, X. and Ma, X., (2012), "Bilinear transform implementation of the SC-PML for general media and general FDTD schemes," *IEEE Transactions on Electromagnetic Compatibility*, volume 54, number 2, pages 343-350. (Cited on page 101.)

Zhu, B., Chen, J., Zhong, W. and Liu, Q. H., (1997), "A hybrid FETD-FDTD method with nonconforming meshes," *Communication Computer Physics*, volume 9, number 3, pages 828-842. (Cited on pages 65 and 66.)